CONSTRAINING CHEMICAL KINETICS OF URANIUM OXIDES IN EXTREME ENVIRONMENTS

BY

MIKHAIL FINKO

DISSERTATION

Submitted in partial fulfillment of the requirements
for the degree of Doctor of Philosophy in Nuclear, Plasma, and Radiological Engineering
in the Graduate College of the
University of Illinois Urbana-Champaign, 2022

Urbana, Illinois

Doctoral Committee:

Professor Davide Curreli, Chair
Professor Nick G. Glumac
Professor Mohan Sankaran
Dr. Harry B. Radousky

Abstract

Current understanding of metallic chemistry in extreme environments, such as nuclear fireballs, remains limited due to the multitude of physical processes and timescales involved. In particular, many chemical and plasma chemical reaction pathways responsible for forming uranium molecular species remain either unknown or unverified. In recent years, this longstanding knowledge gap has been the target of an increasing number of experimental characterizations, which this work aims to leverage to produce an updated model of uranium oxide (UO_x) formation in extreme environments.

To this end, a Monte Carlo Genetic Algorithm (MCGA) is utilized to calibrate a UO_x reaction mechanism using measurements from a plasma flow reactor (PFR). In addition, laser ablation modeling capabilities are assessed for use in future chemical validation studies. These two systems cover a complementary range of detonation-relevant flow regimes and cooling timescales. Bench-top laser ablation systems produce high temperature (>11,600 K) rapidly cooling (ns-μs) uranium plumes following laser-induced vaporization and shock expansion. The PFR, on the other hand, features a steady flow of uranium through a plasma torch (<10,000 K) cooling over longer (ms) timescales. The PFR is uniquely suited for the initial calibration of the reaction mechanism due to the relative ease of modeling the system. Thus, the MCGA optimization is limited to the PFR system in this work. Laser ablation, on the other hand, provides a potential test of the resulting mechanism over a wider range of detonation-relevant conditions. Performing such a test, however, requires first developing a predictive ablation model capable of capturing both the complex fluid dynamics and plasma chemistry of an ablation plume. Therefore, we evaluate the suitability of current

modeling tools towards this problem and subsequently propose a coupled modeling approach for investigating ablation plume dynamics and chemistry. Lastly, synthetic diagnostics of emission and absorption spectroscopy signals are used to facilitate the characterization of both systems by enabling direct comparisons between simulations and measurements.

The optimization of a UO_x reaction mechanism using PFR measurements is the primary scientific result of this work. The MCGA is used to identify dominant reaction channels and corresponding rate coefficients that produce the best agreement with available PFR data. The resulting reaction mechanism is compared against a previously constructed UO_x mechanism, and differences in reaction rates and favorable reaction pathways are identified through a sensitivity analysis. Finally, recommendations for an updated UO_x reaction mechanism are made, with considerations based on the limited constraining dataset.

The secondary scientific result of this work is the development of a one-way coupled radiation hydrodynamics and reactive CFD modeling approach for simulating ns duration pulsed laser ablation in reactive atmospheres. These simulations are used to study the interplay between fluid dynamics and chemistry in low-Z (aluminum and carbon) ablation plumes over ns to μs timescales. As a validation exercise, the ablation model results are compared against high fidelity plume imaging, time-of-flight expansion velocities, and spectroscopic molecular formation measurements. Reasonable agreement is observed across these comparisons and potential future refinements to the modeling approach are identified.

Acknowledgments

First of all, I would like to thank my parents, Valentina and Sergey, for their inestimable support and encouragement over the course of my academic journey. I would also like to thank my brother Anton and my friend Kirill for their support over the years.

I am immensely grateful to my advisor Davide Curreli for his support and guidance throughout my graduate studies. I have greatly benefited from both your mentorship and the research opportunities you afforded to me. Thank you for being an incredible role model of a tireless, meticulous, and caring researcher. It has been an honor and a privilege to learn from you in my time at the university. I would also like to thank the members of the doctoral committee (Nick Glumac, Mohan Sankaran, and Harry Radousky) for improving the quality of this work through their questions and suggestions. Thanks also to all my colleagues at the Laboratory of Computational Plasma Physics for providing valuable feedback and support during my time at the university. Lastly, I would like to thank the entire NPRE department for continuously providing a great learning environment for its students.

This work would not be possible without the support of the Graduate Research Scholar Program at Lawrence Livermore National Laboratory. I am indebted to numerous people at LLNL for assisting me with my research. First, huge thanks to Batikan Koroglu for allowing me to use the plasma flow reactor for this work and helping me with taking the measurements, as well as for the many invaluable discussions over the last few years. I would also like to thank Kate Rodriguez for taking the time to assist with the PFR experiments. On the laser ablation side of things, I would like to thank Jonathan Crowhurst, David Weisz, and Emily Weerakkody for their experimental work and many helpful discussions. Thanks

also to Wesley Keller for sharing his expertise regarding laser ablation modeling. Lastly, I would like to thank (in no particular order) Tim Rose, Kim Knight, Harry Radousky, and Scott Wagnon for various discussions and support during my time at the lab.

This project was sponsored by the DoD, Defense Threat Reduction Agency, grants HDTRA1-16-1-0020 and HDTRA1-20-2-0001. This work was performed in part under the auspices of the U.S. DoE by Lawrence Livermore National Laboratory under Contract DE-AC52-07NA27344. Funding also provided by Laboratory Directed Research and Development grant 20-SI-006 (PI: K. Knight). The FLASH code used in this work was in part developed by the DOE NNSA-ASC OASCR Flash Center at the University of Chicago. The content of the information does not necessarily reflect the position or the policy of the federal government, and no official endorsement should be inferred.

Table of Contents

List of Tables

List of Figures

Chapter 1

Introduction

The study of nuclear fireballs, hot gaseous plumes formed by nuclear detonations, has been the subject of great interest in defense-oriented scientific research for decades. However, despite years of study [2–5], some details of the underlying processes involved in the formation and condensation of nuclear fireballs are still poorly understood. One important aspect of this problem is understanding the physical phenomena and fundamental science behind nuclear debris formation. Since the evolution of a fireball spans a multitude of time scales and involves numerous complex coupled physical processes [6], accurate modeling of debris formation poses a major technical challenge. The issue is further complicated by the difficulty of performing experiments that suitably replicate the physical conditions inside a fireball. Therefore, the development of a robust debris formation model requires leveraging both modern computational capabilities and novel experimental techniques in a unified approach.

The process of debris formation in a nuclear fireball can be roughly separated into several sequential chemical regimes, as illustrated in Figure 1.1. Following the initial detonation, a fireball with temperatures up to hundreds of eVs [6] forms and begins to rapidly cool as it expands and radiates heat. Much of the chemical behavior in the fireball at this stage will be dominated by plasma chemistry and collisional-radiative processes. As regions of the fireball cool further (< 1 eV), molecular formation will commence. Due to the relatively high gas and vapor temperatures, sizable populations of species in excited internal states can be expected to participate in these reactions. Further cooling below saturation temperatures leads to particle inception (nucleation) and growth (condensation, aggregation), eventually culminating in debris formation. In addition to atmospheric and bomb materials,

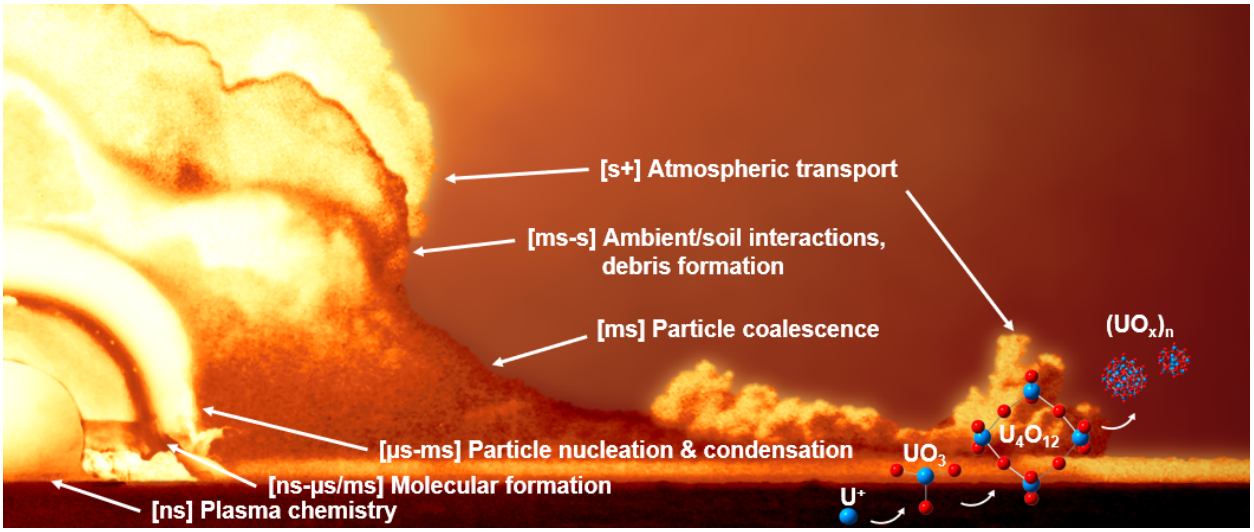

Figure 1.1: Illustration of general physical processes and approximate timescales leading to debris formation in nuclear detonations. Note that the fireball images are for illustration only and do not correspond to timescales shown.

environmental species introduced via entrainment (Fe, Si, etc.) may also participate in these processes. The rate at which these processes proceed also depends on the local temperature conditions. Therefore, debris formation is sensitive to both the composition and the cooling timescales of the system, and may proceed via non-equilibrium chemical kinetics [7].

As one can imagine, the wide range of physical conditions, phenomena, and timescales makes complete characterization of the debris formation process difficult. Consequently, the focus here is on a more specific, and tractable, problem: the formation of uranium oxides (UO_x) in these environments. In a previous work [1], we approached this problem by constructing a UO_x reaction mechanism using available literature information and theoretical estimates. Although the mechanism produced qualitatively reasonable results, it was not validated with respect to experimental measurements. Since then, several experimental studies have been conducted to produce and characterize UO_x plasmas, primarily utilizing either laser ablation [8–14] or plasma flow reactor (PFR) [7, 15] systems. This work aims to use this experimental data to improve upon the previously constructed UO_x mechanism and to develop additional modeling tools for future validation efforts.

The laser ablation and plasma flow reactor systems each possess certain advantages

and disadvantages for analyzing molecular formation in extreme environments. The laser ablation system utilizes a high-intensity laser to volatilize a metal uranium sample, producing a rapidly expanding reactive plasma plume. If performed by a sufficiently powerful laser in atmospheric conditions, the ablation is accompanied by a shock wave at the plume-ambient interface reminiscent of a fireball blast wave. These experiments can produce plumes with maximum temperatures up to tens of eVs that cool over ns–μs timescales [16] and allow for full control of the ambient chemical composition. While this serves as a convenient bench-top surrogate for detonation-like conditions, detailed chemical characterization is difficult to achieve. This is in part due to the small spatial and short temporal scales involved, as well as the complex plume dynamics following the initial shock expansion [17]. This not only makes it challenging to measure well-resolved spatiotemporal species maps, but also imposes a moderate computational cost for solving the corresponding hydrodynamic equations. The plasma flow reactor (PFR), on the other hand, produces a uranium plasma using an inductively coupled plasma (ICP) torch attached to a quartz tube. While the RF plasma is generated by an argon flow, an aqueous uranium solution is introduced into the torch, producing an argon-uranium plasma that cools as it flows downstream. Compared to the laser ablation system, the chemical evolution in the PFR is relatively easy to characterize due to the simple cylindrical geometry and largely laminar flow. This also allows for certain modeling approximations that make the computational evaluation of the chemical kinetics inexpensive. However, the maximum temperatures in the PFR are considerable lower (<1 eV) than in laser ablation [18] and cooling occurs on a ms timescale. Furthermore, the use of an aqueous uranium nitrate solution introduces a baseline background of reactive species (O, H, N) that complicates chemical analysis. Given the above differences, each of these systems serves a particular role in informing an updated UO_x reaction mechanism.

Determining reaction rates from experimental measurements is an example of an inverse problem, where underlying model parameters must be determined based on observed outputs. Depending on the complexity of the corresponding system of equations and the size

of the unknown parameter space, this can be quite challenging. For example, conventional deterministic gradient-based methods [19–21] will struggle to locate a global minimum for problems containing numerous local minima. Such issues can be avoided by utilizing an optimization method capable of continuously exploring the entire parameter space while locating the global minimum. One such method commonly used for chemical kinetics problems is the Monte Carlo Genetic Algorithm (MCGA) [22]. This technique is particularly suitable for the current problem due to both its effectiveness and ease of implementation, as discussed at length below. Regardless of methodology, solving a large inverse problem requires repeated evaluations of the associated model, often numbering in the thousands to millions of runs. While reasonable computational times are achieved when solving for the chemical kinetics in a spatially uniform system, the problem quickly becomes unfeasible when the chemistry is coupled with complex fluid transport. For example, if the chemical kinetics of the PFR are approximated using a 0D model [15], the resulting serial solution times are on the order of seconds or less. By contrast, a 2D axis-symmetric reactive CFD model of the laser ablation system [17] may take hours or days to solve. Therefore, in order to accomplish reasonable optimization times, application of the MCGA in the current work is limited to the PFR system.

Although the PFR serves as an ideal system for calibrating a reaction mechanism, it also features relatively low temperatures ($<$10,000 K [23]) and long cooling timescales (ms). These conditions cover only part of the wide range of temperatures and timescales present in extreme environments. While bench-top laser ablation systems offer the opportunity to study a broader range of detonation-relevant temperature ($\geq$11,600 K) and cooling (ns–μs) conditions, they are also much more difficult to accurately model. Part of this difficulty lies in the multi-physics nature of the problem, where hydrodynamics, radiation transport, and chemical kinetics may all strongly influence the ablation plume dynamics. Even should these behaviors be adequately resolved in a given model, further complications are introduced when attempting to compare said model against experimental measurements. Doing so

requires employing a set of synthetic diagnostics that simulate the output produced by the experimental acquisition process. Here, we examine several modeling approaches for simulating molecular formation in ablation plumes. First, a purely hydrodynamic approach is used, where the initial simulation conditions are calibrated according to experimental measurements. While some experimental agreement is observed when using such a model, its limited predictive capability and high uncertainties make it of limited practical use. Second, we use a radiation hydrodynamics model to simulate the ns-timescale pulsed laser heating and phase transition processes. The resulting plume formation dynamics are found to compare favorably with experimental imaging and time-of-flight measurements. The good agreement observed in these validation tests suggests this as a more predictive ablation model, albeit with limited capabilities for simulating longer timescale viscous transport and chemical kinetics. Finally, a one-way coupling of the two models is performed to treat both the initial laser energy deposition and shock expansion problem and the subsequent reactive plume hydrodynamics problem. As noted above, particular emphasis is placed on arriving to a predictive ablation model that can be validated against optical measurements of bench-top ablation systems. Although the current analysis focuses on low-Z materials as a validation target, the resulting model can serve as a basis for future calibration of UO_x chemical kinetics against laser ablation experiments.

Overall, the research approach undertaken herein can be summarized as follows: to perform an MCGA calibration of the UO_x reaction mechanism using plasma flow reactor data and to produce a predictive laser ablation modeling approach for use in future chemical validation studies.

1.1 Thesis overview

Chapter 2 first provides a broad theoretical overview of low temperature plasma chemical physics that are employed throughout this work. This includes derivations of statistical

mechanics relations describing equilibrium species state populations and thermodynamics. Moreover, relevant reaction kinetics concepts are introduced, including the calculation of equilibrium coefficients and solution of chemical kinetic ODEs and the corresponding first order sensitivity coefficients.

Next, the specifics of each plasma system studied in this work are outlined in Chapter 3. This chapter provides the background information, experimental details, and modeling methodologies for the plasma flow reactor (PFR) and laser ablation systems. This chapter also details the implementation of the Monte Carlo Genetic Algorithm (MCGA) used for solving the inverse problem of extracting reaction rate information from experimental data.

Application of the MCGA for calibrating a uranium oxide reaction mechanism using PFR measurements is the focus of Chapter 4. The chapter begins with an overview of the experimental datasets used to provide constraints for the optimization. Next, a representative temperature profile for the problem is obtained via comparisons between a CFD model and experiments. After identifying reaction channels targeted for optimization based on the available data, the temperature history is used to initiate the MCGA calibration. The results of the Monte Carlo sampling and Genetic Algorithm steps are then discussed and an optimal set of rate coefficients is obtained. These reaction rates are compared against previous literature estimates and recommendations are made for an updated UO_x reaction mechanism.

In Chapter 5, the focus is shifted towards examining laser ablation as a tool for validating chemical kinetics. We begin by outlining the use of synthetic diagnostics in performing comparisons between reactive ablation simulations and spectroscopic studies. We then compare the predictive capabilities of a reactive CFD model and a radiation-hydrodynamic model for reproducing plume characteristics observed in imaging studies. The role of optical effects on the visible plume profile in the latter model is explored by generating synthetic emission maps. Finally, the two models are coupled to study a microsecond timescale reactive aluminum ablation event. Here, synthetic diagnostics are utilized to compare the simulated

evolution of plume chemical composition against species-resolved literature imaging.

Lastly, the main results of the work are summarized and discussed in Chapter 6. Here, we also present possible future refinements to the current approach of obtaining an experimentally calibrated uranium oxide reaction mechanism. This includes outlining areas of improvement in the characterization of both the plasma flow reactor and laser ablation systems through continued combined experimental and modelling efforts.

Chapter 2

Chemical Physics of Low Temperature Plasmas

The problem of modeling the chemical and physical behavior of atmospheric plasmas is an inherently multiphysics one. That is, in order to produce a model suitable for validation against a given experimental system, one must treat a broad range of physical phenomena in combination. Aside from the base chemical kinetic equations needed to study uranium oxide formation, we may need to consider the convective transport and shock dynamics arising from the compressible Euler equations, or the added diffusive and viscous effects of the full Navier-Stokes equations, or the radiative transport that gives rise to the observed emission or absorption spectra. In order to evaluate each of the above phenomena in a hydrodynamic framework, the relevant fluid properties must first be supplied to the model. While this part of the process may be trivial for well-studied systems covering a narrow range of physical conditions (i.e. air near STP), it is an area of some difficulty for metallic and actinide plasmas. As is often the case for these latter systems, the requisite coefficients may be scattered across literature and cover only a limited range of the conditions of interest. In these cases, the missing coefficients must instead be estimated based on available data. The first goal of this chapter is to provide the theoretical means for estimating some of these coefficients. This will be accomplished by utilizing concepts from statistical mechanics, which will also introduce relations that will be vital for performing model-experiment comparisons later in this work. The second goal of this chapter is to provide a brief description of the chemical kinetics considerations that are common for both of the systems studied in this work. Building upon this foundation, the following chapter will detail the system-specific applications of these equations and cover the fluid dynamics relevant for each system.

2.1 Statistical mechanics

The goal of this section is to provide the theoretical basis for calculating the macroscopic properties of an atmospheric plasma from a microscopic description of the constituent particles. The theoretical framework for making this connection is provided by the field of statistical mechanics. The relations provided by statistical mechanics serve as the basis for estimating the thermodynamic, fluid transport, radiative transport, and chemical properties of low temperature plasmas. We begin with a brief derivation of Maxwell-Boltzmann statistics using fundamental concepts from quantum mechanics, statistics, and thermodynamics. Next, the partition functions corresponding to the various degrees of freedom of a given atom or molecule are derived. These partition functions are then used to find expressions for the populations of particles belonging to a particular energy state, with special attention placed on the metallic vapors of interest here. The thermodynamic coefficients typically used for chemical kinetic calculations are then derived based on the partition functions. Lastly, the concept of chemical equilibrium in a plasma and its relation to the thermodynamics of the system is discussed. The aim here is to arrive at the aforementioned relations for low-temperature plasma properties in a (hopefully) concise and intuitive manner, although sacrificing some generality in the process. Books with excellent and detailed descriptions of statistical mechanics include works by Landau and Lifshitz [24], McQuarrie [25], and Capitelli *et al.* [26].

2.1.1 Maxwell-Boltzmann statistics

In atmospheric gaseous systems, it is typical to encounter particle quantities on the order of Avogadro's number. While quantum mechanics provides the eigenstates and eigenenergies of single or few particle systems, it would be an incredibly cumbersome task to explicitly calculate the state of an N-body problem of that magnitude. Instead, we can utilize statistics to connect the microscopic quantum description of particles to the macroscopic properties of

the system. In essence, this will be accomplished by determining the equilibrium distribution of particles among the available eigenstates for the given system. As will be shown, the assumption of large particle numbers will play a central role in this endeavor.

As a first step, we will pick a system of interest to analyze by defining it in terms of some fixed thermodynamic or mechanical parameters. Since quantum mechanics informs us that each particle in the system may be in one of several eigenstates, we will have to consider all the possible combinations of particle states for this system. We will call each of these combinations a microstate of the system and the collection of all possible microstates an ensemble. The ensemble can then be further classified based on the fixed system parameters that we choose. Although the derivation can proceed for several choices of ensembles, we will pick the canonical ensemble here. The three parameters prescribed for a canonical ensemble are the system volume V, temperature T, and number of particles N (also known as an NVT ensemble). Note that the total energy of the system in this ensemble is not fixed and is determined by the combined particle energies for the given conditions.

We will now say that each microstate of the NVT ensemble is given by the distribution of the N particles in the system among the possible eigenstates. The number of particles in a particular state k is given by the occupation number N_k, such that:

$$N = \sum_k N_k \tag{2.1}$$

$$E = \sum_k N_k \varepsilon_k \tag{2.2}$$

where E is the total energy of the system and ε_k is the eigenenergy of state k. Note that Equation 2.2 states that the total energy of the system is simply the sum of the individual particle energies, which implies that interparticle potentials are ignored (i.e. ideal gas approximation). Note also that the eigenenergies can be degenerate, that is, several eigenstates may possess the same eigenenergy, which will come into play later.

We now denote a distribution of particles as $\mathcal{N} = \{N_1, N_2, N_3, \dots\}$. Then, the number of ways in which a given distribution $\mathcal{N}$ may be achieved by arranging N particles among the eigenstates is given by the multinomial coefficient:

$$W(\mathcal{N}) = \frac{N!}{N_1!\, N_2!\, N_3! \dots} = \frac{N!}{\prod_k N_k} \tag{2.3}$$

which can be used to obtain the probability $\mathcal{P}_k$ of finding a k state particle by averaging the fraction of k state particles N_k/N over all possible distributions $\mathcal{N}$ with equal weighting:

$$\mathcal{P}_k = \sum_{\mathcal{N}} \left(\frac{W(\mathcal{N})}{\sum_{\mathcal{N}} W(\mathcal{N})} \right) \frac{N_k(\mathcal{N})}{N} = \frac{1}{N} \frac{\sum_{\mathcal{N}} W(\mathcal{N}) N_k(\mathcal{N})}{\sum_{\mathcal{N}} W(\mathcal{N})} \tag{2.4}$$

which allows us to calculate the average particle energy in the system as:

$$\bar{E} = \frac{E}{N} = \sum_k \varepsilon_k \mathcal{P}_k \tag{2.5}$$

This result essentially accomplishes the stated goal of connecting the microscopic particle eigenstates to the macroscopic system properties. However, the full probability expression provided by Equation 2.4 is too cumbersome for practical applications. This problem can be resolved by once again leveraging the large number of particles we will typically encounter. Namely, it can be shown that the multinomial coefficient given by Equation 2.3 reduces to a delta function about the most probable distribution $\mathcal{N}^*$ as $N_k \to \infty$, that is:

$$\lim_{N_k \to \infty} W(\mathcal{N}) = \begin{cases} W(\mathcal{N}^*), & \mathcal{N} = \mathcal{N}^* \\ 0, & \mathcal{N} \neq \mathcal{N}^* \end{cases} \tag{2.6}$$

such that the probability equation reduces to:

$$\mathcal{P}_k = \frac{1}{N} \frac{W(\mathcal{N}^*) N_k(\mathcal{N}^*)}{W(\mathcal{N}^*)} = \frac{N_k^*}{N} \tag{2.7}$$

where $N_k^* = N_k(\mathcal{N}^*)$ is the occupation number of state k for the most probable distribution $\mathcal{N}^*$. We can then find $\mathcal{N}^*$ by maximizing $W(\mathcal{N})$ subject to (2.1) and (2.2) by using the method of Lagrange multipliers:

$$\frac{\partial}{\partial N_k}\left(\ln W(\mathcal{N}) - \lambda_1 \sum_k N_k - \lambda_2 \sum_k N_k \varepsilon_k\right) = 0 \tag{2.8}$$

where λ_1 and λ_2 are the Lagrange multipliers and we elect to maximize $\ln W(\mathcal{N})$ instead of $W(\mathcal{N})$ in order to allow the use of Stirling's approximation[1] ($\mathcal{N}^*$ is the same for $\ln W(\mathcal{N})$ since logarithms are monotonic functions). Plugging in (2.3), using the Stirling approximation, and remembering that N is fixed (constant) yields:

$$\frac{\partial}{\partial N_k}\left(-\sum_k N_k \ln N_k - \lambda_1 \sum_k N_k - \lambda_2 \sum_k N_k \varepsilon_k\right) = 0 \tag{2.9}$$

carrying out the differentiation:

$$-\ln N_k^* - 1 - \lambda_1 - \lambda_2 \varepsilon_k = 0 \tag{2.10}$$

and rearranging for N_k^*:

$$N_k^* = \exp(-\lambda_1 - 1)\exp(-\lambda_2 \varepsilon_k) \tag{2.11}$$

which finally gives us the occupation numbers of the most probable distribution $\mathcal{N}^*$. Combining this expression with (2.7) and (2.1) yields:

$$\mathcal{P}_k = \frac{\exp(-\lambda_1 - 1)\exp(-\lambda_2 \varepsilon_k)}{\sum_k \exp(-\lambda_1 - 1)\exp(-\lambda_2 \varepsilon_k)} = \frac{\exp(-\lambda_2 \varepsilon_k)}{\sum_k \exp(-\lambda_2 \varepsilon_k)} \tag{2.12}$$

so that the average particle energy given by Equation 2.5 becomes:

$$\bar{E} = \frac{\sum_k \varepsilon_k \exp(-\lambda_2 \varepsilon_k)}{\sum_k \exp(-\lambda_2 \varepsilon_k)} = \frac{1}{q}\sum_k \varepsilon_k \exp(-\lambda_2 \varepsilon_k) \tag{2.13}$$

[1] $\ln x! \approx x \ln x - x = x \ln x/e$

where $q = \sum_k \exp(-\lambda_2 \varepsilon_k)$ is known as a partition function, which will later be used to fully describes the equilibrium thermodynamic state of the system. Note that although we have not explicitly utilized the concept of equilibrium in the above derivation, one can intuitively reason that the equilibrium state of the system corresponds to the most statistically probable one.

The hitherto unknown Lagrange multiplier λ_2 can now be found by expressing the first law of thermodynamics as:

$$\left(\frac{\partial E}{\partial V}\right)_{N,T} = -P + T\left(\frac{\partial P}{\partial T}\right)_{N,V} \tag{2.14}$$

where we have used the Maxwell relation $(\partial S/\partial V)_{N,T} = (\partial P/\partial T)_{N,V}$. Plugging $E = N\bar{E}$ into the left-hand side and using (2.13) yields:

$$-N\bar{P} - \lambda_2 N\left(\overline{PE} - \bar{P}\bar{E}\right) = -P + T\left(\frac{\partial P}{\partial T}\right)_{N,V} \tag{2.15}$$

where $\bar{P}$ and $\overline{PE}$ are defined as:

$$\bar{P} = \frac{1}{q}\sum_k P_k \exp(-\lambda_2 \varepsilon_k) \tag{2.16}$$

$$\overline{PE} = \frac{1}{q}\sum_k P_k \varepsilon_k \exp(-\lambda_2 \varepsilon_k) \tag{2.17}$$

where $P_k = -(\partial \varepsilon_k/\partial V)_{N,T}$ denotes the partial pressure contribution due to the pressure work of particles in state k. Equating $P = N\bar{P}$, plugging P into the right-hand side of (2.15), and carrying out the derivative assuming λ_2 is a function of temperature gives:

$$-\frac{\lambda_2}{T}\left(\overline{PE} - \bar{P}\bar{E}\right) = \frac{\partial \lambda_2}{\partial T}\left(\overline{PE} - \bar{P}\bar{E}\right) \tag{2.18}$$

which gives $-\lambda_2/T = \partial\lambda_2/\partial T$. This relation is satisfied for $\lambda_2 = 1/k_B T$ where k_B is a

constant, which can be shown to be the Boltzmann constant.

We can now express some of the relations derived above in their final forms. Using $\lambda_2 = 1/k_B T$, we get the final expression for the particle partition function in terms of eigenstates:

$$q = \sum_k \exp\left(-\frac{\varepsilon_k}{k_B T}\right) \tag{2.19}$$

where ε_k is again the eigenenergy of state k. It is often also convenient to sum over the energy levels, rather than eigenstates, of the system. Doing so leads to the following expression:

$$q = \sum_i g_i \exp\left(-\frac{\varepsilon_i}{k_B T}\right) \tag{2.20}$$

where g_i is the degeneracy of energy level i; that is, the number of eignestates with energy ε_i. Similarly, we can then express the fraction of particles with energy ε_i as:

$$\frac{N_i}{N} = \frac{n_i}{n} = \frac{1}{q} g_i \exp\left(-\frac{\varepsilon_i}{k_B T}\right) \tag{2.21}$$

where n denotes particle number densities, which will more often be the quantity of interest for practical applications.

Lastly, we note that our discussion so far has focused on the particle partition function q, which describes all the possible particle states for a given configuration (microstate) of the NVT ensemble. However, in order to rigorously calculate the thermodynamic properties of a system, we need to be able to describe all the possible microstates of the ensemble. We have already stated that the energy of a microstate is given by Equation 2.2 and we can in theory express the ensemble partition function Q as:

$$Q = \sum_l \exp\left(-\frac{E_l}{k_B T}\right) = \sum_l \exp\left(-\frac{\sum_{k_l} N_{k_l} \varepsilon_{k_l}}{k_B T}\right) = \sum_l \prod_{k_l} \exp\left(-\frac{N_{k_l} \varepsilon_{k_l}}{k_B T}\right) \tag{2.22}$$

where E_l is the total energy of microstate l and k_l are the available particle states within that

microstate. However, in the above form, it is not readily apparent how Q can be expressed in terms of q. If we instead consider every possible arrangement of N particles over all eigenstates i_j for each particle j, we get:

$$Q^* = \sum_{i_1,\ldots,i_N} \exp\left(-\frac{\varepsilon_{i_1} + \cdots + \varepsilon_{i_N}}{k_B T}\right) = \prod_j^N \sum_{i_j} \exp\left(-\frac{\varepsilon_{i_j}}{k_B T}\right) = q^N \tag{2.23}$$

which is the ensemble partition function for N distinguishable particles. However, since the particles of interest here (i.e. atoms and molecules) are not distinguishable, we must modify (2.23) such that the permutations of a particular state (i.e. $\{i_1, i_2, i_3, \ldots\}$ and $\{i_1, i_3, i_2, \ldots\}$) do not get counted as separate states. Failing to do so would result in an entropy expression that depends on the particle ordering, leading to what is known as the Gibbs paradox [25]. This can be done by modifying the bounds of the sum terms, but this will again prevent an expression in terms of q from being obtained. It turns out, however, that the number of available states for an atmospheric gas at or above room temperature typically far exceeds the number of particles in the system. In this case, it is unlikely that any two particles will have identical states and the particles are then said to obey Boltzmann statistics. This means that $N!$ permutations of the N particle system are possible, and the ensemble partition function can simply be expressed as:

$$Q = \frac{Q^*}{N!} = \frac{q^N}{N!} \tag{2.24}$$

2.1.2 Partition functions

We have now derived general forms for the particle and ensemble partition functions according to Boltzmann statistics as shown by Equations 2.19, 2.20, and 2.24. In order to apply these expressions to calculate the properties of a gas or plasma we must first determine what eigenstates contribute to the particle partition functions and how the corresponding eigenenergies can be computed. We begin by considering the various independent degrees

of freedom for a given particle that contribute to the total particle energy:

$$\varepsilon = \varepsilon_{nuc} + \varepsilon_{tr} + \varepsilon_{int} \tag{2.25}$$

where ε_{nuc}, ε_{tr}, and ε_{int} refer to the nuclear, translational, and internal contributions, respectively. Since the energy states of each contribution are distinguishable, (2.23) tells us that:

$$q = q_{nuc} q_{tr} q_{int} \tag{2.26}$$

that is, that the total partition function is simply the product of the partition functions for each degree of freedom. Since nuclear energy levels are on the order of MeV, the nuclear partition function will be reduced to the ground state degeneracy (i.e. $q_{nuc} = g_{nuc,0}$) for our conditions of interest. Therefore, this term is effectively a constant and can usually be ignored in subsequent calculations.

The translational partition function q_{tr} can be obtained by considering the solution of the time-independent Schrödinger equation for a particle in a cubic box. From basic quantum mechanics, we recall the solution for a 1D infinite square well of length a:

$$\varepsilon_n = \frac{h^2 n^2}{8ma^2} \qquad n = 1, 2, \ldots \tag{2.27}$$

where h is the Planck constant and m is the particle mass. The corresponding partition function is then given by:

$$q_{tr,1D} = \sum_{n=1}^{\infty} \exp\left(-\frac{\varepsilon_n}{k_B T}\right) = \sum_{n=1}^{\infty} \exp\left(-\frac{h^2 n^2}{8ma^2 k_B T}\right) \tag{2.28}$$

where the term inside the sum varies nearly continuously as a function of n for T far from absolute zero (i.e. room temperature), such that the sum can be approximated by the

integral:

$$q_{tr,1D} \approx \int_0^\infty \exp\left(-\frac{h^2 n^2}{8ma^2 k_B T}\right) dn = \left(\frac{2\pi m k_B T}{h^2}\right)^{1/2} a \tag{2.29}$$

where the integration range is extended to include $n = 0$, with the resulting contribution assumed negligible due to the above assumption of a continuous function. Since the three spatial coordinates of the cubic box problem are independent, the total translational partition function is simply the product of the 1D infinite square well solutions for each coordinate:

$$q_{tr} = q_{tr,x} q_{tr,y} q_{tr,z} = (q_{tr,1D})^3 = \left(\frac{2\pi m k_B T}{h^2}\right)^{3/2} V \tag{2.30}$$

where $V = a^3$ is the volume.

As one might expect, the form of the internal partition function q_{int} depends on the structure of the particle in question. For an atom, the only internal energy levels (aside from the nuclear) are electronic. For molecules, additional degrees of freedom arise due to rotational and vibrational motion. Partition functions for these additional degrees of freedom can be found analytically in the case of diatomic molecules using rigid rotor and harmonic oscillator approximations. While extensions of such treatments for polyatomic molecules exist, we will limit our discussion to monatomic and diatomic molecules as these are the species typically observable via optical emission spectroscopy.

For a monatomic molecule, the internal partition function is given by Equation 2.20:

$$q_{int} = q_{el} = \sum_e g_{el,e} \exp\left(-\frac{\varepsilon_{el,e}}{k_B T}\right) \tag{2.31}$$

where $\varepsilon_{el,e}$ and $g_{el,e}$ refer to the energy and degeneracy of electronic level e, respectively. The practical difficulty in finding the electronic partition function of a given molecule lies in calculating ε_{el} and g_{el}. As is often the case in quantum mechanics, an exact solution of this problem is only possible for the hydrogen atom (i.e. Bohr model). Even in this case, one encounters the problem of setting a cutoff criterion for the sum in Equation 2.31

(i.e. e_{max}) as it diverges otherwise [26]. For larger atoms, one must typically employ some approximate method to calculate q_{el}. The simplest and least accurate method is to use a Bohr-like treatment, known as a hydrogenic approximation. Numerical solutions of the Schrödinger equation can also be used to provide a more accurate, albeit computationally costly, approximation. Often the most convenient method is to simply use an existing database of energy levels, such as that of NIST [27]. While this empirical method is the most straightforward one, it is also the least rigorous, as the database is likely to be missing some predicted energy levels. This problem can be mitigated by utilizing semi-empirical methods to interpolate or extrapolate missing energy levels based on the available data and knowledge of the atom's electron configuration [26].

Next, we consider diatomic molecules with a focus on the hetero-nuclear case due to our interest in metal oxide chemistry. As mentioned above, this involves obtaining the partition functions for the vibrational and rotational motion of the molecule. As before, we will initially assume that these two degrees of freedom are independent from each other and from the electronic states of the constituent atoms (Born-Oppenheimer approximation). This assumption implies that the vibrational oscillations are small enough as to have negligible impact on the angular momentum of the molecule, and that the nuclei are approximately stationary relative to the electrons.

The derivation of the vibrational energy levels typically proceeds by considering the general shape of an inter-atomic potential V (i.e. Lennard-Jones). The minimum of this potential is the well depth V_0, which occurs at some equilibrium inter-atomic separation distance r_0 (i.e. $V(r_0) = V_0$). Then, a Taylor expansion of the potential in terms of r_0 gives:

$$V(r) = V_0 + (r - r_0)V'(r_0) + \frac{1}{2}(r - r_0)^2 V''(r_0) + \frac{1}{6}(r - r_0)^3 V'''(r_0) + \dots \tag{2.32}$$

where r is the inter-atomic separation. Noting that $V'(r_0) = 0$ and that the potential can

be freely offset, we can express the potential in a condensed form as:

$$V(d) = \frac{1}{2}kd^2 + \frac{1}{6}\gamma d^3 + \dots \tag{2.33}$$

where $d = r - r_0$ is the vibrational displacement, $k = V''(d = 0)$ is the oscillator force constant, and $\gamma = V'''(d = 0)$ is an anharmonic force constant. The first term in the above equation is the familiar harmonic oscillator potential, whereas the subsequent terms represent smaller anharmonic terms. The well-known solution of the Schrödinger equation for a harmonic oscillator potential is:

$$\frac{\varepsilon_{ho,v}}{hc} = \omega_e \left(v + \frac{1}{2} \right) \tag{2.34}$$

where v is the vibrational quantum number, $\omega_e = \frac{1}{2\pi c}\sqrt{k/\mu}$ is the harmonic wavenumber, μ is the reduced mass, and the factor hc is used to convert units from energy to inverse length. Since these energy levels are not degenerate, we have $g_v = 1$. The harmonic vibrational partition function is then found by plugging (2.34) into (2.20):

$$\begin{aligned} q_{vib,ho} &= \sum_{v=0}^{\infty} \exp\left(-\frac{\omega_e^*}{T}\left(v + \frac{1}{2} \right) \right) = \exp\left(-\frac{\omega_e^*}{2T} \right) \sum_{v=0}^{\infty} \exp\left(-\frac{\omega_e^*}{T} \right)^v \\ &= \frac{\exp(-\omega_e^*/2T)}{1 - \exp(-\omega_e^*/T)} \end{aligned} \tag{2.35}$$

where $\omega_e^* = hc\omega_e/k_B$ and we have used the closed form of a geometric series to obtain the final expression. Lastly, we note than the above derivation uses the convention that the ground vibrational state energy is $\omega_e/2$.

Under the Born-Oppenheimer approximation, we can similarly estimate the rotational motion of the molecule as that of a rigid rotor. This is another standard problem in quantum

mechanics for which the Schrödinger equation gives:

$$\frac{\varepsilon_{rr,J}}{hc} = B_e J(J+1) \tag{2.36}$$

where $B_e = h/8\pi^2 Ic$ is a rotational coefficient expressed in terms of the moment of inertia $I = \mu r_0^2$ and J is the rotational quantum number. The degeneracies of the rotational energy levels are given by $g_J = 2J+1$. The rigid rotor partition function can then be expressed as:

$$\begin{aligned} q_{rot,rr} &= \sum_{J=0}^{\infty} (2J+1) \exp\left(-B_e^* J(J+1)/T\right) \\ &\approx \int_0^{\infty} (2J+1) \exp\left(-B_e^* J(J+1)/T\right) dJ = \frac{T}{B_e^*} \end{aligned} \tag{2.37}$$

where $B_e^* = hcB_e/k_B$ and the integral approximation holds when $B_e^* \ll T$. This is a good approximation for most molecules, where B_e^* is typically on the order of 3 K or less, excluding light molecules containing hydrogen and hydrogen isotopes.

Using (2.35) and (2.37), we obtain the following expression for the Born-Oppenheimer harmonic rigid rotor hetero-nuclear diatomic internal partition function:

$$q_{int} = \sum_{e}^{e_{max}} g_e \exp\left(-\frac{\varepsilon_e}{k_B T}\right) \frac{T}{B_e^*} \frac{\exp(-\omega_e^*/2T)}{1-\exp(-\omega_e^*/T)} \tag{2.38}$$

where e_{max} is the cutoff criterion for the electronic energy levels. Note that the coefficients B_e and ω_e are functions of the electronic state e of the molecule, as they are derived from the inter-atomic potential V.

Lastly, if one wishes to move away from the Born-Oppenheimer harmonic rigid rotor treatment, a number of additional energy terms for anharmonic non-rigid motion and rotational-vibrational coupling must be considered. The largest of these terms are given by:

$$\frac{\varepsilon_{corr,v,J}}{hc} = \underbrace{-\omega_e \chi_e \left(v+\frac{1}{2}\right)^2}_{anharmonic} \underbrace{- D_e J^2 (J+1)^2}_{non-rigid} \underbrace{- \alpha_e \left(v+\frac{1}{2}\right) J(J+1)}_{coupled} \tag{2.39}$$

where χ_e is an anharmonicity coefficient, D_e is a centrifugal distortion coefficient, and α_e is a rotation-vibrational coupling coefficient. As with B_e and ω_e, these coefficients can either be calculated from the inter-atomic potential or estimated from measured spectra. Similar to the electronic partition function discussed previously, evaluating the rovibrational partition function with the above corrections requires setting a cutoff criterion for the sums over the vibrational and rotation states. The rovibrational cutoff criteria are typically selected either based on a physical threshold, for example such that the total energy does not exceed the dissociation energy for the given electronic state, or to avoid numerical issues [28, 29]. The rovibrational partition function with the above corrections is given by:

$$q_{int} = \sum_{e}^{e_{max}} \sum_{v=0}^{v_{max}} \sum_{J=0}^{J_{max}} g_e(2J+1) \exp\left(-\frac{\varepsilon_e + \varepsilon_{ho,v} + \varepsilon_{rr,J} + \varepsilon_{corr,v,J}}{k_B T}\right) \tag{2.40}$$

where v_{max} and J_{max} are the vibrational and rotational cutoff criteria, respectively. Alternatively, an approximate expression for the correction to the harmonic rigid rotor partition function can also be derived [25, 30]:

$$q_{corr} = 1 - \frac{2TD_e^*}{(B_e^*)^2} + \frac{\alpha_e^*}{B_e^*}\left[\exp\left(\frac{\omega_e^*}{T}\right) - 1\right]^{-1} + \frac{2\omega_e^*\chi_e}{T}\left[\exp\left(\frac{\omega_e^*}{T}\right) - 1\right]^{-2} + \ldots \tag{2.41}$$

where, as before, an asterisk denotes a wavenumber quantity expressed in temperature units. The corresponding rovibrational partition function obtained using this expression is given by $q_{rv} = q_{vib,ho} q_{rot,rr} q_{corr}$.

2.1.3 Atomic and diatomic state populations

From the above derivations of the atomic and molecular internal partition functions, we can now obtain expressions for the atomic and molecular energy level populations. For atomic species, the number density of atoms in a given electronic level e is simply given by (2.21)

with electronic partition function q_{el}:

$$n_e = n\frac{g_{el,e}}{q_{el}} \exp\left(-\frac{\Delta E_{i0}}{k_B T}\right) \tag{2.42}$$

where $g_{el,e}$ and ΔE_{i0} are the statistical weight and the energy with respect to the ground state of level e, respectively, and q_{el} is given by (2.31). Several collections of electronic energy levels for uranium atoms and atomic ions will be used in this work to calculate the uranium level populations [31–33]. The uranium atom has a strong optical emission at 591.5 nm, which will be the primary U line used for experimental comparisons here.

Applying (2.21) to the case of a heteronuclear diatomic molecule yields:

$$n_{e,J,v} = n\frac{g_{el,e}}{q_{int}}(2J+1) \exp\left(-\frac{\Delta E_{e0,J0,v0}}{k_B T}\right) \tag{2.43}$$

where the excited level is described by the electronic, rotational, and vibrational quantum numbers e, J, and v, respectively, and q_{int} is the internal diatomic partition function given by (2.38) or (2.40). As demonstrated in the previous section, the above equations require a number of spectroscopic constants as inputs in order to calculate the rovibrational contribution. However, owing to the complexity of the extremely crowded UO emission spectrum, only the ground state spectroscopic constants have been previously estimated in literature [34–38]. The spectroscopic constants and energy levels estimated by Konings *et al.* [38] will be used here to estimate the emission intensity of the 593.55 nm UO band. This band is assumed to be dominated by the [16.845]5–X(1)4 transition (a 0–0 transition) observed by Kaledin *et al.* [37]. However, it should be noted that this band actually consists of a number of closely-spaced rovibrational lines as shown by a recent high-resolution spectroscopic study of uranium LPPs [14]. Lastly, for oxides that are of interest in astrophysical applications, such as AlO, tables and/or polynomial fits of internal partition functions can be found in literature databases [39, 40].

2.1.4 Thermodynamic coefficients

We have mentioned before that the partition function fully describes the equilibrium thermodynamics of the system, but have not yet explicitly shown that to be the case. Doing so will allow us to obtain expressions for calculating the thermodynamic coefficients of a gas described by a given partition function. These coefficients play a particularly vital role in solving for the chemical kinetics of a reactive gas, as will be discussed later.

We begin by considering the expression for the average particle energy given by (2.13), which can be expressed in terms of q as:

$$\bar{E} = \frac{k_B T^2}{q}\left(\frac{\partial q}{\partial T}\right)_{N,V} = k_B T^2 \left(\frac{\partial \ln q}{\partial T}\right)_{N,V} \tag{2.44}$$

where we have used the identity $(df/dx)/f = d(\ln f)/dx$. From (2.2), the total system energy is then:

$$E = N\bar{E} = N k_B T^2 \left(\frac{\partial \ln q}{\partial T}\right)_{N,V} = k_B T^2 \left(\frac{\partial \ln Q}{\partial T}\right)_{N,V} \tag{2.45}$$

where Q is again the ensemble partition function given by (2.24). By the same logic, the system pressure can be expressed as:

$$P = N\bar{P} = N k_B T \left(\frac{\partial \ln q}{\partial V}\right)_{N,T} = k_B T \left(\frac{\partial \ln Q}{\partial V}\right)_{N,T} \tag{2.46}$$

Recalling from the previous section that only the transport partition function q_{tr} is a function of V, we use (2.30) to find:

$$P = N k_B T \left(\frac{\partial \ln q}{\partial V}\right)_{N,T} = \frac{N k_B T}{q_{tr}} \frac{\partial q_{tr}}{\partial V} = \frac{N k_B T}{V} \tag{2.47}$$

which is simply the ideal gas law. Using (2.26), (2.30), (2.45), and (2.47), the system enthalpy

can be expressed as:

$$\begin{aligned} H = E + PV &= k_B T^2 \left(\frac{\partial \ln Q}{\partial T} \right)_{N,V} + N k_B T \\ &= N k_B T^2 \left(\frac{\partial \ln q_{int}}{\partial T} \right)_{N,V} + \frac{5}{2} N k_B T \end{aligned} \tag{2.48}$$

and the heat capacity at constant pressure as:

$$\begin{aligned} C_p &= \left(\frac{\partial H}{\partial T} \right)_{N,V} \\ &= N k_B T^2 \left(\frac{\partial^2 \ln q_{int}}{\partial^2 T} \right)_{N,V} + 2 N k_B T \left(\frac{\partial \ln q_{int}}{\partial T} \right)_{N,V} + \frac{5}{2} N k_B \end{aligned} \tag{2.49}$$

Lastly, we will finally derive an expression for the entropy of the system, which is perhaps the most important quantity in statistical mechanics. We begin by noting that the heat capacity at constant volume for the canonical ensemble can be expressed as:

$$C_v = \frac{dq_{rev}}{dT} = \left(\frac{\partial E}{\partial T} \right)_{N,V} = k_B T^2 \left(\frac{\partial^2 \ln Q}{\partial^2 T} \right)_{N,V} + 2 k_B T \left(\frac{\partial \ln Q}{\partial T} \right)_{N,V} \tag{2.50}$$

where dq_{rev} is the reversible heat change. Using the second and third laws of thermodynamics with the above relation, we get:

$$\begin{aligned} S - S_0 = \int_0^T \frac{dq_{rev}}{T'} &= \int_0^T k_B T' \left(\frac{\partial^2 \ln Q}{\partial^2 T'} \right)_{N,V} + 2 k_B \left(\frac{\partial \ln Q}{\partial T'} \right)_{N,V} dT' \\ &= k_B T' \frac{\partial \ln Q}{\partial T'} + k_B \ln Q \Big|_0^T = k_B T \left(\frac{\partial \ln Q}{\partial T} \right)_{N,V} + k_B \ln Q - S_0 \end{aligned} \tag{2.51}$$

where S is the system entropy and S_0 is the entropy at absolute zero. Canceling out S_0 and

expressing in terms of the particle partition functions yields:

$$\begin{aligned} S &= k_B T \left(\frac{\partial \ln Q}{\partial T} \right)_{N,V} + k_B \ln Q = N k_B \left[T \left(\frac{\partial \ln q}{\partial T} \right)_{N,V} + \ln \frac{q}{N} + 1 \right] \\ &= N k_B \left[T \left(\frac{\partial \ln q_{int}}{\partial T} \right)_{N,V} + \ln q_{int} + \frac{3}{2} \ln \frac{2\pi m k_B T}{h^2} + \ln \frac{V}{N} + \frac{5}{2} \right] \\ &= N k_B \left[T \left(\frac{\partial \ln q_{int}}{\partial T} \right)_{N,V} + \ln q_{int} + \frac{5}{2} \ln T + \frac{3}{2} \ln m - \ln P + S_c \right] \end{aligned} \tag{2.52}$$

where all the constant terms are collected into the S_c term, known as the Sackur-Tetrode constant. Note that the a similar equation for the particle entropy can be obtained by evaluating $\ln W$ using (2.3), (2.11), and (2.19), leading to Boltzmann's entropy formula $S = k_B \ln W$.

Oftentimes, the thermodynamic coefficients found in databases are calculated using the following reduced molar form [32, 41]:

$$\frac{H - H_0}{RT} = T \frac{\partial \ln q_{int}}{\partial T} + \frac{5}{2} \tag{2.53}$$

$$\frac{C_p}{R} = T^2 \frac{\partial^2 \ln q_{int}}{\partial^2 T} + 2T \frac{\partial \ln q_{int}}{\partial T} + \frac{5}{2} \tag{2.54}$$

$$\frac{S}{R} = T \frac{\partial \ln q_{int}}{\partial T} + \ln q_{int} + \frac{3}{2} \ln M + \frac{5}{2} \ln T - \ln P + S_c^* \tag{2.55}$$

where $R = N_A k_B$ is the gas constant, N_A is Avogadro's number, M is the molar mass, H_0 is an enthalpy offset with respect to some common energy reference (i.e. enthalpy of formation), and S_c^* is the Sackur-Tetrode constant in molar units. As will be discussed later, these thermodynamic coefficients are typically tabulated in databases as a function of temperature, with polynomial fitting used to produce computationally inexpensive expressions for use in chemical kinetics solvers.

2.1.5 Chemical equilibrium

Having obtained expressions for the state populations and thermodynamic coefficients of a single species gas, we conclude this section by discussing how these concepts apply to plasma chemistry. First, we consider the differential form of the internal energy of a multi-species gas with a variable number of total particles:

$$dE = TdS - PdV + \sum_i \left(\frac{\partial E}{\partial N_i}\right)_{S,V,N_{j\neq i}} dN_i \tag{2.56}$$

where N_i is the number of particles of species i. For physical convenience, the energy balance is typically re-expressed in terms of a state function with P and T as the natural variables:

$$dG = VdP - SdT + \sum_i \left(\frac{\partial G}{\partial N_i}\right)_{P,T,N_{j\neq i}} dN_i \tag{2.57}$$

where the state function G is known as the Gibbs free energy. Then, the change in the Gibbs free energy due to a chemical reaction at constant pressure and temperature is given by:

$$(dG)_{P,T} = \sum_i \left(\frac{\partial G}{\partial N_i}\right)_{P,T,N_{j\neq i}} dN_i = \sum_i \mu_i dN_i \tag{2.58}$$

where μ_i is the chemical potential of species i. For an elementary chemical reaction, stoichiometric balance dictates that:

$$\sum_i \nu_i dN_i = 0 \tag{2.59}$$

where ν_i is the stoichiometric coefficient of species i, which is positive for a product and negative for a reactant. From the above equation, we see that the change in the number of particles of a given species dN_i can be related to that of another reactant or product via the stoichiometric coefficients (i.e. $dN_2 = \nu_2 dN_1/\nu_1$). Therefore, we can define a quantity $d\xi = dN_i/\nu_i$ that is independent of the reacting species to describe the extent of reaction. Then from (2.58), the change in the Gibbs free energy with respect to the extent of reaction

can be expressed as:

$$\left(\frac{dG}{d\xi}\right)_{P,T} = \sum_i \mu_i \nu_i \tag{2.60}$$

where the condition of chemical equilibrium is satisfied when the above quantity is equal to zero. That is, chemical equilibrium is achieved when the Gibbs free energy is minimized with respect to the extent of reaction.

We will now find an expression for the chemical potential μ_i in the above relation using (2.58) and the results of the previous subsection. First, we note from (2.56) and (2.57):

$$G = E - TS + PV = -k_B T \ln Q + N k_B T = -N k_B T \ln \frac{q}{N} \tag{2.61}$$

where we have used (2.45), (2.47), and (2.52). Then, from the definition of the chemical potential in (2.58), we get:

$$\mu = \left(\frac{\partial G}{\partial N}\right)_{P,T} = -k_B T \ln \frac{q}{N} - N k_B T \left(\frac{1}{q}\frac{\partial q}{\partial N} - \frac{1}{N}\right) = -k_B T \ln \frac{q}{N} \tag{2.62}$$

where we have used (2.21) to get $\partial q/\partial N = q/N$. Now, considering again a multi-species gas and expanding the partition function in terms of the internal and translational contributions yields:

$$\begin{aligned}
\mu_i &= -k_B T \ln \left[\left(\frac{2\pi m_i k_B T}{h^2}\right)^{3/2} \frac{V}{N_i} q_{int,i} \exp\left(-\frac{\varepsilon_{0,i}}{k_B T}\right) \right] \\
&= \varepsilon_{0,i} - k_B T \ln \left[\left(\frac{2\pi m_i k_B T}{h^2}\right)^{3/2} k_B T q_{int,i} \right] + k_B T \ln P_i \\
&= \mu_i^0 + k_B T \ln \frac{P_i}{P_0}
\end{aligned} \tag{2.63}$$

where $P_i = k_B T N_i / V$ is the partial pressure of species i and μ_i^0 is the standard state chemical potential holding all terms that depend on temperature only or are constant, including the formation energy $\varepsilon_{0,i}$, which gives the ground state energy of species i relative to a fixed

energy point used for all species. Here, the standard state is defined by the standard pressure P_0 (typically 1 atm), which is a matter of convention and results in expressing the partial pressure P_i relative to P_0 above. Plugging the above expression into (2.60) and considering chemical equilibrium gives:

$$\left(\frac{dG}{d\xi}\right)_{P,T} = \sum_i \mu_i \nu_i = \sum_i \mu_i^0 \nu_i + k_B T \ln\left[\prod_i \left(\frac{P_{i,eq}}{P_0}\right)^{\nu_i}\right] = 0 \tag{2.64}$$

which can be rearranged as:

$$\prod_i \left(\frac{P_{i,eq}}{P_0}\right)^{\nu_i} = \exp\left(-\frac{\Delta\mu^0}{k_B T}\right) \tag{2.65}$$

where $\Delta\mu^0 = \sum_i \mu_i^0 \nu_i$ is the total change in the standard state chemical potential for the reaction. Expressing the above relation in terms of the species number densities yields:

$$K_{eq} = (n_0)^a \exp\left(-\frac{\Delta\mu^0}{k_B T}\right) \tag{2.66}$$

where $K_{eq} = \prod_i (n_{i,eq})^{\nu_i}$ is known as the equilibrium coefficient, $n_0 = P_0/k_B T$ is the number density at standard pressure, and $a = \sum_i \nu_i$. As the name implies, the equilibrium coefficient K_{eq} can be used to solve for the equilibrium species concentrations of a plasma governed by a given set of reactions (molecular dissociation and ionization, for example). The equilibrium coefficient also plays an important role in expressing the kinetic rate coefficients for reversible reactions, as will be discussed later.

Perhaps the most well known equilibrium coefficient for plasmas is the Saha equation, which can be derived by considering the general ionization/recombination process:

$$A^{\{i\}+} \rightleftharpoons A^{\{i+1\}+} + e^- \tag{2.67}$$

where $A^{\{i\}+}$ denotes a heavy species with ionization level i (with $i = 0$ being neutral). Using

(2.60), the corresponding equilibrium condition for this type of reaction can be expressed as:

$$\mu_i = \mu_{i+1} + \mu_e \tag{2.68}$$

where μ_i and μ_e are the chemical potentials of the heavy species and electrons, respectively. From (2.63), the chemical potential can be expressed in terms of the species number density as:

$$\mu_s = k_B T \ln n_s - k_B T \ln \left[\left(\frac{2\pi m_s k_B T}{h^2} \right)^{3/2} q_{int,s} \exp\left(-\frac{\varepsilon_{0,s}}{k_B T} \right) \right] \tag{2.69}$$

for species s, which can be plugged into (2.68) to get:

$$\begin{aligned} \frac{n_{i+1} n_e}{n_i} &= \left(\frac{2\pi k_B T}{h^2} \frac{m_{i+1} m_e}{m_i} \right)^{3/2} \frac{q_{int,i+1} q_{int,e}}{q_{int,i}} \exp\left(-\frac{\varepsilon_{0,i+1} - \varepsilon_{0,i} + \varepsilon_{0,e}}{k_B T} \right) \\ &= \left(\frac{2\pi m_e k_B T}{h^2} \right)^{3/2} \frac{2 q_{int,i+1}}{q_{int,i}} \exp\left(-\frac{I_i}{k_B T} \right) \end{aligned} \tag{2.70}$$

where $I_i = \varepsilon_{0,i+1} - \varepsilon_{0,i}$ is the ionization potential at ionization level i and we have used $m_{i+1} \approx m_i$, $q_{int,e} = 2$, and $\varepsilon_{0,e} = 0$. The equilibrium ionization populations of a multi-species plasma can then be determined by coupling together a set of Saha equations (2.70) for each species up to a desired ionization level and including charge and mass balance equations. The ionization balance can be most conveniently solved by reformulating the problem as a transcendental equation for the electron number density [42], which can easily be computed using fixed-point iteration or similar methods.

2.2 Chemical kinetics

2.2.1 Chemical kinetics system of equations

The basis of a chemical kinetic model is a system of strongly coupled non-linear ODEs which describe the evolution of each species concentration in time:

$$\frac{\mathrm{d}n_i}{\mathrm{d}t} = \sum_{j}^{\text{reactions}} \Delta\nu_{ij}\dot{R}_j \tag{2.71}$$

where n_i is the number density of species i, $\Delta\nu_{ij}$ is the net stoichiometric coefficient for species i in reaction j, and $\dot{R}_j$ is the reaction rate for reaction j. The reason for the non-linearity of the ODE system comes from the form of $\dot{R}_j$, which the law of mass action gives as:

$$\dot{R}_j = k_j \left(\prod_{s}^{\text{reactants}} (n_s)^{\nu_{sj}} \right)_j \tag{2.72}$$

where k_j is the rate coefficient for reaction j and ν_{sj} is the stoichiometric coefficient of reactant s in reaction j. One intuitive way to examine this expression is to view it as a generalization of a binary hard sphere volumetric collision frequency:

$$\dot{R}_{HS} = \underbrace{(r_a + r_b)^2 \sqrt{\frac{8\pi k_B T}{\mu_{ab}}}}_{k_{HS}} n_a n_b \tag{2.73}$$

where r_a and r_b are the collision radii and $\mu_{ab} = (m_a + m_b)/m_a m_b$ is the reduced mass. The rate coefficient in this case takes the form $k = AT^n$ where A contains all the temperature independent terms and $n = 1/2$. If we further impose the restriction that the reactants must possess enough kinetic energy to overcome an energy barrier E_a in order for the reaction to proceed, then we get the following form for the rate coefficient:

$$k = AT^n \exp\left(-\frac{E_\mathrm{a}}{k_B T}\right) \tag{2.74}$$

where, as before, we assume that Boltzmann statistics hold (hence the exponential term). This form of a rate coefficient expression is widely used and is known as the modified Arrhenius equation.

Depending on the physical system being modeled, the chemical kinetic equations given by (2.71) may also be coupled to a set of fluid transport and energy balance equations. While the problem-specific coupling to the fluid equations will be discussed in the next chapter, we will briefly touch on the energy balance here as it is relevant even for a spatially homogeneous problem. This type of problem is useful for examining the chemical kinetics of a reactive system in isolation and is often referred to as a global (or 0D) kinetic model. For example, if we consider the case of an adiabatic cell kept under constant pressure, then (2.71) can be coupled to a heat balance in the form:

$$n_{tot}\frac{\gamma}{\gamma-1}\frac{\mathrm{d}T}{\mathrm{d}t}=\sum_j\frac{\Delta H_j}{R}\dot{R}_j \tag{2.75}$$

where n_{tot} is the total number density, $\gamma=\bar{C}_p/\bar{C}_p-R$ is the mean heat capacity ratio, R is the gas constant, and ΔH_j an $\dot{R}_j$ are the enthalpy change and reaction rate for reaction j, respectively. This equation is a good approximation for those homogeneous atmospheric pressure plasmas where thermodynamic equilibrium between ions, neutrals, and electrons has been achieved (i.e. Boltzmann statistics hold and the plasma can be described by a single temperature). For example, the plasma chemistry in a atmospheric ablation plume in a quasi-stationary condition (i.e. well after ablation when plume expansion slows considerably) could be approximated using such a model [43].

2.2.2 Principle of detailed balance

According to the principle of microscopic reversibility, the relation between the forward and backward reaction rates for a reversible elementary reaction in chemical equilibrium is given

by:

$$\dot{R}_+ = k_+ \prod_r (n_{r,eq})^{-\nu_r} = k_- \prod_p (n_{p,eq})^{\nu_p} = \dot{R}_- \tag{2.76}$$

where $\dot{R}$ is a reaction rate, k is a rate coefficient, and the subscripts $+$ and $-$ refer to the forward and backward reaction directions, respectively. Note that the negative sign of the stoichiometric coefficients on the reactant side is due to our convention of ν being negative for reactants. From this relation and (2.66), we get:

$$\frac{k_+}{k_-} = \prod_i (n_{i,eq})^{\nu_i} = K_{eq} \tag{2.77}$$

that is, that the equilibrium coefficient describes the correlation between the forward and backward rate coefficients in chemical equilibrium. Furthermore, we can reason that since the rate coefficients k_+ and k_- are independent of the particle number densities, (2.77) will hold even for a system not in chemical equilibrium. That is, intuitively, we can see that if the gas composition is adjusted away from equilibrium while the temperature is kept constant, then (2.76) will be violated, but k_+/k_- will remain the same. The generalization of (2.77) to all the reactions in a chemical system is known as the principle of detailed balance.

For convenience, the equilibrium constant is often expressed in terms of molar thermodynamic coefficients as:

$$K_{eq} = (n_0)^a \exp\left(-\frac{\Delta H}{RT} + \frac{\Delta S}{R}\right) \tag{2.78}$$

where, $n_0 = P_0/k_B T$, $a = \sum_i \nu_i$, and $\Delta H = \sum_i \nu_i H_i$ and $\Delta S = \sum_i \nu_i S_i$ are the enthalpy and entropy changes for the reaction, respectively. As previously mentioned in Section 2.1.4, the temperature dependence of thermodynamic coefficients in chemical kinetic solvers is typically treated using a polynomial fitting of (2.53) - (2.55) to save on computational time. For example, the standard fitting form used in combustion chemistry is the 7 term

polynomial [32] representation:

$$\frac{H_i}{RT} = a_{1,i} + \frac{a_{2,i}}{2}T + \frac{a_{3,i}}{3}T^2 + \frac{a_{4,i}}{4}T^3 + \frac{a_{5,i}}{5}T^4 + \frac{a_{6,i}}{T} \tag{2.79}$$

$$\frac{C_{p,i}}{R} = \frac{1}{R}\frac{\partial H_i}{\partial T} = a_{1,i} + a_{2,i}T + a_{3,i}T^2 + a_{4,i}T^3 + a_{5,i}T^4 \tag{2.80}$$

$$\frac{S_i}{R} = a_{1,i}\ln T + a_{2,i}T + \frac{a_{3,i}}{2}T^2 + \frac{a_{4,i}}{3}T^3 + \frac{a_{5,i}}{4}T^4 + a_{7,i} \tag{2.81}$$

where $a_{j,i}$ are the polynomial coefficients for species i. Plugging (2.79) and (2.81) into (2.78) yields:

$$K_{eq} = (n_0)^a \exp\left(\Delta a_1 (\ln T - 1) + \frac{\Delta a_2}{2}T + \frac{\Delta a_3}{6}T^2 + \frac{\Delta a_4}{12}T^3 + \frac{\Delta a_5}{20}T^4 - \frac{\Delta a_6}{T} + \Delta a_7\right) \tag{2.82}$$

where $\Delta a_j = \sum_i \nu_i a_{j,i}$ are the polynomial coefficient changes for the given reaction.

2.2.3 Chemical sensitivity analysis

Since the chemical kinetic ODEs given by (2.71) are strongly coupled and non-linear, the importance of any given reaction channel depends not only on its rate coefficient, but also on the availability of reactants according to the system conditions and overall reaction mechanism. As a result, overly crude methods of sensitivity analysis (such as manually adjusting rate parameters) are seldom effective when applied to chemical kinetic problems. For example, changing the rate coefficient of a single reaction may affect the formation of a species that does not even participate in the given reaction. Alternatively, changing a reaction rate may have no effect on the system for the given conditions due to compensation by another reaction (non-orthogonal channels). Instead, a common approach is to solve an additional set of ODEs for the dependence of the species number densities $\boldsymbol{n}$ on the reaction coefficients

$\boldsymbol{k}$ alongside the chemical kinetic and heat balance ODEs [44]:

$$\frac{\mathrm{d}}{\mathrm{d}t}\frac{\partial \boldsymbol{n}}{\partial k_j} = \boldsymbol{J}\frac{\partial \boldsymbol{n}}{\partial k_j} + \frac{\partial \boldsymbol{Q}}{\partial k_j} \tag{2.83}$$

where $\partial \boldsymbol{n}/\partial k_j$ are the first-order sensitivity coefficients for reaction j, $\boldsymbol{J} = \partial \boldsymbol{n}/\partial k_j$ is the Jacobian, and $\boldsymbol{Q}$ is the chemical kinetic source term (i.e. right hand side of Equation 2.71). This approach is popular partly due to the ready availability of the Jacobian in implicit solution methods commonly used for solving chemical kinetic ODEs. Solving the above equations yields a time history of sensitivity coefficients, which highlight the dominant reaction channels for producing and consuming a given species at a given simulation time. From the evolution of these coefficients, one can then infer how each reaction pathways contributes to the overall evolution of the species of interest.

Chapter 3

Modeling and Analysis of Plasma Flow Reactor and Laser Ablation Systems

Having detailed some of the key chemical and thermodynamic considerations common to both the plasma flow reactor and laser ablation problems, we will now delve into the modeling and analysis tools specific to each of these systems. To facilitate this, the first two sections of this chapter focus on providing technical overviews of each system, including descriptions of both the experimental and modeling details. As it is a focus of this work, special emphasis is placed on how each system can be used in chemical validation studies. The final section of this chapter is reserved for describing the methodology of the Monte Carlo Genetic Algorithm (MCGA) used for solving the inverse problem of reaction mechanism optimization in this work.

3.1 Plasma flow reactor

What we refer to in this work as the plasma flow reactor (PFR) is essentially an inductively coupled plasma atomic emission spectroscopy (ICP-AES) system tailored towards the study of reaction kinetics and nanoparticle formation and growth. With regards to the study of uranium oxide formation, this system is notable for using an atmospheric plasma that is energetic enough to produce vaporized uranium. Although the same can be said of the laser ablation system discussed later, the two systems differ in a number of ways. First, the PFR features significantly longer cooling timescales (ms) and lower maximum temperatures ($\leq$10,000 K) than laser ablation experiments. This presents a more limited, but also more controlled, cooling regime than the laser ablation setup. Second, the atmospheric plasma

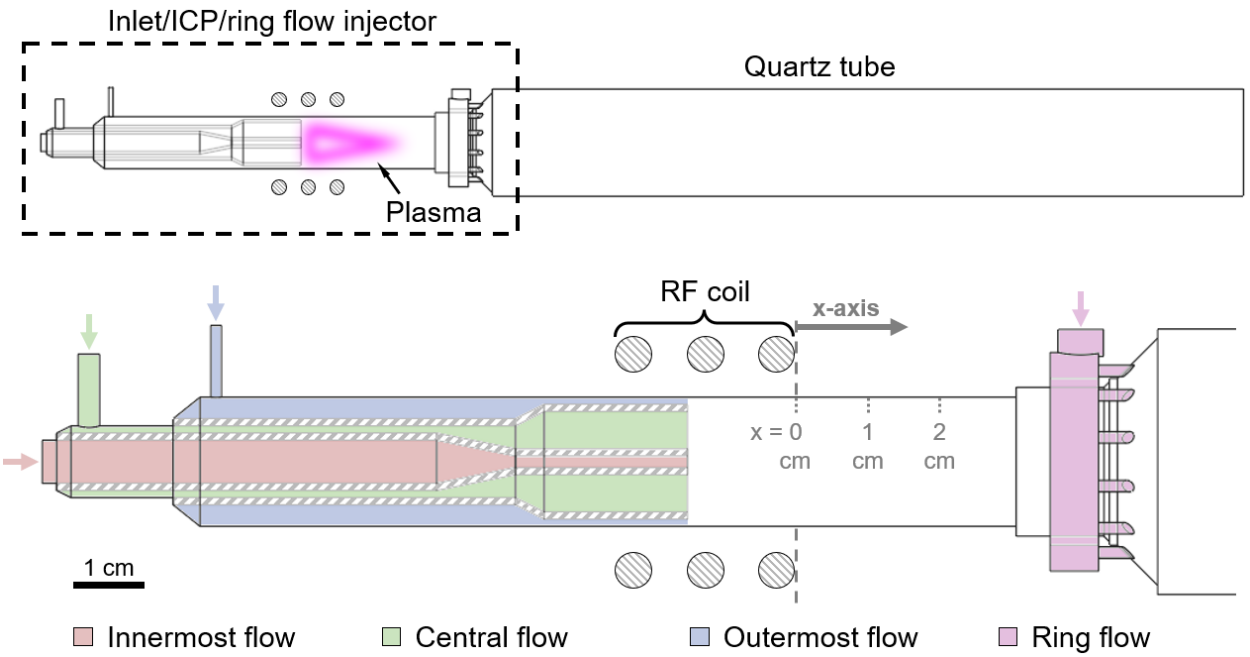

Figure 3.1: Diagram of the plasma flow reactor showing the three concentric annular inlet flow channels, the location of the inductively coupled plasma (ICP) coil, the optional ring flow injector, and the downstream quartz tube.

produced in the PFR lacks the shock expansion inherent in atmospheric laser ablation and the complexities associated with it. As a result, the chemical evolution in the PFR can be more reasonably approximated as a 0D system, significantly reducing the associated computational modeling costs. However, one caveat of using the PFR is the requirement of an aqueous nitrate solution, which introduces a baseline of additional chemical species to the system. Below, we provide a description of the PFR experiments and outline our approach for modeling uranium oxide formation in this system.

3.1.1 System description

A diagram of the PFR used in this work, previously described in the work of Koroglu [15,18], is shown in Figure 3.1. The inlet region of the PFR consists of three concentric annular flow channels, each with a separate flow rate and composition. An aqueous nitrate solution containing the analyte (i.e. uranium) is nebulized into liquid droplets and introduced via

Table 3.1: Number densities, flow rates, and composition of inlet fluids prior to entering the plasma torch region of the flow reactor.

	UO_2	H_2O	NO_3	O_2	Ar
n (cm^{-3})		3.48×10^{22}		2.45×10^{19}	2.45×10^{19}
$\dot{V}$ (L/min)		2.52×10^{-5}		0 – 0.05	1 – 15.4
Molar fraction	4.31×10^{-3}	9.87×10^{-1}	8.62×10^{-3}	1	1
$\dot{N}$ (#/min)	3.78×10^{18}	8.65×10^{20}	7.56×10^{18}	$0 - 1.22 \times 10^{21}$	$(0.25 - 3.77) \times 10^{23}$

the innermost channel (marked in red) using a carrier gas (argon). For a typical argon gas flow rate of 1 L/min, the uranium is about four orders of magnitude less abundant than argon in the innermost flow (i.e. $\sim$100 ppm). In order to enhance oxidation kinetics, additional oxygen gas can also be flown through this channel, with typical flow rates of 10 – 50 mL/min. In addition, the outermost channel (marked in blue) provides an added 12 – 14.5 L/min of argon gas flow to sustain the plasma and to cool the outer quartz wall. No flow is usually added through the central channel (marked in green). Based on the above flow rates, we can expect analyte concentrations on the order of 10 to 100 ppm in the downstream flow, depending on the extent of radial mixing and diffusion. The number densities, flow rates, and composition of the fluid components prior to entering the plasma are listed in Table 3.1, with uranium nitrate split into its component molecules for convenience.

A 40 MHz RF plasma is generated downstream of the inlet channels using an inductive coil surrounding the outer quartz tube. Since the majority of the inlet flow is argon and the plasma is generated at atmospheric pressure, the thermodynamic and transport properties of the plasma can be closely approximated as that of an LTE argon plasma [45, 46]. The plasma and downstream flow temperatures can be modified by adjusting the outermost argon flow rate and the power provided by the power supply. Lastly, an optional ring flow injector can be used to introduce additional argon flow further downstream of the RF coil. Doing so induces additional cooling that can be used to study the temperature dependence of molecular and nanoparticle formation rates, although this feature was not utilized in this

work. Alternatively, a constant diameter quartz tube extension can be connected to the torch when the ring flow injector is not needed. This can be done to reduce the downstream radial transport that may occur due to the channel expansion in the ring flow connector.

Optical emission spectroscopy (OES) is used to track the chemical evolution of the analyte in the PFR. More specifically, light emitted by the plasma is routed to a spectrometer using a fiber optic cable positioned at various axial locations along the flow reactor. A motorized linear translation stage is used to move the fiber optic cable along the x-axis denoted in Figure 3.1, keeping the fiber at a fixed radial distance away from the reactor center. Given the 20 mm outer diameter of the quartz tube and the initial positioning of the fiber optic tip 1-2 mm above the tube, this distance comes to around 11-12 mm. From the numerical aperture of the fiber optic cable (NA = 0.22), an acceptance (half) angle of $\theta_{max} \approx 12.71^o$ is obtained. This yields a rough axial observation range of 5.2 mm along the center of the reactor. The end of the RF coil is used as the reference $x = 0$ axial location for all measurements (as shown in Figure 3.1).

Unfortunately, both the ring flow and constant diameter configurations described above feature optically opaque regions where the flow emission is obscured. These regions cover 0-3 cm and 3-5 cm from the RF coil for the constant diameter extension and the ring flow injector, respectively. Furthermore, as the fiber optic tip is conductive and was not insulated, the minimum axial distance from the RF coil was kept to 1 cm to prevent arcing. Since the flow characteristics in the torch region should be identical for both configurations, the observation limitations can be overcome by combining upstream and downstream data taken with the ring flow and constant diameter configurations, respectively.

3.1.2 Modeling approach

In a previous work, Koroglu *et al.* [18] used a composite 2D and 3D CFD model to simulate the flow field upstream (2D axis-symmetric) and downstream (3D) of the ring flow injector. In the 2D inlet model, the Ohmic heating provided by the RF coil is approximated

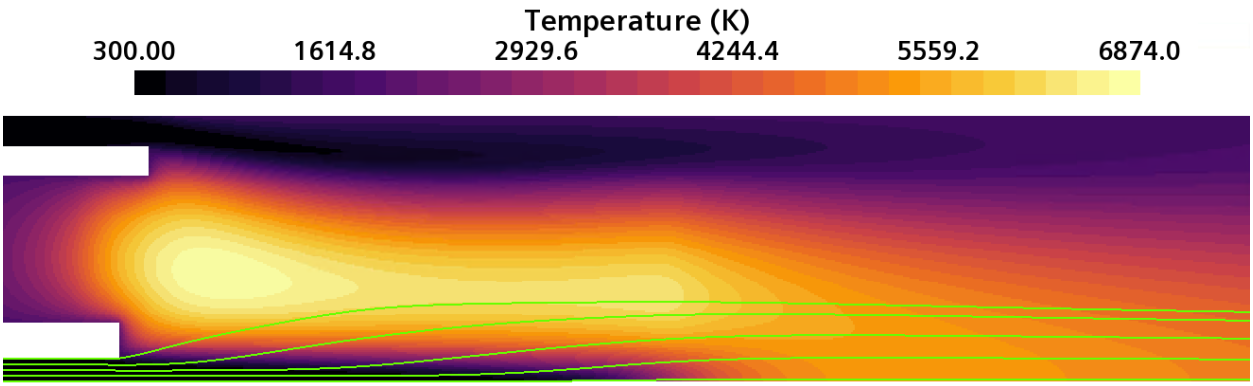

Figure 3.2: Example temperature map from 2D axis-symmetric CFD model of the plasma flow rector, with five Lagrangian streamlines originating from the analyte channel outlined in green.

using a uniform heat source term. Model-experiment comparisons were then performed by extracting a simulated Lagrangian temperature history along a center-adjacent streamline and comparing it with temperature values from Fe emission (Boltzmann plot) and thermocouple measurements. Good agreement was attained through a combination of adjusting the magnitude of the uniform heat source and by axially shifting the extracted temperature profiles. Note that numerous 2D [23, 47, 48] and 3D [49] CFD models solving the fluid and electromagnetic field equations for similar ICP torch configurations have been developed over the years. Although we were able to reproduce and verify one such model [23] within the commercial CFD framework Fluent [50], we encountered issues when attempting to model the PFR configuration used in this work. This may be due to the placement of the RF coil in the current setup, which partially overlaps with the inlet channels, and/or the absence of Ar flow through the middle inlet channel. As good agreement with experiments could not be attained using this model, the aforementioned uniform heat source model was used instead. Only the constant diameter (2D axis-symmetric) component of the model was used, as demonstrated in Figure 3.2, since in this work no data was collected in the downstream regions of the ring-flow configuration.

The above extraction of Lagrangian temperature profiles from the PFR CFD model is especially important in the context of reaction mechanism calibration using emission

measurements. In particular, extracting the temperature/time/distance information for a Lagrangian fluid parcel in the PFR allows for a 0D treatment of an otherwise 2D or 3D problem. That is, instead of simulating the full reactive flow of the PFR, the chemical evolution along a Lagrangian streamline can be solved by using the corresponding temperature history as an input for a 0D chemical kinetic model. The resulting temporal evolution can then be converted to spatial species profiles via the time/distance correlation provided by the streamline. Using these profiles, synthetic species emission intensities can be calculated and compared against spectroscopic measurements. While this approach is approximate, the associated reduction in computational cost compared to a full CFD model is crucial for performing reaction mechanism optimization. Using the temperature history also eliminates the need for an energy conservation equation in the global kinetic model, leaving only a system of ODEs for the species concentrations. This also ensures consistency of the 0D model with experimental conditions due to the matching between the CFD model and the measured temperatures. This type of approach has previously been employed by Koroglu *et al.* to study formation of iron and aluminum oxides in the PFR [15].

Since emission intensity has an exponential dependence on temperature, we expect emission along the flow reactor to be dominated by the highest temperature flow regions (assuming the plasma is optically thin). This will correspond to the center-axis of the PFR downstream of the RF coil, where a fully developed laminar flow is expected to be achieved. In the vicinity of the RF coil, however, the different channel flow rates, non-uniform Ohmic heating, and mixing of the inlet flows will produce a more complicated radial temperature profile. This behavior could potentially be captured within the 0D framework by performing calculations along several Lagrangian streamlines initiated at different radial locations, although with a corresponding increase in computational time. This option is explored later in Section 4.2, but due to the approximate CFD model and a lack of temperature measurements in the upstream coil region, a single representative Lagrangian streamline is used instead.

Once a temperature profile/history is determined, the chemical evolution in the PFR is found by solving the 0D chemical kinetic ODEs previously discussed in Section 2.2.1. A modified version of the ZDPlasKin package [51] is used in this work to perform the integration. The 0D system follows an ideal gas fluid parcel under atmospheric pressure, where the ideal gas law is enforced by adjusting the total number density according to the given temperature profile. The initial condition corresponds to a location inside the analyte flow channel upstream of the ICP coil, where the flow is at room temperature and the analyte molecules are not dissociated. The initial species concentrations are calculated using the experimental molecular flow rates $\dot{N}$ given in Table 3.1 as:

$$n_{0,i} = \frac{P_0}{k_B T_0} \frac{\dot{N}_i}{\sum_j \dot{N}_j} \tag{3.1}$$

where $n_{0,i}$ is the initial number density of molecule i, $P_0 = 1$ atm, and $T_0 = 300$ K. The analyte channel Ar flow rate of 1 L/min is used for this calculation. We assume that the representative Lagrangian streamline experiences limited mixing with Ar flow from the outer channel, such that the Ar to analyte mixing ratio remains constant throughout the simulation.

3.2 Laser ablation

In this work, laser ablation is used as a proxy for studying the plasma chemistry of a nuclear fireball due to the relatively high temperatures (few eV) and fast cooling timescales (ns–μs) present in the system. However, pulsed laser ablation in general is a fairly versatile and powerful tool with myriad uses in material processing and analysis. Material processing applications of laser ablation include machining and surface cleaning [52], nanoparticle and nanostructure synthesis [53–55], and thin films fabrication via pulsed-laser deposition (PLD) [56]. Our interest in the system lies primarily with its use as an analytical tool, more

specifically in laser induced breakdown spectroscopy (LIBS) [57–59]. As the name implies, LIBS refers to volatilizing a target material using a laser pulse and analyzing the chemical composition of the resulting plasma plume from its spectral emission. One common application of LIBS is to serve as a convenient method for determining the identity of a material sample, provided it is done in a chemically inert environment. Conversely, when LIBS is performed in a reactive atmosphere, the plasma- and gas-phase chemical kinetics that take place in the ablation plume can be studied instead [60–63]. LIBS is particularly useful in this capacity when studying the chemical kinetics of refractory metals, like uranium, which are otherwise difficult to vaporize [9, 11, 12, 64, 65]. Below, we provide some background on the typical conditions used for LIBS experiments and how varying these conditions can affect ablation plume dynamics. Moreover, we detail the specifics of the experimental and modeling approaches used in the current work for studying reaction kinetics in ablation plumes.

3.2.1 System description

Ablation plume dynamics produced in LIBS experiments can vary significantly depending on the laser parameters (wavelength, pulse width, energy fluence), the target material, and the ambient pressure and composition [66]. For example, the ambient pressure of the system strongly influences the plume expansion behavior, which ranges from free expansion in a vacuum to spatially confined shock expansion in atmospheric conditions [67]. Similarly, the laser pulse width determines not only the initial material heating mechanism (dictated by pulse duration relative to material relaxation timescales), but also the extent of laser-plume shielding. To keep the scope focused on systems relevant to this work, we will primarily discuss bench-top ablation setups using ns duration pulses at atmospheric pressures. Historically, most LIBS experiments have been performed using such configurations due to their broad availability and applicability. For such systems, the plume expansion will be accompanied by a shock that also shields the target from the pulse. In addition, fluid instabilities may develop in the plume as it expands due to mixing and internal shocks. Understanding how

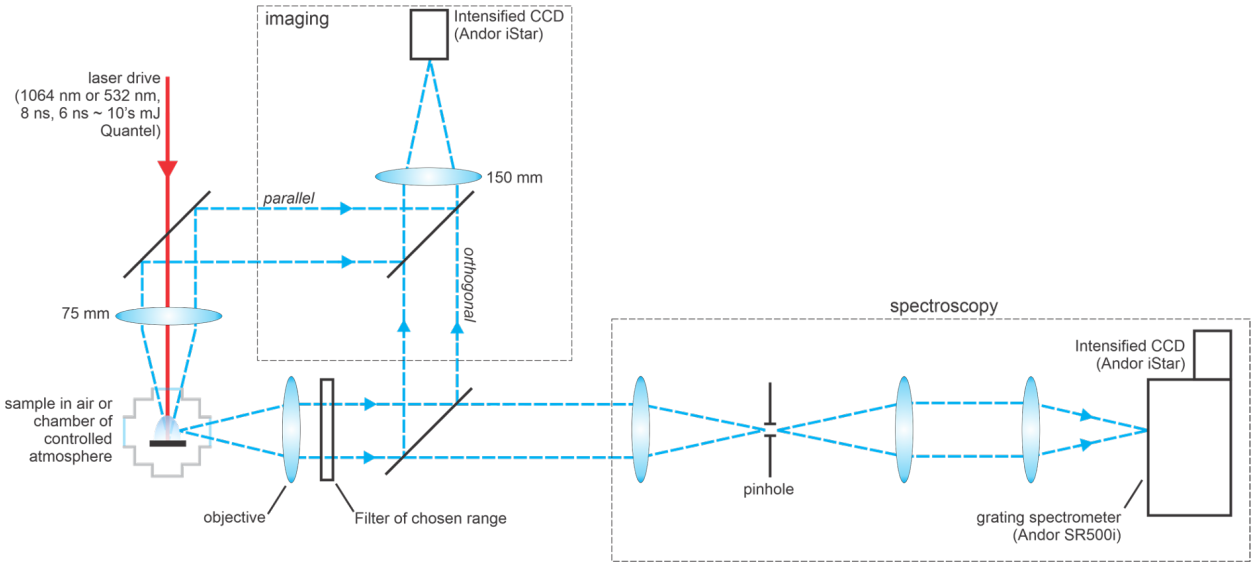

Figure 3.3: Diagram of laser ablation setup that was used to acquire the ICCD plume images examined in this work. Image courtesy of J. Crowhurst (LLNL).

ablation plumes form and evolve is crucial for interpreting LIBS measurements due to the convolution of chemical and fluid dynamic effects in the observed results. These behaviors are most commonly studied in ablation plumes by using optical emission imaging.

Optical imaging studies of laser ablation plumes began soon after the development of the first laser experiments [68, 69]. Since then, a multitude of optical imaging studies aiming to characterize plume dynamics have been performed, covering a wide range of ablation environments, timescales, and laser parameters. Perhaps the most well studied material in this regard is aluminum, with numerous literature works to be found on aluminum plume imaging in atmospheric argon [60, 70–72] and air [60, 73, 74] over sub-microsecond timescales. Several studies concerning the microsecond timescale aluminum plume dynamics and chemistry (i.e. AlO formation) in standard air have also been conducted [61–63]. Additional studies have looked at aluminum ablation in reduced pressure conditions [67, 75, 76] and using ultrafast (femtosecond) lasers [77, 78]. Similar studies have also been performed for copper [79], iron [80], carbon [81–84], and a variety of other materials (including uranium) [11, 64, 85–88].

Several of the imaging studies referenced above serve as validation targets for the modeling efforts in this work. In addition, we also make use of a number of high fidelity intensified

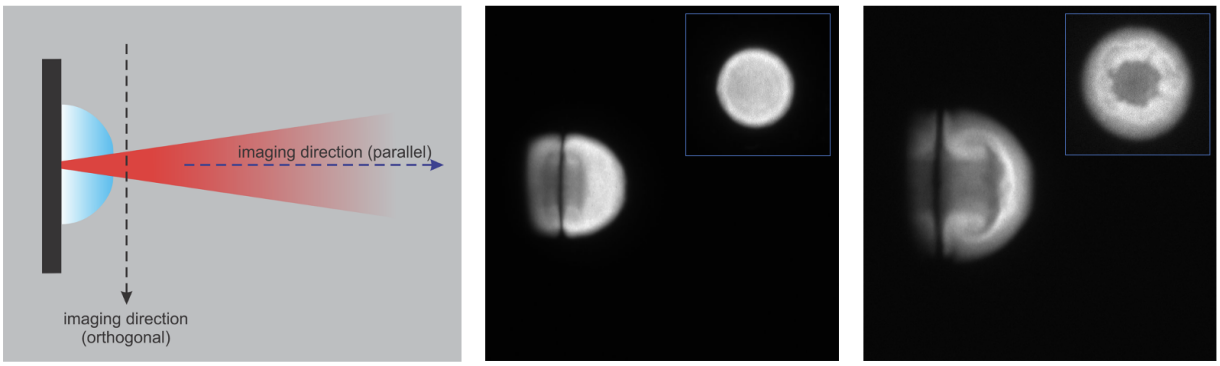

Figure 3.4: Illustrative cartoon and example images of laser ablated carbon plume in atmospheric air, highlighting the two different imaging directions. Images courtesy of J. Crowhurst (LLNL).

charge coupled device (ICCD) images taken by J. Crowhurst at Lawrence Livermore National Laboratory. The experimental laser ablation system used to acquire these images is shown in Figure 3.3. The system uses a 1064 nm Nd:YAG laser with energies up to 100 mJ per pulse. For the images examined in this work, an 8 ns FWHM pulse with an energy of 15 mJ was focused on a 280 μm spot size on the target surface. These laser parameters correspond to an approximate fluence and intensity of 25 J/cm^2 and 4×10^9 W/cm^2, respectively. The spectroscopic diagnostics used include a 0.5 m grating spectrometer with a 2400 grv/mm grating. Imaging diagnostics include one ICCD dedicated to plume imaging, and another ICCD dedicated to spectroscopy, allowing for simultaneous imaging and spectral acquisition. The time resolution of the ICCD imaging is up to 3 ns. The system allows imaging both orthogonal to the incident laser beam direction and parallel to it, as illustrated in Figure 3.4. As part of the model validation in this work, we produce synthetic emission maps along both of these directions.

3.2.2 Modeling approach

In nanosecond laser ablation, the formation and growth of the plasma plume is largely shaped by the dynamics of laser-plume interaction. In a typical ns laser ablation event, the air is initially completely transparent to the laser, and the laser energy is deposited completely

into the material over the first few nanoseconds. During this time, rapid expansion of the material region occurs and produces a corresponding shock front. As the shock front begins to propagate into the surrounding atmosphere, it produces a hot, dense plasma in the surrounding gas along the outer plume edge. Due to the high density and degree of ionization in this region, an increasing fraction of the incoming laser energy begins to be absorbed by the ambient gas plume. Consequently, this outer ambient plasma region increasingly shields the inner material region from the laser as the pulse grows towards peak intensity. Thereafter, the remaining laser energy is largely absorbed in the outer plume region up to the end of the pulse. As a result, it is typical for much of the laser energy to be absorbed by the ambient plasma region that surrounds the ablated material region. This pattern of laser absorption and plume propagation is typical for IR (1064 nm) lasers [72, 89] and has been referred to in literature as a laser-supported detonation (LSD) wave [90, 91].

Over the years, numerous theoretical and computational methods have been used to study the dynamics of nanosecond laser ablation. Early theoretical studies of ns laser ablation focused on treating the laser induced material heating and vaporization processes [92], the expansion dynamics and laser shielding of plasma plumes [90], and the coupling between these material conduction and plume hydrodynamics problems [93]. The two problems are typically bridged by the Knudsen layer [94], which is a region above the material interface where the ablated vapor achieves translational equilibrium within a few mean free paths. This condition relates the temperature and pressure of the evaporated material to the corresponding surface conditions. Many computational models have employed either this Knudsen layer relation [83, 95–98] or else the Clausius-Clapeyron equation [99, 100] to provide a straightforward treatment of the target-plume coupling. Other models have focused solely on either the material heat conduction [101, 102] or plume dynamics [17, 103–105] problem by making simplifying assumptions of how the other processes proceed. For example, the aftermath of laser-material energy deposition has previously been approximated as a high temperature and pressure region that serves as an initial condition for a purely hydrodynamic

simulation [103]. Yet another approach is to solve a single set of fluid dynamic equations for both the target and plume regions, but use material-specific multi-phase equations of state (EOS) to treat the melting and evaporation processes [106–108]. The latter two modeling frameworks are used in this work to study laser ablation plume dynamics and chemistry, as detailed in the subsequent subsections.

3.2.3 Reactive CFD modeling

The first type of ablation model examined in this work uses a purely hydrodynamic approach, wherein the pulsed laser energy deposition is assumed to be instantaneous. That is, instead of simulating the laser-material interaction, phase transition, and plume shielding processes, the simulation is initialized with an equivalent high temperature and pressure material plasma region. This region is shaped as a "crater" located along the material-ambient interface, as shown in Figure 3.5, with dimensions estimated based on the laser spot size and fluence [109]. The figure also shows the boundary conditions for a 2D axis-symmetric treatment of such a problem, consisting of a no-slip condition along the bottom wall, a symmetry condition along the left border, and a non-reflective [110] outflow condition along the outer edge. The initial conditions of the plasma in this "crater" can be estimated based on the incoming pulse energy and factors like the material reflectively for the given laser wavelength. Typically, however, the initial conditions are adjusted to match some set of experimental observations, such as the propagation velocity of the leading shock or spectroscopic temperature measurements.

Since the material phase transition is not simulated directly, the hydrodynamic ablation problem is reduced to that of a single phase fluid. This accordingly lowers the computational complexity of the model, allowing detailed treatments of plasma chemistry and multi-species diffusion to be carried out over μs timescales. Here, we utilize the ANSYS Fluent CFD software [50] to perform such calculations. In particular, a pressure-based solver for compressible, multi-species, reactive fluid flows is used. A Pressure-Implicit with Splitting of Operators (PISO) scheme is used for the pressure-velocity coupling of the segregated pressure-based

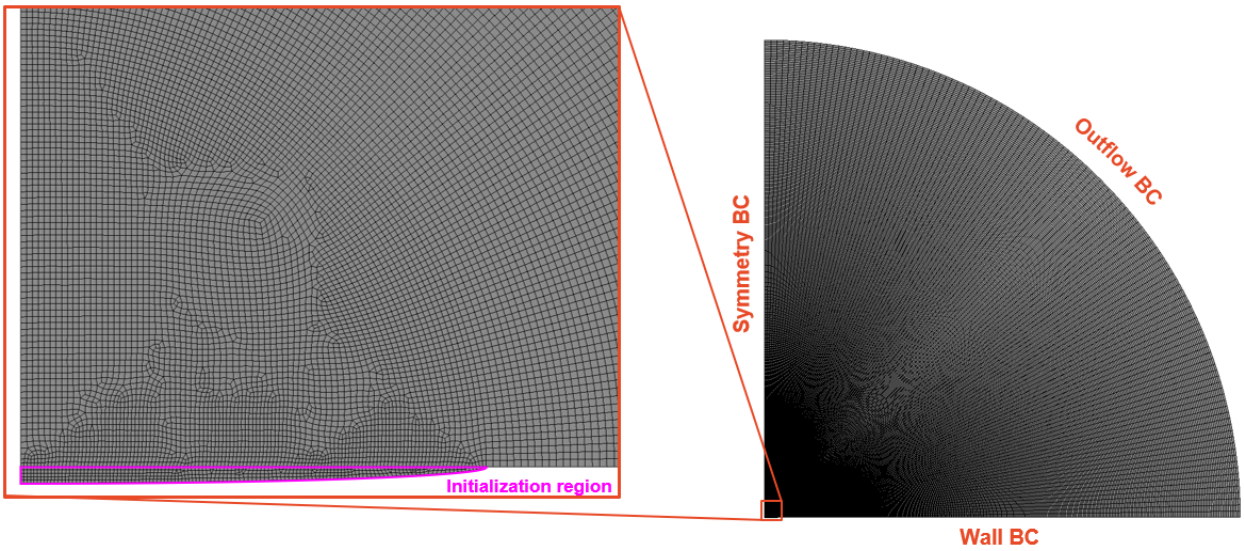

Figure 3.5: An example 2D Fluent mesh used in ablation simulations, with the high temperature and pressure material initialization ("crater") region highlighted. Typical domain sizes are on the order of a few mm, whereas the crater depth is at most 10s of μm deep and 100s of μm wide.

solver [111]. The cell face pressure interpolation procedure is performed using a face centered staggered grid via the PREssure STaggering Option (PRESTO) scheme [112]. A Quadratic Upstream Interpolation for Convective Kinematics (QUICK) type scheme is used for density interpolation and spatial discretization of the convection terms in the fluid equations [113]. Time integration is performed using a bounded second order implicit method [114]. Both inviscid (Euler) and viscous (Navier-Stokes) formulations of the fluid equations have been utilized here. We will proceed by laying out the full Navier-Stokes equations being solved in the viscous case and point out the terms absent in the inviscid case as appropriate. The mass, momentum, energy, and species conservation equations for the reactive Navier-Stokes formulation are:

$$\frac{\partial \rho}{\partial t} + \nabla \cdot (\rho \boldsymbol{v}) = 0 \tag{3.2}$$

$$\frac{\partial (\rho \boldsymbol{v})}{\partial t} + \nabla \cdot (\rho \boldsymbol{v}\boldsymbol{v} + P) = \nabla \cdot \boldsymbol{\Pi} \tag{3.3}$$

$$\frac{\partial (\rho E)}{\partial t} + \nabla \cdot ((\rho E + P)\boldsymbol{v}) = \nabla \cdot (\boldsymbol{\Pi} \cdot \boldsymbol{v}) - \nabla \cdot \boldsymbol{q} + \sum_{i}^{species} \Delta H^{o}_{f,i} \dot{S}_i \tag{3.4}$$

$$\frac{\partial(\rho Y_i)}{\partial t} + \nabla \cdot (\rho Y_i \boldsymbol{v}) = -\nabla \cdot \boldsymbol{\Gamma}_i + m_i \dot{S}_i \tag{3.5}$$

where ρ is the total fluid mass density, $\boldsymbol{v}$ is the advection velocity vector, P is the fluid pressure, $\boldsymbol{\Pi}$ is the viscous stress tensor, E is the total specific energy, and $\boldsymbol{q}$ is the conductive heat flux. The mass conservation of each species i is expressed in terms of the species mass density fraction $Y_i = \rho_i/\rho$, species mass flux $\boldsymbol{\Gamma}_i$, and species rate of production $\dot{S}_i$, which also contributes to the reactive heating source term in the energy balance via the enthalpy of formation $\Delta H^o_{f,i}$. The total specific energy E is given by the sum of the specific internal and mechanical energy:

$$E = h - \frac{P}{\rho} + \frac{\boldsymbol{v} \cdot \boldsymbol{v}}{2}, \quad \text{where} \quad h = \sum_i^{\text{species}} h_i Y_i \tag{3.6}$$

$$h_i = \int_{T_0}^{T} c_{p,i} dT' \tag{3.7}$$

where h_i and $c_{p,i}$ are the specific sensible enthalpy and the specific heat capacity at constant pressure of species i, respectively. The thermodynamic properties of each species are specified using a 7 term polynomial representation, as previously shown in Section 2.2.2. Lastly, the equation of state is described by the ideal gas law $P = \rho RT/\bar{m}$ where $\bar{m}$ is the mean molar weight of the fluid. The viscous stress tensor $\boldsymbol{\Pi}$, conductive heat flux $\boldsymbol{q}$, and species mass flux $\boldsymbol{\Gamma}_i$ appear only in the "viscous" (i.e. Navier-Stokes) formulation. The heat and mass fluxes are given by:

$$\mathbf{q} = \sum_i^{\text{species}} \boldsymbol{\Gamma}_i h_i - \lambda_0 \nabla T \tag{3.8}$$

$$\boldsymbol{\Gamma}_i = \rho Y_i \mathbf{V}_i, \quad \text{where} \quad \mathbf{V}_i = \frac{1}{X_i \bar{m}} \sum_j^{\text{species}} m_j D_{ij} \nabla X_j \tag{3.9}$$

where λ_0 is an effective thermal conductivity coefficient, m_i is the species molar weight, X_i is the species number density fraction, $\mathbf{V}_i$ is the species diffusion velocity, and D_{ij} is the multicomponent diffusion coefficient [115].

3.2.4 Radiation hydrodynamics modeling

While convenient, the idealized initialization procedure used in the above CFD model has a number of issues that make it less than ideal for a validation study. First, it requires calibration of the initial pressure and temperature values with respect to experimental observations, making it difficult to use in a predictive fashion. Second, it does not capture the laser-material energy deposition that is responsible for initiating ablative vaporization and/or phase explosion, instead assuming uniform instantaneous vaporization. Lastly, it ignores the laser-plasma interaction that will take place following ablation and preceding the end of the pulse, which will produce additional non-uniform plume heating.

A number of models (mostly 1D) that solve a material heat conduction equation coupled with Euler equations for plume expansion, including plasma shielding, have been developed over the years [83,97,99,100,116–118]. In particular, the work of Mościcki *et al.* [97] provides a detailed description of incorporating this type of model within the Fluent framework; albeit with an iterative coupling of the target heating and plume expansion portions. A more complete non-Fluent model, including a collisional-radiative kinetic mechanism for the initial non-equilibrium expansion, was also developed by Autrique and colleagues [117]. To our knowledge, this model has only been implemented in 1D and has not been made publicly available. However, in addition to these laser ablation specific models, similar capabilities can be found in radiation-hydrodynamics (rad-hydro) models, which are developed for a wide variety of astrophysical and high energy density physics (HEDP) applications. The use of ultra-intensity short-pulse lasers for plasma production is common in HEDP, although the resulting plasmas are generally much hotter and denser than bench-top ablation plasmas. Nevertheless, such models solve for radiation transport, non-LTE hydrodynamics (i.e. $T_e \neq T_{ion} \neq T_{rad}$), and make use of material equations of state (EOS) that cover a wide range of temperatures and pressures. These features are similarly desirable for overcoming the limitations of the purely hydrodynamic model in simulating the early stages of laser ablation,

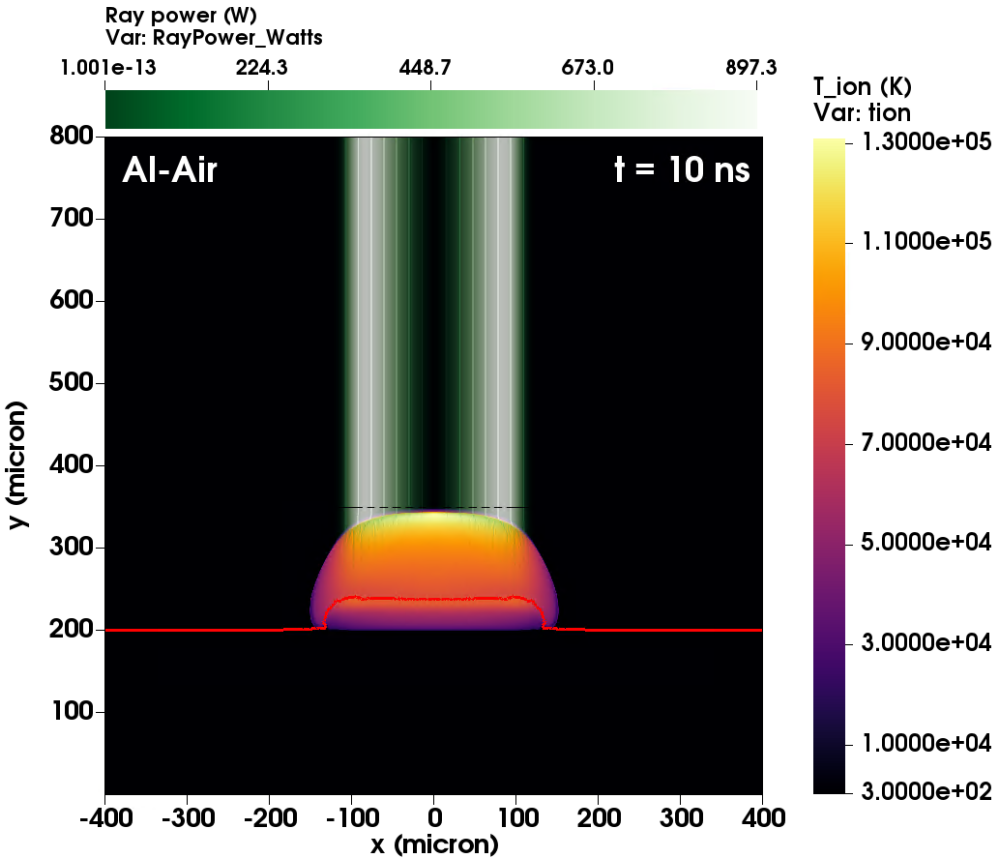

Figure 3.6: Mid-pulse snapshot of ion temperature and ray power in a FLASH simulation of aluminum laser ablation in atmospheric air. The aluminum target is 200 microns thick, as shown by the red contour denoting the aluminum-air interface. The simulation domain is symmetric across the y-axis but was mirrored here for clearer visualization.

thereby allowing for a more predictive modeling approach.

The radiation-hydrodynamics model used in this work is based on a modified version of the "LaserSlab" simulation unit from the FLASH radiation-hydrodynamics code [119, 120]. An example FLASH simulation for a bench-top aluminum laser ablation event in atmospheric air is demonstrated in Figure 3.6. For this type of problem, FLASH solves the compressible Euler equations using a three temperature (ion T_i, electron T_e, and radiation T_r) unsplit hydro solver, including multigroup radiation diffusion and laser energy deposition, as described below. The $3T$ Euler equations are given by:

$$\frac{\partial \rho}{\partial t} + \nabla \cdot (\rho \boldsymbol{v}) = 0 \tag{3.10}$$

$$\frac{\partial(\rho \boldsymbol{v})}{\partial t} + \nabla \cdot (\rho \boldsymbol{v}\boldsymbol{v}) + \nabla P = 0 \tag{3.11}$$

$$\frac{\partial(\rho E)}{\partial t} + \nabla \cdot ((\rho E + P)\boldsymbol{v}) = Q_{\text{las}} - \nabla \cdot \boldsymbol{q} \tag{3.12}$$

where ρ is the mass density, $\boldsymbol{v}$ is the velocity, P is the total pressure, E is the total specific energy, Q_{las} is an energy source due to inverse Bremsstrahlung (IB) laser absorption, and $\boldsymbol{q}$ is the total heat flux due to conduction. The total pressure, specific energy, and conductive heat flux are given by:

$$P = P_i + P_e + P_r \tag{3.13}$$

$$E = E_i + E_e + E_r + \frac{\boldsymbol{v} \cdot \boldsymbol{v}}{2} \tag{3.14}$$

$$\boldsymbol{q} = \boldsymbol{q}_e + \boldsymbol{q}_r = -k_e \nabla T_e + \boldsymbol{q}_r \tag{3.15}$$

where the subscripts i, e, and r refer to ion, electron, and radiation contributions, respectively, and k_e is the electron thermal conductivity. The conservation equations for each of the specific internal energy components are given by:

$$\frac{\partial(\rho E_i)}{\partial t} + \nabla \cdot ((\rho E_i + P_i)\boldsymbol{v}) = \frac{\rho c_{v,e}}{\tau_{ei}} (T_e - T_i) \tag{3.16}$$

$$\begin{aligned} \frac{\partial(\rho E_e)}{\partial t} + \nabla \cdot ((\rho E_e + P_e)\boldsymbol{v}) &= \frac{\rho c_{v,e}}{\tau_{ei}} (T_i - T_e) \\ &\quad - \nabla \cdot \boldsymbol{q}_e + Q_{\text{abs}} - Q_{\text{emis}} + Q_{\text{las}} \end{aligned} \tag{3.17}$$

$$\frac{\partial(\rho E_r)}{\partial t} + \nabla \cdot ((\rho E_r + P_r)\boldsymbol{v}) = \nabla \cdot \boldsymbol{q}_r - Q_{\text{abs}} + Q_{\text{emis}} \tag{3.18}$$

where $c_{v,e}$ is the electron specific heat, τ_{ei} is the electron-ion collision time, and Q_{abs} and Q_{emis} represent the total heat exchange between the electrons and the radiation field due to photon absorption and emission, respectively. These latter terms are obtained by solving a

set of multigroup radiation diffusion equations:

$$\rho \frac{\partial E_{r,g}}{\partial t} = \nabla \cdot \boldsymbol{q}_{r,g} - Q_{\text{abs},g} + Q_{\text{emis},g} \tag{3.19}$$

where g is the photon energy group with frequencies between ν_g and ν_{g+1} and the right hand side terms are given by:

$$\boldsymbol{q}_{r,g} = \frac{c\rho}{3\sigma_{t,g}} \nabla E_{r,g} \tag{3.20}$$

$$Q_{\text{abs},g} = -\sigma_{a,g} c \rho E_{r,g} \tag{3.21}$$

$$Q_{\text{emis},g} = \sigma_{e,g} \frac{8\pi (k_B T_e)^4}{h^3 c^2} \left(P(u_{g+1}) - P(u_g) \right) \tag{3.22}$$

where c is the speed of light, k_B is the Boltzmann constant, h is the Planck constant, and $\sigma_{t,g}$, $\sigma_{a,g}$, and $\sigma_{e,g}$ are the group transport, absorption, and emission opacities, respectively. The group transport opacities are calculated as the Rosseland mean while the group absorption and emission opacities are calculated as the Planck mean. The Planck integral $P(u_g)$ is given by:

$$P(u_g) = \int_0^{u_g} \frac{(u')^3}{\exp(u') - 1} du' \tag{3.23}$$

where $u_g = h\nu_g / k_B T_e$. The remaining source term Q_{las} in (3.17) is due to electron-ion IB absorption of the incident laser, which is proportional to a power loss frequency factor given by:

$$\nu_{IB} = \frac{n_e}{n_c} \nu_{ei} = \sqrt{\frac{2\pi}{m_e}} \frac{4 n_e^2 Z e^4 \ln \Lambda}{3 n_c (k_B T_e)^{3/2}} \tag{3.24}$$

where n_e is the electron number density, ν_{ei} is the electron-ion collision frequency, m_e is the electron mass, Z is the average ionization of the plasma, e is the elementary charge, $\ln \Lambda$ is the Coulomb logarithm, and $n_c = m_e \pi c^2 / \lambda^2 e^2$ is the critical number density at which the laser and plasma frequencies are equal (for a laser with wavelength λ).

A tabulated equation of state (EOS) is used to close the above system of equations. The EOS specifies the partial pressures and energies of the ions and electrons (P_i, P_e, E_i, and

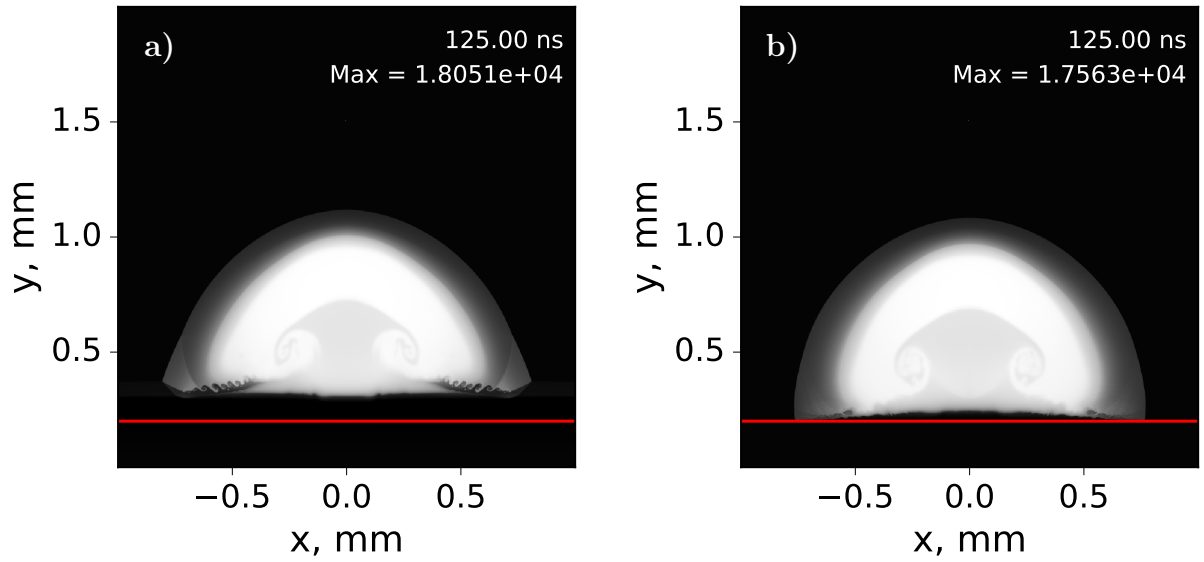

Figure 3.7: Example of normalized plume temperature profiles for Al ablation in air when the Al EOS file used is a) the default LEOS file and b) an LEOS file corrected with ideal gas pressures at or below room temperature. The red line marks the location of the target surface prior to ablation.

E_e above) for a material at a given temperature and density. In addition, the EOS file also specifies the degree of ionization and the multi-group opacities used in the radiation transfer equations. The tabulation of the EOS is done as a pre-processing step, with table lookup/interpolation performed as needed during the simulation. Target material EOS files are obtained from the Livermore EOS database (LEOS) [121,122], whereas an ideal gas EOS with Saha ionization is used for the chamber gas. The multigroup Rosseland and Planck mean opacities for all materials are calculated using the IONMIX code [123]. The opacity calculations assume a Saha ionization balance and employ hydrogenic approximations for calculating electron energy levels and collision cross sections. The EOS is tabulated using 41 points in log space for both temperature and number density (spanning 10^{-2}–10^{2} eV and 10^{16}–10^{24} cm^{-3}, respectively) and 6 photon energy groups for radiation transport (spanning 10^{-1}–10^{5} eV). Note that since the EOS does not treat molecules, the air is always considered to be fully dissociated, resulting in an absolute chamber pressure of $\sim$2 atm.

A notable EOS-related issue encountered in the FLASH simulations is that room temper-

ature solids possess a pressure many times greater than that of the surrounding atmosphere. The resulting pressure gradient at the target-air interface drives artificial advection of the solid into the atmosphere, as shown in Figure 3.7. Several solutions for resolving this unphysical behavior were tested. The simplest workaround involved modifying the material EOS to behave as an ideal gas at or below a threshold temperature (i.e. room temperature), such that the cold solid pressure equals the ambient pressure. This method works well when using cubic interpolated ray tracing, but requires a slight modification for the cell averaged algorithm. In the latter case, the pressure of the material needs to be $\sim$10% higher than the ambient pressure to prevent complete reflection via Snell's law due to the large electron number density discontinuity at the material-air interface. Another solution is to instead disable advection for material cells at or below a threshold temperature. This method only works with the cubic interpolated ray tracing, and produces similar results to the EOS-based fix. The largest differences in plume behavior when switching between these methods occurs near the plume/target interface, with the overall plume shape and expansion rate remaining mostly unaffected. Each of these corrections was found to have stability issues when running the simulation past 100 ns; the cell averaged EOS-based method behaved best in this regard and was therefore employed for all the FLASH results shown in this work.

The radial laser power distribution follows a super-Gaussian profile with $n = 5$, and the laser beam is radially divided into 4096 rays for the ray tracing algorithm. A Gaussian temporal profile is used, and it was found that using a different temporal profile typical for Nd:YAG lasers [101] had little effect on the resulting plume evolution. The laser energy deposition is assumed to proceed by electron-ion inverse Bremsstrahlung (IB) only. Physically, the initial heating of the target material actually occurs by electron-neutral IB but quickly becomes dominated by electron-ion IB once ionization takes place [91]. Since electron-neutral IB is significant only in starting the ablation process and its overall energy contribution is negligible compared to electron-ion IB, it is not included in FLASH. Instead, a minimum ionization fraction threshold of 2% is set for the target material, such that electron-ion IB

alone is sufficient to initiate ablation. This removes the need for calculating an electron-neutral IB heating term while still allowing an initial plasma region to be generated from the target surface.

3.2.5 Coupled radiation hydrodynamics and reactive CFD modeling

Although the radiation hydrodynamics model presented in the previous section is better suited for initializing the laser ablation problem than the preceding CFD model, it is also less suited for solving the post-pulse reactive flow problem. In particular, the FLASH code used in this work does not solve chemical kinetics equations, including reactive heating, or include multi-species transport (although implementations of such are possible [124]). Therefore, in addition to using each of the above frameworks separately, we also perform a model coupling to leverage the strengths and minimize the weaknesses of the two models. In this coupling, the FLASH radiation-hydrodynamics model is used to treat the pulse-duration and ns-timescale phenomena while the reactive CFD Fluent model treats the post-pulse μs timescale expansion. In this way, the predictive capabilities of the FLASH model towards resolving the laser energy deposition problem are coupled with the robust reactive flow solvers used by Fluent. The models are one-way coupled, with the output of the rad-hydro code serving as an initial condition for the reactive CFD model. However, since there are a number of differences between the governing equations used by the two models, the coupling procedure necessarily involves some processing of the FLASH generated data before it can be used in the Fluent model. The specifics of the coupling procedure are detailed below.

The first consideration made in the coupling is the difference in the computational meshes used in the two models. FLASH uses an adaptive mesh refinement (AMR) scheme to generate its mesh which, as the name implies, changes over the course of the simulation. The domain is originally divided into a specified number of square "blocks", and these blocks are refined

(i.e. divided into smaller blocks) based on a criterion that allows for adequate resolution of the specified flow variable gradients at the given location and time. The resulting grid is obviously non-uniform, but is nevertheless structured and rectangular. The mesh used in the Fluent model (Figure 3.5), on the other hand, is unstructured and has mixed triangular and quadrilateral elements, but is fixed. Due to the additional viscous transport and chemical kinetics terms being solved by Fluent, as well as the longer problem times being simulated, the Fluent mesh is relatively coarse when compared to the FLASH mesh. For example, the smallest element size in FLASH is on the order of 0.4 μm, whereas most elements in the Fluent mesh are on the order of 1-2 μm. Therefore, the FLASH mesh is down-sampled prior to interpolating the flow variables onto the Fluent mesh. The effect of the difference in mesh resolution is most noticeable along the shock front, where the FLASH mesh is the finest. Ideally, such discrepancies can be eliminated by utilizing a similarly adaptive mesh in the Fluent simulation, although this may lead to prohibitively long simulation times. Here, we mitigate the issue by interpolating from a later time point in FLASH, as this both lowers the magnitude and lengthens the gradients of the leading and internal shocks. However, completely eliminating the issue would likely require exactly matching the FLASH and Fluent meshing methodologies, which was not done here.

The next consideration in the coupling is the conversion of the FLASH flow variables into equivalent Fluent variables. The information extracted from the FLASH output includes the pressure, temperature, velocity, mass density, and material region variables. Since Fluent assumes local thermodynamic equilibrium (LTE, i.e. $T_i = T_e$), the FLASH solution should be evolved until LTE holds throughout the domain, at which point the LTE temperature field can be transferred directly to Fluent. The velocity flow fields can similarly be used without modification in Fluent. The main difficulty arises when considering the transfer of species information, which also impacts the pressure and mass density variables. Significant discrepancies can arise when converting these variables to a reactive (multi-species) Fluent format due to one of the limitations of the tabulated EOS used in FLASH. Namely, each

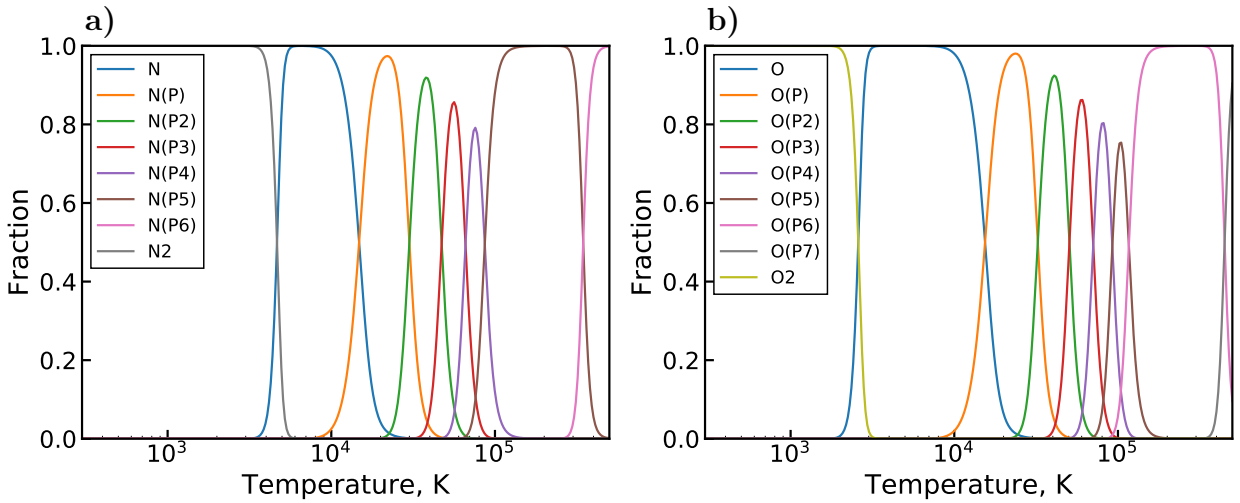

Figure 3.8: Equilibrium (LTE ideal gas) compositions of a) nitrogen and b) oxygen gases at 1 atm, given as heavy species fractions.

material EOS in FLASH is assigned an average atomic mass that is treated as a constant parameter. When mass densities are passed to the EOS, the corresponding material number densities are calculated using this average atomic mass value. This poses no issues when calculating the ion number densities and pressures in plasma regions with full molecular dissociation. However, the calculated number density and pressure will correspond to a fully dissociated state even for conditions where the material should realistically be in a molecular form (i.e. standard air). This does not result in any serious physical discrepancies in FLASH since the correct mass densities are used and the pressure is calculated consistently across materials. However, discrepancies may arise when transferring the FLASH species densities to a reactive Fluent simulation tracking both atomic and molecular species. In laser ablation simulations, these discrepancies are most significant in regions of high pressure and low temperature near the shock front. The extent of molecular dissociation in these regions will also depend on the species being considered, as seen from the equilibrium composition plots in Figure 3.8. If the species densities are transferred directly with no modification, molecular recombination reactions will quickly produce a pressure drop and heat release in these regions. If the species concentrations are first adjusted to maintain consistent

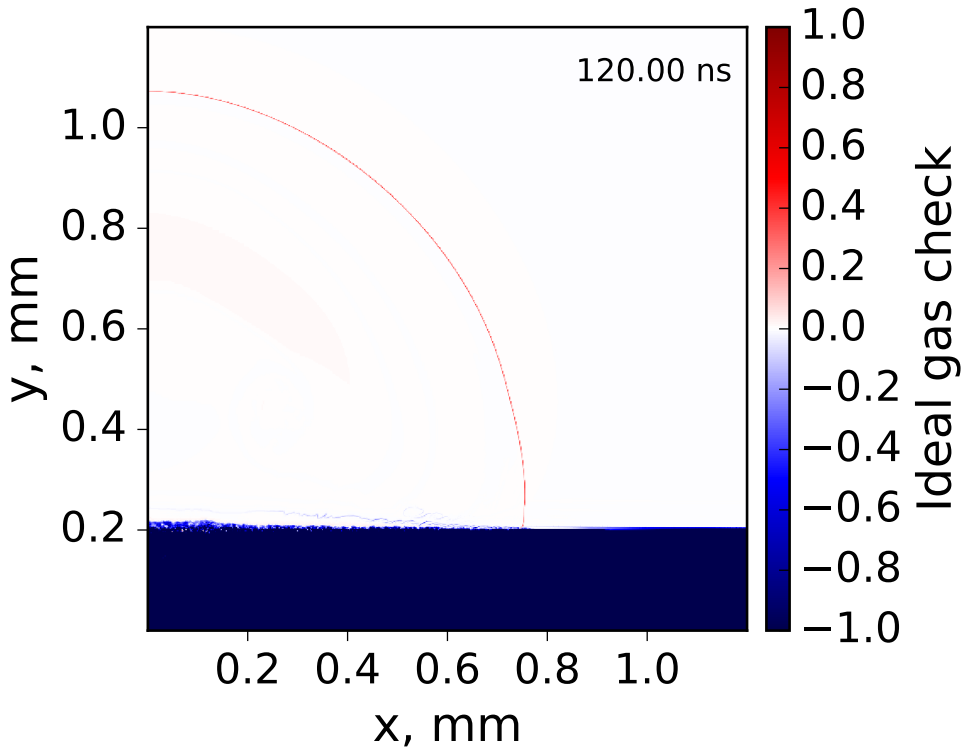

Figure 3.9: Check of ideal gas law behavior in an example FLASH solution snapshot using Equation 3.25.

pressures, discrepancies in mass density arise instead. These issues can be mitigated if the coupling time is picked such that the temperatures near the shock front are sufficiently high for complete dissociation. In this case, only the pressures in the (cold) ambient medium need to be adjusted, which should minimally perturb the flow if the magnitude of the shock far exceeds the ambient pressure. Alternatively, the discrepancies can be eliminated by excluding the responsible molecular species from the Fluent model, although this obviously affects the reaction kinetics of the problem and is thus not desirable.

Aside from the above issues, transferring the flow variables also involves generating the species number densities, as these are not tracked individually by FLASH. Instead, FLASH stores the flow composition in terms of which material(s) occupy a given region. If, again, an LTE ideal gas treatment can be employed, then a Saha/molecular dissociation balance can be solved to estimate the ion and electron number densities in a given region, as previously

shown in Figure 3.8. Since the air EOS used in FLASH here is generated by solving a Saha ionization balance and applying the ideal gas equation, this approach is exact for the air regions. Conversely, since the material EOS files used here do not employ such a treatment, this approach is only approximate in the material regions. To check if this holds true, the deviation of the FLASH solution away from ideal gas behavior can be evaluated as:

$$\delta_{IG} = 1 - \left(1 + \bar{Z}\right) \frac{\rho}{\bar{A}} \left(\frac{P_i}{k_B T_i} + \frac{P_e}{k_B T_e} \right)^{-1} \tag{3.25}$$

where $\bar{Z}$ and $\bar{A}$ are the mean charge and atomic mass, respectively, and the remaining variables follow the conventions presented in Subsection 3.2.4. An example application of this relation for the ablation problem is shown in Figure 3.9. Unsurprisingly, the strongest deviation occurs in the solid and liquid target regions, which should be excluded from the fluid simulation. A deviation is also visible along the leading shock, which appears to be due to a slight mismatch between the temperature and pressure front locations. This is likely numerical, as the displacement is on the order of the smallest mesh length scale of ~ 0.4 microns. Aside from this thin region, both the material and air regions are observed to closely follow ideal gas behavior. This suggests that an ideal gas EOS can be used in Fluent to advance the solution further. To ensure that the fluid flow transferred to Fluent follows an LTE ideal gas behavior, we calculate an equivalent LTE temperature from the FLASH solution as:

$$T_{LTE} = \frac{P_{tot} \bar{A}}{(1 + \bar{Z}) k_B \rho} \tag{3.26}$$

where $P_{tot} = P_i + P_e$ is the total fluid pressure. While LTE is found to be obeyed exactly in the plasma plume interior, deviations do occur in the shock and ambient regions. This is due to the heating of electrons in these regions via radiative transport from the plume. However, since the electron populations in these regions are negligible compared to those of the heavy species, their effect on the effective fluid temperature is minimal. Therefore, the overall fluid temperature most closely follows the ion temperature. Using the above

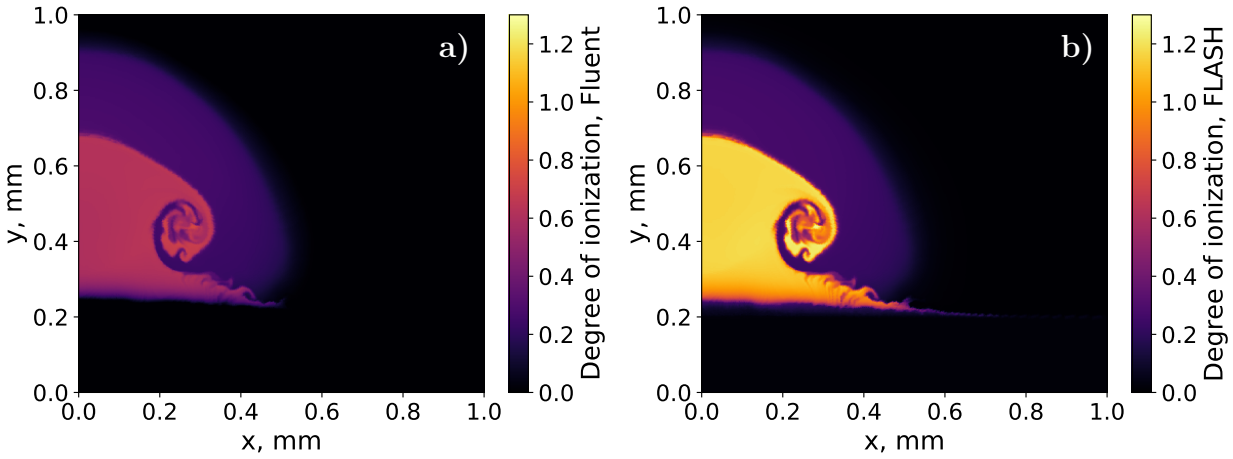

Figure 3.10: Degree of ionization in an example ablation plume using a) Saha and b) LEOS ionization balances for the target material. The highly ionization inner region corresponds to the ablated material, while the weakly ionized outer region corresponds to air, which in both cases is treated using a Saha balance (thus the identical ionization there).

LTE temperature, the Saha ionization/molecular dissociation balance for the fluid can be calculated, yielding the ion and electron species populations. As mentioned above, the total pressure must also be adjusted according to the molecular dissociation fraction in order to keep the mass density consistent. The degree of ionization in the plume found from solving the Saha equation is shown in Figure 3.10. In the same figure, we compare this ionization balance with the original FLASH solution, and sizable deviations are observed in the material region (aluminum here). This is unsurprising, since the material EOS used in FLASH (LEOS) does not use the Saha equation for the ionization balance. Therefore, consistency is difficult to enforce here without reproducing the detailed ionization modeled employed in constructing the EOS, which is not readily available.

Overall, the process of coupling the rad-hydro and reactive CFD simulations requires careful consideration of the assumptions and governing equations used by each model. Using a Fluent mesh of sufficient resolution to resolve the pertinent features of the FLASH solution as well as choosing a solution time where LTE ideal gas approximately holds are critical in maximizing consistency across the models. Even so, discrepancies are bound to arise due to the vast number of differences in the two simulation frameworks. Despite this, the coupled

modeling approach is suitable for performing qualitative experimental comparisons, as will be shown in Chapter 5, and could also potentially be used for quantitative validation studies with further refinement.

3.3 Monte Carlo Genetic Algorithm

The problem of calibrating a reaction mechanism with respect to experimentally measured quantities is an example of an inverse problem, that is, one where the governing equations and solution are known, but the input parameters are not. This type of problem typically does not admit a unique solution, and is instead posed as an optimization problem where the suitability of a solution is dictated by an objective function. The objective function quantifies the statistical deviation of the calculated solution from the true solution. For example, a common objective function is the sum of the squares of the solution residuals:

$$\phi(\boldsymbol{k}) = \sum_{i}^{\text{time}} \left[\boldsymbol{n}_i^{exp} - \boldsymbol{n}_i^{calc}(\boldsymbol{k}) \right]^2 \tag{3.27}$$

where $\boldsymbol{k}$ is a vector containing the reaction rate coefficients and n_i^{exp} and $n_i^{calc}(\boldsymbol{k})$ are the measured and calculated species number densities at time point i, respectively. The optimization problem is solved by employing an iterative procedure that finds an optimal parameter set $\boldsymbol{k}$ that minimizes the objective function ϕ. In the context of the current problem, an optimized $\boldsymbol{k}$ value would represent a set of rate coefficients that closely match the uranium oxide formation rates observed in the laser ablation or PFR experiments. Typically, deterministic nonlinear least squares methods, such as the Gauss-Newton or Levenberg-Marquadt methods [19–21], are employed for such optimization problems. More modern computational techniques, such as neural networks [125], can also be used to this end.

Due to the potentially large parameter space of the UO_x reaction mechanism optimization problem, the solution space may be extremely complex and may contain numerous local min-

ima. Conventional deterministic optimization methods struggle with locating global minima for such problems, instead converging to local minima adjacent to the initialization point. Exhaustive search methods are similarly ineffective due to the computational demand of mapping out a large parameter space. To avoid these issues, we employ a Monte Carlo Genetic Algorithm (MCGA) approach [22] to optimize the UO_x reaction mechanism. This approach combines the Monte Carlo and Genetic Algorithm stochastic optimization methods to achieve global optimization for problems with large parameter spaces. The Monte Carlo portion of the approach uses random sampling of reaction rate parameters to locate regions of good fitness within the solution space. The Genetic Algorithm then optimizes these regions to find the global minimum by using evolutionary processes of migration, selection, mating, and mutation. The stochastic nature of these processes maintains diversity among the optimized parameter sets, thereby avoiding convergence to local minima. Thus, the MCGA approach enables global optimization by searching the entire solution space using Monte Carlo sampling coupled with the parametric diversity inherent in Genetic Algorithm optimization. Furthermore, MCGA can be easily adapted to different experimental systems, since the governing equations of the modeled system need not be reformulated as an inverse problem. Lastly, MCGA is easy to parallelize: the objective function for each parameter set can be evaluated independently, so the evaluation process can be freely split between processors. The robustness, flexibility, and speed of the MCGA approach makes it an excellent tool for producing a calibrated reaction mechanism for uranium oxide formation.

While the MCGA can theoretically be applied to both the laser ablation and PFR experiments, the computational cost of the associated chemical kinetic evaluations limits the practical applicability. As previously discussed in Section 3.2, the highly dynamical nature of laser ablation necessitates the use of fairly sophisticated models (i.e. reactive rad-hydro and/or CFD) for such evaluations. In contrast, Section 3.1 discusses how the chemical kinetics in the PFR can be reasonably approximated using a simple 0D model. Based on prior experience with the above simulations, a 0D kinetic PFR model can be run in a matter of

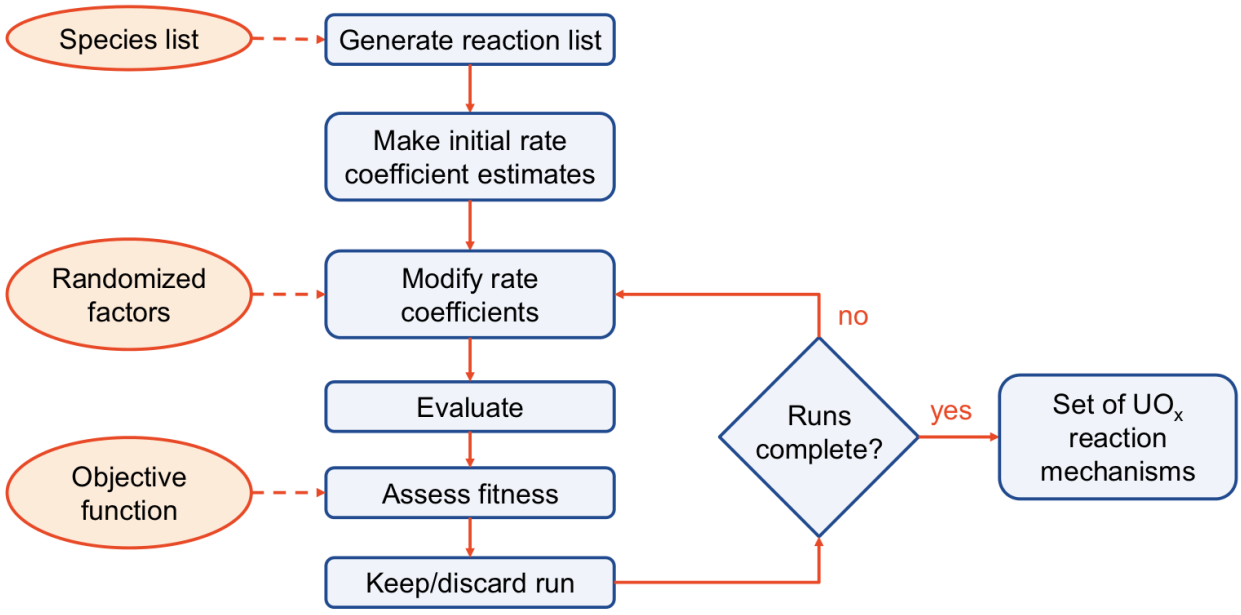

Figure 3.11: Diagram of the Monte Carlo portion of Monte Carlo Genetic Algorithm (MCGA). The set of reaction mechanisms produced by the Monte Carlo process is used as an input for the Genetic Algorithm.

seconds, whereas a laser ablation model might take hours or even days to complete. As a stochastic optimization can easily require many thousands of these evaluations to obtain a good fit, applying MCGA to the current laser ablation models would be unfeasible. Therefore, while the description of the MCGA method below will be presented in a system agnostic fashion, the target application of the MCGA in this work will be the PFR.

A diagram outlining the Monte Carlo portion of the MCGA approach is shown in Figure 3.11. Following the diagram, the Monte Carlo process can be segmented into several key tasks: reaction mechanism generation, rate coefficient modification, model evaluation, and fit assessment. Each of these tasks, and how they fit into the Monte Carlo portion of the algorithm, are detailed below in correspondingly named subsections. All but the first of these tasks are also present in the Genetic Algorithm, as discussed in the last subsection here.

3.3.1 Reaction mechanism generation

The first step of the MCGA process is to construct a set of reaction channels (a reaction mechanism) that will be used for evaluating the chemical behavior of the system. In our previous work [1], we constructed a U-O reaction mechanism for use in uranium-oxygen plasma-chemical laser ablation models. As in that work, the reaction mechanism used in the MCGA consists of two parts. The first part contains the U-O reaction channels that are the target of the optimization while the second part contains supporting reaction channels responsible for the background chemistry. If the experiment used for the calibration procedure uses only argon and oxygen as background gasses (i.e. laser ablation), then the previously constructed mechanism is a sufficient starting point as it includes a detailed oxygen reaction mechanism. However, as mentioned previously, if the plasma flow reactor is used for the calibration, then the chemistry of the nitrate solution must also be accounted for. This introduces two additional reactive chemical species into the system; namely, hydrogen and nitrogen. In this case, the previously used oxygen reaction mechanism must be supplemented by several gas-phase [126–128] and plasma-phase [126,129–131] reaction channels that detail the chemical behavior of an O-H-N plasma.

Of course, including hundreds of additional reversible reaction channels can also have a significant negative effect on the computational performance of the algorithm. This issue is alleviated here by performing a heuristic mechanism reduction step on the supplementary O-H-N mechanism prior to inclusion in the algorithm. The reduction was performed by manually excluding large molecules (>3 atoms) that are unlikely to form in the conditions of interest (2000–5000 K), as well as eliminating extensive reaction networks that track excited atomic and molecular states of minor species. Each step of the reduction was checked by running a test 0D simulation and verifying that uranium oxide formation was minimally affected. Furthermore, the reduced mechanism was verified after each calibration by testing the resulting U-O mechanisms with both the reduced and full O-H-N mechanisms, finding

good agreement. Note that, in the case of the plasma flow reactor, the assumption of LTE and the relatively low temperatures (∼5000 K) in the vicinity of the analyte inlet result in a weakly ionized Ar plasma ($\sim 10^{-5}$ degree of ionization). However, since the chemical species of interest are also dilute in the argon flow, their evolution in the flow will be noticeably affected by plasma-chemistry. Therefore, a number of charged species are retained in the O-H-N mechanism, although some ions are eliminated in the above reduction process. Lastly, since nitrogen is present in relatively small quantities, reactions involving it were reduced considerably, minimally affecting the calculation results while reducing computational time appreciably. The final reduced O-H-N mechanism consists of 44 species and 166 reaction channels, compared to 81 species and 796 reaction channels for the full mechanism. The reaction channels and rate coefficients comprising the full and reduced O-H-N mechanisms are listed in Appendix A.

Once the background (O-H-N) reaction mechanism is constructed, the next step is to generate the U-O reaction mechanism that will be subject to optimization. In the previous work mentioned above [1], the U-O reaction list was based on an analogous metal oxide combustion mechanism [132] appended with additional literature reaction channels. While the resulting U-O reaction mechanism is reasonable, it is far from exhaustive and potentially excludes lesser known reaction channels. Ideally, we wish to consider all possible reaction channels for the optimization process to minimize selection bias. For example, an exhaustive list of reactions between major species (U, UO, UO_2, UO_3, O, O_2, H, H_2, and H_2O) can be generated, as shown in Table 3.2. The optimization process should then automatically determine the dominant reactions from this list, provided that the reaction channels are well constrained by the given experimental data. However, when the optimization data is too limited to provide adequate constraints, over-fitting will occur. As a result, the optimization process can arrive to a mechanism that fits the constraining data well but is otherwise unphysical. In this case, it is preferred to optimize a limited set of reactions that are well constrained by the data. Therefore, the selection of target reaction channels from the full

list of Table 3.2 is based on the available experimental data, as explained later in Section 4.3.

After the reactions of interest are chosen, the starting rate coefficients (k_{est}) for each reaction are estimated. These estimates are made using various first order approximations [133] and are expressed in a modified Arrhenius type-form:

$$k_{est} = AT^n \exp\left(-\frac{E_A}{RT}\right) \tag{3.28}$$

where A is the collision frequency, T is the gas temperature, n is a temperature power constant, E_A is the activation energy, and R is the gas constant. The Simple Collision Theory (SCT) and Simplified Model of Triple Collisions (SMTC) methods are used for calculating binary and three-body rate coefficients, respectively. The collision cross sections for molecules are estimated based on the bond lengths and combined Van der Waals volumes of the constituent atoms. These estimates provide an upper bound on the collision frequency A and a temperature power constant $n = 0.5$ due to a thermal velocity contribution. No *a priori* estimates are made for the activation energy E_A; all reaction channels are initially assumed to be barrierless. The reaction channels are expressed in the exothermic direction to avoid unphysical reverse reaction rates. Note also that bimolecular association reactions are formulated in the high-pressure limit, again to provide an upper bound rate estimate as the starting point.

3.3.2 Rate coefficient modification

Once the target U-O reaction mechanism is generated, the main Monte Carlo loop begins. Each iteration of this loop is independent and consists of evaluating and assessing a modified version of the generated U-O reaction mechanism. Each modified mechanism is produced

Table 3.2: Example of generated U–H–N–O reaction channels.

No.	Reaction	No.	Reaction
1	$U + O \rightleftharpoons UO$	47	$UO + O \rightleftharpoons UO_2$
2	$U + O_2 \rightleftharpoons UO_2$	48	$UO + O_2 \rightleftharpoons UO_3$
3	$U + U + O_2 \rightleftharpoons UO + UO$	49	$UO + UO + O_2 \rightleftharpoons UO_2 + UO_2$
4	$U + UO_2 \rightleftharpoons UO + UO$	50	$UO + UO_3 \rightleftharpoons UO_2 + UO_2$
5	$U + UO_3 \rightleftharpoons UO + UO_2$	51	$UO + O_2 \rightleftharpoons UO_2 + O$
6	$U + U + UO_3 \rightleftharpoons UO + UO + UO$	52	$UO + OH \rightleftharpoons UO_2 + H$
7	$U + O_2 \rightleftharpoons UO + O$	53	$UO + H_2O \rightleftharpoons UO_2 + H_2$
8	$U + OH \rightleftharpoons UO + H$	54	$UO + O + O \rightleftharpoons UO_3$
9	$U + H_2O \rightleftharpoons UO + H_2$	55	$UO + O + OH \rightleftharpoons UO_3 + H$
10	$U + UO_2 + O_2 \rightleftharpoons UO + UO_3$	56	$UO + O + H_2O \rightleftharpoons UO_3 + H_2$
11	$U + UO_3 + O \rightleftharpoons UO_2 + UO_2$	57	$UO + O + H_2 \rightleftharpoons UO_2 + H + H$
12	$U + UO_3 + UO_3 \rightleftharpoons UO_2 + UO_2 + UO_2$	58	$UO + O + H_2O \rightleftharpoons UO_2 + H + OH$
13	$UO + UO + O_2 \rightleftharpoons U + UO_3 + O$	59	$UO + O + H_2O \rightleftharpoons UO_3 + H + H$
14	$U + UO_3 + O_2 \rightleftharpoons UO_2 + UO_2 + O$	60	$UO + O_2 + H \rightleftharpoons UO_2 + OH$
15	$UO + UO + OH \rightleftharpoons U + UO_3 + H$	61	$UO + O_2 + H_2 \rightleftharpoons UO_2 + H_2O$
16	$UO + UO + H_2O \rightleftharpoons U + UO_3 + H_2$	62	$UO + O_2 + O_2 \rightleftharpoons UO_3 + O + O$
17	$U + UO_3 + OH \rightleftharpoons UO_2 + UO_2 + H$	63	$UO + O_2 + H_2 \rightleftharpoons UO_2 + H + OH$
18	$U + UO_3 + H_2O \rightleftharpoons UO_2 + UO_2 + H_2$	64	$UO + O_2 + H_2 \rightleftharpoons UO_3 + H + H$
19	$U + O + O \rightleftharpoons UO_2$	65	$UO + O_2 + OH \rightleftharpoons UO_3 + O + H$
20	$U + O + O_2 \rightleftharpoons UO_3$	66	$UO + O_2 + H_2O \rightleftharpoons UO_2 + OH + OH$
21	$U + O + OH \rightleftharpoons UO_2 + H$	67	$UO + O_2 + H_2O \rightleftharpoons UO_3 + O + H_2$
22	$U + O + H_2O \rightleftharpoons UO_2 + H_2$	68	$UO + O_2 + H_2O \rightleftharpoons UO_3 + H + OH$
23	$U + O + H_2 \rightleftharpoons UO + H + H$	69	$UO + H + H \rightleftharpoons U + H_2O$
24	$U + O + H_2O \rightleftharpoons UO + H + OH$	70	$UO + H + OH \rightleftharpoons UO_2 + H_2$
25	$U + O + H_2O \rightleftharpoons UO_2 + H + H$	71	$UO + OH + OH \rightleftharpoons UO_2 + H_2O$
26	$U + O_2 + O_2 \rightleftharpoons UO_3 + O$	72	$UO + OH + OH \rightleftharpoons UO_3 + H_2$
27	$U + O_2 + H \rightleftharpoons UO + OH$	73	$UO + OH + OH \rightleftharpoons UO_2 + O + H_2$
28	$U + O_2 + H_2 \rightleftharpoons UO + H_2O$	74	$UO + OH + OH \rightleftharpoons UO_3 + H + H$
29	$U + O_2 + OH \rightleftharpoons UO_3 + H$	75	$UO + OH + H_2O \rightleftharpoons UO_3 + H + H_2$
30	$U + O_2 + H_2O \rightleftharpoons UO_3 + H_2$	76	$UO + H_2O + H_2O \rightleftharpoons UO_3 + H_2 + H_2$
31	$U + O_2 + O_2 \rightleftharpoons UO_2 + O + O$	77	$UO_2 + O \rightleftharpoons UO_3$
32	$U + O_2 + H_2 \rightleftharpoons UO + H + OH$	78	$UO_2 + UO_2 + O_2 \rightleftharpoons UO_3 + UO_3$
33	$U + O_2 + H_2 \rightleftharpoons UO_2 + H + H$	79	$UO_2 + O_2 \rightleftharpoons UO_3 + O$
34	$U + O_2 + OH \rightleftharpoons UO_2 + O + H$	80	$UO_2 + OH \rightleftharpoons UO_3 + H$
35	$U + O_2 + H_2O \rightleftharpoons UO + OH + OH$	81	$UO_2 + H_2O \rightleftharpoons UO_3 + H_2$
36	$U + O_2 + H_2O \rightleftharpoons UO_2 + O + H_2$	82	$UO_2 + O + H_2 \rightleftharpoons UO_3 + H + H$
37	$U + O_2 + H_2O \rightleftharpoons UO_2 + H + OH$	83	$UO_2 + O + H_2O \rightleftharpoons UO_3 + H + OH$
38	$U + O_2 + H_2O \rightleftharpoons UO_3 + H + H$	84	$UO_2 + O_2 + H \rightleftharpoons UO_3 + OH$
39	$U + H + OH \rightleftharpoons UO + H_2$	85	$UO_2 + O_2 + H_2 \rightleftharpoons UO_3 + H_2O$
40	$U + OH + OH \rightleftharpoons UO + H_2O$	86	$UO_2 + O_2 + H_2 \rightleftharpoons UO_3 + H + OH$
41	$U + OH + OH \rightleftharpoons UO_2 + H_2$	87	$UO_2 + O_2 + H_2O \rightleftharpoons UO_3 + OH + OH$
42	$U + OH + OH \rightleftharpoons UO + O + H_2$	88	$UO_2 + H + H \rightleftharpoons UO + H_2O$
43	$U + OH + OH \rightleftharpoons UO_2 + H + H$	89	$UO_2 + H + OH \rightleftharpoons UO_3 + H_2$
44	$U + OH + H_2O \rightleftharpoons UO_2 + H + H_2$	90	$UO_2 + OH + OH \rightleftharpoons UO_3 + H_2O$
45	$U + H_2O + H_2O \rightleftharpoons UO_2 + H_2 + H_2$	91	$UO_2 + OH + OH \rightleftharpoons UO_3 + O + H_2$
46	$UO + UO + O \rightleftharpoons U + UO_3$	92	$UO_3 + H + H \rightleftharpoons UO_2 + H_2O$

by adjusting the Arrhenius parameters of the original mechanism as follows:

$$k_{mod} = k_{est} f T^m \exp(-e/T) \tag{3.29}$$

where f is a factor between 10^{-4} and 10^0 randomly sampled from a base 10 log uniform distribution, m is a factor between -3 and 0 randomly sampled from a uniform distribution, and e is a factor between 10^0 and $10^{4.6}$ randomly sampled from a base 10 log uniform distribution. The factor f is intended to compensate for the overestimation of the collision frequency A provided by the initial hard sphere rate estimate k_{est}. The factor m represents a change to the temperature dependence n of the modified Arrhenius form. The factor e represents an adjustment to the activation energy E_A/R. The upper bound value of $e = 10^{4.6}$ is chosen so that the exponential part of Equation 3.29 reduces the reaction rate by four orders of magnitude at the peak plasma temperature of ~ 4500 K. Therefore, if the maximum value of the activation energy is used, the reaction channel is effectively removed from the reaction mechanism, indicating that the activation energy is too high for the reaction to occur in the current system. Conversely, an activation energy of 10^0 indicates that virtually no activation barrier is present for the reaction, and the exponential term in Equation 3.29 will have little effect on the reaction rate. Note that the bounds of these factors are purposefully chosen so as not to exceed the physical upper limit provided by the initial hard sphere rate estimates.

3.3.3 Model evaluation

Next, the modified reaction mechanism is evaluated by solving for the chemical kinetics of the modeled experimental system. As previously discussed, this step is typically the bottleneck with regards to the compute time of both the Monte Carlo and Genetic Algorithm methods. Therefore, it is desirable to limit the complexity of the evaluation step to that of either a global kinetic model (Equation 2.71) or simple 1D models. As previously discussed, the

evaluation time can be reduced even further by first performing a mechanism reduction step on the model reaction mechanism. To minimize the requisite I/O operations, the evaluation output is limited to the temporal (and/or spatial) species number density profiles that can be compared with experimental measurements.

3.3.4 Fit assessment

Lastly, the modeled chemical evolution is compared with the experimentally observed evolution in order to assess the agreement of the modified reaction mechanism. For optical emission measurements in the laser ablation or PFR experiments, this comparison requires converting the number density outputs of the evaluation step to the corresponding emission intensity signals. We refer to this post-processing layer as the synthetic diagnostics step, which involves applying the relations shown in Subsection 2.1.3. However, since the measured and synthetic emission intensities are not calibrated with respect to an absolute reference value, they cannot be compared directly. Theoretically, the measured emission intensities could be related to absolute number densities using a well known reference signal (i.e. strong Ar line). However, the transition probabilities of UO_x species have uncertainties as high as 50% [134], which prohibits an accurate determination of emission-based number densities in this work. Therefore, we will instead normalize both the experimental and modeled emission intensity profiles such that the objective function minimizes the difference in the shapes, rather than magnitudes, of the two profiles. The strongest emission signal is used as the normalization point. That is, the experimental and modeled emission curves are scaled to have the same magnitude at the strongest emission point. Then, the normalized emission curves are compared using an objective function of the form:

$$\phi(\boldsymbol{k}) = \sqrt{\frac{1}{2C}\left[\sum_{c}^{C}(1 - R_{lin,c}^2)^2 + \sum_{c}^{C}(1 - R_{log,c}^2)^2\right]} \tag{3.30}$$

where $R^2_{lin,c}$ and $R^2_{log,c}$ are the weighted linear and logarithmic coefficients of determination for emission curve c given by:

$$R^2_{lin,c} = 1 - \frac{r^2_{lin}(\boldsymbol{k})}{\sigma^2_{lin}} = 1 - \frac{\sum_i^{\mathrm{N}} w_i \left[I_i^{exp} - I_i^{calc}(\boldsymbol{k})\right]^2}{\sum_i^{\mathrm{N}} w_i \left[I_i^{exp} - \bar{I}_{lin}^{exp}\right]^2} \tag{3.31}$$

$$R^2_{log,c} = 1 - \frac{r^2_{log}(\boldsymbol{k})}{\sigma^2_{log}} = 1 - \frac{\sum_i^{\mathrm{N}} w_i \left[\log(I_i^{exp}) - \log(I_i^{calc}(\boldsymbol{k}))\right]^2}{\sum_i^{\mathrm{N}} w_i \left[\log(I_i^{exp}) - \bar{I}_{log}^{exp}\right]^2} \tag{3.32}$$

where $w_i = W_i / \sum_i^{\mathrm{N}} W_i$ is a normalized statistical weight, $\bar{I}_{lin}^{exp} = \sum_i^{\mathrm{N}} w_i I_i^{exp}$ and $\bar{I}_{log}^{exp} = \sum_i^{\mathrm{N}} w_i \log(I_i^{exp})$ are the weighted linear and logarithmic means of measured normalized emission intensities, respectively, and I_i^{exp} and $I_i^{calc}(\boldsymbol{k})$ are the measured and calculated normalized emission intensities at time i, respectively. Here, N represents the number of experimental data points comprising emission curve c. The statistical weight W_i of each data point is given by:

$$W_i = 1 - \left(\frac{\sigma_{bck}}{\sigma_{mol}}\right)_i = 1 - \left(\sqrt{\frac{\sum_j^B \left[S_j^{bck} - \bar{S}^{bck}\right]^2 / B}{\sum_l^M \left[S_l^{mol} - \bar{S}^{bck}\right]^2 / M}}\right)_i \tag{3.33}$$

where σ_{bck} and σ_{mol} are the deviations from the mean background signal ($\bar{S}^{bck}$) of the background (S_j^{bck}) and molecular emission (S_l^{mol}) signals, respectively. This weighting quantifies the strength of a given emission line relative to the strength of the background. Therefore, weakly emitting lines on the order of the background will be weighted lighter when evaluating the objective function compared to strong emission lines.

Equation 3.30 represents a root mean square error (RMSE) of the linear and logarithmic coefficients of determination from the ideal fit value of 1. The use of both linear and logarithmic coefficients is intended to ensure that both large amplitude changes (which dominate the linear fit) and small amplitude changes (which dominate the log fit) in the emission signals are well fitted. In the PFR, for example, the former is constrained by the rapid emission drop-off near the RF coil and the latter by the more gradual emission decay further

downstream.

The final part of the Monte Carlo loop consists of deciding whether to retain or discard the candidate reaction mechanism based on the fitness of the solution. This step serves to build up the set of reaction mechanisms that will be passed to the genetic algorithm for further optimization. The criteria for keeping candidate solutions can be adjusted as needed, but are typically based on exceeding a threshold value for one or more of the fitness metrics calculated above. For example, a simple criterion such as $R^2_{lin} > 0.5$ for all solution curves can be used. If a solution is retained, then the statistical values calculated as part of Equation 3.30 and the corresponding sets of modified rate parameters from Equation 3.29 are stored. It is preferable to keep the selection criterion at this stage lax in order to build up a sizable number of candidate mechanisms. The mechanisms passed to the genetic algorithm can then be selected from these candidates based on the specific fitness metric used by the algorithm.

3.3.5 Genetic algorithm details

The implementation of the genetic algorithm (GA) used here employs a mix of operations from several previously published approaches [22,135,136]. As is often the case with genetic algorithms, the operation parameters used here are largely heuristically chosen based on the observed rates of convergence, fitness improvement, and solution variability. Therefore, while we have attempted to optimize the current approach for the problem at hand, the resulting GA implementation should by no means be considered optimal. Nevertheless, it performs sufficiently well to reliably improve the fitness of a starting population, as later shown in Subsection 4.4.2.

In the GA, the population of each new generation is created by performing a number of genetic operations on the current population, as illustrated in Figure 3.12. Here, a population refers to a set of individuals, where each individual is a reaction mechanism with rate coefficients modified via Equation 3.29. Each individual contains a number of param-

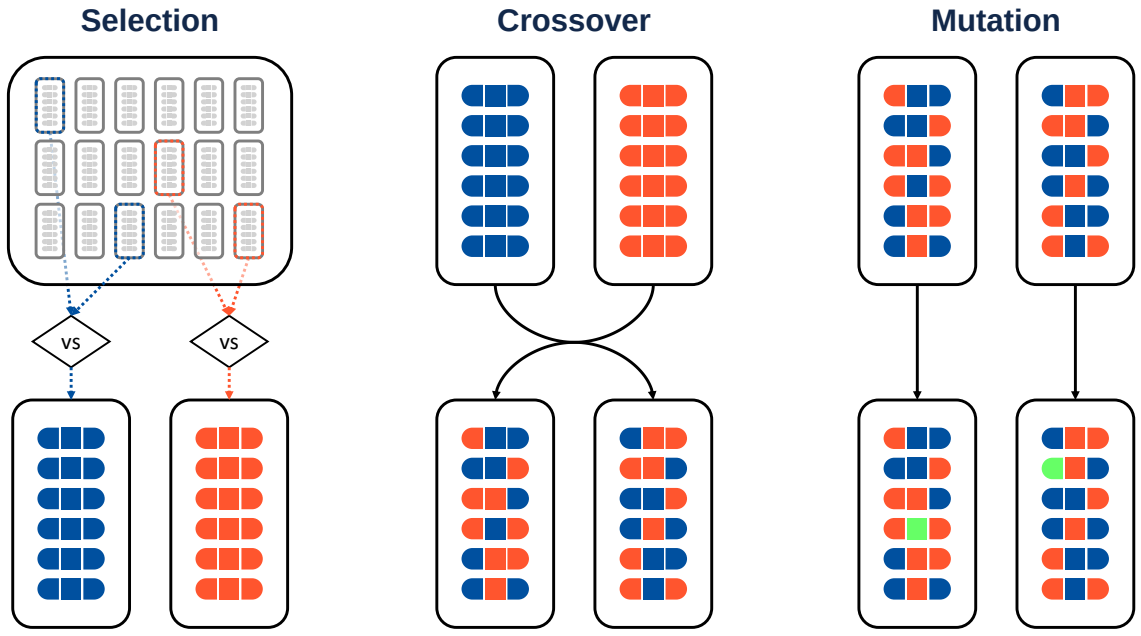

Figure 3.12: Diagram illustrating the selection, crossover, and mutation operations of the Genetic Algorithm portion of Monte Carlo Genetic Algorithm (MCGA). Here each "individual" or "chromosome" (reaction mechanism) is composed of 18 "genes" (6 reaction channels with 3 rate coefficients each).

eters equal to the number of reactions times the number of Arrhenius coefficients (i.e. 3 parameters per reaction). A new generation begins by directly transferring a select number of the fittest individuals (elites) from the current generation to the new one. Here, we select a number of elites equal to 5% of the total population. Next, mate selection is performed using a k-tournament of size $k = 2$ with a 80% probability of selecting the fittest individual in the tournament. That is, each tournament randomly picks 2 individuals from the current population, and the fittest of the two is selected with 80% probability (otherwise the other individual is selected). The entire population participates in the selection process, including elites. Each pair of distinct mates picked in this way then has a chance to reproduce and/or mutate before being added to the new population. The mates may be converted into offspring through uniform crossover, wherein each parameter is switched between the two mates with equal probability, resulting in two offspring individuals. In this

work, the probability of crossover reproduction for a given mate pair is 65%. Regardless of whether reproduction takes place, the two individuals may then also undergo mutation. In this operation, each parameter of an individual is randomized within the bounds specified in Subsection 3.3.2 with 0.8% probability. The probability of mutation is kept low here since even a single re-randomization operation may produce a drastic change in the mechanism behavior. Nevertheless, this mutation probability is found to be sufficient for continuously maintaining a baseline level of diversity via parameter exploration. Since both the reproduction and mutation operations may or may not occur for a given mate pair, it is also possible for a given pair to simply pass directly on to the next generation (i.e. survive). This does not remove them from the selection pool, so it is possible for parents to both survive and reproduce/mutate. However, the uniqueness of each individual in the new population is enforced by discarding duplicate mechanisms as needed. The above operations of selection, reproduction, and mutation are repeated until a new population of the same size as the original is generated.

Since the fitness of the elites is already known, each generation requires evaluating only 95% of the new population. There are various methods for parallelizing this process [137], some of which involve creating sub-populations either to allow for non-synchronized evaluation or to allow for additional evolutionary operations (i.e. migration). Here, we use a simple controller-worker parallelization wherein only the task of evaluation (which is the most computationally demanding task) is split between the number of available processors. Note that, for added genetic diversity, the first generation is constructed by supplementing the initial population (the fittest Monte Carlo individuals) with an equal number of randomly generated individuals [22].

3.3.6 Implementation details

The ZDPlasKin package [51] is used in this work for evaluating the generated plasma chemical reaction mechanisms within the MCGA for the PFR model. The generation, modifica-

tion, and assessment of the reaction mechanisms is performed by various supporting Python scripts. Lastly, several bash scripts are responsible for compiling and running ZDPlasKin and the Python scripts. As mentioned previously, MCGA is an example of a trivially parallel problem, and the bash scripts allow for the required evaluation steps to be easily distributed among available processors and run in parallel. The algorithm was typically run using 288 processors on a Livermore Computing cluster at Lawrence Livermore National Laboratory, completing roughly 4000 problem evaluations per processor per hour. Note that when an optimization uses multiple datasets with different system conditions (i.e. temperature histories and flow rates), the mechanism evaluation step must be performed for each set of conditions, increasing the total run time accordingly.

Chapter 4

Constraining Uranium Oxide Chemical Kinetics using a Monte Carlo Genetic Algorithm

In this chapter, we demonstrate an application of the Monte Carlo Genetic Algorithm (MCGA) for extracting uranium oxide molecular formation rates from plasma flow reactor (PFR) emission measurements. First, we present and analyze the various datasets acquired from the PFR, discussing their limitations and the role they serve in constraining the optimization procedure. Next, we perform a preliminary comparison of the acquired data with a 0D chemical kinetic PFR model utilizing an existing UO_x reaction mechanism. Here, we point out the sensitivity of the 0D model to the temperature profile being used and arrive to a representative temperature history in accordance with available PFR temperature measurements. We then discuss the selection of reaction channels subject to optimization based on the available constraining data and physical arguments regarding the species populations in the flow. The experimental data, representative temperature profile, and list of target reactions are then used to produce an MCGA optimized reaction mechanism. In doing so, we discuss the statistics of the Monte Carlo exploration of the parameter space, the choice of the objective and penalty functions used in the optimization, and the convergence characteristics of the Genetic Algorithm. Finally, we arrive to an optimized reaction mechanism, comparing the result against our previous rate estimates and producing an updated UO_x reaction mechanism. Lastly, we detail the limitations and uncertainties of the current optimization approach that could potentially be improved upon with additional experimental and modeling work.

Table 4.1: Summary of experimental parameters used for each Dataset.

	Position range (cm)	Position increment (cm)	Outer Ar flow rate (L/min)	RF power (W)	Added O_2 flow rate (mL/min)	Number of acquisitions -	Exposure time (s)
Dataset 1	3–8	1	12	1344	0, 25, 50	3*	10
Dataset 2	3–8	0.1	12	1344	0, 10, 20	1	10
Dataset 3	3–8	0.1	10	1440	0	1	10
Dataset 4	1–2.5	0.1	10	1440	0	10	1

* Each acquisition saved separately.

4.1 Experimental emission spectra datasets

Here, we present the various uranium emission datasets collected for this work. While all of the datasets contribute to characterizing the PFR experiment, not all of them are directly included in the final reaction mechanism optimization. Each subsection below details the operating conditions employed for a particular dataset and explains how the data is processed and used in the final optimization. The main parameters varied across the datasets are the regions of observation, the flow temperature (varied via flow rates and RF power), and the availability of oxygen in the analyte flow, as summarized in Table 4.1.

4.1.1 Dataset 1: background signals and measurement uncertainty

The first dataset was collected to study the contribution of background species to the measured UO_x emission spectrum and to quantify the measurement uncertainty of the spectrometer. Unlike subsequent datasets, these measurements did not utilize a motorized translation stage for precisely controlling the location of the fiber optic cable. Instead, the translation stage was manually positioned for each location, requiring the plasma to be extinguished each time the position was changed. As such, measurements were done at 1 cm intervals spanning from 3 to 8 cm away from the RF coil (6 locations total). A 12 L/min Ar outer flow

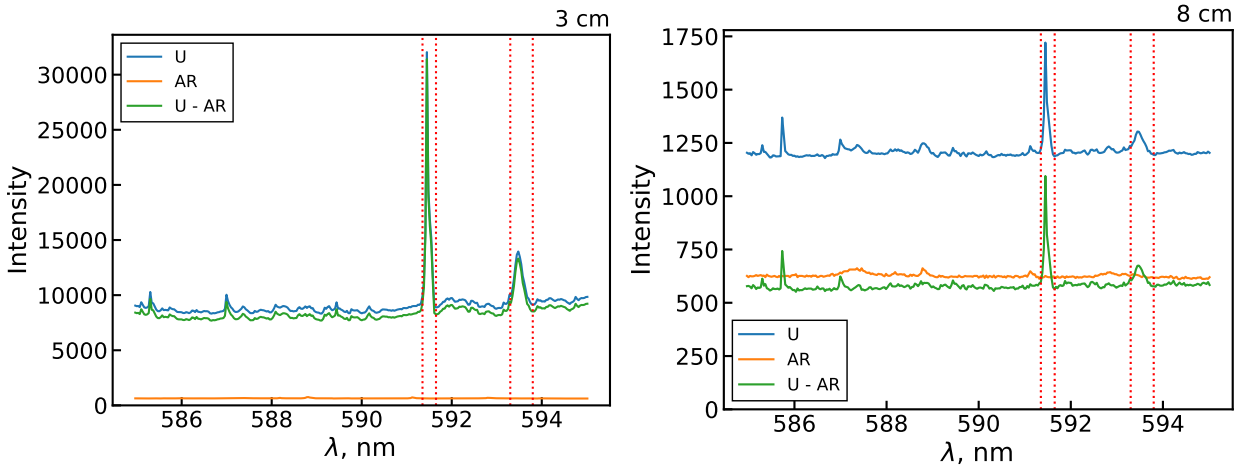

Figure 4.1: Plots showing the uranium, background (argon), and background subtracted uranium emission spectra measured at 3 and 8 cm away from the RF coil. The vertical lines denote the locations of the 591.5 nm U line and the 593.55 nm UO band.

rate and a 1344 W power supply setting were used, and uranium spectra were taken with 0, 25, and 50 mL/min additional O_2 flowing through the inner analyte channel. Uranium spectra were measured 3 times at each location with a 10 second acquisition time. Spectra were acquired in the 573 to 607 nm wavelength range with a resolution of about 0.034 nm.

Examples of uranium and background emission spectra collected 3 and 8 cm away from the RF coil are shown in Figure 4.1. The background (labelled "AR") spectra were measured with only argon and nebulized water flowing through the analyte channel. Therefore, the measured background includes emission due to de-excitation of background species, continuum (thermal) radiation, inherent instrument noise, and any other stray background light. The uranium spectra shown here display significant background signals even when corrected for this measured background, as observed in several previous uranium spectroscopy studies [138]. These studies theorize that this background arises due to the multitude of closely spaced U_xO_y emission lines in the visible spectrum combined with the limited resolution of typical spectrometers. As such, extracting the emission intensity of a given uranium line or band requires first subtracting out this additional background signal. Doing so accurately would either require using a much higher resolution spectrometer or attempting to

deconvolve the peaks of interest using a complete uranium oxide spectral model, both of which lie outside the scope of this work. Instead, we assume that the background peaks are both much weaker and more numerous than the bands of interest, such that a simple offset can be used to approximately separate one from the other. It is difficult to assess the uncertainty introduced by this assumption without a full spectral model of uranium oxide emission. Qualitatively, we can reason that the assumption will generally have a greater impact on the 593.55 nm UO band than the atomic 591.5 nm U line, as the former signal is typically weaker than the latter. Furthermore, as mentioned in Subsection 2.1.3, this UO band consists of several closely spaced rovibrational lines that require a much higher spectral resolution (order of 0.004 nm [14]) to properly resolve. In the same section, we also mention that the UO partition function calculation is approximate due to the limited information on the internal states of the system [38]. Therefore, likely the greatest uncertainty in the current optimization procedure lies with measuring and calculating the signal due to the 0–0 head of the 593.55 nm UO band.

Since the measured (i.e. argon and water) background is effectively negligible compared to the strong U_xO_y background, correcting for it has minimal impact on the results. Therefore, background measurements were typically not performed for subsequent datasets, instead applying only a constant offset based on the total U_xO_y background. Figure 4.2 shows an example of such an offset calculated for this dataset. Here, we select a wavelength range (586 to 586.5 nm) that appears to contain minimal U_xO_y peaks across all locations and use the mean signal in this range as the offset value. After applying this offset, the intensities of the 591.5 nm U line and 593.55 nm UO band are calculated by integrating over the corresponding peaks. This process is repeated for each of the 3 measured spectra at every location, and the resulting means and standard deviations are plotted as a function of distance on the right side of the figure. Most of the resulting uncertainties fall within $\pm 5\%$, as shown in Table 4.2, although uncertainties further downstream increase due to a poorer signal to noise ratio. In addition to the signal to noise ratio, these uncertainties are

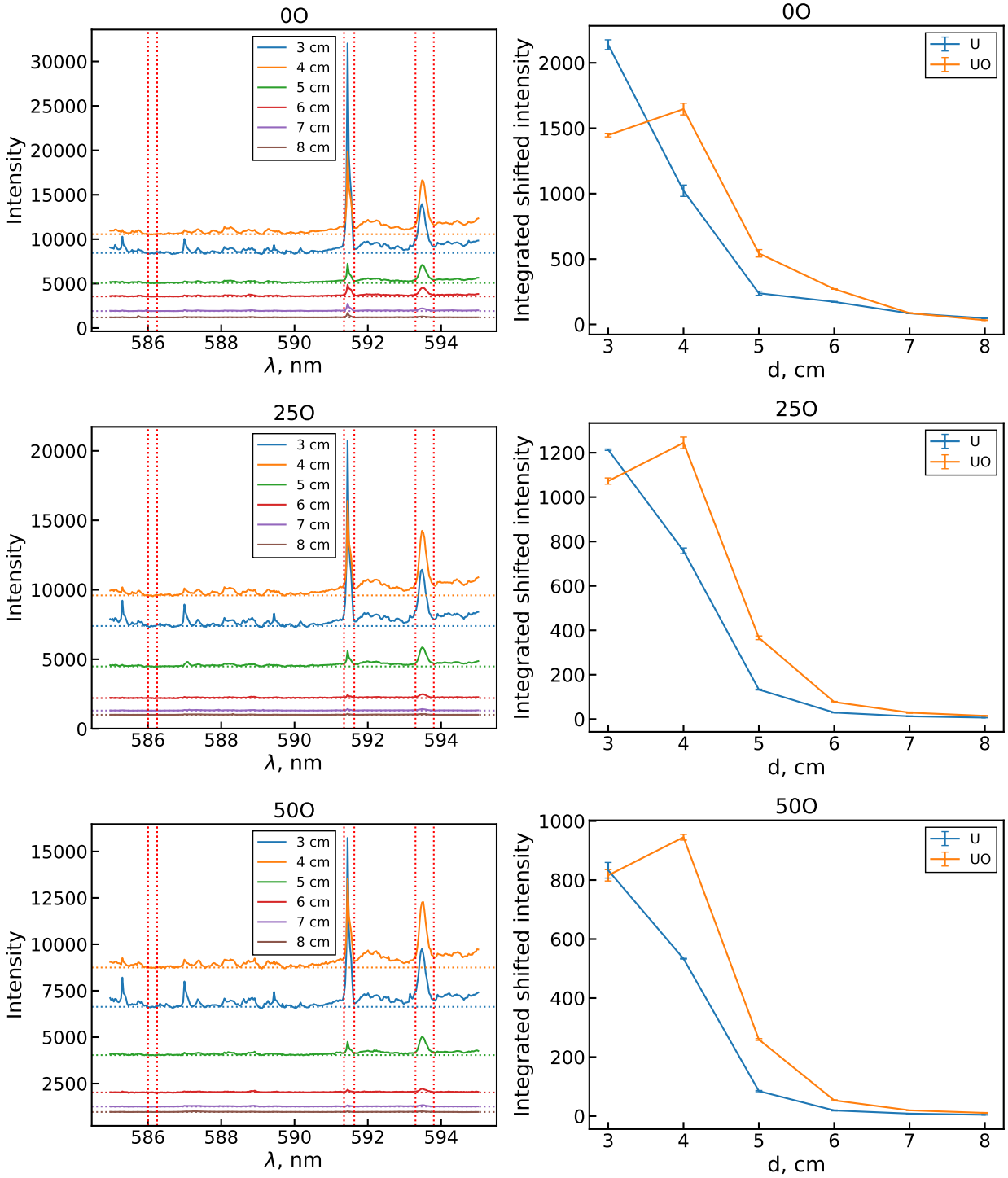

Figure 4.2: Uranium spectra measured between 3 and 8 cm away from the RF coil for 0, 25, and 50 mL/min extra O_2 flow rates. The dashed horizontal lines denote mean signal in the 586 to 586.5 nm range used as the background offset for the line integration shown on the right.

Table 4.2: Uncertainties in integrated shifted emission intensities due to variation in spectrum measurements.

O_2	Species	3 cm	4 cm	5 cm	6 cm	7 cm	8 cm	Mean
0	U	1.74%	4.24%	6.62%	1.66%	1.45%	2.81%	3.09%
	UO	0.96%	2.72%	5.20%	0.68%	2.48%	5.72%	2.96%
25	U	0.26%	1.71%	1.35%	3.56%	10.24%	11.59%	4.78%
	UO	1.30%	2.08%	2.24%	3.42%	9.08%	11.71%	4.97%
50	U	3.18%	0.23%	2.39%	7.47%	3.99%	19.59%	6.15%
	UO	2.35%	1.02%	1.16%	3.56%	0.78%	10.07%	3.16%

also obviously sensitive to the choice of background offset used in processing the data. For example, offsetting based on the minimum signal value in the integration range for each peak yields slightly different uncertainty values, but the maximum and mean uncertainties remain roughly the same.

An odd feature of the uranium spectra shown in Figure 4.2 is that the 4 cm spectrum is generally more intense than the 3 cm spectrum, with the exception of the U peak. While this may appear to be due to U_xO_y formation between 3 and 4 cm, later measurements suggest that this may have instead been due to poor placement of the fiber optic cable. Namely, the 3 cm location corresponds to the end of an opaque region due to the connection between the upstream torch and the downstream quartz tube. Obstruction of the emitting light by this opaque region is likely responsible for the difference in signal strength at 3 and 4 cm. This outlier behavior is more apparent in measurements taken at every millimeter, where a sharp jump in intensity is observed from 3 to 3.1 mm followed by a gradual decrease in intensity thereafter.

4.1.2 Dataset 2: downstream measurements

This dataset utilized operating conditions similar to the first dataset, with the major difference of using a motorized translation stage for positioning the fiber optic cable. This allowed for the measurement location to be adjusted with a much finer resolution and with-

out having to extinguish the plasma. More specifically, measurements for this dataset were done at 1 mm intervals from 3 to 8 cm away from the RF coil (51 locations total). Note that while the relative movement between observation points is very accurate (± 2 μm), the initial positioning of the stage with respect to the RF coil is manual (± 1 mm). The outer argon flow rate (12 L/min) and power supply settings (1344 W) here are the same as the previous dataset. Due to a malfunction in the oxygen flow controller, the additional O_2 flow rate was limited to 20 mL/min for this dataset. Therefore, added oxygen levels of 0, 10, and 20 mL/min were used. As the measurement uncertainty was quantified in the previous dataset, only a single 10 s acquisition time measurement was taken at each location. As mentioned in the previous section, since the U_xO_y background is much stronger than other background signals, no background spectra were acquired for these measurements. Lastly, a higher spectrometer diffraction grating was used here, limiting the observed wavelengths to the 583 to 602 nm range while increasing the spectral resolution to around 0.02 nm.

Figure 4.3 shows the first few spectra from this dataset along with the corresponding integrated shifted intensity values for U and UO over all measured locations. Note that in the 20 mL/min O_2 case, the spectra acquired at a few locations (3.4, 3.7, and 3.8 cm) were discovered to have strong outlier behavior and were thus excluded from the dataset. The integrated intensity plots unambiguously show that the UO signal is monotonically decreasing over the observation range. This holds true even if one accounts for the decrease in the emission intensity due to the expected temperature decline over this distance. This reinforces that the apparent increase in UO signal in the previous dataset is not chemical and is instead tied to the obstruction of the 3 cm emission signal. This is unsurprising, since temperatures in excess of 5000 K are needed to fully dissociate UO, whereas the temperatures at 3 cm fall between 3500 and 4000 K [7,15,18]. Therefore, we expect that peak UO formation happens further upstream of the first measurement location here. Nevertheless, the emission signals in this region do provide some implicit information regarding the formation of UO_2 and UO_3 based on the depletion rate of UO.

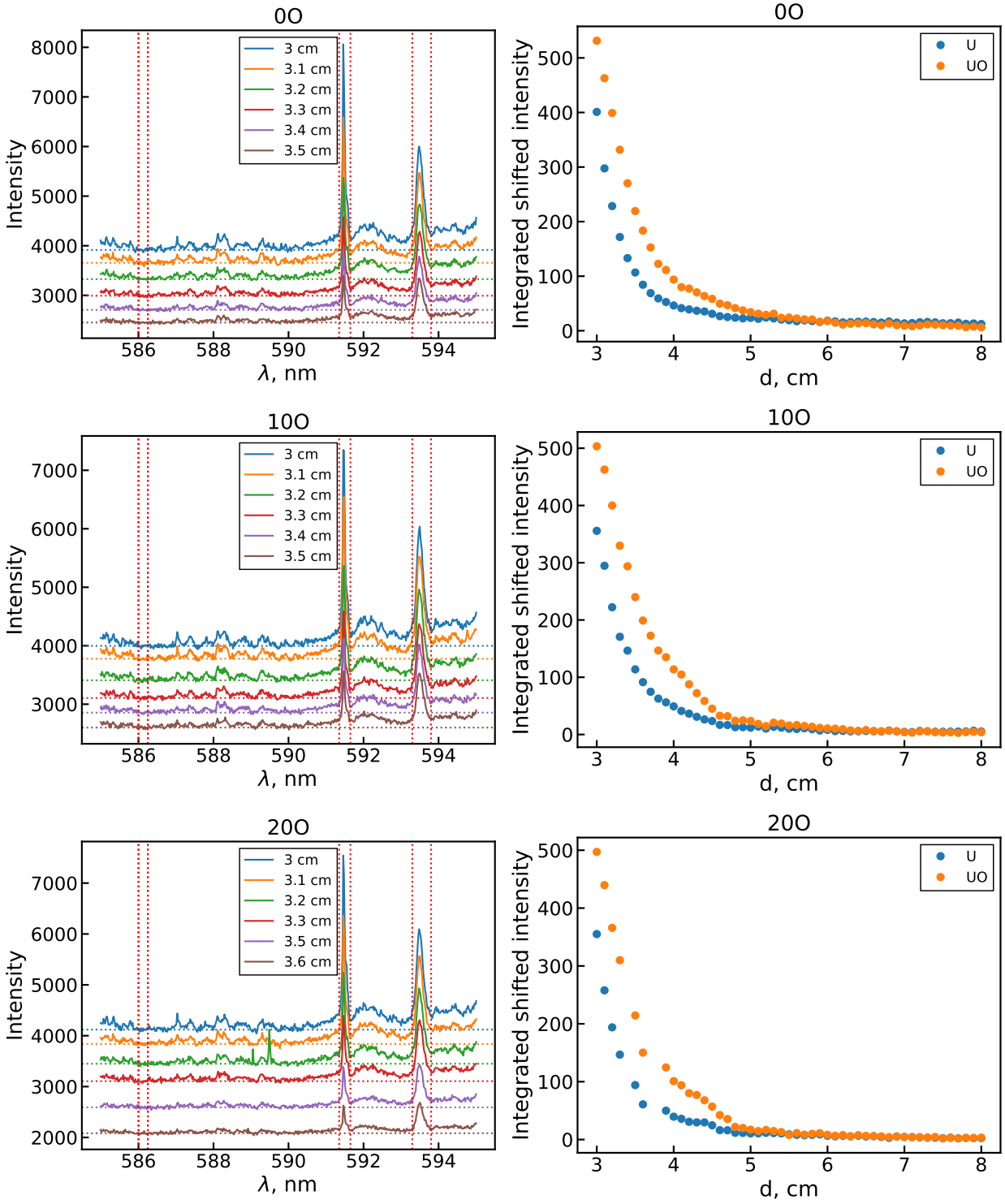

Figure 4.3: Uranium spectra and corresponding integrated shifted line intensities for 0, 10, and 20 mL/min extra O_2 flow rates. Note that outlier spectra found for the 20 mL/min case were excluded here.

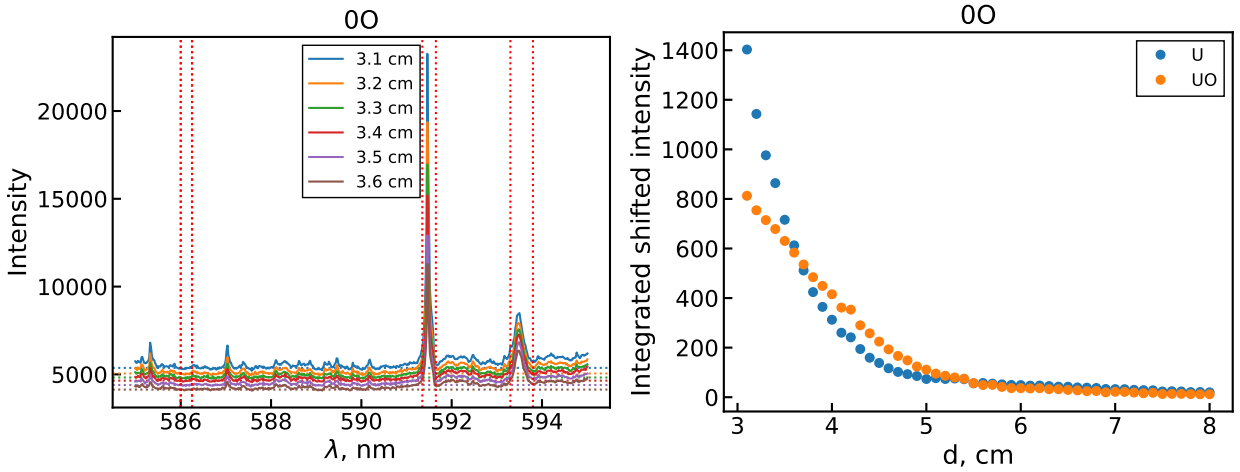

Figure 4.4: Uranium spectra and corresponding integrated shifted line intensities for higher temperature flow conditions induced by lower argon flow rates and higher RF power. Note that the 3 cm measurement is excluded here due to observed emission obstruction as in dataset 1.

4.1.3 Dataset 3: higher-temperature downstream measurements

The operating conditions for this dataset were adjusted to increase the downstream flow temperature by lowering the outer argon channel flow rate to 10 L/min and increasing the RF power to 1440 W. This was done in order to examine the effects of flow temperature on the UO formation rate, since increasing the temperature should effectively shift the UO curve further downstream. No additional analyte O_2 was added during these measurement and all other flow conditions and collection parameters were kept unchanged from dataset 2.

The uranium spectra and integrated shifted peak intensities produced by these higher temperature conditions are shown in Figure 4.4. As expected, these plots show larger intensity values for both U and UO peaks due to the higher rate of de-excitation. Furthermore, the integrated U/UO signal ratio is found to be initially larger compared to the previous dataset, suggesting a higher degree of molecular dissociation. Qualitatively, the integrated signal curves appear to be shifted downstream by around a cm compared to dataset 2, indicating that the changes to the flow conditions have the desired effect on the flow chemistry.

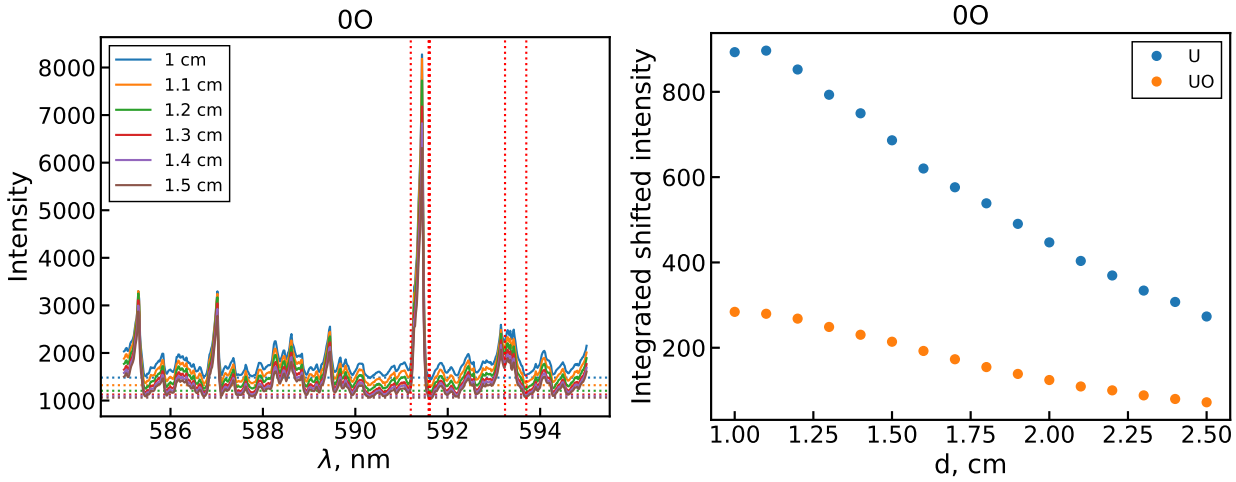

Figure 4.5: Uranium spectra and corresponding integrated shifted line intensities in the torch region of the PFR.

4.1.4 Dataset 4: higher-temperature upstream measurements

In order to measure the upstream behavior of U and UO, the constant diameter quartz tube extension used in the preceding datasets was replaced with a ring-flow connector. As detailed in Subsection 3.1.1, this allows emission measurements to be taken as close as 1 cm away from the RF coil. As such, measurements for this dataset were done between 1 and 2.5 cm in 1 mm intervals. Since the emission signals here are much stronger than in the downstream locations surveyed previously, a 1 second exposure time was used to avoid saturating the detector. To reduce the signal-to-noise ratio, ten 1 second exposures were accumulated and averaged at each location. The flow conditions were kept the same as the previous dataset.

Spectra collected with this configuration are shown in Figure 4.5 along with the corresponding integrated peak intensities. Note that due to the increase in U_xO_y signals in the 586 to 586.25 nm range, the offset here was instead calculated based on the minimum intensity at the base of the U line. In addition, the integration range of the UO band is adjusted here to avoid counting the 593.4 nm U line. This line is not observed in the previous downstream measurements due to the lower U and higher UO concentrations there. Looking

at the integrated intensity plots, it appears that the U signal remains nearly constant for the first two points. This suggests that the U concentration in the flow increases over this range if one accounts for the temperature dependence of the emission line. A similar observation is made for the UO intensity. This effect is likely not chemically driven and may be due to an outlier value at 1 cm, although the cause of this is unclear. Aside from this first point, both the U and UO intensities decrease monotonically over the observed range of upstream locations. This is somewhat surprising, since the temperatures here are expected to be high enough (∼4500 to 5000 K) to at least partially dissociate UO. This would in turn produce an increasing trend in UO concentrations and emission as one moves further downstream. The observed UO trend, however, suggests that UO formation instead happens even further upstream of the first observation point here (i.e. in the coil region). The origin of this behavior can be explained by modeling the chemical evolution of the flow, as will be discussed below.

4.2 Model-experiment comparisons using an unoptimized reaction mechanism

Having reviewed the collected data on U and UO within the flow reactor, we can now check how well the previously constructed U_xO_y reaction mechanism [1] agrees with these measurements. Following the combined CFD and global chemical kinetic modeling approach presented in Subsection 3.1.2, we arrive to the set of results shown in Figure 4.6. Here, two different Lagrangian temperature profiles extracted from the CFD model are used as inputs for the 0D chemical kinetic model. The two profiles differ only in the initial radial position used for calculating the streamline. The first follows a parcel originating from the center of the analyte channel, whereas the second follows a parcel starting near the analyte channel wall. Note that not only do the spatial temperature profiles differ here, but so does the temperature history, as shown by the residence time axis. In both cases, the chemical

evolution in the PFR can be described as follows. At first, the analyte flow consists purely of the constituent reactive molecules UO_2, H_2O, NO_3 (not pictured) and the Ar bath gas at room temperature. As it proceeds downstream, the flow encounters a sharp temperature gradient that decreases the gas number density (via the ideal gas law) and produces rapid dissociation, excitation, and ionization of the analyte molecules. Note that the uranium ionization in this case is almost entirely due to the U + O associative ionization channel present in the U_xO_y mechanism. While H_2O and NO_3 at this stage are effectively fully dissociated into their atomic components, the temperatures are not high enough to fully dissociate uranium oxide molecules. As a result, we see two UO peaks appear; the first due to the initial temperature gradient breaking apart UO_2 in the analyte and the second due to the downstream cooling allowing U + O reactions and electron recombination of UO^+ to take place. After this point, gradual cooling induces formation of higher uranium oxides (UO_2 and UO_3) which eventually deplete the previously formed UO molecules. Due to the availability of free oxygen from the dissociation of other analyte species, uranium saturates towards a higher oxide (UO_3) than its initial analyte form (UO_2).

Although the overarching behavior is similar, there are a number of notable differences in the chemical evolution of the two streamlines that are important for experimental comparisons. First, the strong temperature gradient is encountered further upstream in the wall profile than in the center profile. The center profile in this case follows the cool analyte flow throughout most of the coil region and only becomes heated downstream, where the flow becomes well developed and the temperature maximum shifts to the PFR centerline. The wall streamline, on the other hand, almost immediately enters the hot plasma/gas upon emerging from the analyte channel and only begins cooling upon exiting the coil region. As such, the location of the temperature gradient is offset by about the length of the coil region ($\sim$1.5 cm) between the two profiles. Accordingly, the UO peaks in the wall case are generally located upstream of where they occur for the center case. Note that the same holds true for the higher uranium oxides, since the temperatures in the wall streamline become lower than

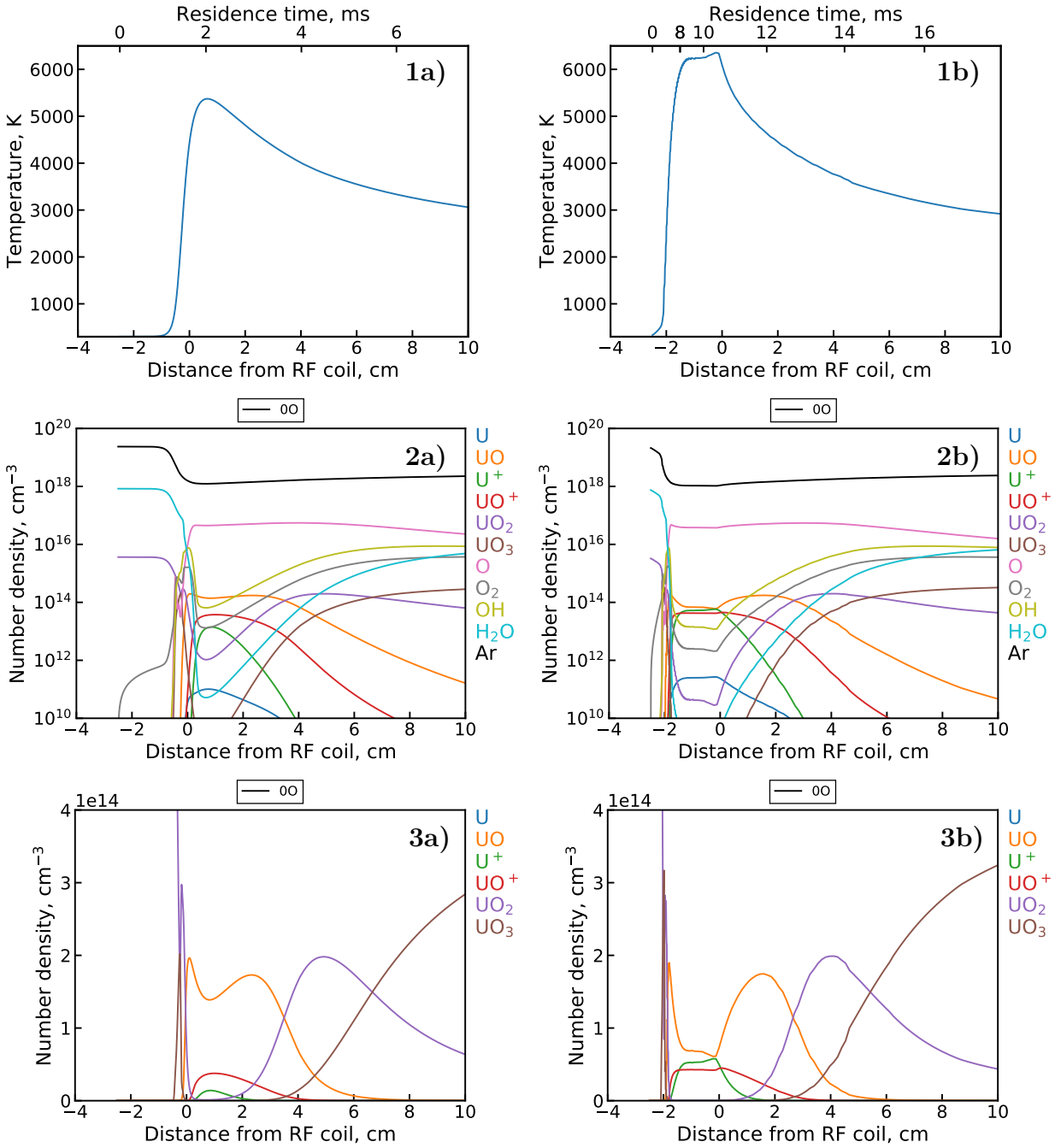

Figure 4.6: Unoptimized 0D UO_x model [1] results showing the 1) temperature profiles and select species concentrations using a 2) logarithmic and 3) linear y-scale. The two temperature histories correspond to Lagrangian streamlines originating from the a) center and b) wall of the analyte channel.

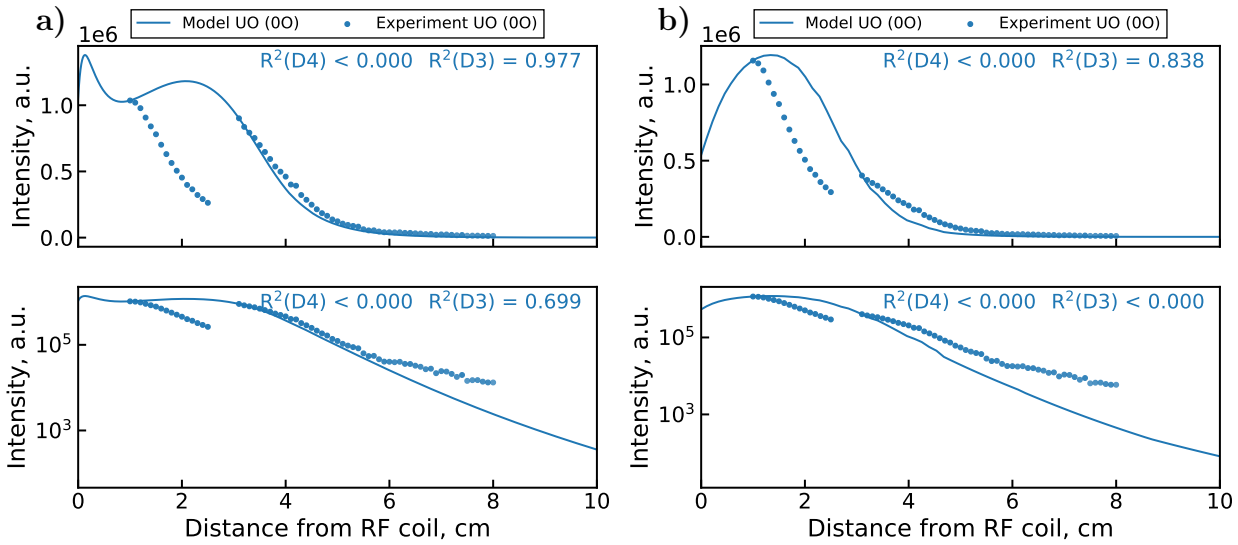

Figure 4.7: Synthetic UO emission profiles (with linear and semi-log axes) generated by the unoptimized 0D UO_x model [1] for Lagrangian streamlines originating from a) center and b) wall of the analyte channel compared with Datasets 3 and 4 measurements. The two datasets are normalized separately with respect to the synthetic profile.

the center streamline by a few 100 K after 1 cm. The other major difference between the two profiles is the higher degrees of ionization and molecular dissociation achieved by the wall profile, which is to be expected given the higher temperatures of that case.

In order to compare these simulation results with our emission measurements, we generate synthetic emission profiles using the modeled temperature and number density curves, as shown in Figure 4.7. Here, the synthetic emission curves are compared against measured values from Datasets 3 and 4, with each experimental set being normalized against the modeled profile based on the strongest emission point. The synthetic emission profiles correspond to the excited state populations (Equation 2.43) responsible for the observed UO band. While the modeled downstream profile agrees reasonably well with Dataset 3, the monotonic decrease in UO intensity observed in Dataset 4 is entirely inconsistent with both of the upstream simulation outputs. A similar result is also achieved by comparing the average of the two synthetic profiles against the measurements. At first glance, this may appear to be due to an underestimation of the reaction kinetics by the utilized reaction mechanism.

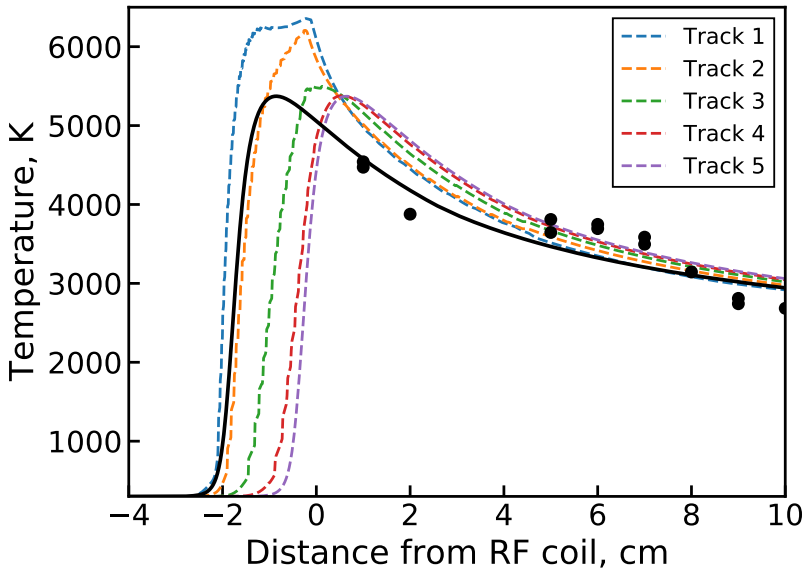

Figure 4.8: Lagrangian temperature histories originating from points uniformly distributed between the wall (Track 1) and center (Track 5) of the analyte channel. The black points show experimental temperature measurements and the black line shows the representative temperature profile used in the MCGA optimization.

However, since the unoptimized reaction mechanism uses hard-sphere collision rate estimates and features several barrierless reaction channels, it actually provides an upper estimate of the true reaction rates. As such, we would expect UO to be formed and depleted faster than experimental measurements suggest, but the opposite holds true here. Therefore, another reason must be responsible for the observed discrepancy. As shown above, the chemical evolution is very sensitive to the temperature profiles used, and this turns out to be the primary driver for the disagreement here.

Figure 4.8 shows a comparison between various Lagrangian temperature profiles produced by the CFD model and available experimental temperature measurements. The experimental temperatures are extracted from the relative intensities of several atomic Fe lines using Equation 2.42 and the line transition probability. This is commonly known as the Boltzmann plot method [18]. The modeled temperature curves here include 3 additional tracks between the wall and center tracks shown previously. The plots show that in the downstream region (>4 cm), the modeled temperature profiles fall within a few 100 K of the measurements and

each other, converging close to a singular value by 10 cm. The experimental agreement is decidedly poorer in the upstream region (1–2 cm), although there are only a few measured temperature values there. The most drastic differences in the modeled profiles appear in the coil region (−2–0 cm), where no temperature measurements are available for comparison. It is clear from this plot that a thorough validation of the CFD model would be required to ensure that the simulated temperature profiles are fully representative of the experimental system. However, this constitutes a major effort that falls outside the scope of the current work. For the purposes of this work, we instead produce an approximate representative temperature profile that reasonably fits the available temperature data. This is done by shifting the center-initiated profile (Track 5 in Figure 4.8) upstream by 1.5 cm, resulting in the black curve shown in the figure. A similar adjustment was performed in previous PFR modeling [15] to attain better agreement with measured temperatures. The modified temperature history corresponds to a case where the plasma heating is weaker and more spatially confined, thereby producing the lower upstream temperatures observed in the experiments. We also generate an additional temperature profile in an identical manner using a lower outer Ar flow rate and RF power in the CFD simulation to enable comparisons with Dataset 2 measurements.

Comparisons between synthetic emission profiles generated using these adjusted temperature histories and the available emission data from Datasets 2, 3, and 4 are shown in Figure 4.9. The synthetic UO emission profile in this case shows surprisingly close agreement with Datsets 3 and 4. However, the model still appear to slightly underpredict the upstream UO depletion rates while overestimating the downstream rates. Poorer agreement is observed for the U profile, which appears to decrease quicker in the model in both upstream and downstream regions. An interesting feature of the U emission data is made apparent here by the semi-logarithmic plots. Namely, the U emission signal appears to saturate towards a minimal value after around 4–5 cm for all datasets. The signal to background ratio for the 591.5 nm U line at these locations remains consistently high, so this behavior cannot

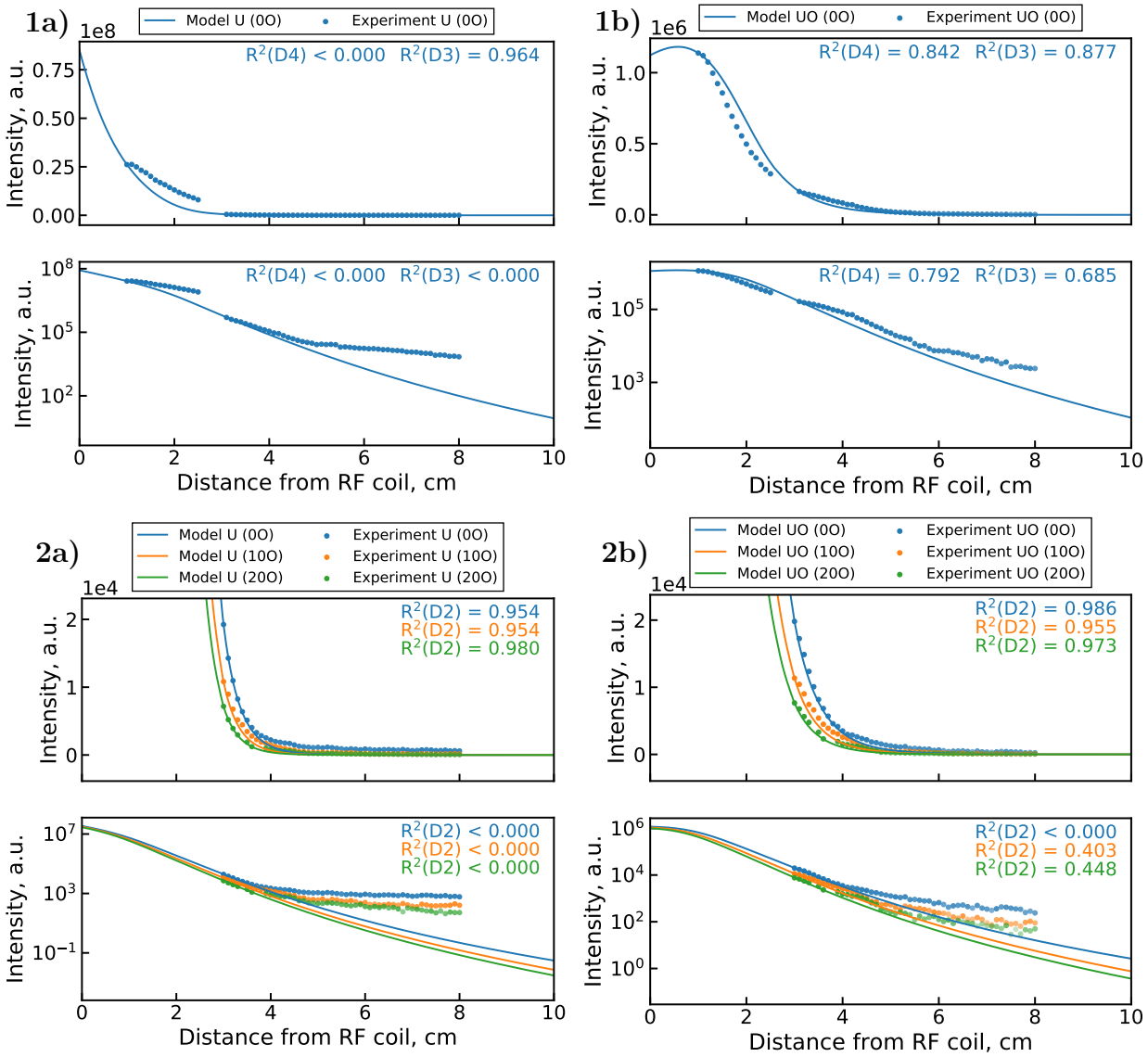

Figure 4.9: Synthetic emission profiles of a) U and b) UO (with linear and semi-log axes) generated by the unoptimized 0D UO_x model [1] using a corrected temperature profile compared with 1) Datasets 3 & 4 and 2) Dataset 2 measurements. The transparency of experimental points indicates signal-to-background ratio.

be attributed to instrument noise or the U_xO_y background. Indeed, this behavior is not observed for the UO band, which is generally weaker than the U line and approaches near-background magnitudes after 6 cm (as indicated by the transparency of the points there). The rough axial resolution of 0.5 cm due to the positioning of the fiber optic cable (calculated in Subsection 3.1.1) is also unlikely to be responsible for this behavior as the saturation feature extends over several centimeters. One possible explanation is that this downstream U signal originates from scattered light emitted in the upstream portion of the PFR. Since the 591.54 nm U emission line is more intense than the 593.55 nm UO band in the upstream region, the scattered light could disproportionately contribute to the downstream U line intensity. Regardless, since this behavior may or may not be chemically driven, it merits special consideration in the optimization procedure, as will be discussed later.

4.3 Selection of reaction channels targeted for optimization

As mentioned in Subsection 3.3.1, the selection of reaction channels targeted for optimization must be based on the available data and the system conditions. This is done in order to avoid possible over-fitting due to inclusion of reactions that are not well constrained by the datasets. Since the rates of potential reaction pathways are not known, an *a priori* sensitivity analysis of an exhaustive mechanism like the one previously shown in Table 3.2 cannot be performed. Instead, we will use physical arguments regarding the species populations in the flow (Section 4.2) and how well they are constrained by the datasets (Section 4.1) to arrive to a final set of reactions. For example, since all the reactive species (i.e. non-Ar) are dilute in the flow, three-body reactions between these species will be relatively infrequent compared to bimolecular reactions. Therefore, the list of possible reaction can be limited to consider only bimolecular reactions, dramatically reducing the number of potential pathways. Furthermore, since the emission measurements comprising the datasets are limited to U and UO,

Table 4.3: U-O reaction channels and initial rate coefficient estimates targeted for optimization.

			k_{est}		
No.	Reaction	$\Delta_r H_{298.15K}$ (kJ/mol)	A (cm^3/s)	n (-)	E_A/R (K)
1	$U + O \rightleftharpoons UO$	−758.237	2.093×10^{-11}	0.5	0.0
2	$U + O_2 \rightleftharpoons UO_2$	−1011.363	1.707×10^{-11}	0.5	0.0
3	$U + O_2 \rightleftharpoons UO + O$	−259.889	1.707×10^{-11}	0.5	0.0
4	$U + OH \rightleftharpoons UO + H$	−328.366	2.114×10^{-11}	0.5	0.0
5	$U + H_2O \rightleftharpoons UO + H_2$	−267.238	2.130×10^{-11}	0.5	0.0
6	$UO + O \rightleftharpoons UO_2$	−751.474	2.116×10^{-11}	0.5	0.0
7	$UO + O_2 \rightleftharpoons UO_3$	−823.213	1.722×10^{-11}	0.5	0.0
8	$UO + O_2 \rightleftharpoons UO_2 + O$	−253.126	1.722×10^{-11}	0.5	0.0
9	$UO + OH \rightleftharpoons UO_2 + H$	−321.603	2.136×10^{-11}	0.5	0.0
10	$UO + H_2O \rightleftharpoons UO_2 + H_2$	−260.475	2.152×10^{-11}	0.5	0.0
11	$U + O \rightarrow UO^+ + e^-$	−201.098	2.093×10^{-11}	0.5	0.0
12	$U + O_2 \rightarrow UO_2^+ + e^-$	−475.259	1.707×10^{-11}	0.5	0.0

the chemistry of higher uranium oxides is not well constrained. While the measurements do somewhat constrain the formation of UO_2 via the UO consumption rate, they contain no information regarding the UO_2 consumption and UO_3 formation rates. Therefore, only reactions involving either U or UO in the exothermic direction are considered for optimization. Applying these selection criteria to the exhaustive reaction list, we obtain a much smaller set of reactions shown in Table 4.3. Note that this list also contains two associative ionization reactions included in our previously constructed reaction mechanism [1]. As shown in Section 4.2, these reactions have a large impact on the uranium plasma chemistry due to the nearly gas-kinetic reaction rate for the $U + O$ associative ionization channel [139]. However, to our knowledge, this behavior has not been well validated. Therefore, we include these channels in the optimization to determine the importance of associative ionization pathways for UO_x formation. Although UO^+ and UO_2^+ are not measured here directly, these reactions are still partially constrained by the available U and UO data.

Table 4.4: U-O reaction channels from previously constructed reaction mechanism [1] that are included in the 0D model but are not optimized due to a lack of constraining data.

			k		
No.	Reaction	$\Delta_r H_{298.15K}$ (kJ/mol)	A ($cm^{3(n-1)}/s$)[a]	n (-)	E_A/R (K)
13	$UO_2 + O_2 \rightleftharpoons UO_3 + O$	−74.129	1.17×10^{-11}	0.5	8915.7
14	$UO_3 \rightleftharpoons UO_2 + O$	570.083	$1.00 \times 10^{+15}$	0.0	73300.3
15	$e^- + U \rightarrow U^+ + 2e^-$	604.421	$\sigma(\varepsilon)$		
16	$e^- + UO \rightarrow UO^+ + 2e^-$	550.956	$\sigma(\varepsilon)$		
17	$e^- + UO_2 \rightarrow UO_2^+ + 2e^-$	529.925	$\sigma(\varepsilon)$		
18	$U + O_3 \rightarrow UO_2^+ + O + e^-$	−367.889	7.750×10^{-13}	0.5	0.0
19	$U + O_3 \rightarrow UO^+ + O_2 + e^-$	−93.728	7.750×10^{-13}	0.5	0.0
20	$U^+ + O_2 \rightleftharpoons UO^+ + O$	−313.358	3.978×10^{-10}	0.0	0.0
21	$UO^+ + O_2 \rightleftharpoons UO_2^+ + O$	−274.161	2.477×10^{-10}	0.0	0.0
22	$UO_2^- + O_2 \rightleftharpoons UO_3^- + O$	−182.126	1.481×10^{-10}	0.0	0.0
23	$UO + O^- \rightleftharpoons UO_2^-$	−699.408	3.037×10^{-9}	0.0	0.0
			1.379×10^{-8}	−0.5	0.0
24	$UO + O_2^- \rightleftharpoons UO_2^- + O$	−300.364	1.105×10^{-9}	0.0	0.0
			5.016×10^{-9}	−0.5	0.0
25	$UO + O_3^- \rightleftharpoons UO_2^- + O_2$	−530.513	9.272×10^{-10}	0.0	0.0
			4.209×10^{-9}	−0.5	0.0
26	$UO_2 + O^- \rightleftharpoons UO_3^-$	−628.404	3.056×10^{-9}	0.0	0.0
27	$UO_2 + O_2^- \rightleftharpoons UO_3^- + O$	−229.360	1.110×10^{-9}	0.0	0.0
28	$UO_2 + O_3^- \rightleftharpoons UO_3^- + O_2$	−459.509	9.302×10^{-10}	0.0	0.0
29[b]	$UO_x^+ + e^- + e^- \rightarrow UO_x + e^-$	N/A[c]	9.821×10^{-9}	−9/2	0.0
30[b]	$UO_x^+ + e^- + M \rightarrow UO_x + M$	N/A[c]	3.118×10^{-23}	−3/2	0.0

[a] Units n is the reaction order (i.e. 1/s, cm^3/s, cm^6/s for 1st, 2nd, 3rd order reactions).
[b] $0 < x < 2$.
[c] Varies depending on the value of x.

In addition to the UO_x reaction channels subject to optimization by the MCGA, we also consider a number of supplementary uranium reaction pathways that are not adjusted by the algorithm. These reaction channels are shown in Table 4.4 and consist mainly of plasma chemical reactions (ionization, recombination, charge exchange) as well as reactions between UO_2 and UO_3. The reaction rates of these channels are kept fixed due to a lack of constraining experimental data. Nevertheless, these reactions provide pathways for uranium plasma chemistry and higher oxide formation to take place within the model. Lastly, the

reduced background (O-H-N) reaction mechanism previously discussed in Subsection 3.3.1 is similarly included as a supplemental set of fixed reaction channels.

4.4 MCGA reaction mechanism calibration

With the experimental data, representative temperature profiles, and target reaction mechanism in place, we can now use the MCGA to produce an experimentally calibrated UO_x reaction mechanism. Below, we will present the results of the Monte Carlo sampling and Genetic Algorithm optimization steps of the MCGA. In addition, we will perform a sensitivity analysis to determine the dominant reaction pathways in the optimized mechanism. Lastly, we will compare the MCGA optimized mechanism against our previous UO_x mechanism and produce an updated set of recommended UO_x rate coefficients.

4.4.1 Monte Carlo: exploration of parameter space

As previously discussed in Section 3.3, the purpose of the Monte Carlo step of the MCGA is to perform a preliminary survey of the problem parameter space and generate a starting population for the Genetic Algorithm. As such, a very relaxed criterion for retaining candidate mechanisms is used at this stage. Namely, that the linear-scale coefficient of determination must be positive for all modeled species profiles produced by the mechanism (i.e. $R^2_{lin} > 0$). This criterion was found to be satisfied by about 8.61% of generated mechanisms (based on 2.3 million samples). Analyzing the distributions of the remaining 200,000 candidate mechanisms with respect to the fitness statistics can yield insights regarding the constraints provided by the data.

Figure 4.10 shows distributions of the MC generated mechanisms within the space of R^2_{lin} and R^2_{log} for each species and O_2 flow rate in Dataset 2. Each plot also displays the percentage of the 200,000 candidate mechanisms that fall within the displayed R^2_{log} bounds. Based on these percentages and the shown distributions, it is clear that log-space fitting of

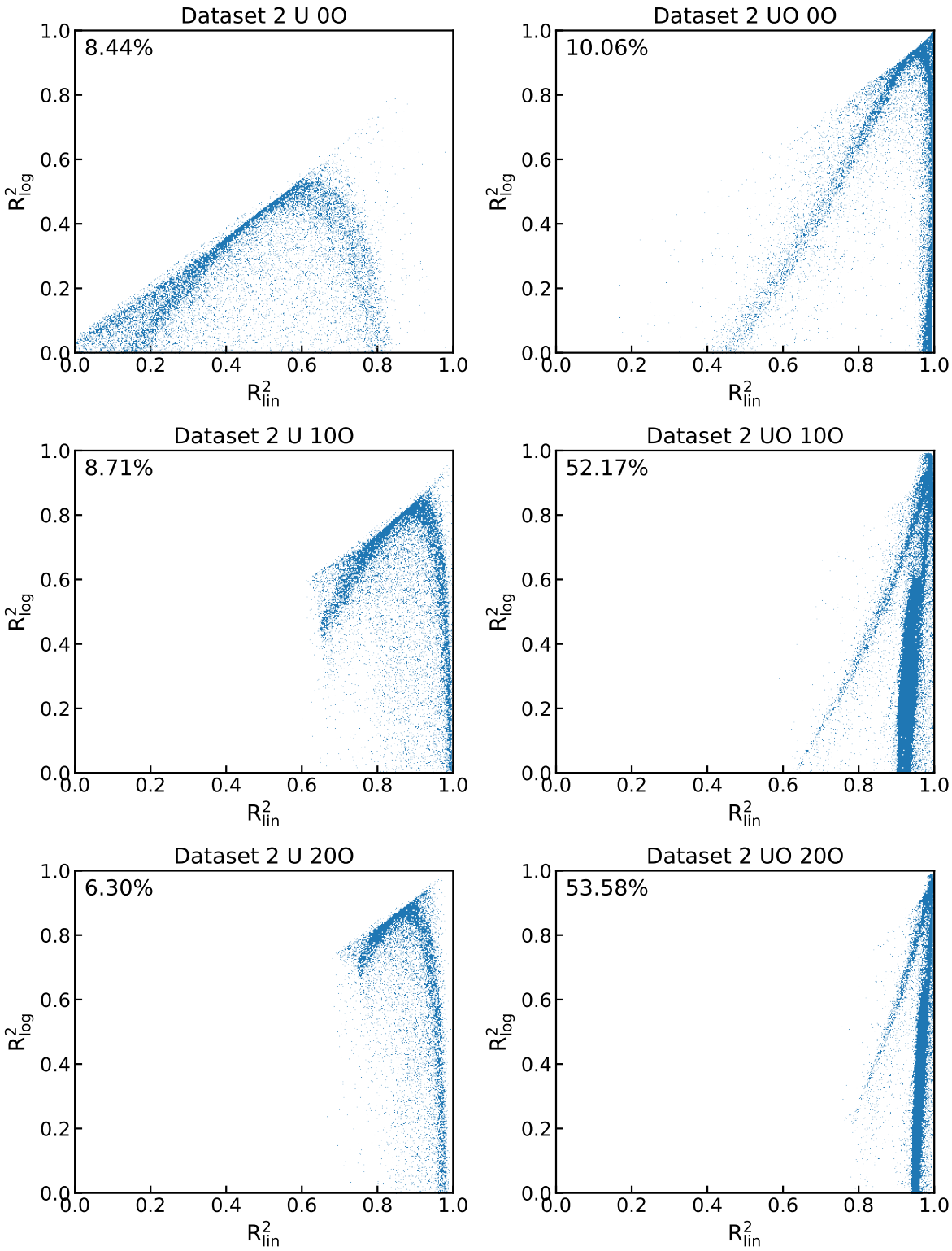

Figure 4.10: Distribution of linear and log space fitness of Monte Carlo generated candidate mechanisms for Dataset 2. The percentage in each plot represents the subset of all mechanisms that fall into the R^2_{log} bounds for the given data.

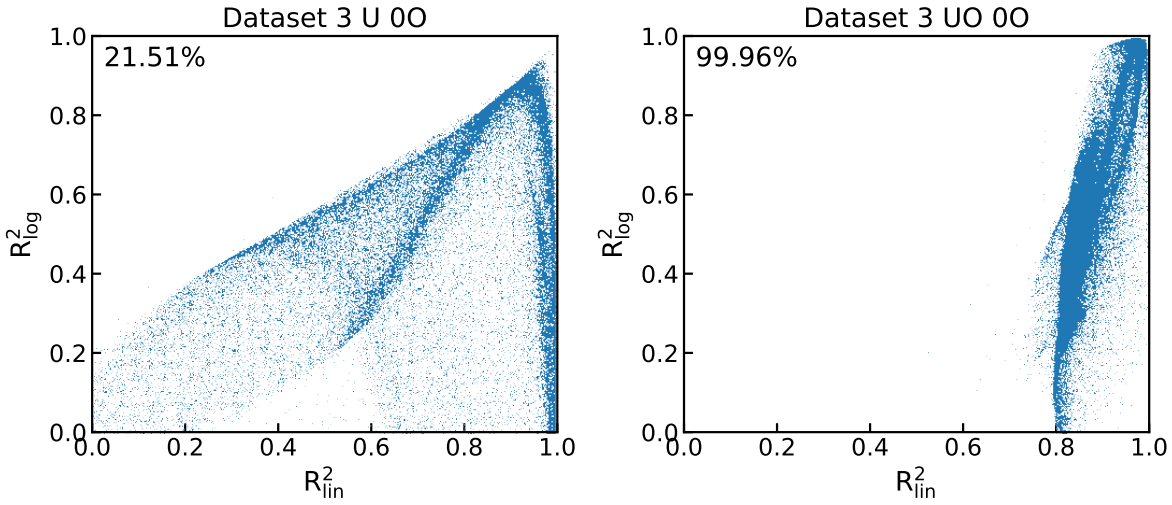

Figure 4.11: Distribution of linear and log space fitness of Monte Carlo generated candidate mechanisms for Dataset 3. The percentage in each plot represents the subset of all mechanisms that fall into the R^2_{log} bounds for the given data.

the data is more challenging than linear-space fitting. This is demonstrated by the generally wider distribution of solutions across R^2_{log}, compared to the abundance of mechanisms in the $R^2_{lin} > 0.8$ region for most data. This makes sense given the downstream locations of this dataset, where the small amplitude gradual decay of the emission signal is dominant in log-space. The problem is exacerbated by the previously highlighted downstream saturation of the U signal, as indicated by the poorer fitness of the U data compared to the UO data. The poorest fitting is observed for the 0 extra O_2 flow case, where even the linear-space fitting of U is sub-optimal. The UO data for this condition also appears relatively difficult to fit, given the lower abundance of suitable solutions compared to the other flow conditions (i.e. 10% vs 50%). For these other flow conditions (10 and 20 mL/min O_2), virtually all the displayed solutions satisfy $R^2_{lin} > 0.6$, with especially good fitting of the UO data. Across all the U data, we observe that while linear and log behavior is correlated up to moderate fitness (shown by the nearly-linear increasing trend), excellent linear fitting comes at a cost to capturing small signal variations (shown by the steep drop-off near $R^2_{lin} = 1$). In the case of the UO data, increased linear fitness strongly correlates to increased log fitness along two dominant super-linear trends.

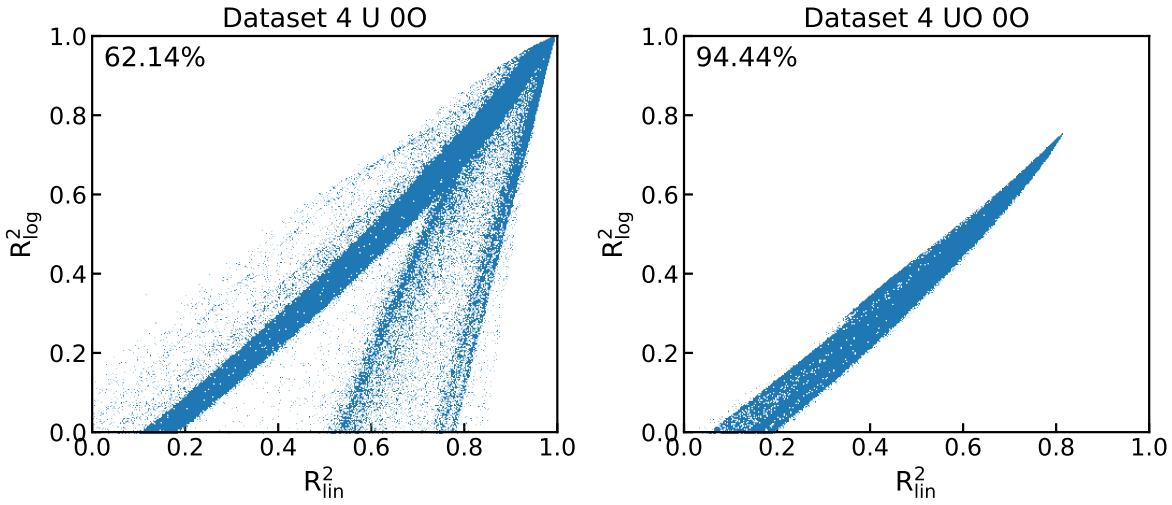

Figure 4.12: Distribution of linear and log space fitness of Monte Carlo generated candidate mechanisms for Dataset 4. The percentage in each plot represents the subset of all mechanisms that fall into the R^2_{log} bounds for the given data.

Similar observations can be made for the higher-temperature downstream case of Dataset 3, as shown in Figure 4.11. Again, the U data presents a much wider range of fitness values than UO, while linear-scale agreement of the UO data is good for nearly all mechanisms. However, these plots do show higher percentages of suitable mechanisms and a relative abundance of well fitting solutions compared to Dataset 2. This may suggest that the current PFR model better captures the conditions of Dataset 3 than those of Dataset 2. That is, if the optimization difficulty is inversely proportional to the model-experiment agreement, then an easier optimization corresponds to a more accurate model. Since the model is highly sensitive to the temperature history used, the differences in optimization difficulty could then be indicative of the suitability of the temperature profiles used for the given flow conditions.

Lastly, Figure 4.12 shows the MC fitness distributions for the upstream measurements of Dataset 4. These plots show a predominant near-linear correlation between the two fitness statistics for both the U and UO data. The U data shows several additional super-linear trends, suggesting again that R^2_{lin} fitting provides a weaker constraint than R^2_{log}, although less so than in previous datasets. The UO data, on the other hand, suggests that the two metrics provide nearly equal constraints. A notable feature of the UO distribution is the

lack of solutions with $R^2 > 0.8$. This is tied to the previously discussed hard-sphere limit on the reaction rate coefficients, which in turn imposes an upper limit on the UO formation and consumption rates according to the model temperature profile. Since the upstream experimental emission signal appears to decay quicker than our hard-sphere model prediction (Figure 4.9), we expect the hard-sphere UO fitness to be an upper limit, which Figure 4.12 confirms. Again, this limitation is likely driven by the approximate temperature histories used in the PFR model.

In addition to the above statistical values, each MC run also stores the maximum and minimum synthetic emission signals in the experimental observation range for each species. These values can be used to check if the magnitudes of the U and UO emission signals produced by the candidate reaction mechanisms are in reasonable agreement with measurements. Without this check, it is possible to attain a fit that appears excellent based on the normalized emission curves, but produces species densities that are too low for a physically detectable signal. To avoid such a scenario, we implemented a penalty function that checks the maximum ratio of synthetic emission intensities $I_{U/UO} = I_U/I_{UO}$. The synthetic intensity due to an electronic de-excitation of species s from an upper state 2 to a lower state 1 can be calculated as:

$$I_s = \frac{hc}{4\pi\lambda} n_{2,s} A_{21,s} \tag{4.1}$$

where h is the Planck constant, c is the speed of light, λ is the line wavelength, $n_{2,s}$ is the excited state population (Equation 2.43), and $A_{21,s}$ is the transition probability. The transition probability values used are $A_{21,U} = 3.15 \times 10^6$ s^{-1} for the 591.54 nm U line and $A_{21,UO} = 3.8 \times 10^9$ s^{-1} for the 0–0 head of the 593.55 nm UO band. The $A_{21,U}$ value is taken from experimental measurements of branching ratios and radiative lifetimes with a given uncertainty of $\pm 11.8\%$ [140], although older studies have yielded values spanning (1.56 – 4.4) $\times 10^6$ s^{-1} [134]. The $A_{21,UO}$ value is obtained from an *ab initio* calculation of the X(1)4

– [16.845]5 oscillator strength $f_{12,UO} = 0.2008$ [141] using:

$$A_{21} = \frac{2\pi q_e^2}{\varepsilon_0 m_e c \lambda^2} \frac{g_1}{g_2} f_{12} \tag{4.2}$$

where q_e is the elementary charge, ε_0 is the vacuum permittivity, m_e is the electron mass, and g_2 and g_1 are the degeneracies of the upper and lower levels, respectively. Note that for the above value of $A_{21,UO}$, we have assumed $g_1 = g_2 = 2$. While $g_1 = 2$ is known for the X(1)4 ground state [38], the g_2 term is later canceled out by a g_2 factor in $n_{2,UO}$ when calculating I_{UO}. Therefore, g_2 does not need to be known as long as the same value is for calculating both $A_{21,UO}$ and $n_{2,UO}$. No uncertainty value is given for the oscillator strength $f_{12,UO}$, so an accuracy of $\pm 50\%$ is assumed as a worst case scenario. Since the reported values of $A_{21,U}$ also fall within a similar error margin, the calculated ratio $I_{U/UO}$ may be off by up to a factor of 3. The maximum $I_{U/UO}$ of the upstream Dataset 4 measurements ranges between 3 and 7 depending on whether the integrated or the peak intensities are used. This provides a rough range of $1 < I_{U/UO} < 21$ for the modeled ratio. Calculating the species number densities corresponding to the lower bound $I_{U/UO} = 1$, we find $n_{UO}/n_U \approx 120$. Accordingly, the mean and max values of $I_{U/UO} = 11$ and $I_{U/UO} = 21$ yield $n_{UO}/n_U \approx 11$ and $n_{UO}/n_U \approx 5.5$, respectively. Due to the inverse correlation between $I_{U/UO}$ and n_{UO}/n_U, we use the following penalty function:

$$\phi_p = 1 - \frac{\log(I_{U/UO}/\bar{I}_{U/UO})^2}{\log(I_{U/UO}^{min}/\bar{I}_{U/UO})^2} \tag{4.3}$$

where $\bar{I}_{U/UO} = 11$ and $I_{U/UO}^{min} = 1$. The penalty function is formulated similar to an R_{log}^2 term in order to include it directly in the objective function (3.30) along with the other fitness metrics. The function most strongly discourages solutions where $n_{UO}/n_U \gg 10$ to prevent locating solutions with good fitness but unreasonably low U densities.

After incorporating the above penalty term, we can now use the objective function ϕ

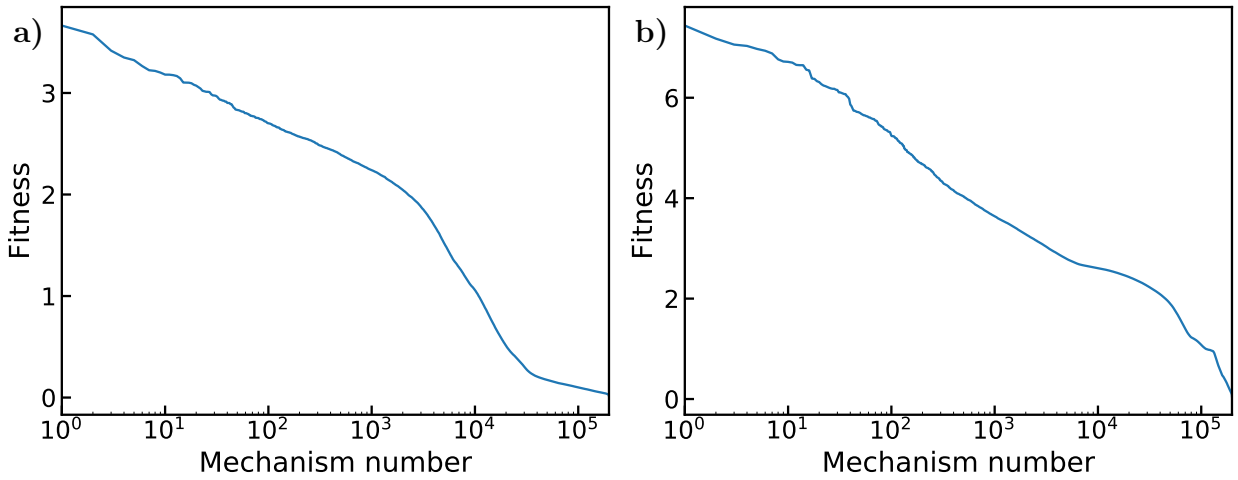

Figure 4.13: Sorted fitness values of MC generated candidate mechanisms when a) complete objective function is used and b) R^2_{log} for U is excluded from the objective function.

to calculate the fitness of each reaction mechanism generated by the MC sampling. Due to our formulation of ϕ being minimized for the best fit, we will define fitness as $1/\phi$ for easier visualization. Figure 4.13 shows the sorted fitness values of the MC mechanism samples using two variations of ϕ. The first variation includes all terms in the objective function:

$$\phi_1 = \sqrt{\frac{1}{N}\left[\sum_{D}^{2,3,4\,U,UO}\sum_{s}(1-R^2_{lin,D,s})^2 + \sum_{D}^{2,3,4\,U,UO}\sum_{s}(1-R^2_{log,D,s})^2 + (1-\phi_p)^2\right]} \tag{4.4}$$

whereas the second variation excludes R^2_{log} terms for atomic uranium:

$$\phi_2 = \sqrt{\frac{1}{N}\left[\sum_{D}^{2,3,4\,U,UO}\sum_{s}(1-R^2_{lin,D,s})^2 + \sum_{D}^{2,3,4\,\;UO}\sum_{s}(1-R^2_{log,D,s})^2 + (1-\phi_p)^2\right]} \tag{4.5}$$

where D refers to the Datasets (including various oxygen flow conditions), s refers to the species, and N represents the total number of terms in each case. The latter formulation is included here due the observed anomalous saturation of the downstream U signal. The previously discussed difficulty of fitting this behavior suggests that it may not be driven by chemistry, in which case it should not be used to constrain the UO_x reaction mechanism. This

difficulty is also apparent from the above plots, as the maximum fitness of ϕ_1 is about half that of ϕ_2. For both formulations, only about 5% of the generated mechanism have fitness values higher than 1/3 of the max fitness case. Furthermore, only a few hundred mechanisms (out of 200,000) fall within the top 20% of fitness. This subset of top mechanisms serves as the initial population for the genetic algorithm.

4.4.2 Genetic Algorithm: fitness optimization

Having determined the appropriate objective and penalty functions from analyzing the Monte Carlo sampling results, we can now use the genetic algorithm to obtain the optimal UO_x reaction mechanism. In order to ensure that the GA generated mechanism is reliable, we will perform 4 separate GA optimizations here. These optimizations represent combinations of the two objective functions described in the previous section (i.e. ϕ_1 or ϕ_2) initialized using either an optimal or sub-optimal set of MC generated mechanisms. That is, the first two optimizations use the ϕ_1 and ϕ_2 objective functions with the corresponding fittest MC populations. The other two optimizations instead swap the initial populations used for each objective function, such that the starting GA population is sub-optimal in each case. This is done in order to check whether the GA is able to reliably arrive to the same optimal fitness regardless of the starting population. The initial populations consist of the 200 fittest mechanisms from the MC sampling step. The overlap between the fittest mechanisms for the two objective functions is only 2 mechanisms out of 200. Lastly, for both the optimal and sub-optimal populations, 200 MC samples of any fitness are also added to the initial population. Therefore, the total starting GA population consists of 400 individuals (mechanisms).

Results from GA optimizations using ϕ_1 (all R^2_{log} terms) with optimal and sub-optimal initial populations are shown in Figure 4.14. Looking at the evolution of the population fitness, we see that that the fitness increases most drastically within the first 40–60 generations. During this time, the diversity of the initial population is leveraged by crossover

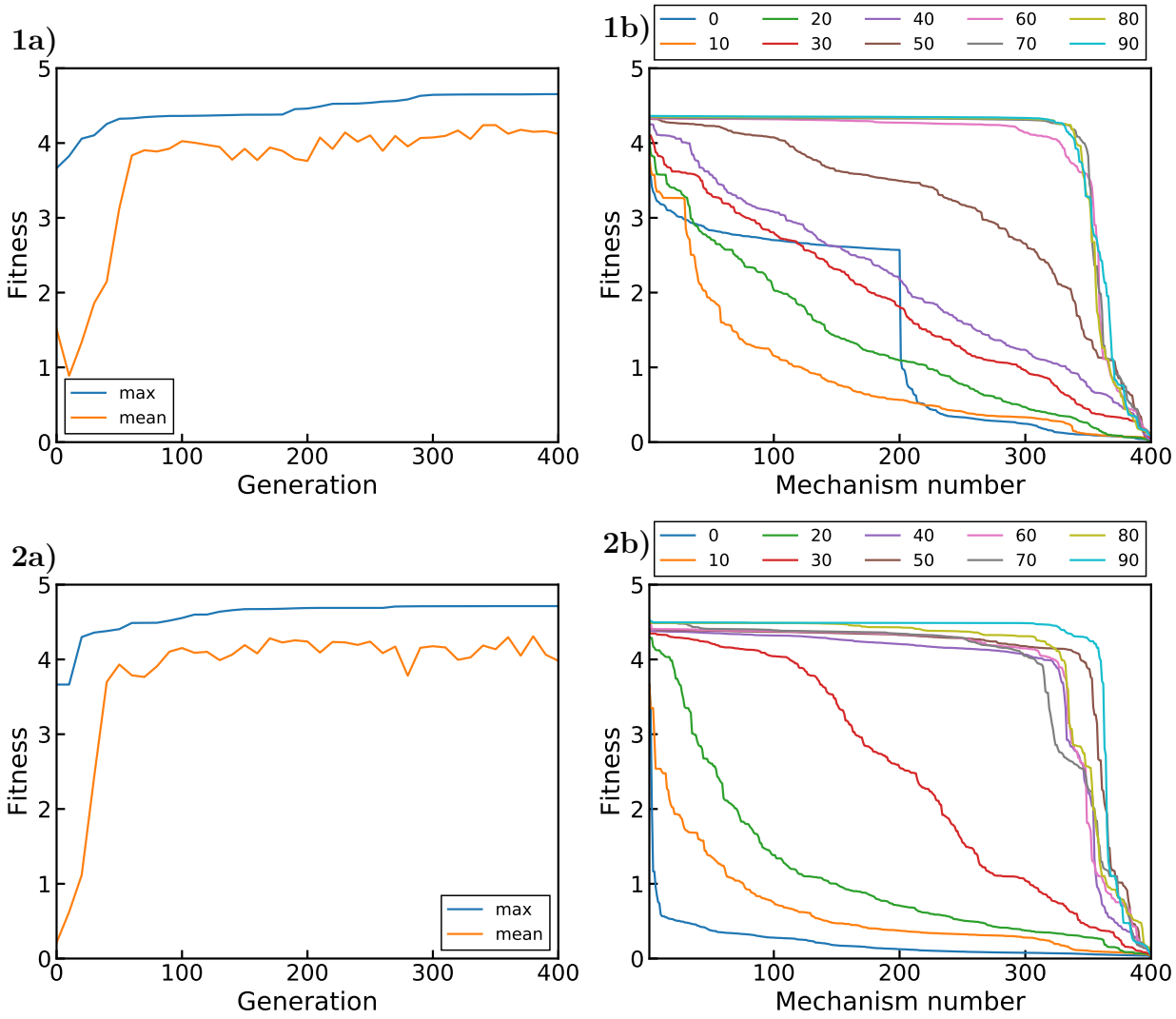

Figure 4.14: GA optimization results using ϕ_1 (all R^2_{log} terms) initialized with 1) optimal and 2) sub-optimal MC generated mechanisms. Plots a) show the mean and maximum fitness as a function of generation while plots b) show sorted fitness profiles for the first 90 generations.

reproduction to rapidly locate high fitness regions in the parameter space. This improves the overall fitness of the population (as evidenced by the mean curve) and locates fitter individuals to displace the starting "elites" (increasing the max fitness). After the first 100 generations, much of the population is homogenized towards a similar fitness value. Past this point, mutations provide the primary source of diversity for parameter exploration, leading to continued gradual fitness improvement. After 400 generations, both the optimal and sub-optimal starting populations appear to saturate towards a similar fitness value. Note that while the fittest starting mechanism here is shared by the optimal and sub-optimal populations, the final fittest mechanisms differ. Curiously, the sub-optimal starting case here displays a higher rate of improvement than the optimal case, but this is likely a stochastic occurrence.

Figure 4.15 presents the same set of plots for the GA optimizations using ϕ_2 (R^2_{log} excluded for U). The overall evolution of the GA population here is very similar to that of the previously examined case. Despite initially possessing a considerably less fit population (both in mean and maximum), the sub-optimal run is again observed to arrive to a similar fitness as the optimal run. In this case, the fitness of the latter case is higher than for the former, but this gap would likely close as the evolution is continued. Regardless, the above 4 runs show that the GA optimization performs reliably and arrives to similar fitness values regardless of the initial population used. However, the sub-optimal and optimal cases do not converge to an identical fitness value for either objective function over the 400 generations observed here. As mentioned above, this may in part be due to the limited number of generations performed and the choice of GA properties dictating parameter exploration and convergence rates. This behavior may also be inherent to the optimization problem itself due to the limited range of conditions provided by the constraining data and the non-orthogonality of certain reaction channels. These considerations can be illustrated by examining the rate coefficients predicted by the optimized populations.

The main reaction channels and corresponding mean rate coefficients for the 4 optimized

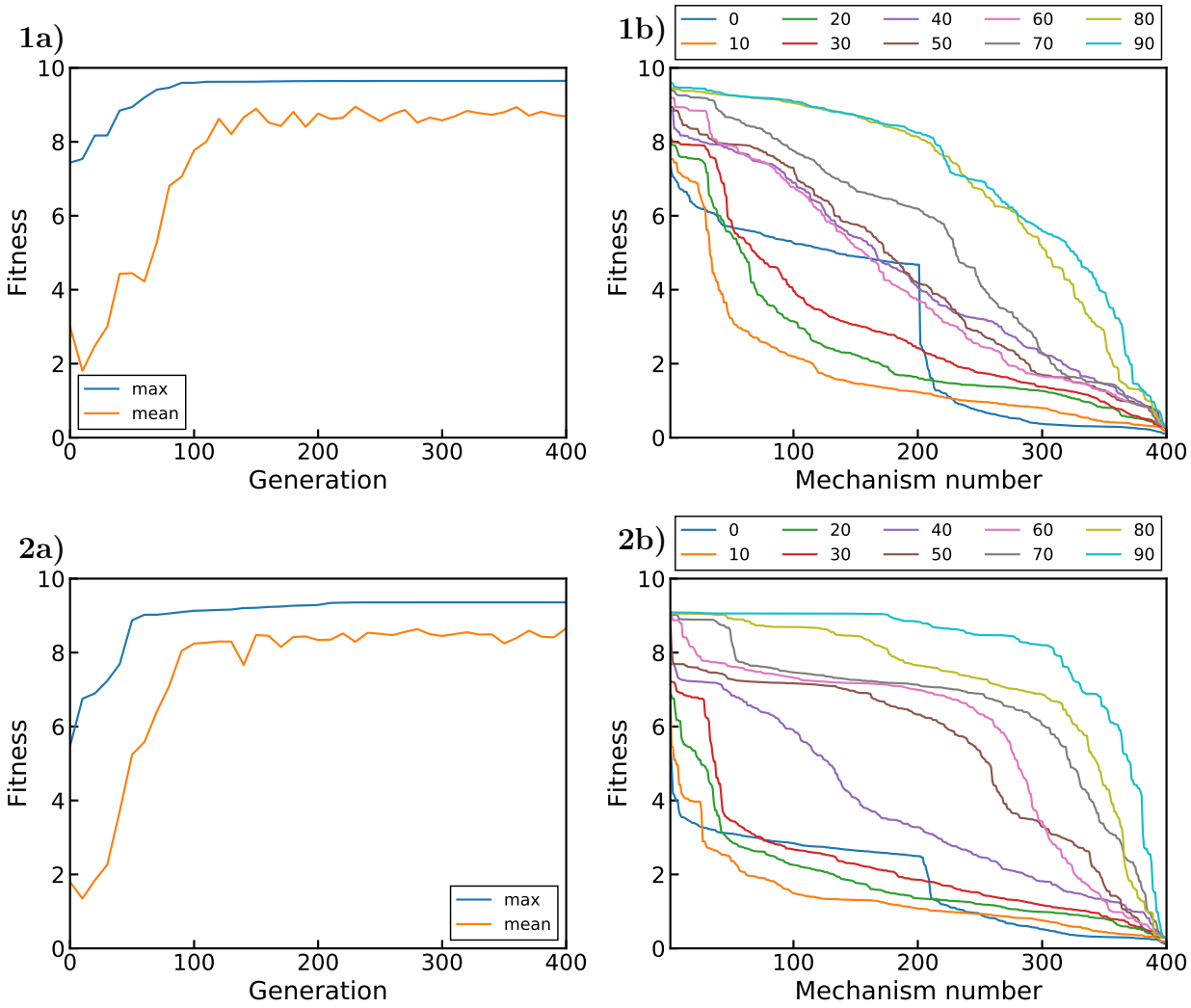

Figure 4.15: GA optimization results using ϕ_2 (no R^2_{log} for U) initialized with 1) optimal and 2) sub-optimal MC generated mechanisms. Plots a) show the mean and maximum fitness as a function of generation while plots b) show sorted fitness profiles over the first 90 generations.

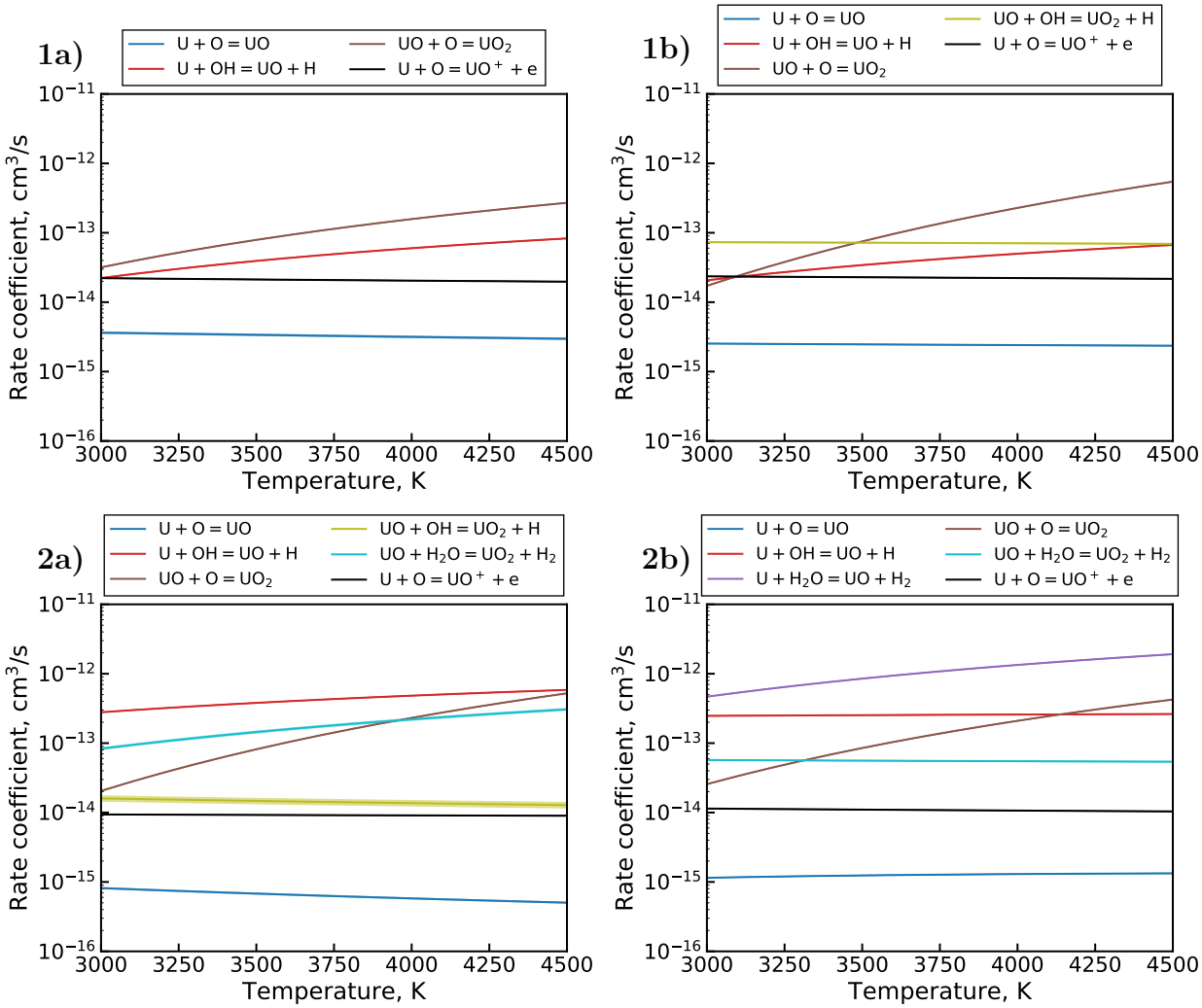

Figure 4.16: Mean reaction rate coefficients ($\bar{k}$) of GA populations optimized using 1) ϕ_1 and 2) ϕ_2 initialized with a) optimal and b) sub-optimal MC generated mechanisms. The means are calculated from mechanisms falling within 0.1% of the top fitness ($\sim$ 300 mechanisms in each case) for reactions that satisfy $\bar{k} > \sigma_k$ (where σ_k is the standard deviation of k).

populations are plotted in Figure 4.16. The dominant reactions here are not identified via a sensitivity analysis, but rather by examining the statistical variation in rate coefficients across the optimized populations. Each plot only shows reactions for which the standard deviation of the rate coefficient does not exceed the mean (based on mechanisms within 0.1% of the top fitness). This condition is satisfied for at most 7 out of the 12 optimized reactions channels, meaning that the remaining reactions are not well constrained by the current data. Only 4 reactions appear consistently constrained, as indicated by their appearance in all optimization cases. The remaining 3 reactions appear in only some of the optimized populations and are therefore only partially constrained. This is likely due to the non-orthogonality of the various reaction pathways. That is, channels like U + O, U + OH, and U + H_2O or UO + O, UO + OH, and UO + H_2O can compensate for one another since they perform the same operation on the constrained species (i.e. adding O to U or UO). Although the different oxygen flow conditions of Dataset 2 constrain this behavior somewhat, the range of O_2 flow rates is limited and only downstream locations are covered. These reactions could be better constrained by incorporating upstream measurements taken over a wider range of O_2 conditions or with reduced H_2O concentrations (i.e. using a desolvating nebulizer). Furthermore, the current dataset is limited in the range of temperatures and cooling rates covered, which also inhibits the location of a global optimum. This is related to the Arrhenius coefficient themselves, since similar reaction rates can be achieved using different combinations of coefficients if the reaction is active over a limited temperature range in the system. Based on the above observations, the lack of convergence towards a singular global optimum appears to stem more from the limited constraining data rather than from a shortcoming of the genetic algorithm. Even so, 4 reactions appear relatively well constrained by the current optimization and can therefore serve as potential refinements on our previous first order rate estimates.

Before moving on to constructing the updated reaction mechanism, we will first discuss which objective function will be used to provide the optimized reaction rates. In particular,

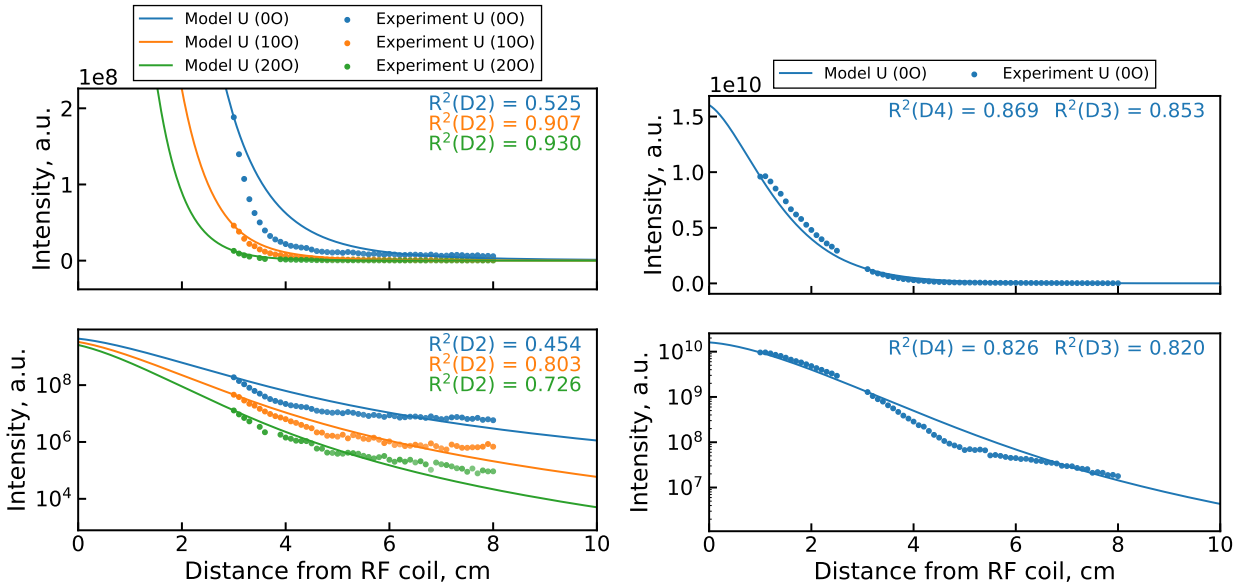

Figure 4.17: Synthetic uranium emission profiles produced by GA optimized mechanism using ϕ_1 (all R^2_{log} terms) compared against Datasets 2, 3, and 4 measurements.

we would like to check if the saturation of the downstream U signal is captured by the ϕ_1 optimized mechanism. Figure 4.17 shows the synthetic U emission profiles produced by this mechanism compared to the full experimental dataset. Although the ϕ_1 MCGA result produces substantially improved fitting of the upstream data over the unoptimized mechanism (Figure 4.9), it is clear that the downstream behavior is poorly captured. In fact, while the R^2 values are mostly adequate (outside of the 0 O_2 Dataset 2 case), neither the 3–5 cm decrease nor the 5–8 cm saturation behavior is well matched across all data. This indicates that the saturation is either driven by a non-chemical effect or by chemical pathways that are absent in the current mechanism. Since this downstream behavior is never observed in the model regardless of the mechanism used, we will consider it an invalid constraint for the current optimization problem. Therefore, the ϕ_2 optimized mechanism will serve as the final output of the MCGA. As shown in the next section, this result adequately captures the 3–5 cm decrease in U intensity, although the subsequent saturation is not observed.

Table 4.5: Comparison between final MCGA optimized and previously constructed [1] UO_x mechanisms.

		k^{a}_{mcga}			k_{lit}		
No.	Reaction	A (cm^3/s)	n (-)	E_A/R (K)	A (cm^3/s)	n (-)	E_A/R (K)
1	$U + O \rightleftharpoons UO$	1.942×10^{-11}	−1.25	209.88		-	
2	$U + O_2 \rightleftharpoons UO_2$		-		3.360×10^{-12}	0.50	12910.0
3	$U + O_2 \rightleftharpoons UO + O$		-		3.360×10^{-12}	0.50	5161.7
4	$U + OH \rightleftharpoons UO + H$	1.346×10^{-13}	0.32	5505.1		-	
5	$U + H_2O \rightleftharpoons UO + H_2$		-			-	
6[b]	$UO + O \rightleftharpoons UO_2$	1.950×10^{-11}	0.31	28020.3	8.084×10^{-13}	0.27	3582.4
7[b]	$UO + O_2 \rightleftharpoons UO_3$		-		4.325×10^{-11}	−0.23	−7503.5
8	$UO + O_2 \rightleftharpoons UO_2 + O$		-		3.800×10^{-11}	0.17	0.0
9	$UO + OH \rightleftharpoons UO_2 + H$	1.309×10^{-12}	−0.56	2.03		-	
10	$UO + H_2O \rightleftharpoons UO_2 + H_2$	1.488×10^{-13}	0.36	10422.0		-	
11	$U + O \rightarrow UO^+ + e^-$	2.495×10^{-14}	−0.12	51.3	1.025×10^{-12}	0.50	0.0
12	$U + O_2 \rightarrow UO_2^+ + e^-$		-		7.747×10^{-14}	0.50	0.0

[a] only well-constrained reaction channels included here (see Figure 4.16 for selection process).
[b] literature rate calculated for reverse process, reversed here by fitting over $300 < T < 10{,}000$ K.

4.4.3 Analysis of optimized reaction mechanism

The final set of optimized UO_x reaction channels and corresponding rate coefficients obtained by the MCGA are shown in Table 4.5. The table also displays relevant reaction channels from the previously constructed UO_x mechanism [1]. Note that for the MCGA optimized mechanism, only well-constrained rate coefficients are listed (see Figure 4.16). The listed rate coefficients for both mechanisms are also plotted as a function of temperature in Figure 4.18. Since the unoptimized reaction mechanism did not consider interactions with H_xO_y molecules, only a few reaction channels are present in both mechanisms. This is exacerbated by the elimination of $UO_x + O_2$ reaction channels by the MCGA optimization due to the relative abundance of OH in the PFR flow. Therefore, only two reaction pathways (R6 and R11) can be directly compared between the two mechanisms. From Figure 4.18, we can see that the MCGA optimized rate coefficient for the former reaction is at least an order of magnitude below the literature estimate. For the latter reaction, the difference is even

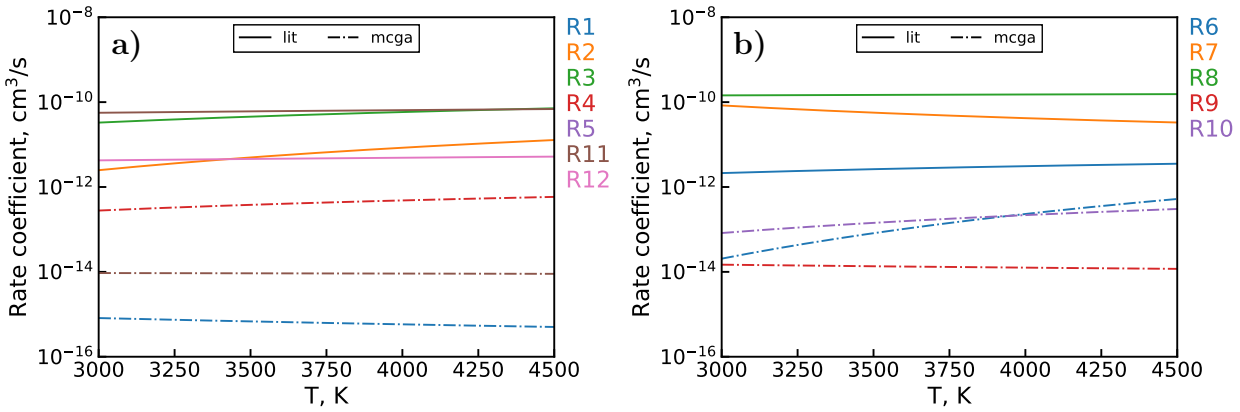

Figure 4.18: Comparison of literature [1] and MCGA optimized rate coefficients for a) U + H_xO_y and b) UO + H_xO_y channels in Table 4.5.

larger, at around 4 orders of magnitude. This is to be expected, considering that the previous literature estimates largely rely on first order hard-sphere collision rate estimates. This is also apparent as a general trend in the plots, which show that all the unoptimized estimates lie an order of magnitude or more above the optimized rate coefficients.

A number of insights pertinent for refining the previously constructed mechanism can be gleaned from these rates. First, we note that the U + O pathway in the optimized mechanism is dominated by the associative ionization channel (R11) over the molecular association reaction (R1). This behavior is in partial agreement with previous cross section measurements [139], which suggest that the molecular association channel is entirely closed. In our optimized mechanism, however, the two channels differ by only around an order of magnitude. Furthermore, the optimized R11 rate coefficient suggests a much lower cross section than observed in the above experiments. The optimized pathway is also found to be effectively barrierless, which is in agreement with the study. Next, we note some similarity in the optimized R4 and unoptimized R3 channels, particularly with regards to the activation energy [142]. This may indicate that the abstraction mechanism for U colliding with either OH or O_2 proceeds in a similar manner. Comparing the two reaction further, we see that the optimized collision rate is about two orders of magnitude lower than the hard sphere estimate. Nevertheless, the overall optimized rate coefficient is still high relative to the other

optimized reactions, as seen in Figure 4.18. Moving on to R6, we observe a large discrepancy in activation energy between the optimized result and our previous estimate. The activation energy in the unoptimized rate coefficient comes from an Eyring-estimate adjusted according to an analogous semi-empirical calculation for an Al oxidation mechanism [1, 143]. The unoptimized barrier value is essentially a biproduct of the above adjustment, as the Eyring estimate itself is barrierless. The strong temperature dependence of this channel for all MCGA results (see Figure 4.16) suggests that the sizable activation barrier of the optimized rate is physically significant. The collision rate for this channel is observed to be close to the hard sphere limit, which offsets the effect of the large activation barrier. Thus, the overall rate coefficient is found to be within an order of magnitude of the unoptimized channel at 4500 K and is around the same value as R4 at this temperature. Next, the R9 abstraction reaction appears to be effectively barrierless, and has an overall low collision rate comparable to the R11 associative ionization channel. The lack of an activation barrier for the analogous unoptimized R8 abstraction channel is simply due to a lack of literature information, so a definitive comparison between R8 and R9 is not attempted. Lastly, R10 appears as the last major reaction channel in the optimized mechanism, with a collision rate similar to R4 (albeit with a higher activation energy). Despite the relatively large rate coefficient, this reaction pathway can be expected to be important only in the downstream portion of the PFR due to its dependence on H_2O.

To analyze where in the PFR flow the dominant reaction channels are most active, we also calculate the first-order sensitivity coefficients given by Equation 2.83. The results of the sensitivity calculation for U and UO along the PFR for Dataset 3 and 4 conditions are shown in Figure 4.19. In addition to the optimized channels, these plots also include the fixed UO_2/UO_3 formation reactions R13 and R14 from Table 4.4. From these plots we see that R1, R4, and R11 play the greatest role in the upstream (<3 cm) evolution of U, while R1 and R13 become dominant further downstream (>3 cm). The UO sensitivity plots show that the upstream UO evolution is relatively insensitive to the reaction mechanism as a whole.

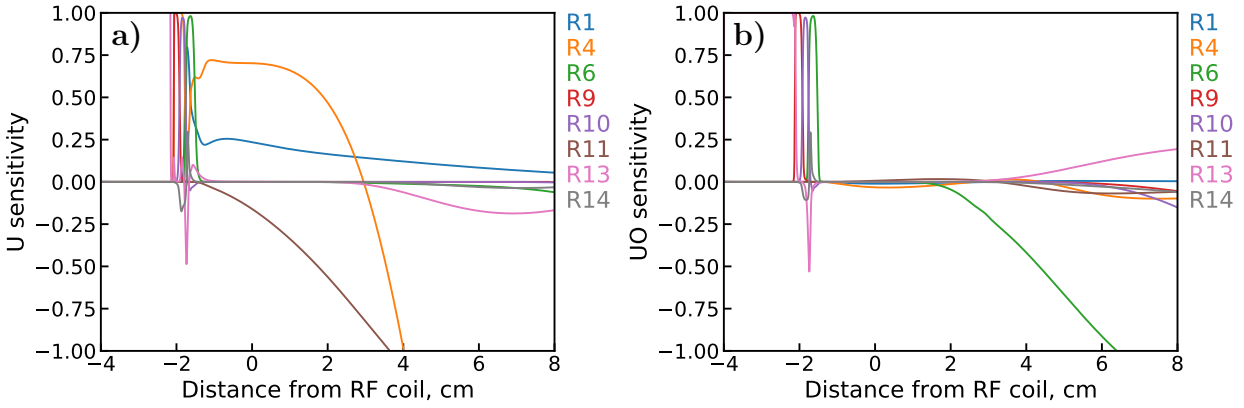

Figure 4.19: First-order sensitivity coefficients (see Subsection 2.2.3) for a) U and b) UO using the MCGA optimized mechanism for Dataset 3 & 4 conditions.

Further downstream, UO is most sensitive to R6 and R13. The remaining optimized channels from Table 4.5, R9 and R10, appear to make finer adjustments to the downstream UO evolution. Overall, it appears that the upstream behavior of the mechanism is constrained mainly by U data, while both U and UO measurements play a role in constraining the downstream behavior.

Next, we take a look at the species number densities produced by the optimized reaction mechanism, as shown in Figure 4.20. Compared to the unoptimized results of Figure 4.6, the MCGA mechanism produces markedly less uranium ions in the coil region due to the lower R11 associative ionization rate. Although this results in a higher population of neutral U, it is still about an order of magnitude less abundant than UO. More precisely, a peak upstream intensity ratio of $I_{U/UO} \approx 6$ is found when using the optimized mechanism, which corresponds to $n_{UO}/n_U \approx 20$. A similar value is obtained across all the other MCGA optimizations discussed in the previous section. While this value falls within the $I_{U/UO}$ range estimated in Subsection 4.4.1, a more thorough calibration of the absolute densities would be needed to validate this result.

To examine in detail the fitness of the optimized mechanism, the final uranium synthetic emission profiles and constraining datasets are plotted in Figure 4.21. As expected, the MCGA mechanism produces improved fitting of most experimental data when compared to

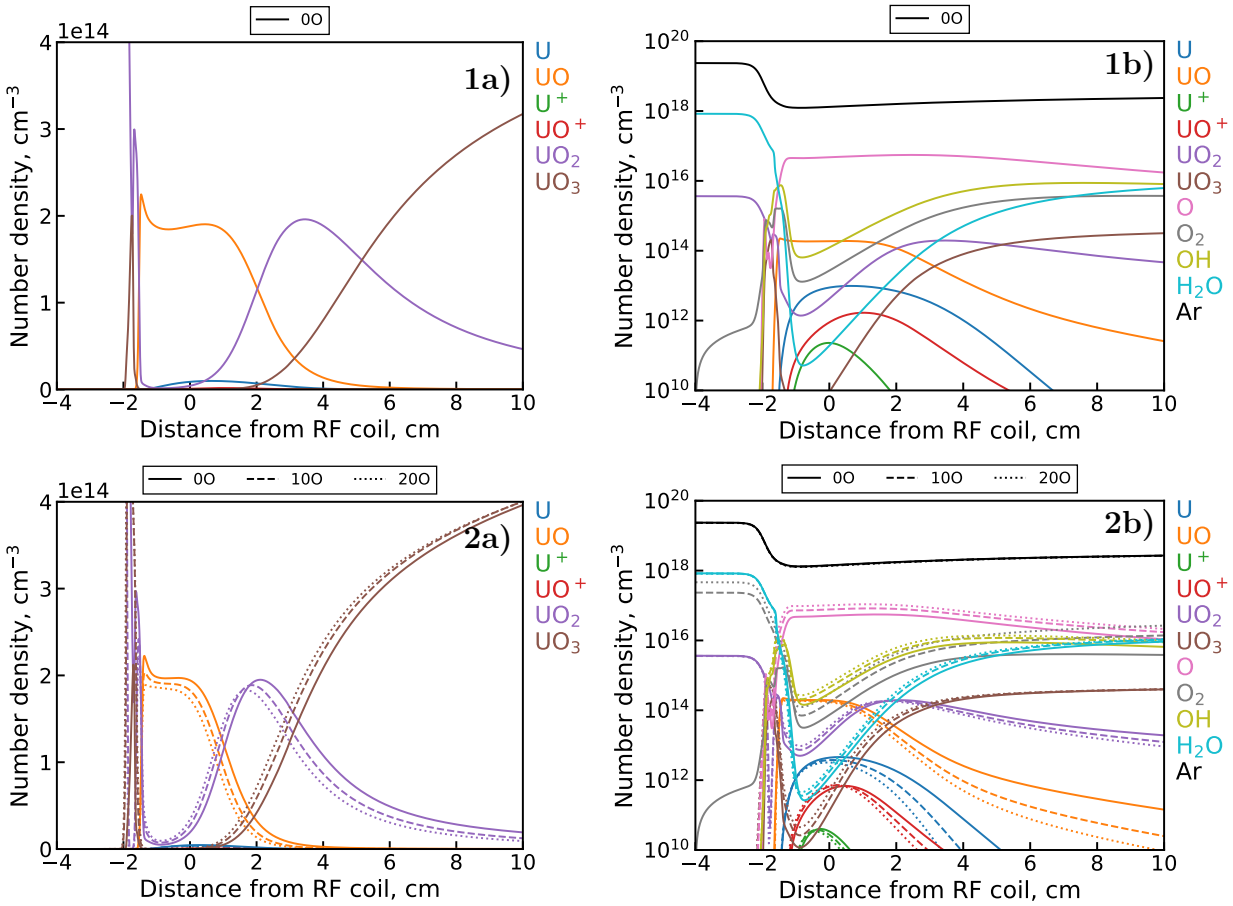

Figure 4.20: Modeled number density profiles of select species predicted by the MCGA optimized UO_x mechanism for 1) Dataset 3 & 4 and 2) Dataset 2 conditions using a) linear and b) logarithmic y-scale.

the unoptimized results of Figure 4.9. The biggest discrepancy here is due to the choice of the ϕ_2 objective function that excludes the downstream low amplitude saturation of the U signal. As discussed previously, this behavior is not used as a constraint here as it is unclear whether it is driven by chemical or optical effects. However, the optimized mechanism produces an excellent fit of the upstream (< 5 cm) U data. The mechanism also produces good fitting of both the upstream and downstream UO data. As discussed previously in Subsection 4.4.1, the partial fitting of the upstream UO data provided by dataset 4 is limited by the approximate representative temperature profile used here.

Finally, we can discuss recommending a new set of UO_x reactions and corresponding

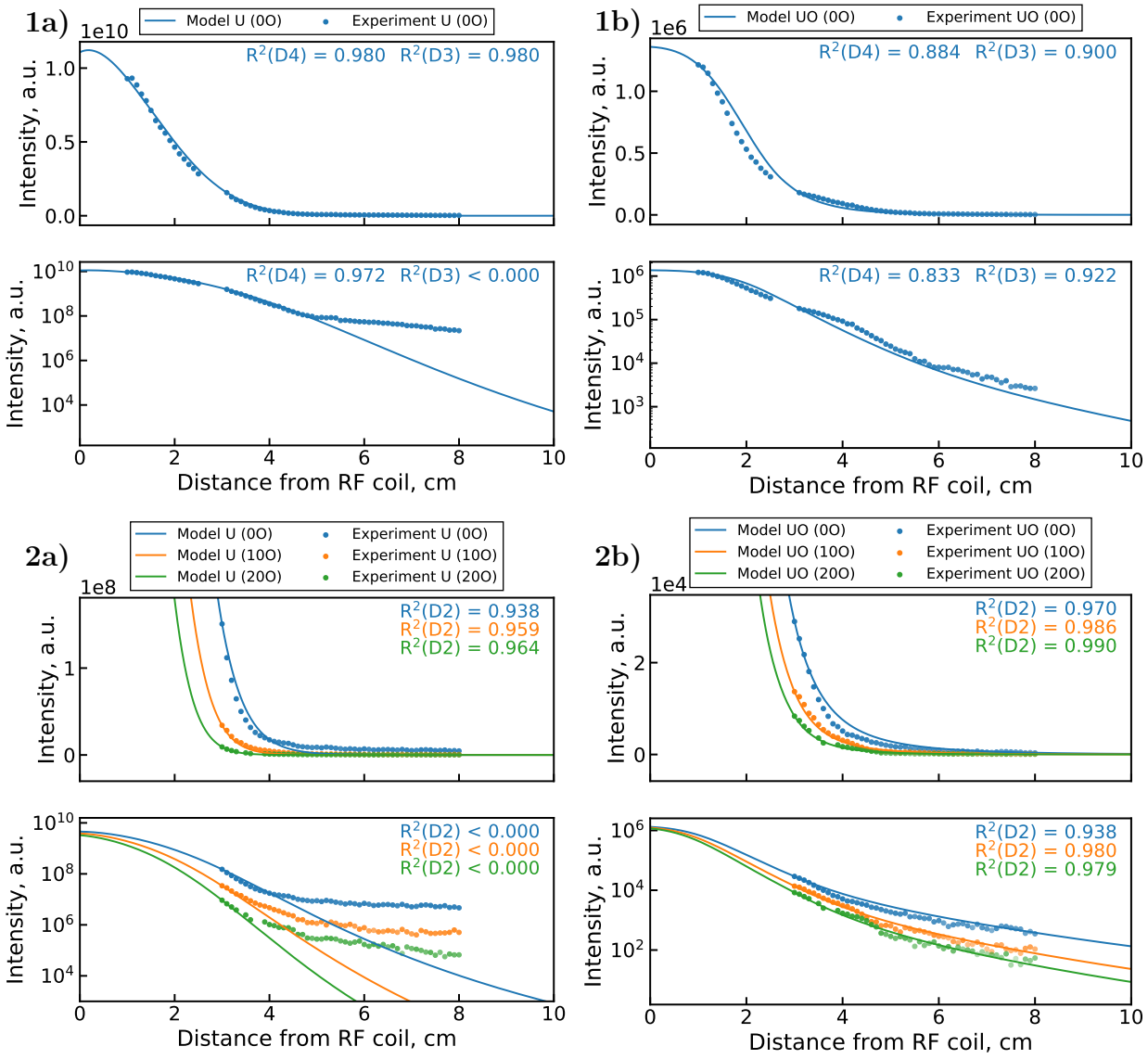

Figure 4.21: Synthetic emission profiles of a) U and b) UO (with linear and semi-log axes) generated by the GA optimized UO_x mechanism compared with 1) Datasets 3 & 4 and 2) Dataset 2 measurements. The transparency of experimental points indicates signal-to-background ratio.

Table 4.6: U-O reaction channels and recommended rate coefficients based on the MCGA optimization.

			k_{new}		
No.	Reaction	$\Delta_r H_{298.15K}$ (kJ/mol)	A (cm^3/s)	n (-)	E_A/R (K)
1	$U + O \rightleftharpoons UO$	−758.237	1.942×10^{-11}	−1.25	209.88
2[a]	$U + O_2 \rightleftharpoons UO_2$	−1011.363	2.050×10^{-13}	0.32	12910.0
3[a]	$U + O_2 \rightleftharpoons UO + O$	−259.889	2.050×10^{-13}	0.32	5161.7
4	$U + OH \rightleftharpoons UO + H$	−328.366	1.346×10^{-13}	0.32	5505.1
5	$U + H_2O \rightleftharpoons UO + H_2$	−267.238		-	
6	$UO + O \rightleftharpoons UO_2$	−751.474	1.950×10^{-11}	0.31	28020.3
7[b]	$UO + O_2 \rightleftharpoons UO_3$	−823.213	1.868×10^{-12}	−0.56	0.0
8[b]	$UO + O_2 \rightleftharpoons UO_2 + O$	−253.126	1.868×10^{-12}	−0.56	0.0
9	$UO + OH \rightleftharpoons UO_2 + H$	−321.603	1.309×10^{-12}	−0.56	2.03
10	$UO + H_2O \rightleftharpoons UO_2 + H_2$	−260.475	1.488×10^{-13}	0.36	10422.0
11	$U + O \rightarrow UO^+ + e^-$	−201.098	2.495×10^{-14}	−0.12	51.3
12[c]	$U + O_2 \rightarrow UO_2^+ + e^-$	−475.259	2.035×10^{-16}	−0.12	0.0

[a] A and n modifications based on analogous OH channels, literature E_A [142].
[b] A and n modifications based on analogous OH channels, no E_A assumed.
[c] based on cross section 2 orders of magnitude below R11 [139].

rates based on the MCGA optimized mechanism. Unfortunately, since only a handful of reaction channels are shared across the unoptimized and optimized reaction mechanisms (see Table 4.5), much of these recommendations must rely on arguments by analogy. In particular, since the competition between $UO_x + O_2$ and $UO_x + OH$ channels is not well constrained, we will estimate the collision rates of the former based on the optimized rates of the latter. Doing so results in about 2 and 4 orders of magnitude decrease in the $U + O_2$ and $UO + O_2$ rate coefficients, respectively. Similarly, the collision rate of the $U + O_2$ associative ionization channel can be approximately adjusted based on the optimized $U + O$ channel according to cross section ratios found in literature [139]. No changes are made to the activation energies of these reactions. Applying the above adjustments, we obtain the updated reaction mechanism shown in Table 4.6. Although this updated mechanism fits the constraining data slightly worse than the optimized mechanism, it still produces a

much better overall fit than the unoptimized mechanism. Overall, the updated mechanism predicts slower kinetics for both U and UO formation (with U kinetics being impacted more than UO), which is expected given the upper limit hard sphere estimates employed in the previous mechanism. A potentially important point of the updated mechanism is the lower branching ratio between the associative ionization and neutral pathways of the U+O channel, which suggests that the neutral pathway is not completely eliminated in favor of associative ionization as previously thought [139].

4.5 Discussion

In this chapter, we have outlined an MCGA-based approach for calibrating a UO_x reaction mechanism using emission measurements from PFR experiments. We have attempted to do so using minimal *a priori* assumptions regarding the choice of target reaction channels and their potential rate coefficients. Consistency between the 0D PFR model and experiments was provided by using a representative temperature profile that is in-line with available temperature measurements. The Monte Carlo sampling and Gentic Algorithm steps carried out in the optimization demonstrated the exploration of the problem parameter space and refinement towards a fitness maximum, respectively. The resulting optimized UO_x reaction mechanism was analyzed, highlighting several dominant reaction channels not previously considered in the unoptimized mechanism. Based on these findings, recommendations were finally made regarding UO_x formation rates in O-H-N environments. While the MCGA calibration was successful, its predictive capability is limited by the scarcity of constraining data and the uncertainties of key model parameters. In the following discussion, we will highlight the shortcomings of the current approach and suggest ways in which it can be improved upon in the future.

We begin by discussing some of the critical assumption made by the 0D chemical kinetic treatment of the PFR in this work. First, the temperature histories used in the current

0D model are calibrated with respect to only a handful of measured temperature values, none of which are acquired within the coil region. Since the simulated chemical evolution is very sensitive to the temperature history, a thorough characterization of the experimental temperature profiles should be undertaken to ensure that the model conditions are consistent with experiments. In addition to temperature measurements based on emission spectra, the plasma temperature in the coil region could potentially be measured using a standard plasma diagnostic such as a Langmuir probe. Furthermore, the approximation of a uniform Ohmic heating source in the current CFD model should be replaced with a solution of Maxwell's equations. In this way, the power deposited into the plasma in the model can be tied directly to the current supplied to the coils, avoiding manual calibration of the model parameters. A full set of axial temperature measurements would then allow for a validation of the CFD model, ensuring that the predicted temperature profiles are in close agreement with experiments. Second, the model assumes that the analyte to argon mixing ratio remains constant over the course of the 0D simulation. In reality, the mixing ratio will begin to change starting at the outlet of the annular flow channels and will continue to evolve downstream. This issue could be rectified in the future by using the CFD model to produce characteristic mixing ratio profile(s) in addition to the temperature profile(s) used in the current simulations. Lastly, the current 0D approach should be adjusted to account for the radial distribution of species and temperatures within the PFR flow. This could be accomplished by running the 0D model for several Lagrangian traces initiated at various radial points and then averaging over the resulting synthetic emission profiles. Since the computational cost will increase with the number of streamlines followed, the number of radial points should be selected with regards to both accuracy and speed.

Several additional improvements could also be made to the experimental methodology and analysis used here. First, given the importance of OH and H_2O in the MCGA optimized mechanism, both oxygen and hydrogen fugacity should be varied in the constraining datasets. This could potentially be achieved by using a desolvating nebulizer, which removes water

droplets present in the analyte solution prior to introduction into the plasma. This would drastically reduce the baseline O and H concentrations in the flow, allowing the competition between $UO_x + O_2$ and $UO_x + OH$ channels to be studied. Second, the experimental dataset could be expanded to include information on higher uranium oxide formation (i.e. UO_2 and UO_3), using Fourier-transform infrared spectroscopy (FTIR), for example. However, this would also necessitate extending the atomic and diatomic emission calculations used here to larger molecules, which is potentially challenging for uranium species. Third, the 593.55 nm UO band should be better resolved using a higher spectrometer grating. As mentioned before, the entire UO band is integrated in the current optimization due to insufficient spectral resolution. Since the UO emission signal here is modeled as the 0–0 head of this band, this serves as a potentially major source of uncertainty in the optimization. Resolving the 0–0 head, or deconvolving it using a detailed spectral model of UO, would minimize this uncertainty. Lastly, a relatively straightforward way to improve the MCGA generated mechanism is to use a larger dataset for the optimization. This includes measuring emission in both the upstream and downstream regions over a wider range of flow rates, temperatures, and analyte concentrations.

Chapter 5

Modeling of Plume Dynamics and Chemical Kinetics in Laser Ablation Experiments

The goal of this chapter is to demonstrate how diagnostic considerations impact the validation of reactive laser ablation simulations and to present a coupled modeling approach for carrying out such a validation. The first two subsections demonstrate the use of synthetic diagnostics in bridging the gap between a reactive CFD model and various spectroscopic measurements of ablation plumes. Here we discuss how the attenuation of emitted light and other diagnostic effects impact the observed chemical composition of a uranium ablation plume. We also analyze the spatial and temporal convolution of the plume species concentrations due to the use of a light source in absorption measurements. These considerations are shown to be important for comparing simulations to experiments and highlight the need for a reliable ablation model as a starting point. In the third subsection, we attempt to address this need by producing an experimentally validated predictive ablation model for use in chemical kinetic studies. This is accomplished by focusing on simulating ablation plumes for relatively well characterized materials (carbon and aluminum). High-fidelity images and time-of-flight measurements for these materials serve as validation targets for the plume dynamics of a reactive CFD model and a radiation-hydrodynamics model. While the radiation-hydrodynamics model is found to be much more suitable for simulating the initial ablation process, it is limited to an inviscid chemically inert treatment. Therefore, the two models are subsequently coupled to simulate both the ns timescale plume dynamics and μs timescale chemical kinetics of aluminum ablation in air. Comparisons are then drawn between the coupled model and species-resolved plume imaging studies found in literature, concluding with a discussion on future areas of improvement for this simulation approach.

5.1 Modeling uranium ablation emission signals for various oxygen fugacity atmospheres

We begin with a discussion on the effects of emission attenuation in an ablation plume on the observed chemical composition of the plume. In particular, we consider the problem of modeling a set of experiments designed to characterize the formation of UO in laser ablated uranium plumes. In these studies (performed by D. Weisz at Lawrence Livermore National Laboratory), uranium is ablated in a chamber filled with a given oxygen-argon mixture and the resulting plume emission spectra are collected. The spatially integrated UO/U emission intensities are then plotted against the oxygen fugacity to analyze the correlation between ambient oxygen concentration and oxide formation in the plume. For modeling these experiments, we utilize the viscous formulation of the reactive CFD framework discussed in Subsection 3.2.3. The simulations assume an initial ablation region with dimensions of 4 μm $\times$ 100 μm and a representative pressure and temperature of 35 MPa and 11600 K, respectively [17]. Running the model, we obtain spatio-temporal maps of U and UO number densities for ablation in the same ambient compositions as the experiments. However, as in the PFR calibration, an additional layer of synthetic diagnostics must be applied to compare these modeled number densities against the emission measurements. In particular, the model output should be adjusted to produce a depth-integrated visible emission intensity map that accounts for self-absorption and/or scattering of light travelling within the plume [73].

The above synthetic diagnostics can be implemented by obtaining 3D maps of the flow fields using the cylindrical symmetry of the 2D model results and then solving a 1D radiation transfer equation along the new depth axis. In doing so, a number of emission and absorption mechanisms can be considered. For example, the visible emission spectrum is likely to be initially dominated by Bremsstrahlung (free-free) and recombination (free-bound) emission. However, as the plume expands and cools, de-excitation (bound-bound) can be expected to overtake as the dominant emission mechanism [96, 144]. Similarly, we may wish to consider

the reverse processes that result in absorption, such as inverse Bremsstrahlung (free-free), photoionization (free-bound), and photoexcitation (bound-bound). Scattering, being non-local in nature, significantly complicates this picture and is typically ignored for the sake simplicity. In addition, the contributions from each of the above processes not only depend on the local temperatures and densities, but also vary depending on the photon energy. This latter dependence is typically treated by dividing the spectral range of interest into a discrete number of groups (multigroup approach).

As a starting point, we will consider a simplified treatment of the radiation transfer problem here to demonstrate the impact of absorption on the observed plume profiles. Assuming that radiation transport is much faster than the fluid velocity, the 1D gray (i.e. single photon energy group) solution of the radiative transfer equation with no background source or scattering [145] yields:

$$I(x,y) = \int_{z_0}^{z} I_0(\sqrt{x^2+z'^2}, y)\exp(-\tau(x,y,z',z))dz' \tag{5.1}$$

where z_0 is the starting depth for the integration, I_0 is the non-attenuated modeled emission intensity, and τ is the optical depth given by:

$$\tau(x,y,z',z) = \int_{z'}^{z} \alpha(\sqrt{x^2+z''^2}, y)dz'' \tag{5.2}$$

where α is simply an absorption coefficient, as attenuation due to scattering will be neglected here. The above equations utilize the aforementioned assumption of cylindrical symmetry via the $\sqrt{x^2+z^2}$ terms. To calculate the optical depth, we use a simple absorption coefficient derived from a dispersion relation for a cold collisional unmagnetized plasma [146]:

$$\alpha = \frac{\omega}{c}\sqrt{-\frac{1}{2}(1-\beta) + \frac{1}{2}\sqrt{(1+\beta)^2 + \left(\frac{\nu}{\omega}\beta\right)^2}} \qquad \text{where} \quad \beta = \frac{\omega_{pe}^2}{\omega^2+\nu^2} \tag{5.3}$$

where ω is the frequency of the emitted wave, c is the speed of light, $\nu = \sigma v_{th,e} n_n$ is the

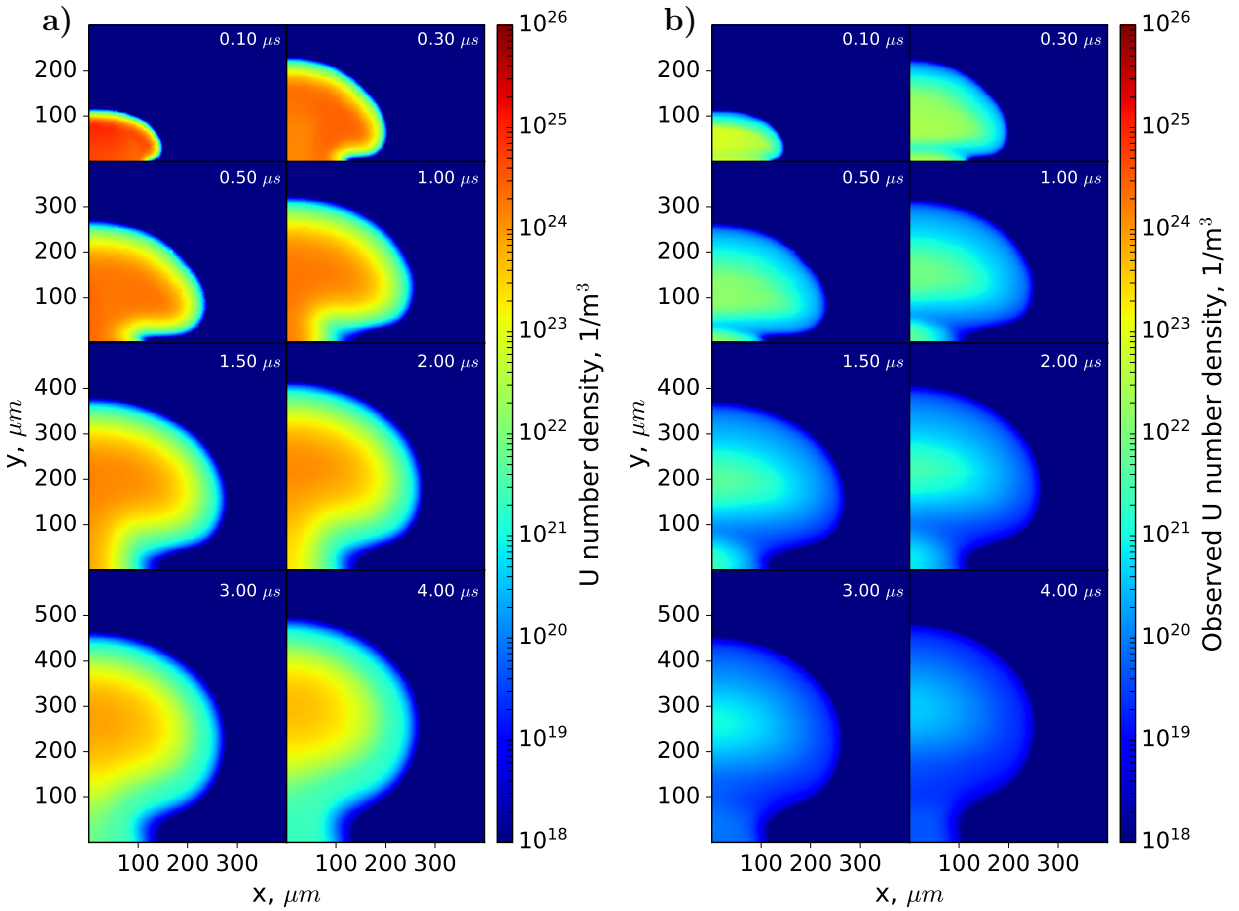

Figure 5.1: The a) modeled and b) synthetically "observed" uranium number density profiles for a uranium plume expanding in 100% O_2. The "observed" number density is lower due to the spatial integration along the z axis (facing out of page) that occurs when performing the attenuation calculation via Equation 5.1.

electron-neutral collision frequency, and $\omega_{pe} = \sqrt{e^2 n_e / \varepsilon_0 m_e}$ is the electron plasma frequency. In the preceding expressions, σ is the electron-neutral collision cross section, $v_{th,e}$ is the thermal electron velocity, n_n is the neutral species number density, e is the elementary charge, n_e is the electron number density, ε_0 is the vacuum permittivity, and m_e is the electron mass. This absorption coefficient accounts for the damping of the propagating wave due to electron-neutral collisions. In later sections, a more robust absorption calculation including all free-free and bound-bound interactions will be discussed.

The following procedure is used to generate synthetic emission signals from the 2D reactive ablation model. First, the plume temperature and number density maps are used to

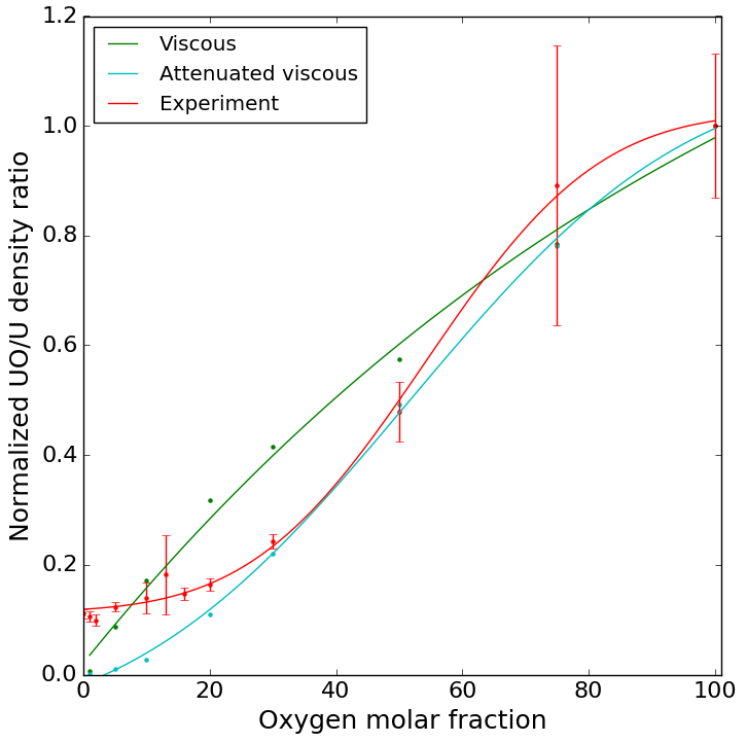

Figure 5.2: Comparison of simulated UO/U number density ratios across several oxygen molar fractions in argon carrier gas with experimental data.

calculate emission intensity profiles for the 591.54 nm U line and the 593.55 nm UO band, as in Chapter 4. Next, the attenuated emission intensity is integrated along the depth axis using Equation 5.1. Figure 5.1 demonstrates the effect of this integration when applied to the 2D uranium number density maps. From the figure, we can observe that the weakest emission occurs in the "rim" region between the "cap" and "stem" of the plume, where the low density plume edge is widest. Similarly, the "cap" and "stem" regions contribute the most to the observed signal due to the high densities there. Since the U and UO emission signals captured in the experiments are summed over the entire observed space, the modeled attenuated emission profiles are then uniformly spatially integrated. Lastly, the synthetic emission measurements are time-integrated over 1 μs after a 1 μs delay to match the acquisition parameters used in the experiments. The above simulations and corresponding synthetic diagnostics are repeated and applied for each ambient oxygen molar concentration used in the experiments (1%, 5%, 10%, 20%, 30%, 50%, 75% and 100% O_2 in argon).

The results of the synthetic fugacity study are shown in Figure 5.2. The figure uses normalized UO/U intensity values due to the high uncertainties of uranium transition probabilities. The "Viscous" curve denotes the unattenuated normalized UO/U number density ratio, whereas the "Attenuated viscous" curve denotes the result obtained after accounting for emission attenuation via Equation 5.1. As can be seen from the figure, the attenuated curve more closely matches the non-linear shape of the experimentally observed fugacity profile. The most glaring discrepancy between the modeled and measured fugacity curves occurs for fugacities under 20%. In this region, we observe that the model does not predict the experimentally observed saturation of the UO/U ratio, since the ratio instead decreases to a near-zero value at 1% O_2 concentration. This behavior may be due to the presence of an oxide layer on the uranium samples, which may provide the requisite oxygen for UO formation even in the absence of ambient oxygen. This behavior also persists when the same spot on the target is pulsed several times prior to measurement, which may suggest that the oxidation layer is much thicker than the laser absorption skin depth.

5.2 Modeling uranium ablation absorption measurements in reduced pressure environments

The synthetic diagnostics were also tested for several absorption experiments of uranium ablation plumes (performed by E. Weerakkody at the University of Illinois at Urbana-Champaign [14]). The absorption signals in these experiments are acquired over a relatively long duration (>20 μs) due to the use of a 7–9 μs FWHM xenon flash lamp. In addition, since the flash lamp is focused on a particular spot in the plume, the corresponding spatial integration is non-uniform and spans a limited solid angle. Lastly, the experiments use a higher fluence laser ($\sim$ 316 J/cm^2) in a low vacuum (15 Torr) atmosphere, producing a much larger plume than in the above fugacity study. In order to produce a plume of the observed radius ($\sim$4–5 mm), large initial pressures (350 MPa) and temperatures (1.5×10^6

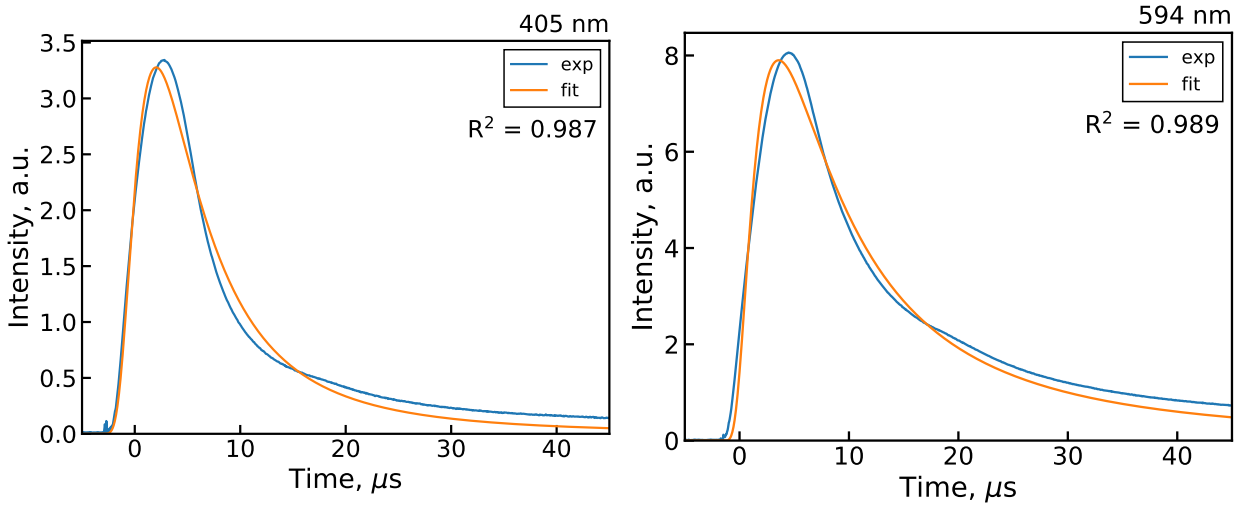

Figure 5.3: Example xenon flash lamp response curves for 405 nm and 594 nm spectral regions and the corresponding Fréchet fits used for synthetic diagnostics.

K) were used for the idealized 5 μm $\times$ 185 μm uranium "crater". However, the plume was observed to rapidly cool due to the high pressure expansion in low vacuum, dropping to peak temperatures of 80,000 K in the first 100 ns. Since an inert N_2 atmosphere was used in the experiments, the modeled reactions were limited to electron impact ionization and recombination for U. Although measurements were only taken up to 15 μs, the plume expansion was simulated up to 30 μs to allow for temporal integration over at least 15 μs of the $\sim$8 μs FWHM heavy-tailed flash lamp signal. Synthetic diagnostics in this case included spatial integration of the species number densities over a narrow cone of light focused parallel to the target surface and temporal integration over the flash lamp signal (fitted using a Fréchet distribution, as shown in Figure 5.3). The spatial integration was done at several radial points along the plume, as shown in Figure 5.4. Note that an exact location for the plume center was not determined experimentally, so the experimental measurements are centered relative to the outer measured points instead. This likely contributes to the apparent mismatch in the spatial distributions. The model results are reflected across the axis of symmetry for easier comparison.

Looking at the experimental data, we see that U^+ is generally more populous than U by

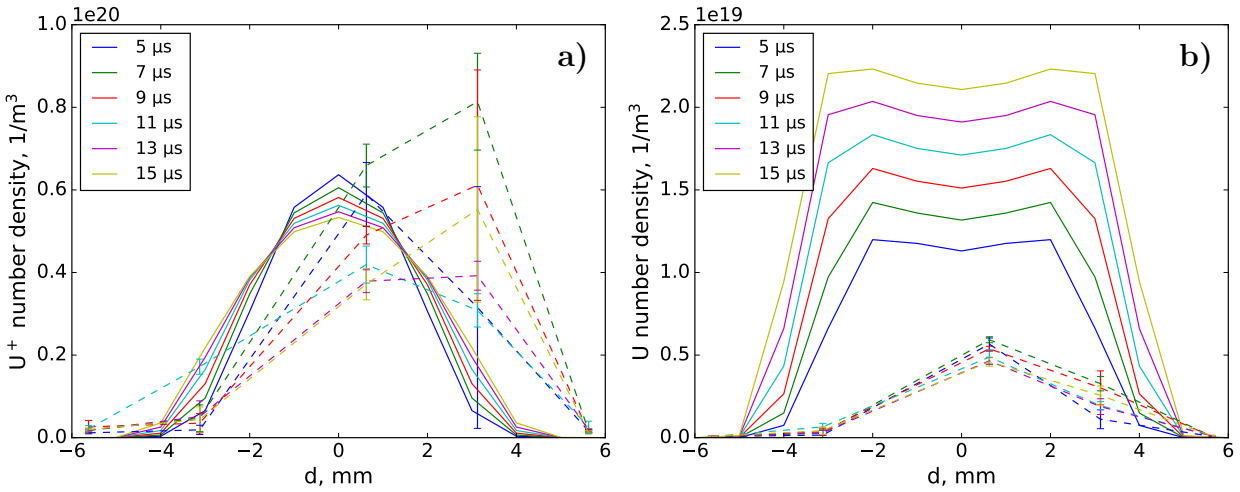

Figure 5.4: Comparison of modeled (solid) and experimental (dashed) profiles of a) U^+ and b) U number densities at various delay times for U ablation in 15 Torr N_2. The experimental uncertainties are calculated from 3 separate measurements at each radial point.

an order of magnitude even up to 15 μs. The modeled U^+ concentrations compare favorably with experiments, whereas U is overestimated by a factor of 2 or more. Measurements closest to the assumed center show both U and U^+ increasing from 5 to 7 μs and then decreasing from 7 to 15 μs. The increase could be due to internal transport, while the consequent decrease is likely due to diffusive expansion. The simulations, on the other hand, predict a consistent decrease in U^+ and increase in U over the entire time range. This occurs due to electron recombination induced by plume cooling converting U^+ into U. However, we also observe diffusive expansion in the model based on the broadening of the U^+ profiles. The recombination rate may be overestimated due to the lower temperatures in the modeled plume, which were about 1000–2000 K lower than the experimental estimates. While these results are not in complete agreement, they do demonstrate the importance of the spatial and temporal synthetic diagnostics in interpreting and comparing simulations and measurements.

5.3 Modeling and validation of low-Z laser ablation in reactive atmospheric environments

The preceding sections demonstrate the importance of considering the details of the experimental acquisition process when modeling reactive laser ablation studies. However, the above model-experiment comparisons also come with significant uncertainties and/or discrepancies. We would like to minimize these disagreements in order to ensure that such comparisons serve as a reliable source of chemical information. However, it is difficult to pinpoint the cause of the discrepancies due to the uncertainties of both the underlying optical and material properties of uranium and the predictive capability of the ablation model itself. Here, we will investigate the latter issue by assessing how adequately our ablation models capture the plume dynamics observed in various imaging experiments. In order to decouple this problem from the uncertainties inherent in modeling uranium plasmas, we will focus on more well characterized ablation materials (carbon and aluminum) for this validation exercise.

Our main validation targets for this endeavor are a set of high fidelity intensified charge coupled device (ICCD) images, shown in Figure 5.5, that clearly resolve distinct internal plume features over a ns-timescale expansion. The plasma plumes in these images are produced by ablating carbon tape and aluminum targets in air using an 8 ns FWHM, 1064 nm laser. The experimental setup was previously described in Subsection 3.2.1. These images represent an integration of the observed plume emission over the entire visible spectrum. In addition to displaying the internal structure of the plume, these images also show a well-resolved outer plume interface. By tracking the location of this interface, an estimate of the plume expansion velocity can be obtained. This measurement provides a quantitative validation target for the expansion rates predicted by our ablation models. Lastly, we note that the dramatic differences in internal features for these two materials provide valuable information on the impact of material properties on the ablation dynamics.

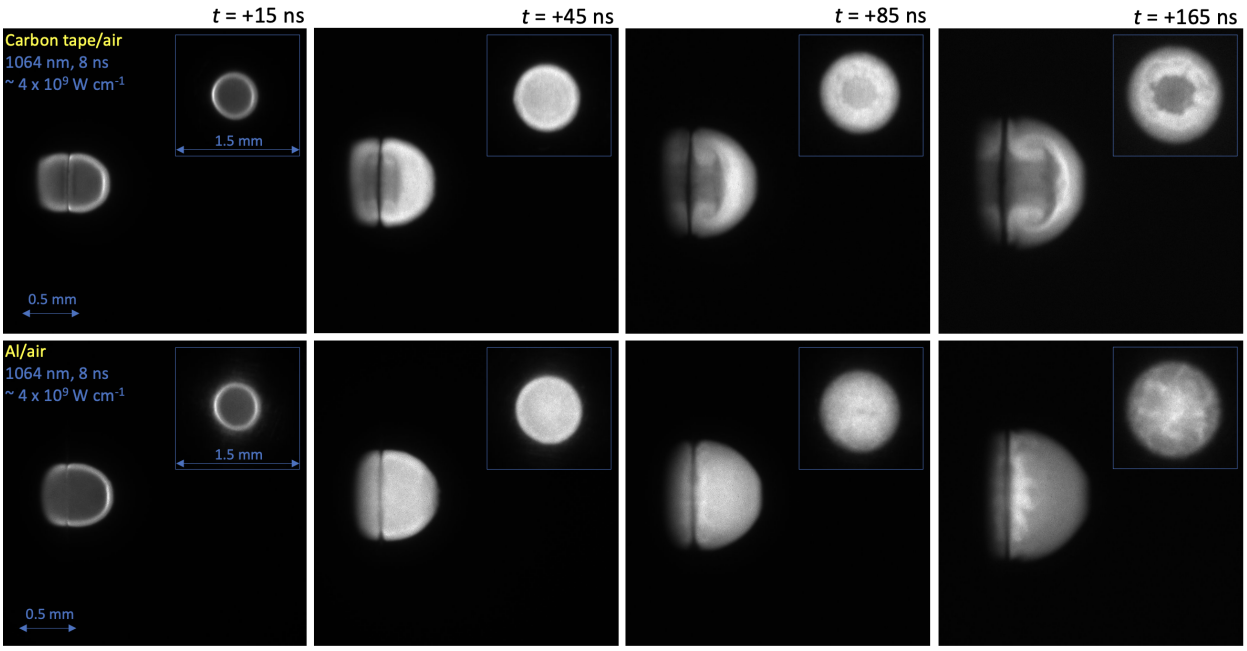

Figure 5.5: ICCD images of laser ablated carbon (top) and aluminum (bottom) plumes in atmospheric air at various delay times with respect to the pulse midpoint. The main images are orthogonal to the drive while the insets are along the drive (see illustration of Figure 3.4). Images courtesy of J. Crowhurst (LLNL).

As a continuation of the validation tests in the preceding sections, we will first compare these ICCD images against our reactive CFD model. As will be shown, this model produces results that are in partial agreement with the images and plume expansion velocities. However, a much better agreement is observed when a radiation hydrodynamics model is employed instead, as we will also show later.

5.3.1 Reactive CFD modeling

First, a reactive CFD model similar to those presented in the previous two sections is constructed. Again, the idealized "crater" initialization procedure previously outlined in Subsection 3.2.3 is employed. The dimensions of the initial region are based on the laser spot diameter of 280 μm and an ablation crater depth of 5 μm observed for similar laser fluences [109]. The initial temperatures and pressures in this region are again qualitative tuned to fit experimental observations, this time using plume imaging and time-of-flight front ve-

locities as the matching metric. Initial values of 20 GPa and 250,000 K (∼21.5 eV) are found to have good agreement with experiments. These initial parameter values are kept the same for both the carbon and aluminum ablation cases. The initial species concentrations in the "crater" region are calculated using an ideal gas Saha balance for a singly ionized plasma. For the reaction network, a reduced atmospheric re-entry reaction mechanism [147] is combined with electron-impact ionization rate coefficients derived from literature cross sections [148]. However, utilizing the full reversible mechanism was found to produce convergence issues, which may be due to the stiffness of the reactive ODEs in the initial high temperature and pressure regions of the solution. To remedy this, the reaction mechanism is reduced further down to contain only endothermic reactions (ionization, molecular dissociation). This assumption is partly justified by the high temperature conditions, which will prevent molecular formation throughout much of the plume on the timescales of interest here (< 200 ns). Only singly positively charged ion species are considered here.

Since the emission intensities captured in the ICCD images are proportional to the local temperature conditions, we first examine the modeled normalized temperature profiles, as shown in Figure 5.6. A number of similarities and differences between the carbon and aluminum cases are evident from these plots. In both cases the outer plume expansion appears similar to a spherical blast wave, with the aluminum plume expanding faster than the carbon plume. The aluminum plume also appears to be consistently hotter than the carbon plume. While the plume temperatures at 15 ns appear similar for the two cases (cool inner and hot outer regions), substantial differences are apparent after 45 ns. As will be discussed, this behavior is driven primarily by differences in the molecular mass of the ablation materials. We note also that distinct fluid features begin forming along the material-air interface after 45 ns and continue to evolve up to 165 ns. These fine features are likely due to fluid instabilities driven by density gradients (Rayleigh-Taylor) or internal shocks (Richtmyer-Meshkov) produced by the reflection of rarefaction waves from the target surface.

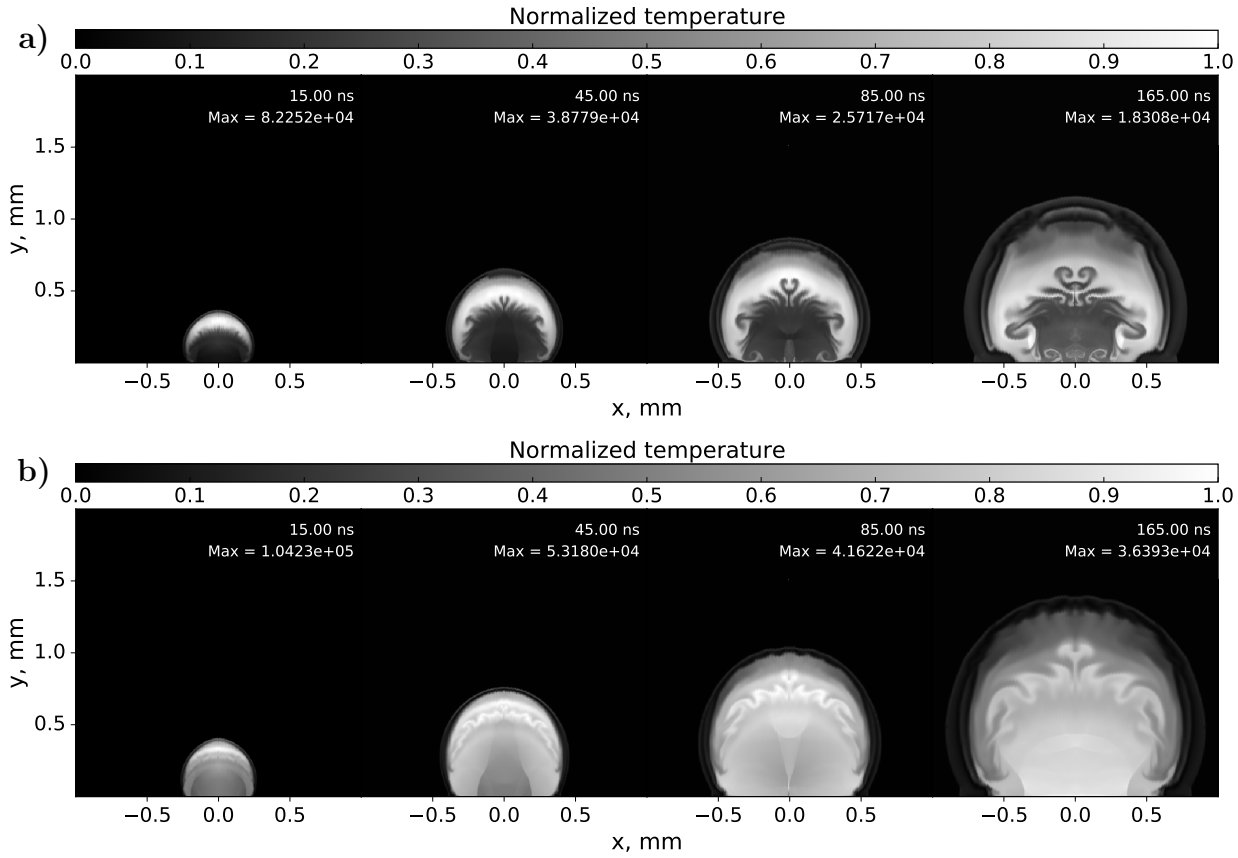

Figure 5.6: Modeled normalized temperature profiles of a) carbon and b) aluminum ablation plumes in atmospheric air at various delay times. The temperature magnitudes are normalized for each delay time, with the maximum temperature listed below the delay time.

To better understand the differences in the plume dynamics for the two case, we first examine how the ablation plume forms. In both cases, the plasma plume is generated due to the rapid expansion of the over-pressurized material region into the surrounding air. More specifically, the expansion compresses and heats the air above the ablating material, ionizing it and producing an outwardly propagating shock wave. This behavior can be observed from the species number density profiles along the plume centerline shown in Figure 5.8. Here, we see that while the inner plume regions consist of fully ionized ablated material (C^+ or Al^+), the outer plume contains only fully ionized air species (N^+, O^+, Ar^+). The plume regions corresponding to the ablated material and the air plasma are visualized in Figure 5.7.

Although the ablation mechanism is the same for the two cases, differences in material

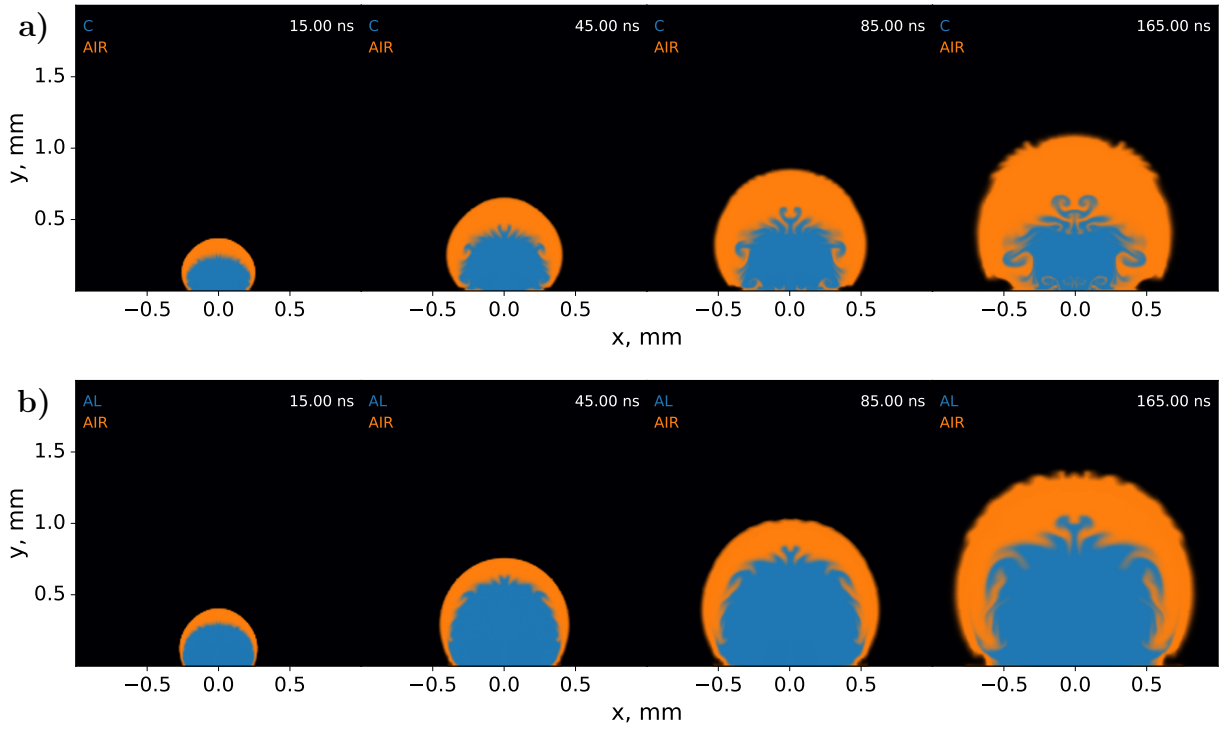

Figure 5.7: Modeled plume profiles denoting the material and air plasma regions for the a) carbon and b) aluminum cases. Note that the maps do not display number density information, but simply highlight regions where a given composition is the majority.

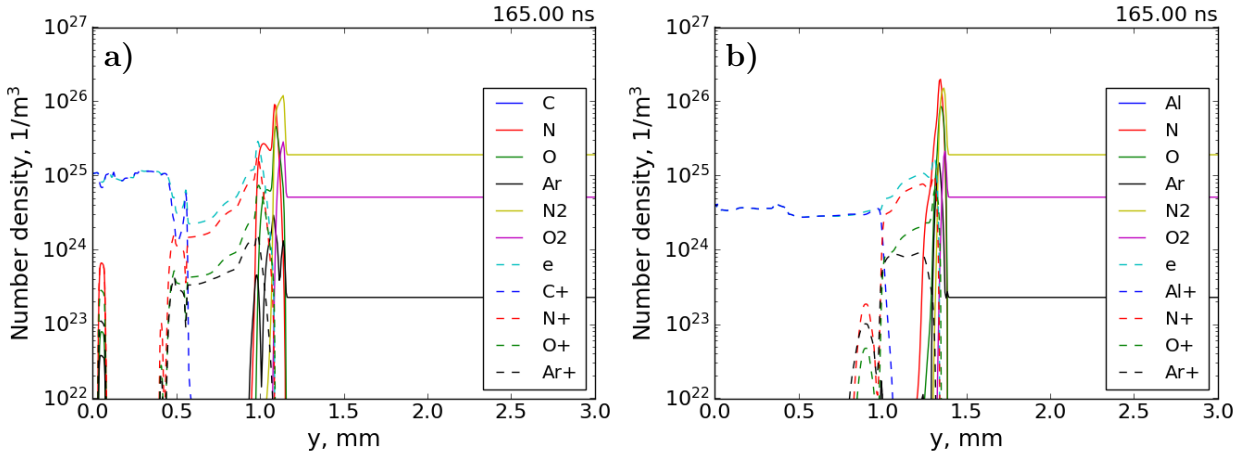

Figure 5.8: Modeled species number densities along ablation plume centerline for carbon (left) and aluminum (right) at 165 ns.

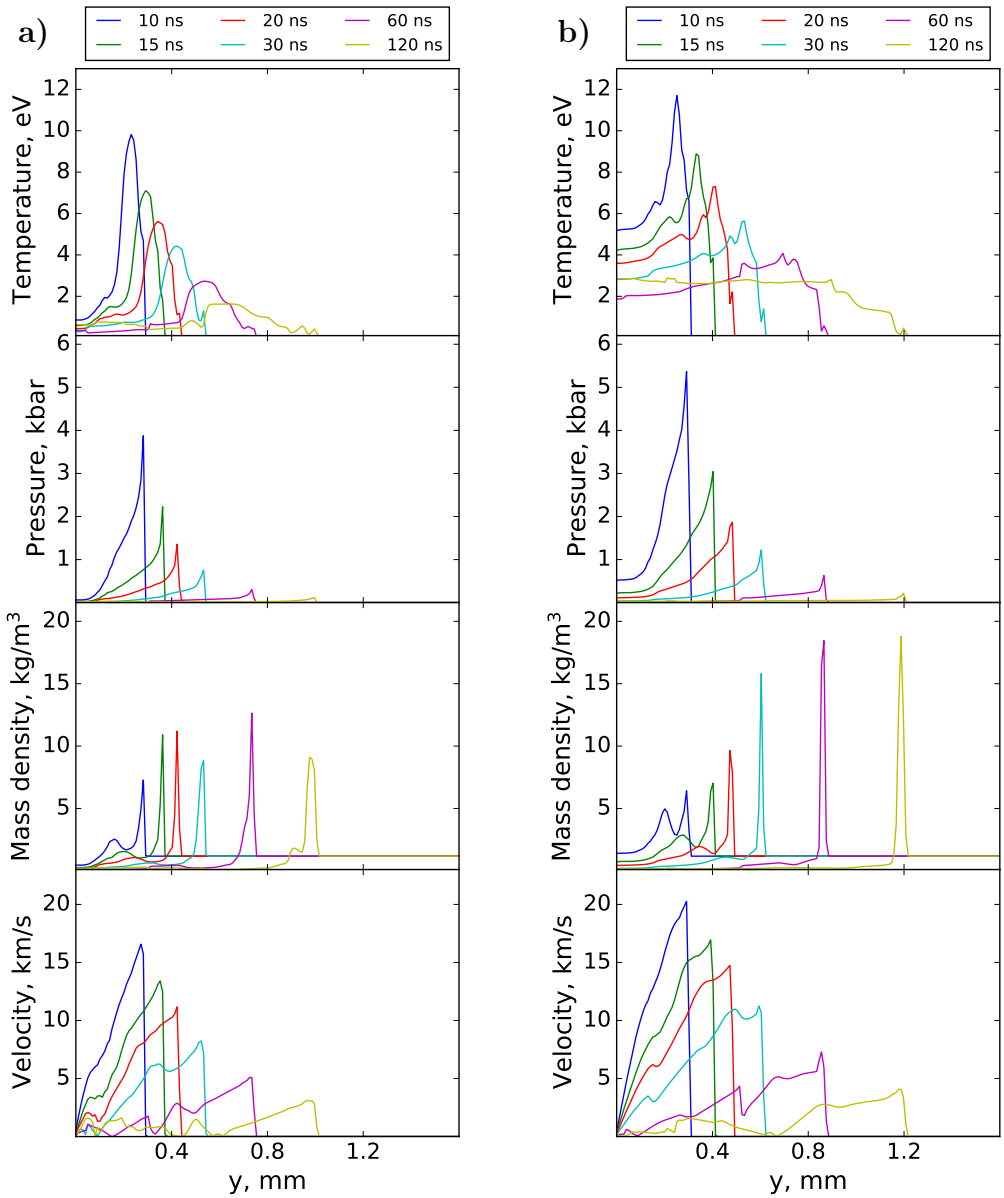

Figure 5.9: Temperature, pressure, mass density, and velocity profiles along the plume centerline over the first 120 ns for a) carbon and b) aluminum.

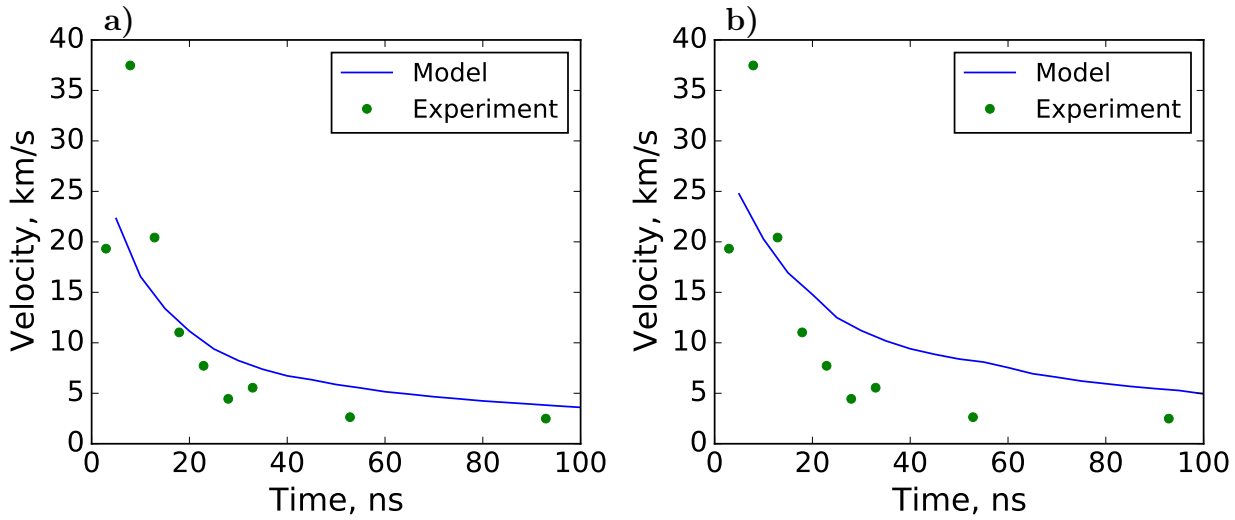

Figure 5.10: Comparison of modeled and measured shock front velocity for a) carbon and b) aluminum. Note that the experimental measurements in both plots are for aluminum ablation.

properties impact how the energy is distributed between the air plasma and the ablated material. Since the same temperature and pressure values were used to initialize both cases, the starting material number densities are the same. However, due to its higher mass, the starting kinetic energy is more than doubled in the aluminum case. This results in the production of a higher magnitude shock for this case, as seen from the centerline fluid moment profiles shown in Figure 5.9. Furthermore, the mean atomic mass of air is higher than that of carbon, even when the constituent air molecules are dissociated. These differences in mass and kinetic energy are responsible for the faster expansion and slower cooling of the aluminum case.

In addition to the qualitative corroboration of the modeled temperature maps against the ICCD images, we also perform a quantitative comparison of the plume expansion velocity using time-of-flight measurements. While these measurements were only performed for aluminum, they are plotted with respect to both of the modeled cases in Figure 5.10. The plots show generally reasonable agreement between model and experiment, although the measured expansion appears to be more rapid initially and less rapid at later times. Better

agreement is observed for carbon, as it was used as the calibration target for the starting conditions. The agreement could be improved by further tweaking the initial conditions for the two cases individually, but this is unlikely to affect the overall behavior described above. It should also be noted that the experimental uncertainties are highest for the first and second points, although they have not been quantified.

5.3.2 Radiation hydrodynamics modeling

Next, laser ablation simulations of the experiments were performed using the radiation-hydrodynamics FLASH code (detailed in Subsection 3.2.4). The carbon and aluminum simulations are identical in all respects save for the material properties (mass density, atomic number, atomic mass) and the material EOS used. A graphite EOS was used for the carbon tape targets and an aluminum EOS for the polished Al targets. As in the experiments, both simulations use a 15 mJ, 1064 nm, 8 ns FWHM laser with a spot size of 280 μm (fluence of $\sim$25 J/cm^2) oriented perpendicular to the target surface. A 1.6 mm $\times$ 2 mm 2D cylindrical computational domain is used, with a 200 μm thick target region along the bottom and the remainder of the domain being occupied by air.

As in the previous section, we again begin our comparison with the ICCD images by first looking at the modeled plume temperature maps. Figure 5.11 shows the simulated normalized ion temperature profiles for the aluminum and carbon cases at several time points up to 125 ns. We first note that the maximum temperatures and outer plume shapes are nearly identical in the two cases, the latter observation also holding true for the experimental ICCD images. The main differences for the two materials are observed inside the plume, where a distinct low temperature region observed for aluminum is seemingly absent for carbon. At first glance, it appears that the model is predicting inner plume features directly opposite those observed in the ICCD images. However, an inner "mushroom"-like region is actually present for both simulated materials and corresponds to the location of the ablated material within the plume, as shown in Figure 5.12. The remainder of the plume, then, consist of an

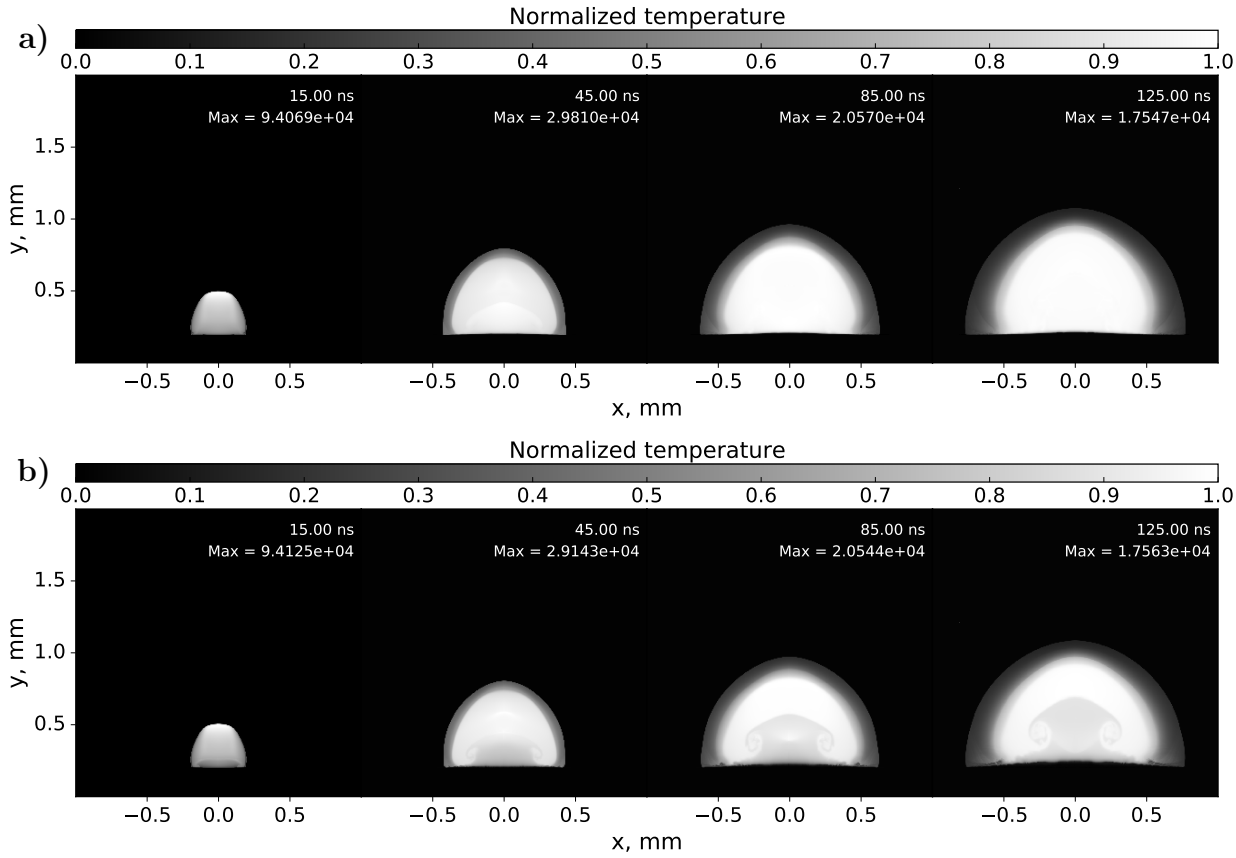

Figure 5.11: Normalized temperature maps for a) carbon and b) aluminum. The temperature is normalized with respect to each snapshot, and the maximum temperature (in K) is written below the corresponding delay time.

air plasma that envelops the material, and this air region expands and cools at roughly the same rate for both materials. While this behavior appears superficially similar to that of the pure hydrodynamic model from the previous section, the plume formation dynamics differ. Here, the air plasma is initially formed via inverse Bremsstrahlung absorption of incident laser energy in front of the ablated aluminum, where the air is sufficiently compressed and heated by the expanding aluminum plasma. Subsequently, the dense air plasma expands into the ambient air, producing a strong shock at the plasma-ambient interface that propagates outward, as discussed further below. Overall, the primary difference in the temperature maps for the two modeled materials is the lower temperatures in the material region for the aluminum case. However, the ICCD images suggest a more dramatic difference in plume

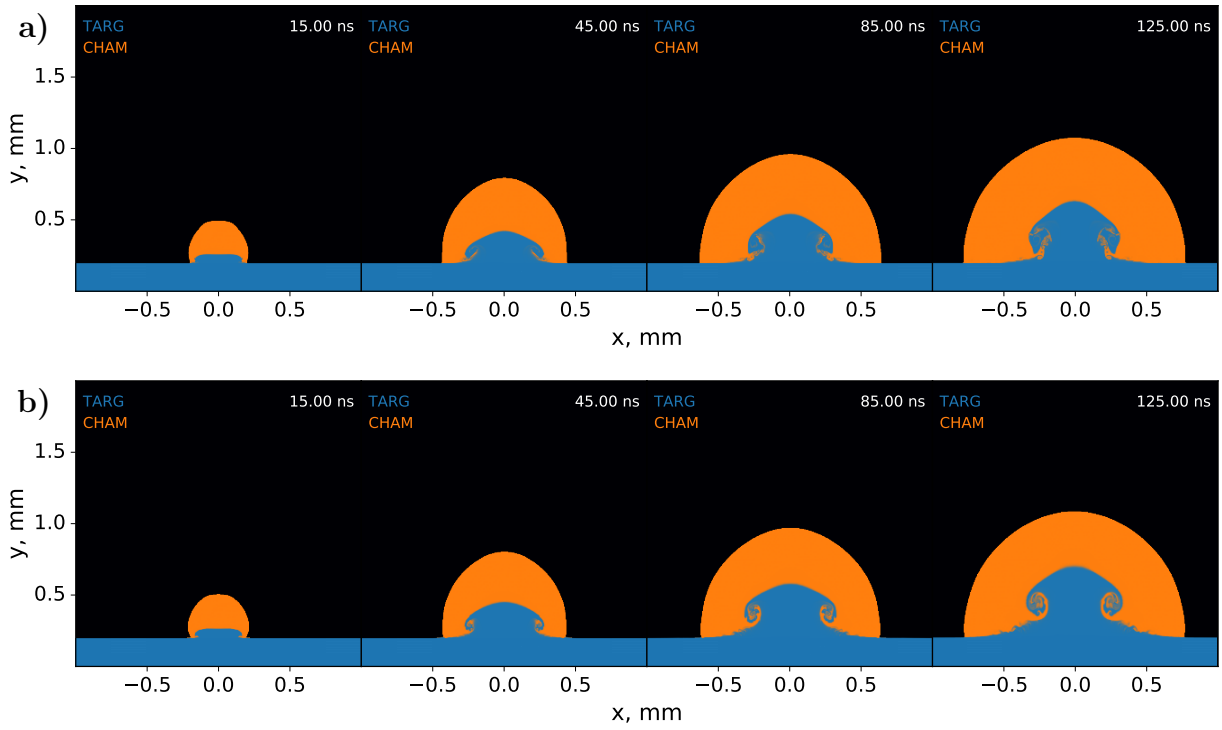

Figure 5.12: Maps of the material (labeled "TARG") and air (labeled "CHAM") regions in the model for a) carbon and b) aluminum ablation. For air, only regions hotter than room temperature are plotted to show the extent of the air plume.

dynamics should be present. Possible reasons for this discrepancy are discussed further below.

A more quantitative comparison of various fluid moments is shown in Figure 5.13, which shows 1D profiles along the plume centerline at various time points. Here, we can clearly see the shock front along the outer plume edge advancing nearly identically for both materials. Peak temperature, pressure, and velocity values of around 11 eV, 9 kbar, and 22 km/s, respectively, are observed around the midpoint of the pulse duration (10 ns). Within the material region, we see lower temperatures and higher pressures, mass densities, and velocities for aluminum. Note that these temperature profiles correspond to the ion temperature, which is found to be close to the electron temperature (within a few 100 K) throughout most of the plume. The largest deviations between the electron and ion temperatures occur in the laser absorption region in the vicinity of the shock front, where differences of up to a few

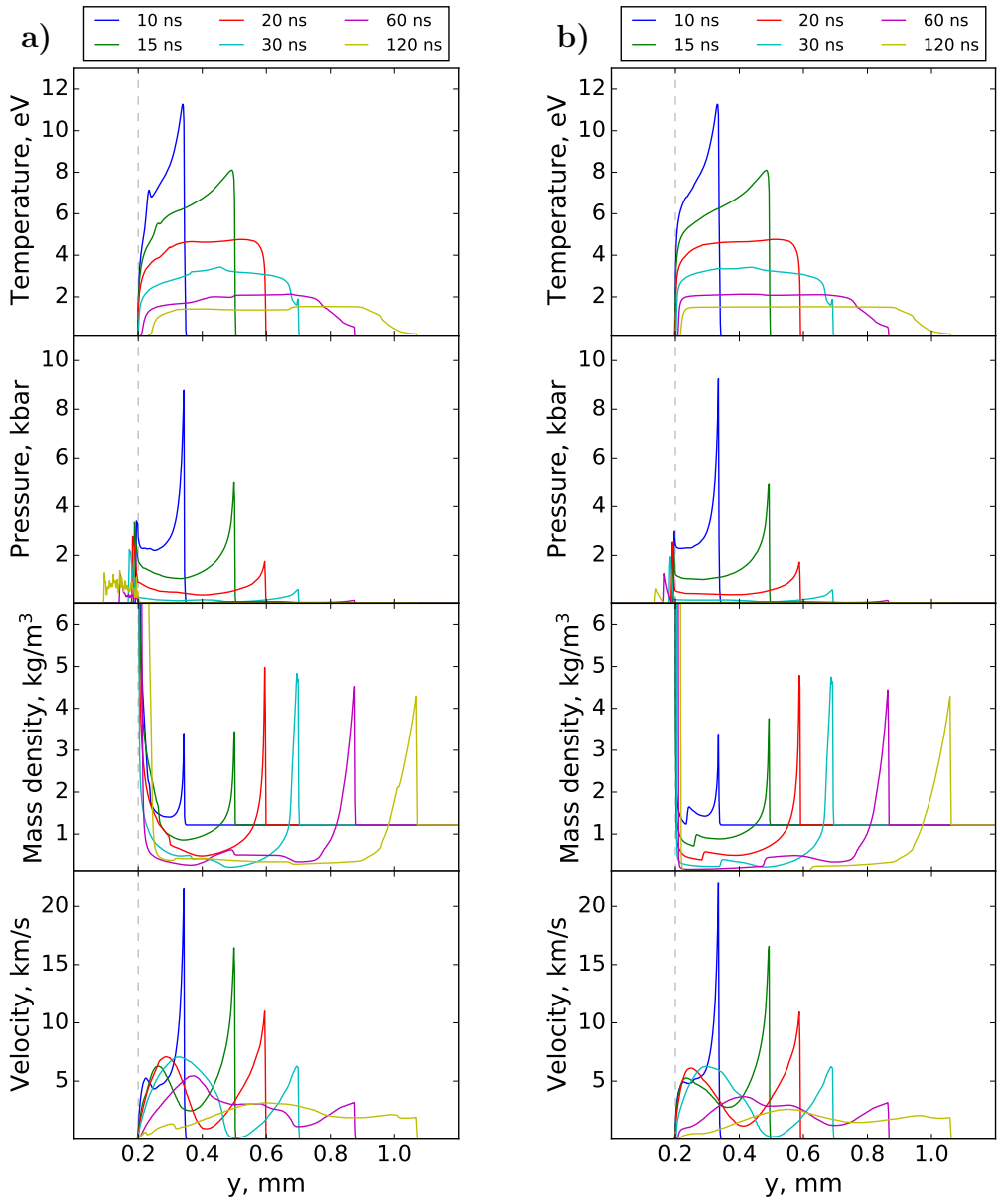

Figure 5.13: Temperature (ion), pressure, mass density, and velocity profiles along the plume centerline over the first 120 ns for a) aluminum and b) carbon. The dashed gray line denotes the initial location of the material–air interface.

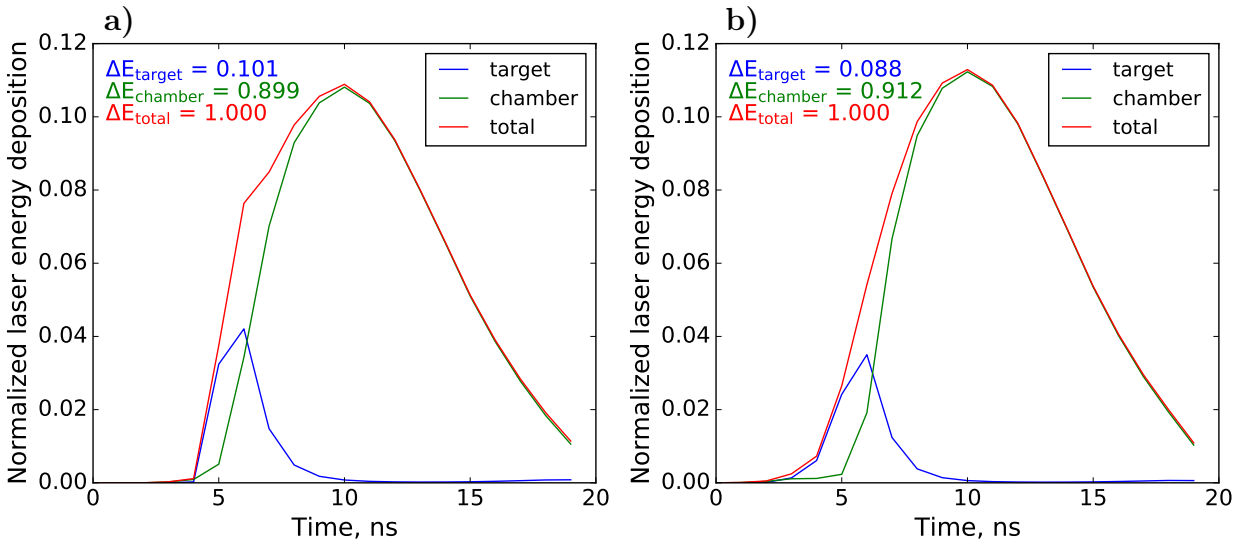

Figure 5.14: Normalized laser energy deposition profiles for a) aluminum and b) carbon.

1000 K appear. This indicates that, in the current model, local thermodynamic equilibrium (LTE, i.e. $T_i = T_e$) is observed throughout most of the plume following the initial laser energy deposition period.

Figure 5.14 shows the normalized laser energy deposition into the target (material) and chamber (air) regions of the plume as a function of time. Initially, the air is completely transparent to the laser, and the laser energy is deposited completely into the material over the first ∼5 ns. During this time, rapid expansion of the dense material plasma occurs and produces a corresponding shock front. As the shock front begins to propagate into the surrounding atmosphere, it produces a hot, dense air plasma along the outer plume edge. Due to the high density and degree of ionization in this region, an increasing fraction of the incoming laser energy begins to be absorbed by the air plume. Consequently, the air plume increasingly shields the inner material region from the laser as the pulse advances towards peak intensity at 10 ns, as shown in Figure 5.15. Thereafter, the remaining laser energy is completely absorbed in the air plume region up to the end of the pulse at 20 ns. As a result, most of the laser energy (∼90%) is absorbed by the air plume, which explains the similar shape of the outer plume edge for both materials. This behavior appears to be in

line with the experimental ICCD images, where the outer plume looks similar regardless of the material being ablated, even when the inner plume dynamics vary substantially. This pattern of laser absorption and plume propagation is typical for IR (1064 nm) lasers [72, 89] and has been referred to in literature as a laser-supported detonation (LSD) wave [90, 91].

The above figure also illustrates a potential issue with the current simulation; namely, that the laser deposition treatment for metals and non-metals is nearly identical. Since the ray tracing is performed in the geometric optics limit [149], Fresnel's equations are not solved, and partial reflection and transmission due to refractive index gradients cannot occur [150]. We speculate that the experimentally observed differences in inner plume dynamics between aluminum and carbon could be due to such effects. In particular, the high reflectivity of aluminum for 1064 nm light may result in less energy deposition in the material region while depositing a comparable amount of energy in the air plume region. Such a behavior would be more consistent with the ICCD images of aluminum ablation in the current work, as well as a higher fluence (160 J/cm^2) experiment found in literature [60]. Another potential source of discrepancies could be the exclusion of phase explosion [151] as an ablation mechanism in the current model. Phase explosion occurs when a superheated metastable fluid returns to an equilibrium liquid-vapor (binodal) state through rapid homogeneous nucleation of vapor bubbles that decay into a mixture of vapor and liquid droplets [101, 152]. Depending on the laser parameters and the material being ablated, phase explosion can occur at various fluence thresholds [152–155], and may take place hundreds of ns or even tens of μs after pulse heating [156, 157]. In both experimental studies and corresponding thermal models [117,118,158,159], phase explosion appears as a dominant ablation mechanism for aluminum at fluences comparable to the current experiments (20 J/cm^2). Incorporating the effects of phase explosion on the ablation dynamics would require using a mixed-phase treatment for the material EOS [108]. It should also be noted that in the case of aluminum and other metals, carbon-like inner plume features are observed if the surface is allowed to oxide prior to ablation. This effect may also be tied to the above physical phenomena via a change in

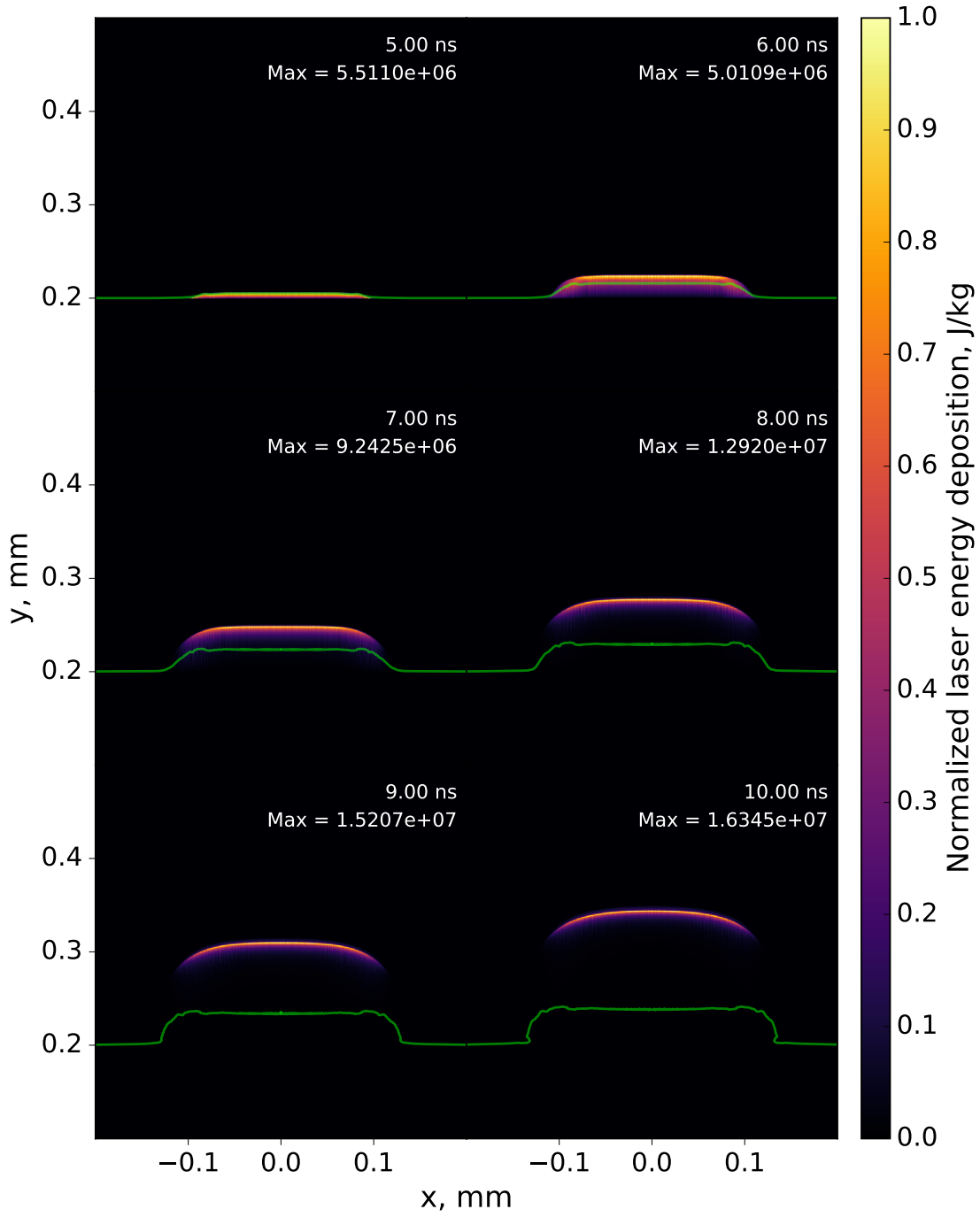

Figure 5.15: Normalized specific laser energy deposition in the aluminum ablation model demonstrating the shielding of the laser pulse by the air plasma. The green contour line denotes the aluminum/air interface.

reflectivity or a lowering of the phase explosion threshold.

As in Section 5.1, we now attempt to make a direct comparison with the ICCD images by applying synthetic diagnostics to the above simulation results. Utilizing the same formulation as Equation 5.1, but using a non-gray model, yields the following multi-group radiative transfer relation:

$$I(z) = \sum_{g}^{G} \left(\int_{z_0}^{z} \bar{\eta}_g(z') \exp(-\tau_g(z', z)) dz' \right) \tag{5.4}$$

where $I(z)$ is the intensity observed at distance z away from the origin z_0 due to emission from G photon energy groups, with mean group emissivities $\bar{\eta}_g$ and group optical depth τ_g given by:

$$\tau_g(z', z) = \int_{z'}^{z} \bar{\kappa}_g(z'') dz'' \tag{5.5}$$

where $\bar{\kappa}_g$ is the mean group absorption coefficient. Here, Planck mean opacities are used for the mean group optical coefficients [123]. Since scattering is ignored here, the above equation is easy to solve numerically. The main difficulty in using this calculation for the purpose of synthetic diagnostics lies in estimating the group emissivity and absorption coefficients. An important consideration in calculating these coefficients is the condition of thermodynamic equilibrium between the radiation field and the plasma [145]. If such an equilibrium condition is reached, then the emissivity at a given photon frequency ν is proportional to the absorption coefficient via the Kirchoff-Planck relation:

$$\eta_\nu(n, T) = \kappa_\nu(n, T) B_\nu(T) \tag{5.6}$$

where B_ν is the Planck function, n is the the heavy particle number density, and T is the equilibrium temperature. In this case, both collisional and radiative processes follow a detailed balance such that electrons and ions are Maxwellian and the radiation field is Planckian. We can expect this behavior in optically thick regions of a plasma, where the photon mean free path is much smaller than the characteristic length scales and radiative

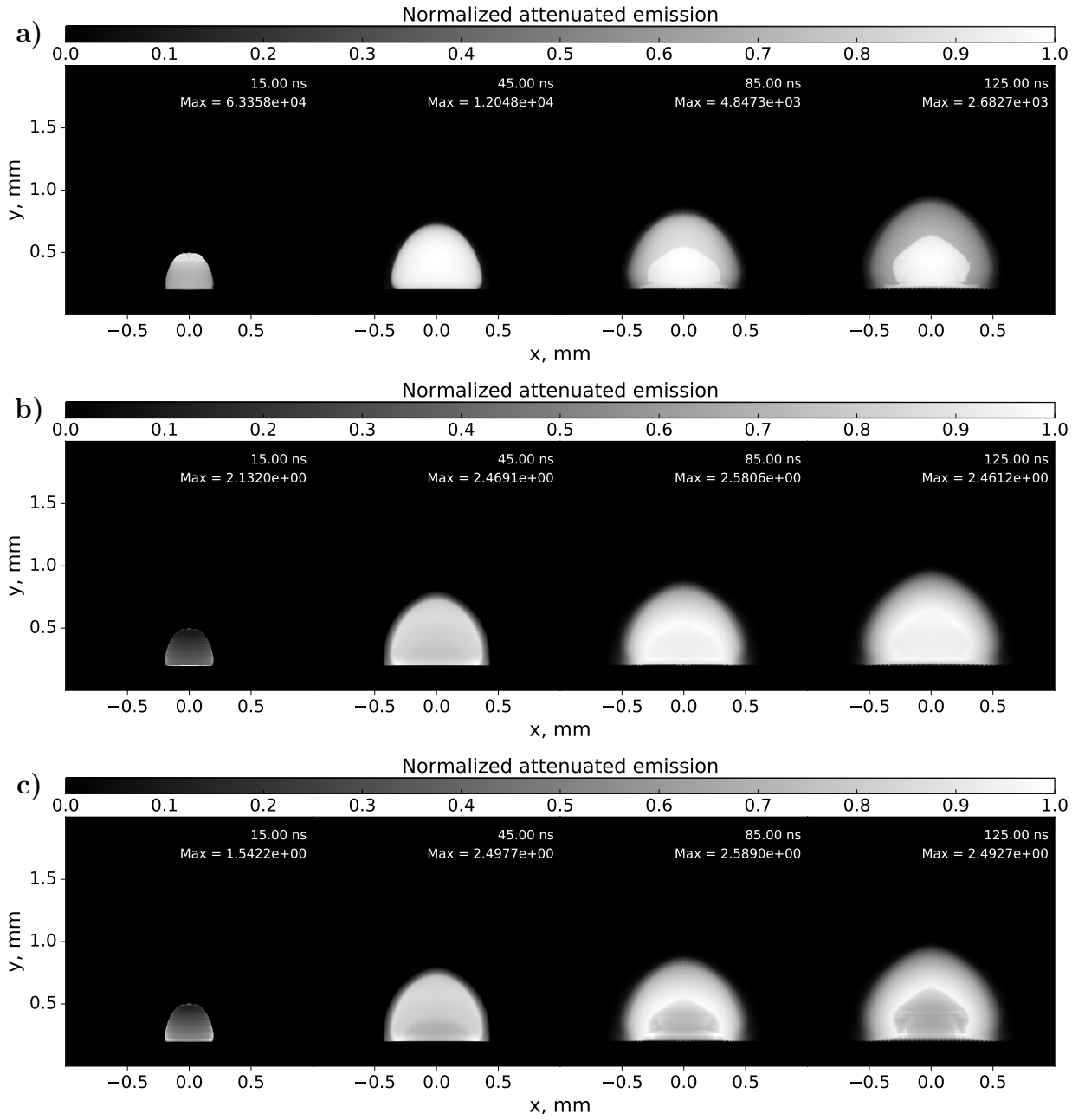

Figure 5.16: "Front" view of synthetic attenuated carbon plume emission using 20 photon energy groups in the visible range. IONMIX calculated Planck mean absorption coefficients are used along with a) IONMIX calculated Planck mean emissivities, b) Planck function emissivity, and c) Planck function emissivity with carbon absorption and emission reduced by an order of magnitude.

transport is essentially a diffusion process. When radiation transport is more non-local (i.e. longer photon mean free paths) but collisional processes remain dominant over radiative ones, the radiation field will begin to deviate from a Planckian distribution while the electrons and ions remain thermal. While the radiation field in this case may no longer be Planckian, it is often approximated as such, albeit using a temperature corresponding to the radiation energy density (i.e. T_r). Of course, due to the highly transient and inhomogeneous nature of an ablation plume, the electrons and ions can also deviate from a common distribution during an ablation event [160]. However, since laser ablation in this work takes place in atmospheric conditions and the laser pulse is relatively long and low fluence, the plasma is highly collisional and we can expect the ions and electrons to thermalize fairly rapidly. Indeed, significant differences in ion and electron temperatures ($T_e - T_i > 1000$ K) in the modeled plume are only observed during the laser pulse in thin regions near the shock front. Therefore, for much of the plume expansion, the plasma may be approximately treated as a 2 temperature system ($T_i = T_e \neq T_r$). If the spatial and temporal variations in the plume state are small enough to maintain this condition locally, the plasma is said to be in local thermodynamic equilibrium (LTE) [16]. Note that an LTE plasma may also be adequately described by a single temperature if the radiation field is sufficiently local, but this need not be the case in general. As mentioned previously, the opacities and emissivities used here were generated by the IONMIX code [123]. Although IONMIX can calculate opacities using separate radiation and plasma temperatures, FLASH passes only a single temperature for calculating the Planck and Rosseland means. Furthermore, IONMIX makes heavy use of hydrogenic approximations in its opacity calculations (i.e. for collision parameters and partition functions). Lastly, as previously discussed, FLASH treats radiation transfer as a diffusion process, which is an approximation that breaks down at the outer plume boundary. The net effect of the aforementioned issues is that the radiation temperature predicted by the model is likely in closer equilibrium with the plasma temperature than should realistically be the case. As a result, using these opacity values to calculate synthetic plume emission maps is

likely to produce significant discrepancies, as will be shown below. A more robust collisional-radiative model [161] would likely be needed to capture the non-equilibirum behavior of the radiation field and produce emission maps consistent with experimental observations.

Here, we will demonstrate how geometric and optical considerations can impact observed plume emission features by applying (5.4) to the carbon ablation model results. Figure 5.16 shows three synthetic emission tests obtained in this manner using different emission and absorption opacities. In the first test (a), the IONMIX calculated Planck mean opacities were used for the group emissivities $\bar{\eta}_g$ and absorption coefficients $\bar{\kappa}_g$, summing contributions from 20 groups in the visible range. The resulting images are quite dissimilar from the experimental ICCD images. The plume appears completely opaque at 45 ns and the target (carbon) plume regions appear brighter than the air regions in the subsequent 85 and 125 ns images. The result for 15 ns also differs due to the absence of a dark inner region with a bright border that would suggest moderately high absorption in the air plume. The second test (b) differs from the first by replacing the emission term with the Planck function (i.e. unity Planck mean emission opacity). The resulting emission maps are much closer to the observed ICCD images, with a largely opaque plume at 15 ns strongly emitting from the edges, and a dark material region surrounded by brighter air emission for the remaining time points. The third test (c) improves this agreement further by reducing the absorption and emission coefficients of the target material by an order of magnitude. This results in an even darker inner plume shape that strongly resembles the ICCD images. A comparison between the ICCD images for carbon ablation and synthetic emission maps made by applying this third test calculation to the carbon case are shown in Figure 5.17. In this figure, we also show how the use of an additional observation angle ("top" view) can further assist in the model-experiment comparisons. The purpose of the above tests is to demonstrate the importance of optical considerations when making comparisons to ICCD images, and to highlight what plume properties these considerations might be correlated with. Although the best agreement in the above tests is seen when using a Planckian emissivity, a similar result

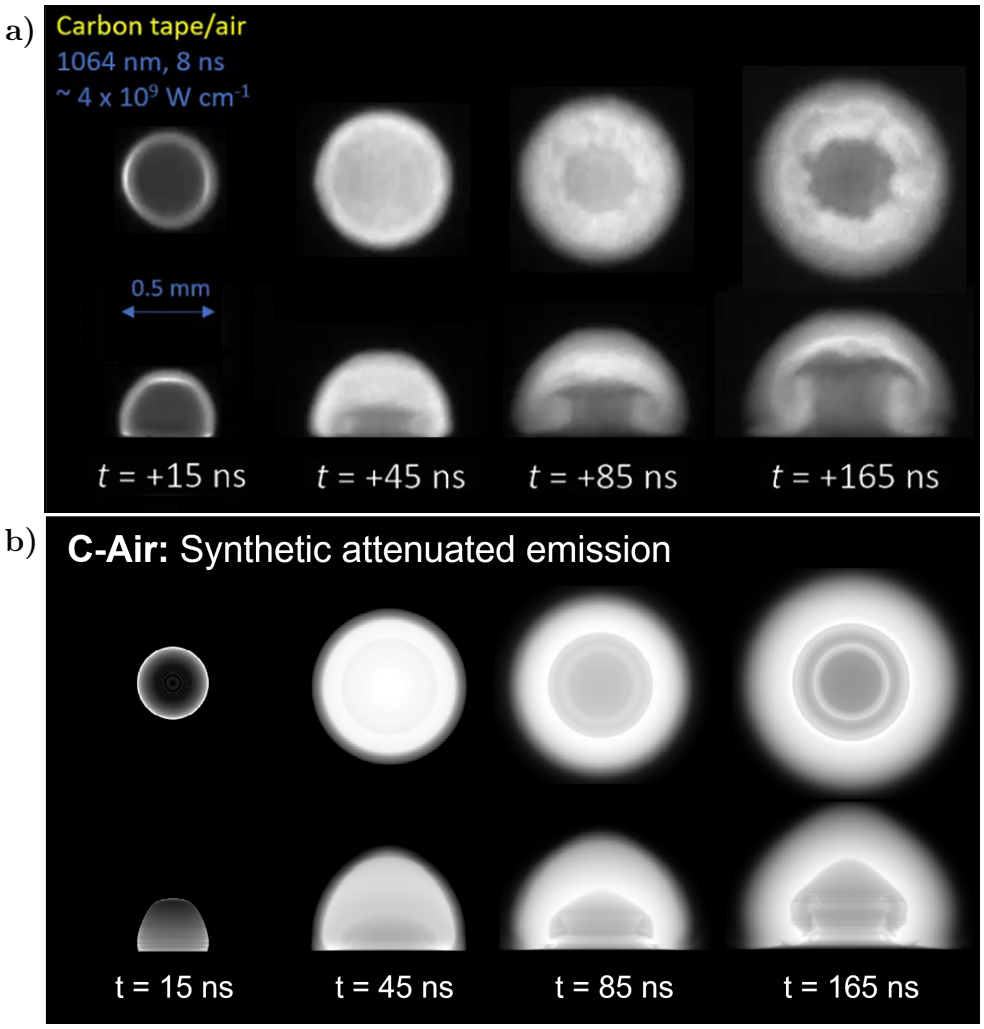

Figure 5.17: Comparison between a) experimental ICCD images and b) simulated synthetic depth-integrated emission maps for carbon ablation in air. The simulated images are generated using a Planck function emissivity with IONMIX calculated Planck mean absorption coefficients summed over 20 photon energy groups in the visible range. The emissivity and absorption coefficients are also reduced by an order of magnitude for the carbon regions only. The same spatial scale is used for both the ICCD images and simulation results.

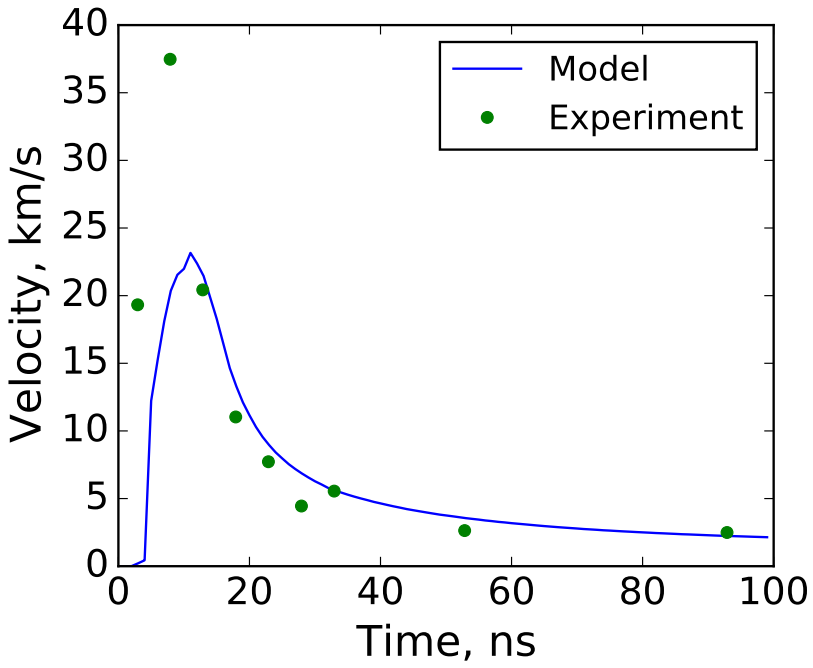

Figure 5.18: Comparison of modeled and measured shock front velocity for aluminum ablation.

may be produced by opacities calculated using a more robust non-hydrogenic collisional-radiative model rather than IONMIX.

In addition to the qualitative ICCD image comparisons, we have also compared time-of-flight measurements for the shock front velocity with the modeled result, as shown in Figure 5.18. The plot shows fairly good agreement between model and experiment, with the largest discrepancies occurring at the earliest times where the measurement uncertainty is greatest. Note that the plotted velocity is the expansion rate of the outer plume edge rather than the maximum velocity. As previously shown in Figure 5.13, the outer air plume edge decelerates faster than the inner material plume, such that the maximum velocity is found along the inner material plume edge after ~30 ns. This behavior can also be observed in both the 2D model plots and the ICCD images, where the inner material region expands faster than the surrounding air region. In fact, later time (μs) ICCD images also show that the material region eventually expands past the furthest extent of the air plasma region,

further confirming this behavior.

To summarize, good agreement is found between the model and experiments regarding the shape and expansion rate of the outer plume edge, as well as the formation, shape, and expansion rate of inner plume features for carbon ablation. However, the experimentally observed differences in plume dynamics between pure aluminum and carbon targets were found to not be captured by the current radiation hydrodynamics model. The two most likely sources of this discrepancy are the simplified laser ray tracing and deposition model, which does not account for material reflectivity, and the exclusion of mixed-phase effects, such as phase explosion due to material superheating. Nevertheless, the current aluminum ablation model may still provide an adequate estimate of ablation dynamics for targets that are unpolished and/or have an oxide layer. We have also demonstrated how optical effects contribute to the appearance of the observed experimental emission maps, and improved the model-experiment agreement further in doing so. Overall, while some discrepancies with experiments remain, the model presents a substantial improvement in predictive capability over the purely hydrodynamic model.

5.3.3 Coupled radiation hydrodynamics and reactive CFD modeling

In Subsection 3.2.1, we mentioned the wealth of aluminum ablation imaging studies found in literature. Among these works, several are focused in particular on resolving the plasma chemistry and/or molecular formation in aluminum ablation plumes [61–63]. Furthermore, these studies use similar fluences and pulse widths as the experiments modeled above and are also performed in standard air. The availability of this data presents an opportunity to extend our modeling analysis towards studying the chemistry of aluminum ablation plumes over μs-timescales. This is accomplished by coupling the above radiation hydrodynamics model to the reactive CFD model discussed earlier in this chapter.

As previously mentioned in Subsection 3.2.5, the choice of the coupling time point must be made with consideration for how closely the solution at that point follows an ideal gas LTE behavior. At the same time, the difference in the meshing methodologies and resolution must also be kept in mind. Here, we start the Fluent simulation from the end of the FLASH simulation presented in the previous section by picking 120 ns as the coupling time. Picking an earlier time point, such as 50 ns, was found to produce stronger numerical discontinuities in the Fluent solution, and was therefore avoided. This is likely at least in part due to the relatively coarse mesh used in the Fluent solution, which may have difficulty resolving the finer shock front features of earlier time points. Similarly, using the 120 ns solution results in some numerical discontinuities due to the model differences previously discussed in Subsection 3.2.5 (such as inclusion of molecules in Fluent). Additionally, in order to avoid transferring non-gaseous zones to Fluent, the FLASH solution is vertically offset by 260 μm prior to interpolating onto the Fluent mesh. This eliminates both the solid Al target regions as well as liquid Al zones near the target/plume interface.

As with the other Fluent simulations, a quarter-circle (5×5 mm) computational domain is used (previously shown in Figure 3.5), although it lacks the elliptical crater region of the purely hydrodynamic simulations. The fixed nonuniform mesh features around 135,000 cells, with face lengths ranging from a micron near the origin to 30 microns along the outer domain edge. The Fluent simulation solves the reactive Navier-Stokes equations and uses the multicomponent formulation for calculating the species diffusion coefficients. A timestep of 1 ns is used and the solution is advanced out to 10 μs.

The reaction mechanism used in the Fluent model is based on a reduced air plasma reaction mechanism [147], an aluminum oxide formation mechanism [162], and several electron-impact ionization cross sections [148]. The three-body electron recombination rates are calculated using equilibrium coefficients (i.e. Saha recombination) by expressing ionization processes as reversible reactions. As aluminum oxide formation is the focus here, the full reaction mechanism for Al_xO_y generation was used, whereas only a few dominant reactions

Table 5.1: Reduced reaction mechanism used in Fluent for the aluminum ablation plasma chemistry.

No.	Reaction	A (cm^3/s)[a]	n (-)	E_A/R (K)	Ref.
1	$e^- + Al \rightleftharpoons e^- + e^- + Al^+$		$\sigma(T)$[b]		[148]
2	$e^- + N \rightleftharpoons e^- + e^- + N^+$		$\sigma(T)$[b]		[148]
3	$e^- + O \rightleftharpoons e^- + e^- + O^+$		$\sigma(T)$[b]		[148]
4	$e^- + Al^+ \rightleftharpoons e^- + e^- + Al^{+2}$		$\sigma(T)$[b]		[148]
5	$e^- + N^+ \rightleftharpoons e^- + e^- + N^{+2}$		$\sigma(T)$[b]		[148]
6	$e^- + O^+ \rightleftharpoons e^- + e^- + O^{+2}$		$\sigma(T)$[b]		[148]
7	$Al + O + M \rightleftharpoons AlO + M$	8.272E−31	−1.0	0.0000E+00	[162]
	Third-body enhancement coefficient(s): $O_2 = 1.1$				
8	$Al + O_2 \rightleftharpoons AlO + O$	3.836E−11	0.17	0.0000E+00	[162]
9	$AlO + O_2 \rightleftharpoons AlO_2 + O$	1.182E−11	0.5	1.3150E+04	[162]
10	$Al_2O \rightleftharpoons AlO + Al$	1.000E+15	0.0	6.7036E+04	[162]
11	$Al_2O_3 \rightleftharpoons Al_2O_2 + O$	3.000E+15	0.0	4.9144E+04	[162]
12	$Al_2O_3 \rightleftharpoons AlO_2 + AlO$	3.000E+15	0.0	6.3915E+04	[162]
13	$AlO_2(+M) \rightleftharpoons AlO + O(+M)$	1.000E+15	0.0	4.4565E+04	[162]
	Low pressure limit	1.513E−11	0.5	4.7710E+04	
	Troe parameters: 0.5E0, 1.000E−30, 1.000E+30				
14	$Al_2O_2(+M) \rightleftharpoons AlO + AlO(+M)$	1.000E+15	0.0	5.9336E+04	[162]
	Low pressure limit	1.827E−11	0.0	6.2670E+04	
	Troe parameters: 0.5E0, 1.000E−30, 1.000E+30				
15	$Al_2O_2(+M) \rightleftharpoons Al + AlO_2(+M)$	1.000E+15	0.0	7.4937E+04	[162]
	Low pressure limit	1.827E−11	0.5	7.5682E+04	
	Troe parameters: 0.5E0, 1.000E−30, 1.000E+30				
16	$Al_2O_2(+M) \rightleftharpoons Al_2O + O(+M)$	1.000E+15	0.0	5.2466E+04	[162]
	Low pressure limit	1.827E−11	0.5	5.9132E+04	
	Troe parameters: 0.5E0, 1.000E−30, 1.000E+30				
17	$N_2 + M \rightleftharpoons N + N + M$	1.162E−02	−1.6	1.1320E+05	[147]
	Third-body enhancement coefficient(s): $N, N^+, O, O^+ = 4.28$				
18	$N_2 + e^- \rightleftharpoons N + N + e^-$	1.162E+01	−1.6	1.1320E+05	[147]
19	$N_2 + O \rightleftharpoons N + NO$	1.063E−06	−1.0	3.8370E+04	[147]
20	$NO + M \rightleftharpoons N + O + M$	8.303E−09	0.0	7.5500E+04	[147]
	Third-body enhancement coefficient(s): $N, N^+, O, O^+ = 20$				
21	$NO + O \rightleftharpoons N + O_2$	1.395E−11	0.0	1.9450E+04	[147]
22	$O^+ + NO \rightleftharpoons N^+ + O_2$	2.325E−19	1.9	1.5300E+04	[147]
23	$O_2 + M \rightleftharpoons O + O + M$	3.321E−03	−1.5	5.9500E+04	[147]
	Third-body enhancement coefficient(s): $N, N^+, O, O^+ = 5$				

[a] 1/s and cm^6/s for single and three–body reactions, respectively.
[b] calculated from electron-impact cross sections integrated over Maxwellian EEDF.

were kept from the air plasma mechanism. Furthermore, air was approximated as a mixture of N_2 and O_2 only, which reduces the number of species and reactions that must be considered. In total, the reaction mechanism consists of 18 species and 23 reversible reactions.

As before, we begin by first looking at the fluid moments of the coupled model solution, starting with the plume centerline profiles shown in Figure 5.19. The early time profiles (up to 520 ns) show numerous internal shocks being generated and propagated inside the plume, as signified by the appearance of additional peaks in the temperature, pressure, and velocity profiles. While internal shocks are also present in the FLASH solution, they are amplified by the discrepancies in the meshes, physical models, and solver strategies used by the two coupled codes. As will be shown later, the net effect is that these shocks induce additional convective transport that distorts the shape of the ablated aluminum regions in the plume. These internal shocks are also likely responsible for the observed compression of the leading shock between 120 and 170 ns, which increases the pressure and mass density at the plume front. Nevertheless, these perturbations relax over the first few hundred ns of the solution and are almost entirely damped out by 1 μs, as the second plot in Figure 5.19 shows. One notable feature of the plume expansion at these later timescales is the increasing separation of the leading shock from the plume front. This is evident by the low temperature (< 2500 K) region between the plasma edge and the shock front that grows and cools as the simulation progresses. As will be shown later, the low temperatures in this wake region allows molecular recombination of air to take place. Thereafter, the shock front diminishes in magnitude as the expansion continues and eventually leaves the domain around 4.5 μs. No numerical reflection waves associated with the shock front leaving the domain are observed. The plume itself also cools significantly by 5 μs, appearing to saturate at around 7500 K with an increasingly uniform temperature profile. Lastly, the velocity profiles continue to peak in the inner plume regions, following the trend of the aluminum plasma "filling out" the surrounding air plume.

Next, we examine the normalized temperature maps of the ablation plume shown in

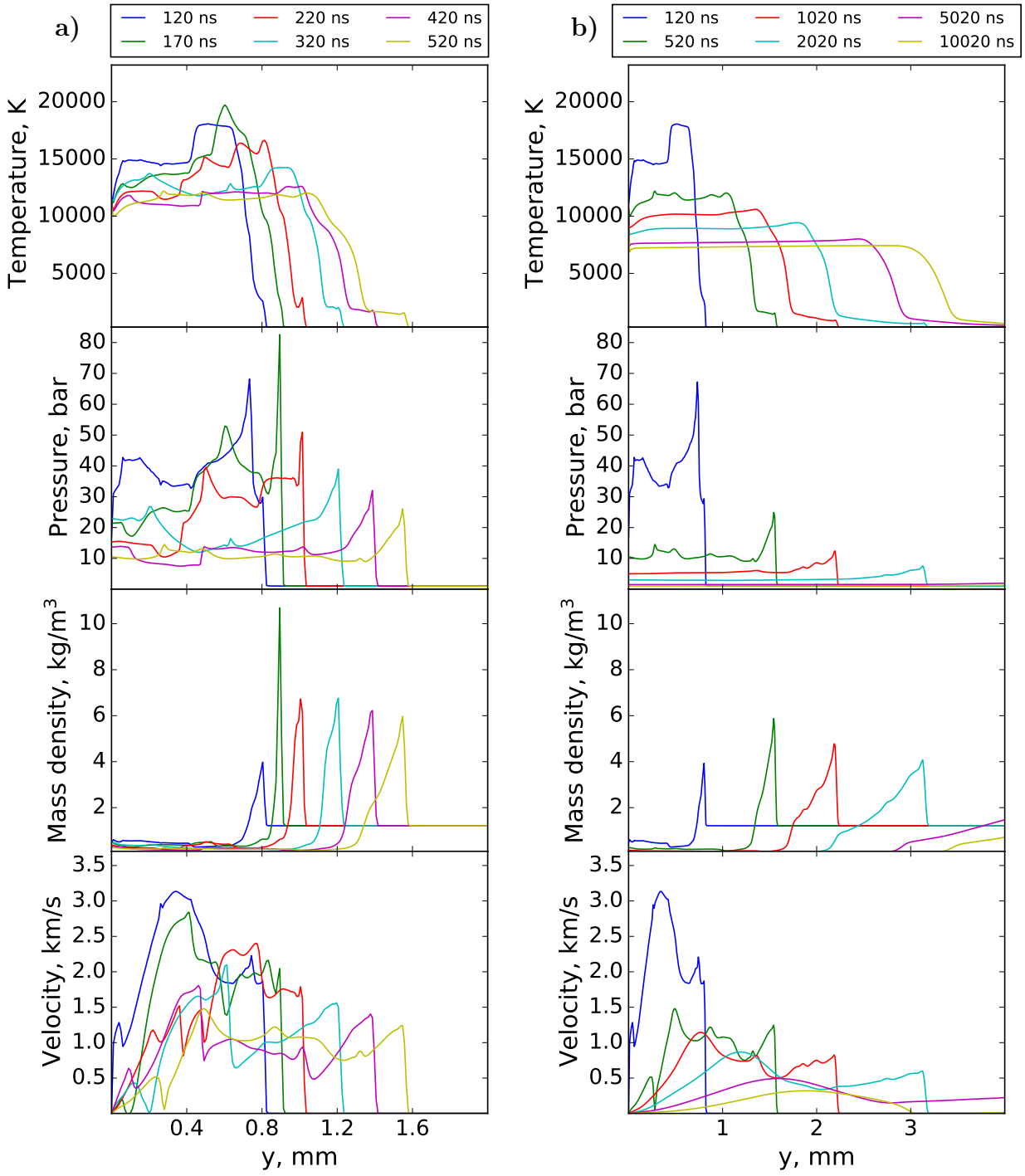

Figure 5.19: Temperature, pressure, mass density, and velocity profiles along the plume centerline in the coupled aluminum ablation model up to a) 520 ns and b) 10020 ns.

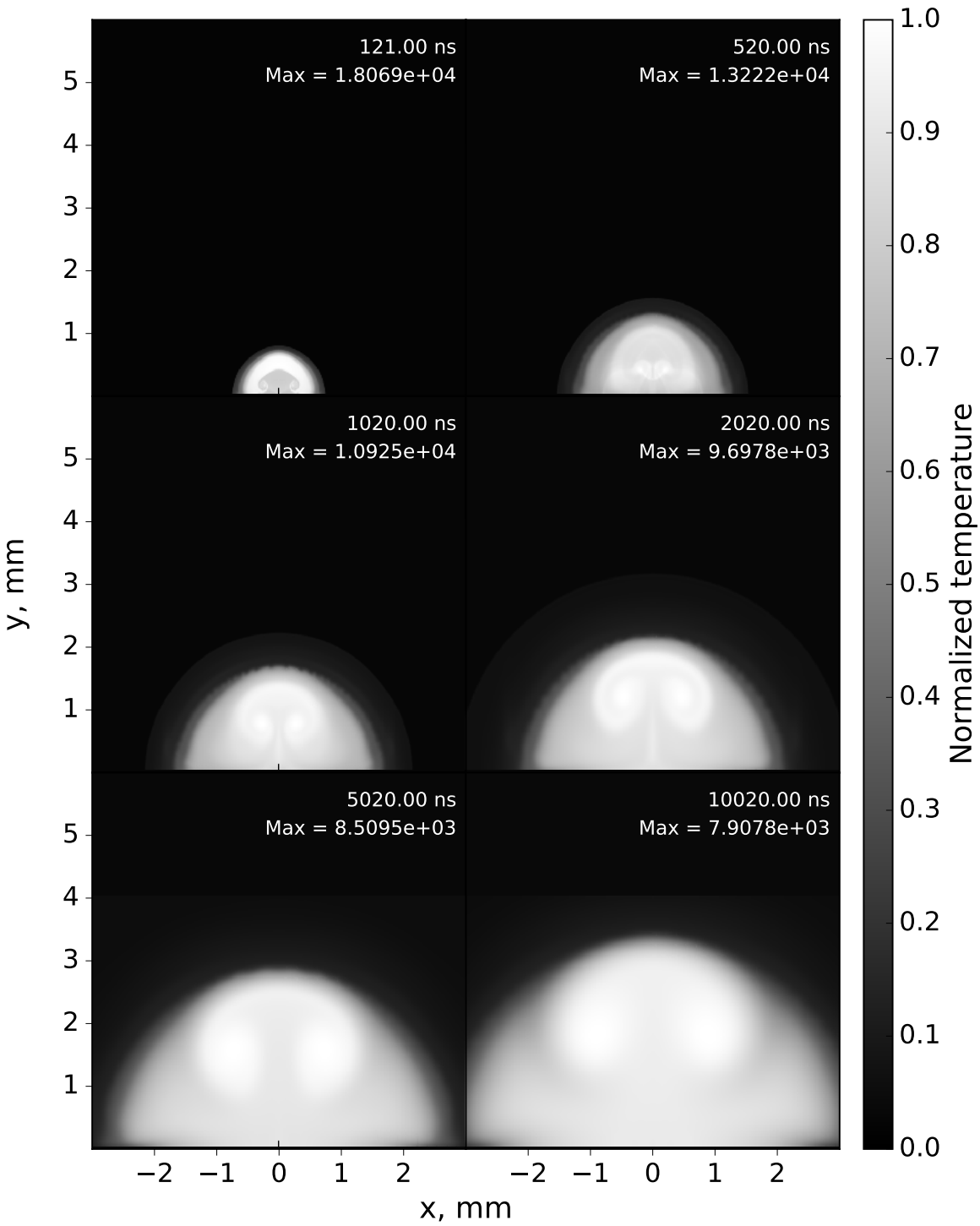

Figure 5.20: Normalized plume temperature maps in the coupled aluminum ablation model up to 10 μs.

Figure 5.20. As seen in the centerline profiles, the plume temperature tends towards a more uniform distribution over the course of the μs expansion. Nevertheless, a hotter region corresponding to the location of the ablated aluminum persists over the expansion. Note that initially (i.e. 120 ns) the ablated aluminum is cooler than the surrounding air plasma, but this trend is reversed by 1 μs. This may be in part due to differences in the internal energy available for heat release via electron recombination in the aluminum and air regions. Initially, the aluminum region is more ionized ($\bar{Z} \approx 0.7$) than the surrounding air plasma ($\bar{Z} < 0.3$), due to the lower ionization potential of aluminum (5.99 eV) compared to oxygen (13.62 eV) and nitrogen (14.53 eV). While this also means that electron recombination is less exothermic for aluminum, it may nevertheless contribute to a slower cooling rate in the aluminum regions if recombination is more rapid there. The differences in recombination rates for various plume regions will be discussed in greater detail further below. Regardless, the continued expansion of the plume coupled with internal mixing and diffusion results in a gradual equilibration between the aluminum and air regions from 1 to 10 μs. Over this time, the temperature difference between the two regions shrinks from being on the order of 1000-2000 K to that of only a few 100 K. Lastly, we once again note that this hotter aluminum region is transported past the outer plume edge over this time period. This can be more clearly seen by plotting the distribution of species concentrations inside the plume.

Figure 5.21 shows additive color plots of the normalized neutral Al, O, and N concentrations in the ablation plume. Here, each species concentration map is normalized separately with respect to its own maximum before being overlaid together to produce the plot. This plot supports many of the observations made above with regard to the temperature maps. Namely, that the later time (>1 μs) high temperature regions correspond to the location of the ablated aluminum, which continuously expands in the surrounding air plasma. Here, we clearly see the shrinking distance between the leading edges of the aluminum and air plasmas, with the aluminum plasma advancing into the plume edge after 5 μs. As will be discussed, the cooler temperatures in this edge region combined with the abundance of

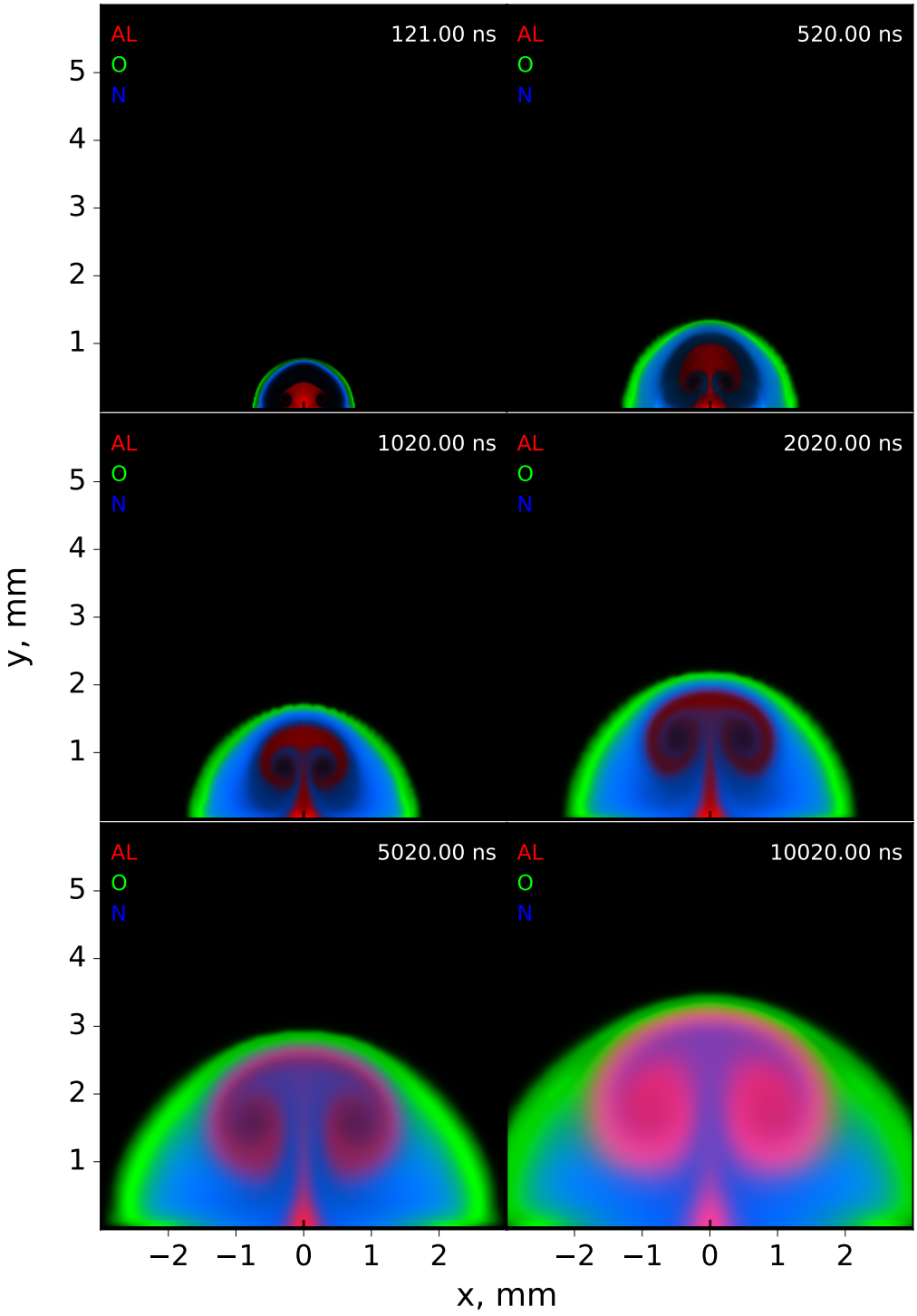

Figure 5.21: Additive color plots of normalized neutral Al, O, and N number densities in the coupled aluminum ablation model demonstrating the aluminum plasma expanding inside the surrounding air plume up to 10 μs.

atomic oxygen there leads to aluminum oxide formation.

Although the ablated aluminum region maintains a "mushroom"-like shape throughout the simulation, the final aluminum distribution is noticeably different from the initial one. In the first microsecond, the air plasma is transported inward into the aluminum plume, compressing the middle of the aluminum plasma while also pushing it upward. This produces a final distribution that is densest near the target surface as well as in the outer "cap" region, where inward convection is evident. Although this follows the trends observed in the FLASH model, the shape is likely further perturbed by the propagation of internal shocks in the first 500 ns, as the changes are most drastic over this time period.

A few additional points about the chemistry and transport of the air plume regions can also be noted from these plots. For example, the separation between the regions most abundant in O and N can be explained by the higher bond energy of N_2 compared to O_2. The temperatures in the region of high O density are not high enough to effectively dissociate N_2, meaning that the gas there consists primarily of N_2 and O. The concentration of N atoms instead peaks closer to the plume core, where the temperatures are high enough to dissociate N_2. We can also see the increase in N density over time in these inner regions due to electron recombination. The effect of diffusive transport on the species populations also becomes apparent over time, as evidenced by the mixing of Al and N between 5 and 10 μs. Lastly, we note that at these later times, atomic oxygen is observed to appear along the target surface under the air plasma. This may be due to inward convection of cool air at the intersection between the outer plume edge and the target surface, which is then heated by the plasma such that O_2 dissociation occurs. However, as no vaporized aluminum is present in this region, AlO formation there does not take place.

To analyze the chemical kinetics of the coupled model in more detail, the plume center-line species number density profiles are plotted in Figure 5.22. The 121 ns species profiles demonstrate several of the previous discussion points. Namely, that the aluminum region is initially more ionized than the surrounding air plasma and that molecular dissociation

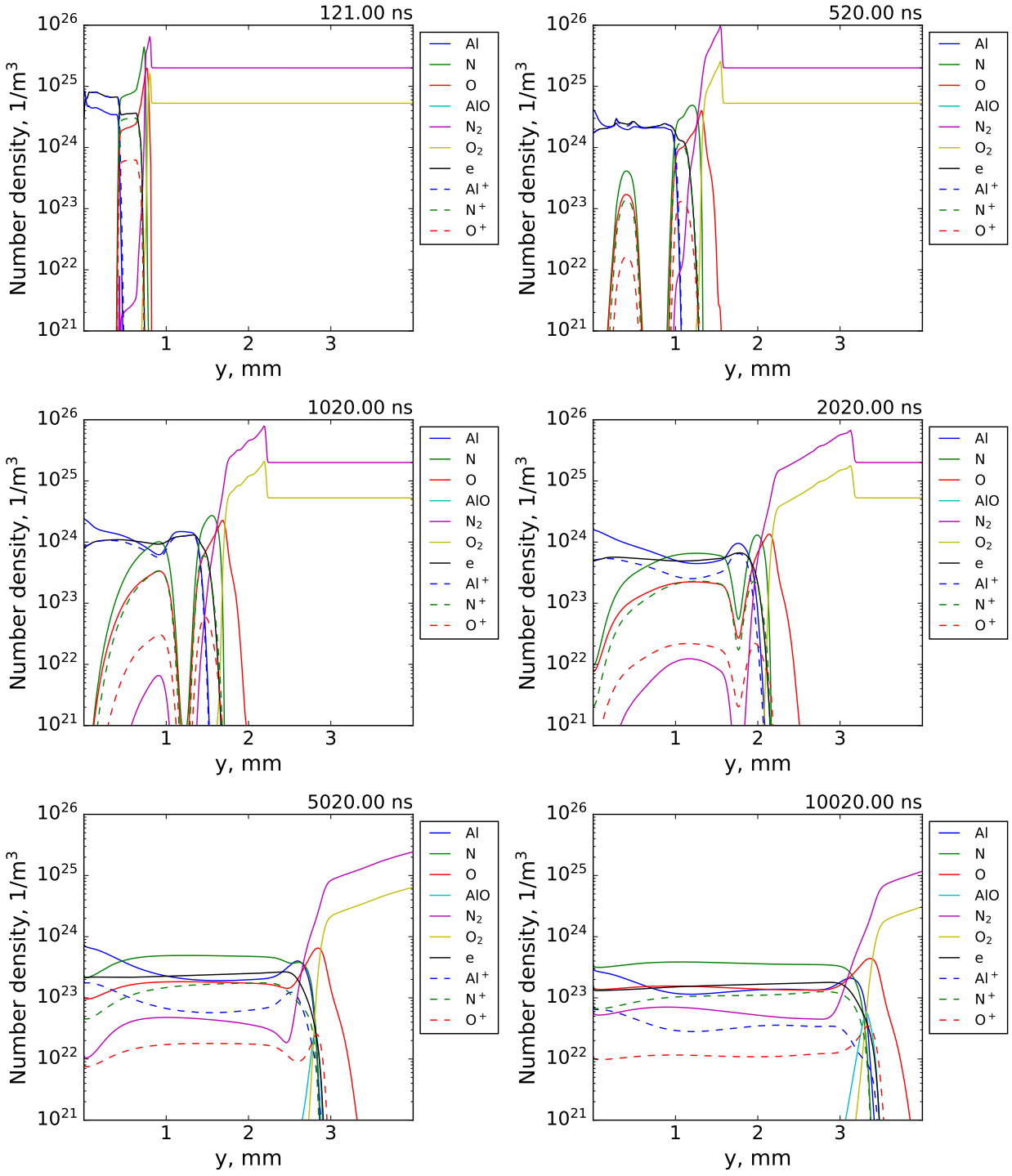

Figure 5.22: Species number density profiles along the plume centerline in the coupled aluminum ablation model up to 10 μs.

of N_2 peaks closer to the plume core than that of O_2. Focusing on the plasma chemistry, we see that recombination drives the Al ionization fraction below 50% by 1 μs and below $\sim 20\%$ after 5 μs. This is approximately in line with the equilibrium ionization fractions at these temperatures, suggesting that the ionization/recombination timescales for aluminum are shorter than the fluid transport timescales. This does not appear to be the case for the air species, which appear to be recombining much slower than aluminum. This is particularly evident for nitrogen, which has an ionization fraction of 20% after 5 μs, far from the equilibrium values of $< 1\%$ for $T < 9000$ K. This behavior is driven by differences in the electron-impact ionization cross sections for these species. These cross sections determine both the ionization and recombination timescales due to the reversible formulation used for these reactions, as listed in Table 5.1. While this guarantees that species are driven towards a Saha ionization balance, the exponential decrease in ionization rates for low temperatures accordingly lowers the recombination rates. Therefore, while the ionization balance is moving towards equilibrium, the timescale of equilibration may be underestimated. Ideally, the recombination rates should be validated in order to ensure that the plasma chemistry in the plume proceeds at the expected pace.

Shifting attention towards molecular formation, we note the appearance of AlO at the plume edge after 5 μs. This corresponds to the arrival of the ablated aluminum to the cool O-rich outer plume region, as previously pointed out in Figure 5.21. The formation of AlO at this intersection continues as the aluminum plasma moves further outward, as conveyed by the broader higher density AlO region at 10 μs. Although not pictured, higher oxides (i.e. AlO_2 and Al_2O) also begin forming here, albeit in small quantities ($AlO/Al_xO_y > 100$). Note that while both atomic oxygen and aluminum are available elsewhere in the plume, the high temperatures (>7000 K) in these regions prevent molecular formation from taking place.

Lastly, we again generate synthetic emission maps from the model results in order to perform a more direct comparison with experimental imaging. However, since the focus

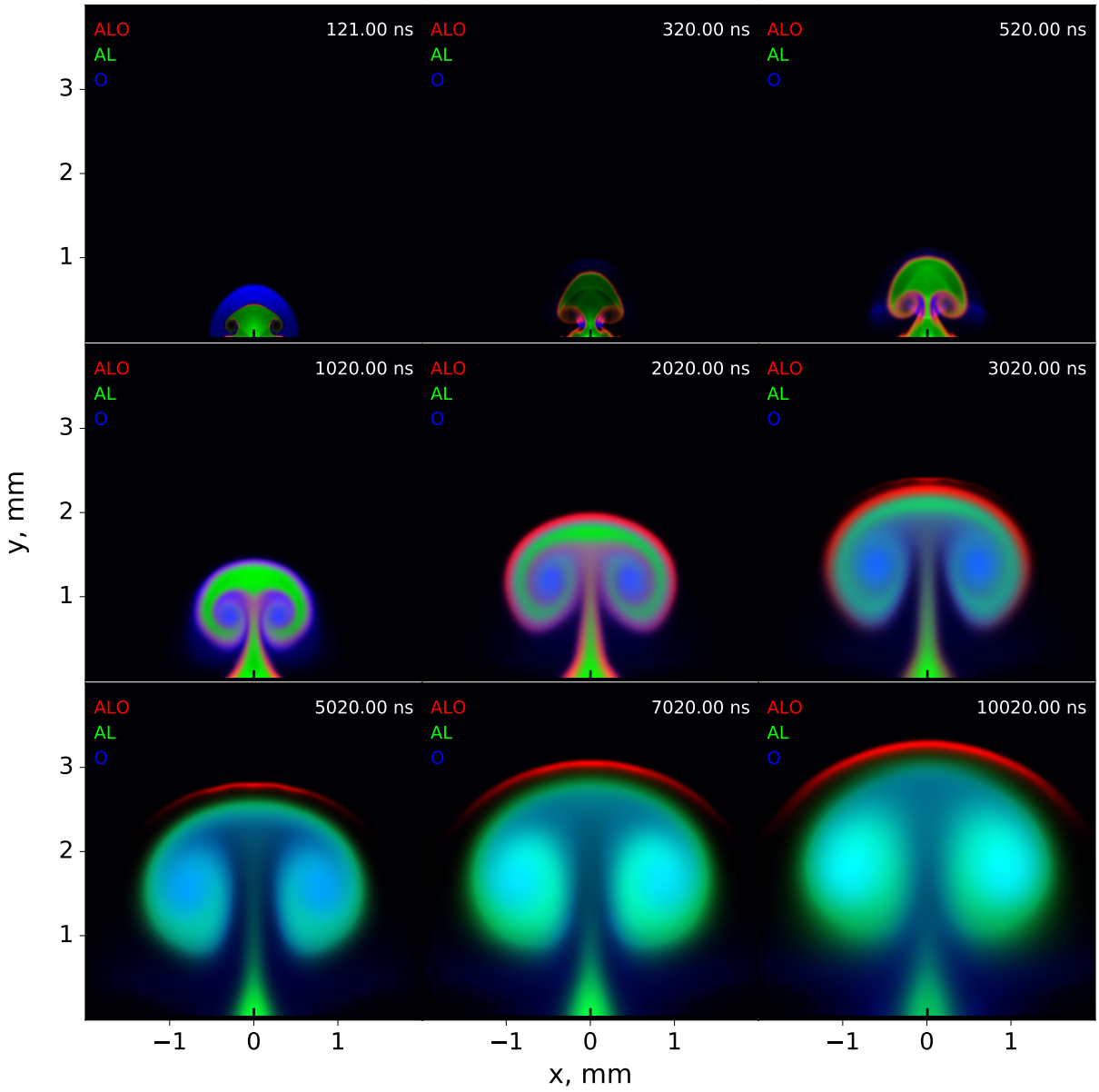

Figure 5.23: Additive color plots of the normalized synthetic emission intensity maps for O (777.194 nm), Al (394.4 nm and 396.152 nm), and AlO ($B^2\Sigma^+ \rightarrow X^2\Sigma^+$ 0–0 band head, 484.2 nm) in the coupled aluminum ablation model. No depth-wise integration of the emission signals is performed here.

here is on the chemical composition of the plume, the required synthetic diagnostics differ from those of Subsection 5.3.2. Instead of analyzing emission across all wavelengths in the visible spectrum, we can target select emission lines for each species of interest. Following literature imaging experiments [61–63], we model emission intensities from the 777.194 nm line of O I ($^5P_3 \rightarrow {}^5S^o_2$) [27], the 394.4 nm and 396.152 nm lines of Al I ($^2S_{1/2} \rightarrow {}^2P^o_{1/2}$ and $^2S_{1/2} \rightarrow {}^2P^o_{3/2}$) [27], and the 484.2 nm 0–0 head of the $B^2\Sigma^+ \rightarrow X^2\Sigma^+$ AlO band [34]. The resulting normalized 2D emission maps are visualized using additive color plots in Figure 5.23. Unlike in the previous section, no depth-wise integration of the emission signal is done here. Among the above imaging studies, the synthetic diagnostics utilized here most closely follow the imaging methodology of Ran and colleagues [62]. Since the pulse parameters used here differ from the literature studies cited above and since the imaging therein only resolves course plume features, we will limit our discussion to qualitative comparisons.

The synthetic emission maps for the first 520 ns show little beyond what has been previously discussed. Note that oxygen emission is hard to see in these early images due to normalization with respect to dense regions generated by internal shocks. Another artifact of the normalization process is the misleading appearance of AlO emission around the aluminum plasma in the first 2 μs. While some AlO does form in these regions, it does so in quantities insufficient to produce a detectable signal (due to negligible concentration). Nevertheless, the evolution of the emitting Al and O regions at these times is meaningful, and falls in line with our previous observations. As seen in the 1D species profiles, AlO begins forming strongly along the leading edge of the aluminum plasma after 5 μs. The AlO region subsequently grows as the aluminum plasma continues to expand into the cool oxygen-rich plume edge up to 10 μs. Emission in the core of the plume remains dominated by O and Al over this entire period, again due to temperatures unfavorable for molecular formation (>7000 K). This behavior mostly agrees well with the imaging done by Ran and colleagues [62], with the largest discrepancy being the lack of AlO formation along the target surface. AlO formation in this region is also observed in the works of Harilal [61] and Mat-

sumoto [63]. In the current model, temperatures in this region remain too high to form AlO, although the previously mentioned transport of cool air from the edge of the plume near the target surface may change this at later times. This discrepancy may be driven by the vertical offset applied to the FLASH solution in the coupling procedure. While this offset prevents liquid aluminum zones from being transferred to the Fluent model, it also removes some of the cooler aluminum vapor near the target surface that might otherwise react to form AlO. Lastly, we note that the AlO imaging of Matsumoto and colleagues [63] also suggests a "mushroom"-like shape for the aluminum ablation plume that is in line with the current model. Overall, the coupled simulation approach shows reasonable qualitative agreement with available AlO imaging studies and could potentially be used to inform quantitative model-experiment validation in the future.

5.4 Discussion

Here, we have examined a one-way coupled radiation-hydrodynamics and reactive CFD modeling approach as a method for studying chemical kinetics of laser ablated plumes. The plume expansion and chemical evolution predicted by the coupled model is in reasonable agreement with available ICCD images, although a few areas of potential refinement are apparent. Nevertheless, the coupled model presents a substantial improvement in predictive capability over the purely hydrodynamic models previously used to study uranium ablation. We have also demonstrated how synthetic diagnostics can be used to bridge the gap between modeled and experimental results. This has been done by calculating synthetic emission or absorption signals from the simulated plume profiles and performing spatial and/or temporal integration to match the experimental acquisition process. Combining these synthetic diagnostics with a validated ablation model provides a promising avenue for performing a detailed characterization of UO_x chemical kinetics in the future.

A major area of future study for the radiation-hydrodynamics ablation model is capturing

the differences in the observed inner plume features for carbon and aluminum targets. More broadly, these differences appear to be driven at least partially by the target reflectivity, which are not treated by the Snell's law ray tracing used in the current rad-hydro model. Using an updated ray tracing algorithm that allows for partial reflection via ray splitting calculated according to Fresnel's equations could elucidate the role of reflectivity on the plume shape. As we have also mentioned, the inclusion of mixed-phase effects, such as phase explosion, may also help explain the observed discrepancies in plume dynamics. Lastly, the synthetic emission calculation could be improved in the future by using more accurate opacity coefficients, which are unreliable in the current model due to the use of hydrogenic approximations.

Above, we have also outlined two short-term areas of improvement for the coupled modelling approach. First, the electron ionization/recombination reactions should be re-examined to ensure that accurate recombination timescales are captured for all species in the ablation plume. Second, the coupling along the target-plume interface should be refined to more accurately treat the inward convective transport of ambient air to this region. Long-term improvements may include minimizing the initial numerical shocks produced by the model coupling and performing a detailed synthetic emission study akin to that of the radiation-hydrodynamics subsection. In addition, extending the microsecond treatment to include turbulence may be important, as high-fidelity ICCD images reveal an increasingly asymmetric plume over these timescales.

Chapter 6

Conclusion

In this work, we have produced an updated UO_x reaction mechanism and constructed a coupled modeling approach for informing chemical kinetic studies of laser ablation experiments. The UO_x reaction mechanism was obtained by performing a Monte Carlo Genetic Algorithm (MCGA) optimization constrained by emission measurements from a plasma flow reactor (PFR). The final ablation model involved coupling of a radiation hydrodynamics and a reactive CFD model, allowing for a treatment of both the initial laser energy deposition and ns timescale expansion along with the subsequent detailed chemical evolution and multi-species diffusion over μs timescales. Both the MCGA and laser ablation efforts have made extensive use of synthetic diagnostics to perform comparisons between model and experiment outputs.

The MCGA reaction mechanism optimization begins with a review of the U and UO emission spectra collected from the PFR. For these spectra, measurement errors of less than 5% were found throughout the upstream portion of the reactor, with values generally increasing further downstream, at most reaching 20%. Additional sources of uncertainty were identified due to the strong thermal U_xO_y background and the insufficient spectral resolution for resolving the rovibrational peaks of the UO band. The emission data used for constraining the optimization was shown to cover both the upstream and downstream regions of the PFR by switching between two configurations for the system. In these datasets, oxygen flow rates and temperature conditions were varied to provide additional constraints. In modeling the emission produced by the PFR, several Lagrangian temperature histories produced by a CFD simulation were examined. These profiles were then used to run a 0D chemical

kinetic model using a previously constructed UO_x reaction mechanism. A representative temperature profile was then chosen according to available temperature measurements and the modeled UO emission trends. Here, we also noted the sensitivity of the 0D model to the temperature history used, and highlighted this as one area of future improvement. Finally, the UO_x reaction channels targeted for optimization were selected based on the available constraining data and supplemented by approximate rates for unconstrained reactions.

The MCGA optimization is initiated with the Monte Carlo sampling step using the above data and model parameters. The exploration of the problem parameter space by the sampling demonstrates difficulties in fitting certain features of the constraining datasets. Among these is an apparent saturation of the U emission signal towards a near constant value in the downstream portion of the flow and limited fitting of the upstream UO decay. The former is hypothesized to be caused by scattering of strong upstream U emission while the latter to be caused by the approximate temperature profile used. In light of these observations, two objective functions are selected to be used in the Genetic Algorithm, differing only in the inclusion of the downstream U signal as a constraining factor. Furthermore, a penalty term is included in both objective functions to account for the approximate range of U to UO intensity ratios observed in experiments. The Genetic Algorithm step is then performed by optimizing the best fitting mechanisms produced by the MC sampling for both objective functions. Across all optimizations, the current GA implementation is found to improve fitness most drastically over the first 100 generations, slowly converging to an optimal value thereafter. The optimal reaction mechanisms are found to be consistently dominated by 4 reaction channels, with remaining channels either being entirely eliminated or playing a secondary role in the chemical evolution of the system. Due to its relative abundance in the system, OH is found to be a major source of oxygen for the uranium molecules, whereas O_2 channels are effectively eliminated. This points to the need for including hydrogen fugacity as an additional parameter varied within the experimental datasets. Lastly, as the saturating behavior of U in the downstream region is not found to be well fitted by any mechanisms,

it is not used as a constraint for selecting the final optimized reaction mechanism.

Finally, the optimal MCGA generated UO_x reaction mechanism is compared against the previously constructed unoptimized mechanism. While some similarities are found between overlapping reaction channels, the optimized reaction mechanism in general predicts rate coefficients that are 2-4 orders of magnitude lower than previously employed hard sphere estimates. Owing to the importance of OH in the PFR, a direct comparison cannot be made for many reaction channels, as reactions with OH were not considered in the unoptimized mechanism. Nevertheless, a recommendation for an updated set of rate coefficients is made based on the general trends observed for the overlapping reaction channels. Improvement of the MCGA optimization is pointed out to rely on reducing the various sources of uncertainty in the current approach. These include resolving the crowded UO_x spectrum, obtaining accurate partition functions and transition probabilities for U species, obtaining a larger set of constraining data covering a wider range of conditions, and improving the 0D treatment of the PFR.

The laser ablation portion of the work begins with an evaluation of a previously used reactive CFD model for agreement with emission and absorption measurements for uranium ablation. Here, we highlight the importance of utilizing synthetic diagnostics to provide a direct comparison between simulations and experiments. While some agreement is found for both an emission-based oxygen fugacity study and absorption-based number density measurements, a better understanding of the plume dynamics is sought to improve the model confidence. To this end, we perform a validation of the ablation model using high-fidelity plume imaging for well-characterized ablation materials (carbon and aluminum). In doing so, the agreement between the fluid model and experimental imaging and expansion velocities is found to be partial, at best. This, combined with the need for adjusting initial model parameters in accordance with experiment, motivates the search for a more predictive ablation model.

Next, we evaluated a radiation hydrodynamics model as a potential refinement on the

experimentally calibrated purely hydrodynamic approach. The radiation hydrodynamics model captures the initial laser energy deposition within the absorption skin depth of the target material and the subsequent shock-producing expansion into the ambient atmosphere. The rapid heating and ionization of the ambient air by the propagating shock produces a hot, dense, highly absorbing air plasma along the shock front. This region is found to effectively shield the ablated material from the incident laser after the midpoint of the pulse. This description is consistent with a laser-supported detonation wave common to ablation using IR wavelength ns duration laser pulses. A series of synthetic emission maps were then calculated based on the plume properties (temperatures and densities) and approximate material opacities. These synthetic plume images display a progression from a mostly opaque plume with a thin bright outline to an opaque "mushroom"- like shape growing within an expanding bright hemispherical region. The opaque inner region at these later times is found to correspond to the ablated material, while the surrounding bright region denotes an air plasma generated by the initial shock and heated by the incident laser. This evolution is found to be in good agreement with experimental plume imaging for carbon targets. However, drastic differences in the observed inner plume features for aluminum targets are not captured by the current model. This discrepancy is preliminarily attributed to either material reflectivity effects or mixed-phase explosive boiling. Lastly, a comparison with time-of-flight measurements of the plume expansion velocities is also found to show generally good agreement.

The above model is then coupled to a reactive CFD model and evolved up to microsecond timescales. Over this timeframe, the plume is observed to continue cooling to temperatures below 1 eV, but remaining too hot for molecular formation to take place within the inner plume region. However, AlO formation becomes apparent along the top outer plume edge at later times. This molecular formation is found to occur due to the continued outer transport of the ablated aluminum within the surrounding air plasma, which introduces aluminum into a cool outer air region abundant in O atoms. In addition, while some convective transport

of cool air under the plume is observed, it is not rapid enough to form AlO there over the duration of the simulation. These qualitative observations are in partial agreement with various experimental imaging studies. The strongest points of agreement are the approximate times at which AlO begins forming in the plume, the location of the molecular formation along the outer plume edge, and the "mushroom"-like shape of the ablated material region. The main discrepancy lies in the lack of AlO formation along the target-plume interface, which is attributed to an offset made in the coupling procedure to avoid transferring liquid regions into the CFD model.

6.1 Future work

As areas of potential improvement for the current modeling and experimental approaches have already been detailed in Sections 4.5 and 5.4, here we will instead focus on future extensions of the work. For example, as motivated in the introduction, a broader range of debris formation processes can be considered by coupling the molecular formation modeling of this work to a particle formation and growth model. As ex-situ particle collection is relatively straightforward in both the PFR and laser ablation systems, this can provide an additional source of constraining information regarding the chemical kinetics of UO_x. Of course, modeling the particle formation processes is far from trivial and also introduces an additional share of uncertainties when considering the structure and properties of U_xO_y molecular clusters. The coupling between the chemical kinetic and particle formation processes can also be potentially challenging, although convenient implementations expressing particle processes as equivalent reaction channels exist [163]. Due to the computational expense of solving these additional conservation equations, such an extensions is most plausible for a 0D treatment of the PFR.

Another natural extension of the current work is to validate the MCGA-optimized UO_x reaction mechanism over a wider range of detonation-relevant conditions by incorporating it

into a laser ablation model. To accomplish this, a procedure similar to Section 5.3 could be followed, wherein the early-time plume dynamics are validated prior to tackling the problem of μs timescale plume chemistry. As discussed there, the availability of reliable material properties for uranium poses one potential challenge for performing such an analysis. Since the current coupled ablation model has been limited to low-Z materials, there may also be additional complications when treating ablation of high-Z materials. For example, the much larger mass discrepancy between the ablated material and ambient air could affect the evolution of plume dynamics due to momentum transfer differences. Lastly, such an investigation could also shed light on the effects of an oxide layer on the uranium laser ablation fugacity experiments discussed in Section 5.1.

As mentioned in the introduction, the current analysis can also be extended by studying the interplay between uranium and other detonation-relevant species (such as Fe, Si, and Al) in forming oxides and debris particles. Considering the differences in oxidation kinetics, stable molecular forms, and material/transport properties for each of these species, the range of combined behaviors is likely broad and complex. Although uranium is certainly the least well-characterized material out of the above selection, validating the chemical kinetics of all the mentioned species separately for the conditions of interest would be preferred prior to considering combined effects. These effects could then be studied for both the PFR and laser ablation systems by considering mixed analyte solutions and alloy or composite/powder targets, respectively.

References

[1] Finko M S, Curreli D, Weisz D G, Crowhurst J C, Rose T P, Koroglu B, Radousky H B and Armstrong M R 2017 *J. Phys. D: Appl. Phys.* **50** 485201

[2] Freiling E C 1961 *Science* **133** 1991–1998

[3] Miller C F 1960 A theory of formation of fallout from land-surface nuclear detonations and decay of the fission products Tech. Rep. USNRDL-TR-425 U.S. Naval Radiological Defense Laboratory San Francisco, CA

[4] Freiling E C and Kay M A 1966 *Nature* **209** 236–238

[5] Crocker G R, O'Connor J D and Freiling E C 1966 *Health Phys.* **12** 1099–1104

[6] Glasstone S and Dolan P J 1977 *The Effects of Nuclear Weapons* 3rd ed (Alexandria, VA: U.S. Department of Defense)

[7] Koroglu B, Dai Z, Finko M, Armstrong M R, Crowhurst J C, Curreli D, Weisz D G, Radousky H B, Knight K B and Rose T P 2020 *Anal. Chem.* **92** 6437–6445

[8] Hartig K C, Ghebregziabher I and Jovanovic I 2017 *Sci. Rep.* **7** 1–9

[9] Hartig K C, Harilal S S, Phillips M C, Brumfield B E and Jovanovic I 2017 *Opt. Express* **25** 11477–11490

[10] Weisz D G, Crowhurst J C, Siekhaus W J, Rose T P, Koroglu B, Radousky H B, Zaug J M, Armstrong M R, Isselhardt B H, Savina M R, Azer M, Finko M S and Curreli D 2017 *Appl. Phys. Lett.* **111** 034101

[11] Harilal S S, Brumfield B E, Glumac N and Phillips M C 2018 *Opt. Express* **26** 20319–20330

[12] Skrodzki P J, Burger M, Jovanovic I, Phillips M C, Brumfield B E and Harilal S S 2018 *Opt. Lett.* **43** 5118–5121

[13] Weerakkody E N, Weisz D G, Crowhurst J, Koroglu B, Rose T, Radousky H, Stillwell R L, Jeffries J R and Glumac N G 2020 *Spectrochim. Acta B* **170** 105925

[14] Weerakkody E N and Glumac N G 2021 *J. Phys. D: Appl. Phys.* **54** 125201

[15] Koroglu B, Wagnon S, Dai Z, Crowhurst J C, Armstrong M R, Weisz D, Mehl M, Zaug J M, Radousky H B and Rose T P 2018 *Sci. Rep.* **8** 10451

[16] Zhang S, Wang X, He M, Jiang Y, Zhang B, Hang W and Huang B 2014 *Spectrochim. Acta B* **97** 13–33

[17] Finko M S and Curreli D 2018 *Phys. Plasmas* **25** 083112

[18] Koroglu B, Mehl M, Armstrong M R, Crowhurst J C, Weisz D G, Zaug J M, Dai Z, Radousky H B, Chernov A, Ramon E, Stavrou E, Knight K, Fabris A L, Cappelli M A and Rose T P 2017 *Rev. Sci. Instrum.* **88** 093506

[19] Tadi M and Yetter R A 1998 *Int. J. Chem. Kinet.* **30** 151–159

[20] Lee H S and Litzinger T A 2003 *Combust. Flame* **135** 151–169

[21] Maraun D, Horbelt W, Rust H, Timmer J, Happersberger H P and Drepper F 2004 *Int. J. Bifurc. Chaos* **14** 2081–2092

[22] Berkemeier T, Ammann M, Krieger U K, Peter T, Spichtinger P, Pöschl U, Shiraiwa M and Huisman A J 2017 *Atmos. Chem. Phys.* **17** 8021–8029

[23] Xue S, Proulx P and Boulos M I 2001 *J. Phys. D: Appl. Phys.* **34** 1897–1906

[24] Landau L D and Lifshitz E M 1959 *Statistical Physics* 2nd ed (Oxford: Pergamon Press)

[25] McQuarrie D A 1976 *Statistical Mechanics* (New York, NY: Harper & Row)

[26] Capitelli M, Colonna G and D'Angola A 2012 *Fundamental Aspects of Plasma Chemical Physics: Thermodynamics* (*Springer Series on Atomic, Optical, and Plasma Physics* vol 66) (Berlin-Heidelberg: Springer-Verlag)

[27] Kramida A, Ralchenko Y, Reader J and NIST ASD Team 2018 NIST atomic spectra database (version 5.6.1) `https://physics.nist.gov/as`

[28] Irwin A W 1987 *Astron. Astrophys.* **182** 348–358

[29] Popovas A and Jørgensen U G 2016 *Astron. Astrophys.* **595** A130

[30] Lewis G N and Merle R 1961 *Thermodynamics* 2nd ed (New York, NY: McGraw-Hill)

[31] Palmer B A, Keller R A and Engleman R 1980 An atlas of uranium emission intensities in a hollow cathode discharge Tech. Rep. LA-8251-MS Los Alamos Scientific Lab Los Alamos, NM

[32] McBride B J and Gordon S 1992 Computer program for calculating and fitting thermodynamic functions Tech. Rep. NASA-RP-1271 National Aeronautics and Space Administration Washington, D.C.

[33] Blaise J and Wyart J F Selected constants energy levels and atomic spectra of actinides `http://web2.lac.u-psud.fr/lac/Database/Contents.html`

[34] Huber K P and Herzberg G 1979 *Molecular Spectra and Molecular Structure* (Boston, MA: Springer)

[35] Heaven M C, Nicolai J P, Riley S J and Parks E K 1958 *Chem. Phys. Lett.* **119** 229–233

[36] Kaledin L A, McCord J E and Heaven M C 1994 *J. Mol. Spectrosc.* **164** 27–65

[37] Kaledin L A and Heaven M C 1997 *J. Mol. Spectrosc.* **185** 1–7

[38] Konings R J M, Beneš O, Kovács A, Manara D, Sedmidubský D, Gorokhov L, Iorish V S, Yungman V, Shenyavskaya E and Osina E 2014 *J. Phys. Chem. Ref. Data* **43** 013101

[39] Sauval A J and Tatum J B 1984 *Astrophys. J. Suppl. Ser.* **56** 193–209

[40] Barklem P S and Collet R 2016 *Astron. Astrophys.* **588** A96

[41] Burcat A and Ruscic B 2016 Ideal gas thermochemical database with updates from active thermochemical tables Tech. rep. Technion - Israel Institute of Technology Haifa, Israel

[42] Zaghloul M R 2004 *Phys. Rev. E* **69** 026702

[43] Hermann J, Lorusso A, Perrone A, Strafella F, Dutouquet C and Torralba B 2015 *Phys. Rev. E* **92** 053103

[44] Turanyi T 1990 *J. Math. Chem.* **5** 203–248

[45] Devoto R S 1967 *Phys. Fluids* **10** 354

[46] Devoto R S 1973 *Phys. Fluids* **16** 616

[47] Bernardi D, Colombo V, Ghedini E and Mentrelli A 2003 *Eur. Phys. J. D* **27** 55–72

[48] Punjabi S B, Barve D N, Joshi N K, Das A K, Kothari D C, Ganguli A A, Sahasrabhude S N and Joshi J B 2019 *Processes* **7** 133

[49] Bernardi D, Colombo V, Ghedini E and Mentrelli A 2003 *Eur. Phys. J. D* **22** 279–285

[50] ANSYS Inc. 2017 *ANSYS Fluent Version 18.0 Users Guide*

[51] Pancheshnyi S, Eismann B, Hagelaar G J M and Pitchford L C 2008 Computer code ZDPlasKin `http://www.zdplaskin.laplace.univ-tlse.fr`

[52] Bäuerle D 2011 *Laser Processing and Chemistry* 4th ed (Berlin-Heidelberg: Springer-Verlag)

[53] Eliezer S, Eliaz N, Grossman E, Fisher D, Gouzman I, Henis Z, Pecker S, Horovitz Y, Fraenkel M, Maman S and Lereah Y 2004 *Phys. Rev. B* **69** 144119

[54] Podagatlapalli G K, Hamad S, Sreedhar S, Tewari S P and Venugopal Rao S 2012 *Chem. Phys. Lett.* **530** 93–97

[55] Kim M, Osone S, Kim T, Higashi H and Seto T 2017 *KONA Powder Part. J.* **34** 80–90

[56] Cheung J T 1994 History and fundamentals of pulsed laser deposition *Pulsed Laser Deposition of Thin Films* ed Chrisey D B and Hubler G (New York: Wiley) pp 1–22

[57] Tognoni E, Palleschi V, Corsi M and Cristoforetti G 2002 *Spectrochim. Acta B* **57** 1115–1130

[58] Cremers D A and Radziemski L J 2013 *Handbook of Laser-Induced Breakdown Spectroscopy* 2nd ed (Chichester, UK: Wiley)

[59] Anabitarte F, Cobo A and Lopez-Higuera J M 2012 *ISRN Spectrosc.* **2012** 1–12

[60] Bai X, Cao F, Motto-Ros V, Ma Q, Chen Y and Yu J 2015 *Spectrochim. Acta B* **113** 158–166

[61] Harilal S S, Brumfield B E, Cannon B D and Phillips M C 2016 *Anal. Chem.* **88** 2296–2302

[62] Ran P, Hou H and Luo S N 2017 *J. Anal. At. Spectrom.* **32** 2254–2262

[63] Matsumoto A, Ohba H, Toshimitsu M, Akaoka K, Ruas A, Wakaida I, Sakka T and Yae S 2019 *Spectrochim. Acta B* **155** 56–60

[64] Weisz D G, Crowhurst J C, Finko M S, Rose T P, Koroglu B, Trappitsch R, Radousky H B, Siekhaus W J, Armstrong M R, Isselhardt B H, Azer M and Curreli D 2018 *J. Phys. Chem. A* **122** 1584–1591

[65] Harilal S S, Murzyn C M, Kautz E J, Edwards M K, Sinkov S I, Bisson S E, Mitra S S and Martin J B 2021 *J. Anal. At. Spectrom.* **36** 150–156

[66] Harilal S S, Freeman J, Diwakar P and Hassanein A 2014 Femtosecond laser ablation: Fundamentals and applications *Laser-Induced Breakdown Spectroscopy* (*Springer Series in Optical Sciences* vol 182) ed Musazzi S and Perini U (Berlin-Heidelberg: Springer-Verlag) 4th ed

[67] Harilal S S, Bindhu C V, Tillack M S, Najmabadi F and Gaeris A C 2003 *J. Appl. Phys.* **93** 2380–2388

[68] Harris T J 1963 *IBM J. Res. Dev.* **7** 342–344

[69] Ready J F 1963 *Appl. Phys. Lett.* **3** 11–13

[70] Bai X, Ma Q, Motto-Ros V, Yu J, Sabourdy D and Nguyen L 2013 *J. Appl. Phys.* **113** 013304

[71] Bai X, Ma Q, Perrier M, Motto-Ros V, Sabourdy D, Nguyen L, Jalocha A and Yu J 2013 *Spectrochim. Acta B* **87** 27–35

[72] Ma Q, Motto-Ros V, Bai X and Yu J 2013 *Appl. Phys. Lett.* **103** 204101

[73] Pakhal H R, Lucht R P and Laurendeau N M 2008 *Appl. Phys. B* **90** 15–27

[74] Hussein A E, Diwakar P K, Harilal S S and Hassanein A 2013 *J. Appl. Phys.* **113** 143305

[75] Thareja R K and Sharma A K 2006 *Laser Part. Beams* **24** 311–320

[76] Dawood M S, Hamdan A and Margot J 2015 *AIP Adv.* **5** 107143

[77] Diwakar P, Harilal S, Phillips M and Hassanein A 2015 *J. Appl. Phys.* **118** 043305

[78] Harilal S S, Diwakar P K, Polek M P and Phillips M C 2015 *Opt. Express* **23** 15608–15615

[79] Li X, Wei W, Wu J, Jia S and Qiu A 2013 *J. Appl. Phys.* **113** 243304

[80] Mahmood S, Rawat R S, Zakaullah M, Lin J J, Springham S V, Tan T L and Lee P 2009 *J. Phys. D.: Appl. Phys.* **42** 135504

[81] Kushwaha A and Thareja R K 2008 *Appl. Optics* **47** G65–71

[82] Al-Shboul K F, Harilal S S and Hassanein A 2011 *Appl. Phys. Lett.* **99** 131506

[83] Mościcki T, Hoffman J and Szymański Z 2018 *J. Appl. Phys.* **123** 083305

[84] Irimiciuc S A, Hodoroaba B C, Bulai G, Gurlui S and Craciun V 2020 *Spectrochim. Acta B* **165** 105774

[85] Harilal S S 2009 *J. Appl. Phys.* **102** 123306

[86] Cirisan M, Jouvard J M, Lavisse L, Hallo L and Oltra R 2011 *J. Appl. Phys.* **109** 103301

[87] Mościcki T 2016 *Int. J. Opt.* **2016** 5438721

[88] Hermann J, Axente E, Craciun V, Taleb A and Pelascini F 2018 *Spectrochim. Acta B* **143** 63–70

[89] Ma Q, Motto-Ros V, Fabrice Laye J Y, Lei W, Bai X, Zheng L and Zeng H 2012 *J. Appl. Phys.* **111** 053301

[90] Raizer Y P 1965 *Sov. Phys. JETP* **21** 1009–1017

[91] Root R G 1989 Modeling of post-breakdown phenomena *Laser-Induced Plasmas and Applications* ed Radziemski L J and Cremers D A (New York, NY: Marcel Dekker) pp 69–103

[92] Ready J F 1965 *J. Appl. Phys.* **36** 462–468

[93] Anisimov S I 1968 *Sov. Phys. JETP* **27** 182–183

[94] Knight C J 1979 *AIAA J.* **17** 519–523

[95] Gusarov A V, Gnedovets A G and Smurov I 2000 *J. Appl. Phys.* **88** 4352–4364

[96] Aghaei M, Mehrabian S and Tavassoli S H 2008 *J. Appl. Phys.* **104** 053303

[97] Mościcki T, Hoffman J and Szymański Z 2011 *Arch. Mech.* **63** 99–116

[98] Autrique D, Chen Z, Alexiades V, Bogaerts A and Rethfeld B 2012 *AIP Conf. Proc.* **1464** 648

[99] Bogaerts A, Chen Z, Gijbels R and Vertes A 2003 *Spectrochim. Acta B* **58** 1867–1893

[100] Sakai T 2009 *J. Propuls. Power* **25** 406–414

[101] Porneala C and Willis D A 2006 *Int. J. Heat Mass Transf.* **49** 1928–1936

[102] Stafe M 2012 *J. Appl. Phys.* **112** 123112

[103] Harilal S S, Miloshevsky G V, Diwakar P K, LaHaye N L and Hassanein A 2012 *Phys. Plasmas* **19** 083504

[104] Miloshevsky A, Harilal S S, Miloshevsky G V and Hassanein A 2014 *Phys. Plasmas* **21** 043111

[105] Shabanov S V and Gornushkin I B 2014 *Spectrochim. Acta B* **100** 147–172

[106] Wu B, Shin Y C, Pakhal H, Laurendeau N M and Lucht R P 2007 *Phys. Rev. E* **76** 026405

[107] Cao Y, Zhao X and Shin Y C 2013 *J. Laser Appl.* **25** 032002

[108] Keller W J, Shen N, Rubenchik A M, Ly S, Negres R, Raman R N, Yoo J H, Guss G, Stolken J S, Matthews M J and Bude J D 2019 *J. Appl. Phys.* **125** 085103

[109] Cristoforetti G, Legnaioli S, Palleschi V, Tognoni E and Benedetti P A 2008 *J. Anal. At. Spectrom.* **23** 1518–1528

[110] Thompson K W 1987 *J. Comp. Phys.* **68** 1–24

[111] Issa R I 1986 *J. Comput. Phys.* **62** 40–65

[112] Patankar S V 1980 Numerical heat transfer and fluid flow Computational and Physical Processes in Mechanics and Thermal Sciences ed Minkowycz W J and Sparrow E M (Washington, DC: Hemisphere) pp 118–120

[113] Leonard B P 1979 *Comput. Method. Appl. M.* **19** 59–98

[114] ANSYS Inc. 2017 *ANSYS Fluent Version 18.0 Theory Guide*

[115] Monchick L, Yun K S and Mason E A 1963 *J. Chem. Phys.* **39** 654–669

[116] Mazhukin V I, Nossov V V and Smurov I 2007 *J. Appl. Phys.* **101** 024922

[117] Autrique D, Alexiades V and Khanal H 2013 *Electron. J. Differ. Eq.* **20** 1–14

[118] Zhang Y, Zhang D, Wu J, He Z and Deng X 2017 *AIP Adv.* **7** 075010

[119] 2021 FLASH v4.6.2 URL `http://flash.uchicago.edu/site/flashcode/`

[120] Fryxell B, Olson K, Ricker P, Timmes F X, Zingale M, Lamb D Q, MacNeice P, Rosner R, Truran J W and Tufo H 2000 *Astrophys. J. Suppl. Ser.* **131** 273–334

[121] More R M, Warren K H, Young D A and Zimmerman G B 1988 *Phys. Fluids* **31** 3059–3078

[122] Young D A and Corey E M 1995 *J. Appl. Phys.* **78** 3748–3755

[123] MacFarlane J J 1989 *Comput. Phys. Commun.* **56** 259–278

[124] Attal N, Ramaprabhu P, Hossain J, Karkhanis V, Uddin M, Gord J and Roy S 2015 *Comput. Fluids* **107** 59–76

[125] Lemes N H T, Borges E and Braga J P 2007 *J. Braz. Chem. Soc.* **18** 1342–11347

[126] Capitelli M, Ferreira C M, Gordiets B F and Osipov A I 2000 *Plasma Kinetics in Atmospheric Gases* (*Springer Series on Atomic, Optical, and Plasma Physics* vol 31) (Berlin-Heidelberg: Springer-Verlag)

[127] Varga T, Nagy T, Olm C, Zsély I, Pálvölgyi R, Valkó É, Vincze G, Cserháti M, Curran H and Turányi T 2015 *Proc. Combust. Inst.* **35** 589–596

[128] Zhang Y, Mathieu O, Petersen E L, Bourque G and Curran H J 2017 *Combust. Flame* **182** 122–141

[129] Starikovskaia S M, Starikovskii A Y and Zatsepin D V 2001 *Combust. Theory Modelling* **5** 97–129

[130] Murakami T, Niemi K, Gans T, O'Connell D and Graham W G 2013 *Plasma Sources Sci. Technol.* **22** 015003

[131] Schröter S, Wijaikhum A, Gibson A R, West A, Davies H L, Minesi N, Dedrick J, Wagenaars E, de Oliveira N, Nahon L, Kushner M J, Booth J P, Niemi K, Gans T and O'Connell D 2018 *Phys. Chem. Chem. Phys.* **20** 24263–24286

[132] Huang Y, Risha G A, Yang V and Yetter R A 2009 *Combust. Flame* **156** 5–13

[133] Carr R W 2007 Modeling of chemical reactions *Comprehensive Chemical Kinetics* vol 42 ed Carr R W (Amsterdam, Netherlands: Elsevier) pp 43–99

[134] Doidge P S 1995 *Spectrochim. Acta B.* **50** 209–263

[135] Elliott L, Ingham D B, Kyne A G, Mera N S, Pourkashanian M and Wilson C W 2004 *Prog. Energy Combust. Sci.* **30** 297–328

[136] Sikalo N, Hasemann O, Schulz C, Kempf A and Wlokas I 2015 *Int. J. Chem. Kinet.* **47** 695–723

[137] Cantú-Paz E 1997 A survey of parallel genetic algorithms Tech. Rep. 97003 University of Illinois at Urbana-Champaign Champaign, IL

[138] Kautz E J, Weerakkody E N, Finko M S, Curreli D, Koroglu B, Rose T P, Weisz D G, Crowhurst J C, Radousky H B, DeMagistris M, Sinha N, Levin D A, Dreizin E L, Phillips M C, Glumac N G and Harilal S S 2021 *Spectrochim. Acta B* **185** 106283

[139] Fite W L, Lo H H and Irving P 1974 *J. Chem. Phys.* **60** 1236–1250

[140] Mandal P K, Das R C, Seema A U, Sahoo A C, Shah M L, Pulhani A K, Manohar K G and Dev V 2014 *Appl. Phys. B* **116** 407–413

[141] Tyagi R, Zhang Z and Pitzer R M 2014 *J. Phys. Chem. A.* **118** 11758

[142] Zeng X L, Huang S Q and Ju X H 2013 *J. Radioanal. Nucl. Chem.* **298** 481–484

[143] Catoire L, Legendre J F and Giraud M 2003 *J. Propul. Power* **19** 196–202

[144] Hong M H, Lu Y F and Bong S K 2000 *Appl. Surf. Sci.* **154** 196–200

[145] Mihalas D and Mihalas B W 1984 *Foundations of radiation hydrodynamics* (Berlin-Heidelberg: Oxford University Press)

[146] Laroussi M 1995 *Int. J. Infrared Milli.* **16** 2069–2083

[147] Martin A, Cozmuta I, Wright M J and Boyd I D 2015 *J. Thermophys. Heat Tr.* **29** 222–238

[148] Lennon M A, Bell K L, Gilbody H B, Hughes J G, Kingston A E, Murray M J and Smith F J 1988 *J. Phys. Chem. Ref. Data* **17** 1285–1363

[149] Kaiser T B 2000 *Phys. Rev. E* **61** 895–905

[150] Basko M M and Tsygvintsev I P 2017 *Comput. Phys. Commun.* **214** 59–70

[151] Martynyuk M M 1977 *Combust. Explos. Shock Waves* **13** 178–191

[152] Bulgakova N M and Bulgakov A V 2001 *Appl. Phys. A* **73** 199–208

[153] Porneala C and Willis D A 2006 *Appl. Phys. Lett.* **89** 211121

[154] Porneala C and Willis D A 2009 *J. Phys. D.: Appl. Phys.* **42** 155503

[155] Hoffman J, Chrzanowska J, Kucharski S, Moscicki T, Mihailescu I N, Ristoscu C and Szymanski Z 2014 *Appl. Phys. A* **117** 395–400

[156] Yoo J H, Jeong S H, Greif R and Russo R E 2000 *J. Appl. Phys.* **88** 1638–1649

[157] Pakhomov A V, Thompson M S and Gregory D A 2003 *J. Phys. D.: Appl. Phys.* **36** 2067–2075

[158] Gragossian A, Tavassoli S H and Shokri B 2009 *J. Appl. Phys.* **105** 103304

[159] Lutey A H A 2013 *J. Appl. Phys.* **114** 083108

[160] Stapleton M, McKiernan A and Mosniera J 2005 *J. Appl. Phys.* **97** 064904

[161] Autrique D, Gornushkin I, Alexiades V, Chen Z, Bogaerts A and Rethfeld B 2013 *Appl. Phys. Lett.* **103** 174102

[162] Starik A M, Savel'eva A M and Titova N S 2015 *Combust. Explos. Shock Waves* **51** 197–222

[163] Pope C J and Howard J B 1997 *Aerosol Sci. Tech.* **27** 73–94

[164] Flitti A and Pancheshnyi S 2009 *Eur. Phys. J. Appl. Phys.* **45** 21001

[165] Carbone E, Graef W, Hagelaar G, Boer D, Hopkins M, Stephens J, Yee B, Pancheshnyi S, van Dijk J and Pitchford L 2021 *Atoms* **9** 16

[166] Itikawa Y and Mason N 2005 *J. Phys. Chem. Ref. Data* **34** 1–22

[167] Phelps A V and Pitchford L C 1985 *Phys. Rev. A* **31** 2932–2949

[168] Phelps A V 1985 Tabulations of collision cross sections and calculated transport and reaction coefficients for electron collisions with o_2 Tech. Rep. 28 JILA Information Center Boulder, CO

[169] Morgan W LXCat: Morgan database `https://lxcat.net/Morgan` retrieved on March 19, 2020

[170] Laher R R and Gilmore F R 1990 *J. Phys. Chem. Ref. Data* **19** 277–305

[171] Hayashi M 1979 *J. Phys., Colloq.* **40** C7/45–C7/46

[172] Yamabe C, Buckman S J and Phelps A V 1983 *Phys. Rev.* **27** 1345–1352

[173] Itikawa Y 2006 *J. Phys. Chem. Ref. Data* **35** 31–53

[174] Itikawa Y 2009 *J. Phys. Chem. Ref. Data* **38** 1–20

[175] Marques L, Jolly J and Alves L L 2007 *J. Appl. Phys.* **102** 063305

[176] Riahi R, Teulet P, Ben Lakhdar Z and Gleizes A 2006 *Eur. Phys. J. D* **40** 223–230

[177] Itikawa Y 2016 *J. Phys. Chem. Ref. Data* **45** 033106

[178] Hayashi M LXCat: Hayashi database `https://lxcat.net/Hayashi` retrieved on March 19, 2020

[179] Tennyson J and Brown D LXCat: QUANTEMOL database `https://lxcat.net/QUANTEMOL` retrieved on March 19, 2020

[180] Itikawa Y and Ichimura A 1990 *J. Phys. Chem. Ref. Data* **19** 637–651

[181] Biagi S F LXCat: Biagi database `https://lxcat.net/Biagi` retrieved on March 19, 2020

[182] Kossyi I A, Kostinsky A Y, Matveyev A A and Silakov V P 1992 *Plasma Sources Sci. Technol.* **1** 207–220

[183] Nandi D, Krishnakumar E, Rosa A, Schmidt W F and Illenberger E 2003 *Chem. Phys. Lett.* **373** 454–459

[184] Janev R K, Langer W D, Evans Jr K and Post Jr D E 1987 *Elementary Processes in Hydrogen-Helium Plasmas: Cross Sections and Reaction Rate Coefficients* (Berlin: Springer-Verlag)

[185] Deutsch H, Becker K, Probst M, Zhu W and Märk T D 2008 *Int. J. Mass Spectrom.* **277** 151–154

[186] Pedersen H B, Djuric N, Jensen M J, Kella D, Safvan C P, Schmidt H T, Vejby-Christensen L and Andersen L H 1999 *Phys. Rev. A: At., Mol., Opt. Phys.* **60** 2882–2899

[187] Guerra V L, Sá P A and Loureiro J 2004 *Eur. Phys. J. Appl. Phys.* **28** 125–152

[188] Gordiets B F, Ferreira C M, Guerra V L, Loureiro J, Nahorny J, Pagnon D, Touzeau M and Vialle M 1995 *IEEE Trans. Plasma Sci.* **23** 750–768

Appendix A

Full O-H-N reaction mechanism

Here, the full list of reactions used to model the O-H-N background plasma chemistry in the plasma flow reactor (PFR) is tabulated. This reaction mechanism is based on the N-O plasma chemical reaction mechanism of Flitti and Pancheshnyi [164] included with ZDPlasKin [51], which is in turn based on the work of Capitelli and colleagues [126]. These N-O channels are supplemented here by several additional neutral [127,128] and plasma [129–131] reaction pathways for O-H-N species. Cross sections for electron-impact reactions in the mechanism were retrieved primarily from the LXCat database [165]. The rate coefficients for these reactions were obtained by integrating the cross sections over a Maxwellian electron energy distribution function (EEDF) and fitting the resulting rates for $T_e \leq 1$ eV. This was done primarily to speed up the 0D PFR model, which assumes a Maxwellian LTE plasma.

Table A.1: Full O-H-N reaction mechanism.

No.	Reaction	A (cm^3/s)[a]	n (-)	E_A (K)	Ref.
	Zeldovich Mechanism				
1[b]	$N + O_2 \rightleftharpoons NO + O$	1.500×10^{-14}	1.000	3269.9	[128]
2[b]	$N + NO \rightleftharpoons N_2 + O$	1.873×10^{-11}	0.140	0.0	[128]
3[b]	$N + OH \rightleftharpoons NO + H$	6.310×10^{-11}	0.000	0.0	[128]
	NO_2 sub-mechanism				
4[b]	$NO + O(+M) \rightleftharpoons NO_2(+M)$	2.159×10^{-9}	−0.750	0.0	[128]
	Low pressure limit	2.603×10^{-23}	−2.870	780.5	
	Troe parameters: 0.962, 10.0, 7962				
5[b]	$NO_2 + H \rightleftharpoons NO + OH$	2.507×10^{-10}	0.000	182.2	[128]
6[b]	$NO_2 + O \rightleftharpoons NO + O_2$	1.744×10^{-10}	−0.520	0.0	[128]
7[b]	$NO + HO_2 \rightleftharpoons NO_2 + OH$	3.487×10^{-12}	0.000	−250.1	[128]
8	$NO_2 + HO_2 \rightleftharpoons HNO_2 + O_2$	3.072×10^{-23}	3.260	2507.5	[128]
9	$NO_2 + HO_2 \rightleftharpoons HONO + O_2$	3.172×10^{-24}	3.320	1531.8	[128]

Table A.1: (Continued)

No.	Reaction	A (cm^3/s)[a]	n (-)	E_A (K)	Ref.
10[b]	$NO_2 + NO_2 \rightleftharpoons NO_3 + NO$	1.594×10^{-14}	0.730	10517.0	[128]
11	$NO_2 + H_2 \rightleftharpoons HNO_2 + H$	3.969×10^{-22}	3.150	15633.0	[128]
12	$NO_2 + H_2 \rightleftharpoons HONO + H$	1.918×10^{-24}	3.890	13074.0	[128]
13[b]	$NO_2 + NO_2 \rightleftharpoons NO + NO + O_2$	7.472×10^{-12}	0.000	13888.0	[128]
	N_2O sub-mechanism				
14	$N_2O(+M) \rightleftharpoons N_2 + O(+M)$	1.690×10^{11}	0.000	29012.0	[128]
	Low pressure limit	1.196×10^{-9}	0.000	28890.0	
	M: $O_2 = 1.4$, $N_2 = 1.7$, $H_2O = 12.0$, NO = 3.0, $N_2O = 3.5$				
15	$N_2O + H \rightleftharpoons N_2 + OH$	1.063×10^{-16}	1.840	6789.4	[128]
16	$NH + NO \rightleftharpoons N_2O + H$	2.989×10^{-10}	−0.350	−122.8	[128]
17	$N_2O + H \rightleftharpoons N_2 + OH*$	2.657×10^{-10}	0.000	25312.0	[128]
18	$N_2O + O \rightleftharpoons N_2 + O_2$	6.127×10^{-12}	0.000	8019.3	[128]
19	$N_2O + O \rightleftharpoons NO + NO$	1.519×10^{-10}	0.000	13929.0	[128]
20	$N_2O + OH \rightleftharpoons N_2 + HO_2$	2.159×10^{-26}	4.720	18398.0	[128]
21	$N_2O + OH \rightleftharpoons HNO + NO$	1.993×10^{-28}	4.330	12621.0	[128]
22	$N_2O + NO \rightleftharpoons NO_2 + N_2$	8.801×10^{-19}	2.230	23290.0	[128]
23	$N_2O + H_2 \rightleftharpoons N_2 + H_2O$	3.487×10^{-10}	0.000	16355.0	[128]
	NO_3 sub-mechanism				
24[b]	$NO_2 + O(+M) \rightleftharpoons NO_3(+M)$	5.812×10^{-12}	0.240	0.0	[128]
	Low pressure limit	6.894×10^{-28}	−1.500	0.0	
	Troe parameters: 0.71, 1E−30, 1700, 1E30				
25[b]	$NO_3 + H \rightleftharpoons NO_2 + OH$	9.963×10^{-11}	0.000	0.0	[128]
26[b]	$NO_3 + O \rightleftharpoons NO_2 + O_2$	1.661×10^{-11}	0.000	0.0	[128]
27[b]	$NO_3 + OH \rightleftharpoons NO_2 + HO_2$	2.325×10^{-11}	0.000	0.0	[128]
28[b]	$NO_3 + HO_2 \rightleftharpoons NO_2 + O_2 + OH$	2.491×10^{-12}	0.000	0.0	[128]
29[b]	$NO_3 + NO_2 \rightleftharpoons NO + NO_2 + O_2$	8.303×10^{-14}	0.000	1479.5	[128]
	HNO sub-mechanism				
30	$NO + H(+M) \rightleftharpoons HNO(+M)$	2.491×10^{-9}	−0.410	0.0	[128]
	Low pressure limit	1.103×10^{-27}	−1.750	0.0	
	Troe parameters: 0.82, 1.0E−30, 1.0E30, 1.0E30				
	M: $H_2 = 2.0$, $H_2O = 10.0$, Ar = 0.75, $O_2 = 1.5$				
31	$HNO + H \rightleftharpoons NO + H_2$	7.306×10^{-13}	0.720	327.1	[128]
32	$HNO + O \rightleftharpoons NO + OH$	3.819×10^{-11}	0.000	0.0	[128]
33	$HNO + OH \rightleftharpoons NO + H_2O$	5.978×10^{-11}	0.000	0.0	[128]
34	$HNO + NO_2 \rightleftharpoons NO + HONO$	7.340×10^{-20}	2.640	2033.0	[128]
35	$HNO + HNO \rightleftharpoons N_2O + H_2O$	1.494×10^{-15}	0.000	1560.0	[128]
	HON sub-mechanism				
36	$HON + M \rightleftharpoons NO + H + M$	8.469×10^{-5}	−1.730	8074.2	[128]
37	$HON + H \rightleftharpoons HNO + H$	3.985×10^{-11}	0.000	0.0	[128]
38	$HON + H \rightleftharpoons NH + OH$	1.661×10^{-11}	0.000	0.0	[128]
39	$HON + O \rightleftharpoons NO + OH$	1.162×10^{-10}	0.000	0.0	[128]

Table A.1: (Continued)

No.	Reaction	A (cm^3/s)[a]	n (-)	E_A (K)	Ref.
40	$HON + OH \rightleftharpoons HONO + H$	6.642×10^{-11}	0.000	0.0	[128]
41	$HON + O_2 \rightleftharpoons NO_2 + OH$	1.661×10^{-12}	0.000	2500.0	[128]
	HONO sub-mechanism				
42	$NO + OH(+M) \rightleftharpoons HONO(+M)$	1.827×10^{-10}	−0.300	0.0	[128]
	Low pressure limit	6.535×10^{-25}	−2.400	0.0	
	Troe parameters: 0.81, 1.0E−30, 1.0E30, 1.0E30				
43	$HONO + H \rightleftharpoons HNO + OH$	9.365×10^{-14}	0.860	2516.1	[128]
44	$HONO + H \rightleftharpoons NO + H_2O$	1.348×10^{-17}	1.890	1937.4	[128]
45	$HONO + O \rightleftharpoons NO_2 + OH$	1.993×10^{-11}	0.000	2999.2	[128]
46	$HONO + OH \rightleftharpoons NO_2 + H_2O$	1.411×10^{-12}	0.000	−260.2	[128]
47	$HONO + NO_2 \rightleftharpoons HONO_2 + NO$	3.321×10^{-13}	0.000	16455.0	[128]
48	$HONO + HONO \rightleftharpoons NO_2 + NO + H_2O$	5.795×10^{-25}	3.640	6109.1	[128]
	HNO_2 sub-mechanism				
49	$HNO_2(+M) \rightleftharpoons HONO(+M)$	2.500×10^{14}	0.000	16254.0	[128]
	Low pressure limit	4.151×10^{-10}	0.000	15851.0	
	Troe parameters: 1.149, 1.0E−30, 3125, 1.0E30				
50	$HNO_2 + O \rightleftharpoons NO_2 + OH$	2.823×10^{-16}	1.500	1006.4	[128]
51	$HNO_2 + OH \rightleftharpoons NO_2 + H_2O$	6.642×10^{-11}	0.000	0.0	[128]
	$HONO_2/HNO_3$ sub-mechanism				
52	$NO_2 + OH(+M) \rightleftharpoons HONO_2(+M)$	2.707×10^{-11}	0.000	0.0	[128]
	Low pressure limit	8.631×10^{-23}	−3.000	0.0	
	Troe parameters: 0.14, 1.0E−30, 1.0E30, 1.0E30				
53	$HONO_2 + H \rightleftharpoons HONO + OH$	6.343×10^{-19}	2.300	3510.5	[128]
54	$HONO_2 + H \rightleftharpoons NO_2 + H_2O$	1.010×10^{-22}	3.300	3162.7	[128]
55	$HONO_2 + H \rightleftharpoons NO_3 + H_2$	9.233×10^{-16}	1.500	8252.8	[128]
56	$HONO_2 + OH \rightleftharpoons NO_3 + H_2O$	1.710×10^{-14}	0.000	−624.0	[128]
57	$HNO_3 + H \rightleftharpoons HONO + OH$	6.343×10^{-19}	2.300	3510.5	[128]
58	$HNO_3 + H \rightleftharpoons NO_2 + H_2O$	1.010×10^{-22}	3.300	3162.7	[128]
59	$HNO_3 + H \rightleftharpoons NO_3 + H_2$	9.233×10^{-16}	1.500	8252.8	[128]
60	$HNO_3 + OH \rightleftharpoons NO_3 + H_2O$	1.710×10^{-14}	0.000	−624.0	[128]
	H_2-O_2 sub-mechanism				
61[b]	$H + O_2 \rightleftharpoons O + OH$	2.289×10^{-11}	0.243	3656.1	[127]
62[b]	$O + H_2 \rightleftharpoons H + OH$	4.493×10^{-20}	2.750	1614.2	[127]
63[b]	$OH + H_2 \rightleftharpoons H + H_2O$	3.627×10^{-17}	1.803	811.4	[127]
64[b]	$OH + OH \rightleftharpoons O + H_2O$	5.716×10^{-20}	2.296	−888.0	[127]
65[b]	$H + H + M \rightleftharpoons H_2 + M$	5.906×10^{-29}	−1.478	67.1	[127]
	M: $H_2 = 2.5$, $H_2O = 12$				
66[b]	$O + O + M \rightleftharpoons O_2 + M$	1.700×10^{-32}	−0.500	0.0	[127]
	M: $H_2 = 2.5$, $H_2O = 12$, Ar = 0.83				
67[b]	$O + H + M \rightleftharpoons OH + M$	1.300×10^{-29}	−1.000	0.0	[127]
	M: $H_2 = 2.5$, $H_2O = 12$, Ar = 0.75				

Table A.1: (Continued)

No.	Reaction	A (cm^3/s)[a]	n (-)	E_A (K)	Ref.
68[b]	$H + OH + M \rightleftharpoons H_2O + M$	3.640×10^{-24}	−2.600	−28.6	[127]
	M: H_2 = 2.5, H_2O = 12, Ar = 0.38				
69[b]	$H + O_2(+M) \rightleftharpoons HO_2(+M)$	7.722×10^{-12}	0.440	0.0	[127]
	Low pressure limit	5.168×10^{-29}	−1.239	0.0	
	Troe parameters: 6.700E−01, 1.0E−30, 1.0E+30, 1.0E+30				
	M: H_2 = 1.4837, H_2O = 12.034, Ar = 0.5396				
70[b]	$H + HO_2 \rightleftharpoons H_2 + O_2$	1.893×10^{-14}	1.083	140.3	[127]
71[b]	$HO_2 + H \rightleftharpoons OH + OH$	1.065×10^{-10}	0.000	60.0	[127]
72[b]	$HO_2 + O \rightleftharpoons OH + O_2$	5.397×10^{-11}	0.000	0.0	[127]
73[b]	$HO_2 + OH \rightleftharpoons H_2O + O_2$	4.858×10^{-16}	1.441	−543.6	[127]
74[b]	$HO_2 + HO_2 \rightleftharpoons H_2O_2 + O_2$	2.159×10^{-13}	0.000	−412.8	[127]
		2.055×10^{-10}	0.000	2643.5	
75[b]	$OH + OH(+M) \rightleftharpoons H_2O_2(+M)$	3.567×10^{-19}	2.322	−861.7	[127]
	Low pressure limit	5.405×10^{-33}	−0.203	−1094.3	
	Troe parameters: 4.300E−01, 1.0E−30, 1.0E+30, 1.0E+30				
	M: H_2O = 5., Ar = 0.67, O_2 = 0.8, H_2O_2 = 5.13, H_2 = 2.47				
76[b]	$H_2O_2 + H \rightleftharpoons H_2O + OH$	4.002×10^{-11}	0.000	1005.4	[127]
77[b]	$H_2O_2 + H \rightleftharpoons H_2 + HO_2$	5.380×10^{-7}	−1.249	1880.8	[127]
78[b]	$H_2O_2 + O \rightleftharpoons OH + HO_2$	1.586×10^{-17}	2.000	1005.4	[127]
79[b]	$H_2O_2 + OH \rightleftharpoons H_2O + HO_2$	2.889×10^{-12}	0.000	80.5	[127]
		1.260×10^{-10}	0.000	1840.9	
80	$H + O + M \rightleftharpoons OH* + M$	4.136×10^{-35}	0.000	1513.2	[127]
	M: H_2 = 1., H_2O = 6.5, O_2 = 0.4, N_2 = 0.4, Ar = 0.35				
81	$OH* + H_2O \rightleftharpoons OH + H_2O$	9.847×10^{-12}	0.500	−217.8	[127]
82	$OH* + H_2 \rightleftharpoons OH + H_2$	4.899×10^{-12}	0.500	−112.4	[127]
83	$OH* + N_2 \rightleftharpoons OH + N_2$	1.793×10^{-13}	0.500	−314.5	[127]
84	$OH* + OH \rightleftharpoons OH + OH$	9.980×10^{-12}	0.500	−193.5	[127]
85	$OH* + H \rightleftharpoons OH + H$	2.175×10^{-12}	0.500	−42.3	[127]
86	$OH* + Ar \rightleftharpoons OH + Ar$	2.806×10^{-12}	0.000	1047.2	[127]
87	$OH* + O_2 \rightleftharpoons OH + O_2$	3.487×10^{-12}	0.500	−121.1	[127]
	Rotational excitation and relaxation by electron impact				
88[b,c]	$e^- + H_2O \rightarrow e^- + H_2O(r_0)$	2.359×10^{-4}	−0.805	128.4	[166]
89[b,c]	$e^- + H_2O \rightarrow e^- + H_2O(r_1)$	1.053×10^{-5}	−0.297	129.5	[166]
90[b,c]	$e^- + H_2O \rightarrow e^- + H_2O(r_2)$	1.527×10^{-7}	−0.254	0.0	[166]
91[b,c]	$e^- + H_2O \rightarrow e^- + H_2O(r_3)$	1.231×10^{-7}	−0.396	264.1	[166]
92[b,c]	$e^- + H_2O(r_0) \rightarrow e^- + H_2O$	2.359×10^{-4}	−0.805	128.4	[166]
93[b,c]	$e^- + H_2O(r_1) \rightarrow e^- + H_2O$	6.366×10^{-6}	−0.240	0.0	[166]
94[b,c]	$e^- + H_2O(r_2) \rightarrow e^- + H_2O$	2.985×10^{-7}	−0.328	59.4	[166]
95[b,c]	$e^- + H_2O(r_3) \rightarrow e^- + H_2O$	1.312×10^{-7}	−0.403	176.6	[166]
	Vibrational excitation / de-excitation by electron impact				
96[c]	$e^- + N_2 \rightarrow e^- + N_2(v_1)$	1.146×10^{-15}	1.294	2490.5	[167]

Table A.1: (Continued)

No.	Reaction	A (cm^3/s)[a]	n (-)	E_A (K)	Ref.
		1.000×10^{-4}	-0.866	21659.0	
97[c]	$e^- + N_2 \rightarrow e^- + N_2(v_2)$	1.000×10^{-4}	-0.912	22534.0	[167]
98[c]	$e^- + N_2 \rightarrow e^- + N_2(v_3)$	2.816×10^{-3}	-1.286	25213.0	[167]
99[c]	$e^- + N_2 \rightarrow e^- + N_2(v_4)$	4.269×10^{-3}	-1.361	26781.0	[167]
100[c]	$e^- + N_2 \rightarrow e^- + N_2(v_5)$	3.182×10^{-3}	-1.348	27383.0	[167]
101[c]	$e^- + N_2 \rightarrow e^- + N_2(v_6)$	5.894×10^{-3}	-1.420	29283.0	[167]
102[c]	$e^- + N_2 \rightarrow e^- + N_2(v_7)$	1.000×10^{-4}	-1.069	28202.0	[167]
103[c]	$e^- + N_2 \rightarrow e^- + N_2(v_8)$	1.000×10^{-4}	-1.140	30429.0	[167]
104[c]	$e^- + N_2(v_1) \rightarrow e^- + N_2$	1.000×10^{-4}	-0.867	18915.0	[167]
105[c]	$e^- + N_2(v_2) \rightarrow e^- + N_2$	3.502×10^{-3}	-1.307	21978.0	[167]
106[c]	$e^- + N_2(v_3) \rightarrow e^- + N_2$	3.277×10^{-3}	-1.444	23546.0	[167]
107[c]	$e^- + N_2(v_4) \rightarrow e^- + N_2$	2.189×10^{-4}	-1.495	23389.0	[167]
108[c]	$e^- + N_2(v_5) \rightarrow e^- + N_2$	9.437×10^{-20}	0.000	10000.0	[167]
109[c]	$e^- + N_2(v_6) \rightarrow e^- + N_2$	9.437×10^{-20}	0.000	10000.0	[167]
110[c]	$e^- + N_2(v_7) \rightarrow e^- + N_2$	9.437×10^{-20}	0.000	10000.0	[167]
111[c]	$e^- + N_2(v_8) \rightarrow e^- + N_2$	9.437×10^{-20}	0.000	10000.0	[167]
112[b,c]	$e^- + O_2 \rightarrow e^- + O_2(v_1)$	7.737×10^{-12}	0.627	50910.0	[168]
		4.102×10^{-5}	-1.230	5846.4	
113[b,c]	$e^- + O_2 \rightarrow e^- + O_2(v_2)$	1.149×10^{-11}	0.497	49809.0	[168]
		3.331×10^{-5}	-1.300	8740.4	
114[b,c]	$e^- + O_2 \rightarrow e^- + O_2(v_3)$	1.192×10^{-6}	-1.068	10537.0	[168]
115[b,c]	$e^- + O_2 \rightarrow e^- + O_2(v_4)$	2.017×10^{-8}	-0.753	11525.0	[168]
116[b,c]	$e^- + O_2(v_1) \rightarrow e^- + O_2$	2.887×10^{-5}	-1.475	12488.0	[168]
117[b,c]	$e^- + O_2(v_2) \rightarrow e^- + O_2$	1.166×10^{-6}	-1.500	14620.0	[168]
118[b,c]	$e^- + O_2(v_3) \rightarrow e^- + O_2$	2.965×10^{-4}	-1.464	6597.5	[168]
119[b,c]	$e^- + O_2(v_4) \rightarrow e^- + O_2$	6.359×10^{-7}	-1.132	9331.5	[168]
120[b,c]	$e^- + H_2O \rightarrow e^- + H_2O(v_1)$	1.444×10^{-6}	-0.653	2901.6	[169]
121[b,c]	$e^- + H_2O \rightarrow e^- + H_2O(v_2)$	1.455×10^{-5}	-0.818	5543.4	[169]
122[b,c]	$e^- + H_2O(v_1) \rightarrow e^- + H_2O$	9.324×10^{-7}	-0.612	2222.5	[169]
123[b,c]	$e^- + H_2O(v_2) \rightarrow e^- + H_2O$	2.830×10^{-8}	-0.202	4055.2	[169]
	Vibrational-translational relaxation				
124	$N_2(v_1) + N_2 \rightarrow N_2 + N_2$	3.090×10^{-16}	2.866	20431.0	[126]
125	$N_2(v_2) + N_2 \rightarrow N_2(v_1) + N_2$	6.180×10^{-16}	2.866	20431.0	[126]
126	$N_2(v_3) + N_2 \rightarrow N_2(v_2) + N_2$	9.270×10^{-16}	2.866	20431.0	[126]
127	$N_2(v_4) + N_2 \rightarrow N_2(v_3) + N_2$	1.236×10^{-15}	2.866	20431.0	[126]
128	$N_2(v_5) + N_2 \rightarrow N_2(v_4) + N_2$	1.545×10^{-15}	2.866	20431.0	[126]
129	$N_2(v_6) + N_2 \rightarrow N_2(v_5) + N_2$	1.854×10^{-15}	2.866	20431.0	[126]
130	$N_2(v_7) + N_2 \rightarrow N_2(v_6) + N_2$	2.163×10^{-15}	2.866	20431.0	[126]
131	$N_2(v_8) + N_2 \rightarrow N_2(v_7) + N_2$	2.472×10^{-15}	2.866	20431.0	[126]
132	$N_2 + N_2 \rightarrow N_2(v_1) + N_2$	3.090×10^{-16}	2.866	23796.0	[126]
133	$N_2(v_1) + N_2 \rightarrow N_2(v_2) + N_2$	6.180×10^{-16}	2.866	23796.0	[126]

Table A.1: (Continued)

No.	Reaction	A (cm^3/s)[a]	n (-)	E_A (K)	Ref.
134	$N_2(v_2) + N_2 \rightarrow N_2(v_3) + N_2$	9.270×10^{-16}	2.866	23796.0	[126]
135	$N_2(v_3) + N_2 \rightarrow N_2(v_4) + N_2$	1.236×10^{-15}	2.866	23796.0	[126]
136	$N_2(v_4) + N_2 \rightarrow N_2(v_5) + N_2$	1.545×10^{-15}	2.866	23796.0	[126]
137	$N_2(v_5) + N_2 \rightarrow N_2(v_6) + N_2$	1.854×10^{-15}	2.866	23796.0	[126]
138	$N_2(v_6) + N_2 \rightarrow N_2(v_7) + N_2$	2.163×10^{-15}	2.866	23796.0	[126]
139	$N_2(v_7) + N_2 \rightarrow N_2(v_8) + N_2$	2.472×10^{-15}	2.866	23796.0	[126]
140	$N_2(v_1) + N \rightarrow N_2 + N$	2.309×10^{-17}	0.500	0.0	[126]
141	$N_2(v_2) + N \rightarrow N_2(v_1) + N$	4.619×10^{-17}	0.500	0.0	[126]
142	$N_2(v_3) + N \rightarrow N_2(v_2) + N$	6.928×10^{-17}	0.500	0.0	[126]
143	$N_2(v_4) + N \rightarrow N_2(v_3) + N$	9.238×10^{-17}	0.500	0.0	[126]
144	$N_2(v_5) + N \rightarrow N_2(v_4) + N$	1.155×10^{-16}	0.500	0.0	[126]
145	$N_2(v_6) + N \rightarrow N_2(v_5) + N$	1.386×10^{-16}	0.500	0.0	[126]
146	$N_2(v_7) + N \rightarrow N_2(v_6) + N$	1.617×10^{-16}	0.500	0.0	[126]
147	$N_2(v_8) + N \rightarrow N_2(v_7) + N$	1.848×10^{-16}	0.500	0.0	[126]
148	$N_2 + N \rightarrow N_2(v_1) + N$	2.309×10^{-17}	0.500	3365.5	[126]
149	$N_2(v_1) + N \rightarrow N_2(v_2) + N$	4.619×10^{-17}	0.500	3365.5	[126]
150	$N_2(v_2) + N \rightarrow N_2(v_3) + N$	6.928×10^{-17}	0.500	3365.5	[126]
151	$N_2(v_3) + N \rightarrow N_2(v_4) + N$	9.238×10^{-17}	0.500	3365.5	[126]
152	$N_2(v_4) + N \rightarrow N_2(v_5) + N$	1.155×10^{-16}	0.500	3365.5	[126]
153	$N_2(v_5) + N \rightarrow N_2(v_6) + N$	1.386×10^{-16}	0.500	3365.5	[126]
154	$N_2(v_6) + N \rightarrow N_2(v_7) + N$	1.617×10^{-16}	0.500	3365.5	[126]
155	$N_2(v_7) + N \rightarrow N_2(v_8) + N$	1.848×10^{-16}	0.500	3365.5	[126]
156	$N_2(v_1) + O \rightarrow N_2 + O$	1.353×10^{-9}	0.357	862.6	[126]
157	$N_2(v_2) + O \rightarrow N_2(v_1) + O$	2.706×10^{-9}	0.357	862.6	[126]
158	$N_2(v_3) + O \rightarrow N_2(v_2) + O$	4.059×10^{-9}	0.357	862.6	[126]
159	$N_2(v_4) + O \rightarrow N_2(v_3) + O$	5.412×10^{-9}	0.357	862.6	[126]
160	$N_2(v_5) + O \rightarrow N_2(v_4) + O$	6.765×10^{-9}	0.357	862.6	[126]
161	$N_2(v_6) + O \rightarrow N_2(v_5) + O$	8.118×10^{-9}	0.357	862.6	[126]
162	$N_2(v_7) + O \rightarrow N_2(v_6) + O$	9.471×10^{-9}	0.357	862.6	[126]
163	$N_2(v_8) + O \rightarrow N_2(v_7) + O$	1.082×10^{-8}	0.357	862.6	[126]
164	$N_2 + O \rightarrow N_2(v_1) + O$	1.353×10^{-9}	0.357	4228.1	[126]
165	$N_2(v_1) + O \rightarrow N_2(v_2) + O$	2.706×10^{-9}	0.357	4228.1	[126]
166	$N_2(v_2) + O \rightarrow N_2(v_3) + O$	4.059×10^{-9}	0.357	4228.1	[126]
167	$N_2(v_3) + O \rightarrow N_2(v_4) + O$	5.412×10^{-9}	0.357	4228.1	[126]
168	$N_2(v_4) + O \rightarrow N_2(v_5) + O$	6.765×10^{-9}	0.357	4228.1	[126]
169	$N_2(v_5) + O \rightarrow N_2(v_6) + O$	8.118×10^{-9}	0.357	4228.1	[126]
170	$N_2(v_6) + O \rightarrow N_2(v_7) + O$	9.471×10^{-9}	0.357	4228.1	[126]
171	$N_2(v_7) + O \rightarrow N_2(v_8) + O$	1.082×10^{-8}	0.357	4228.1	[126]
172[b]	$O_2(v_1) + O_2 \rightarrow O_2 + O_2$	2.064×10^{-22}	3.033	9076.1	[126]
173[b]	$O_2(v_2) + O_2 \rightarrow O_2(v_1) + O_2$	4.128×10^{-22}	3.033	9076.1	[126]
174[b]	$O_2(v_3) + O_2 \rightarrow O_2(v_2) + O_2$	6.192×10^{-22}	3.033	9076.1	[126]

Table A.1: (Continued)

No.	Reaction	A (cm^3/s)[a]	n (-)	E_A (K)	Ref.
175[b]	$O_2(v_4) + O_2 \rightarrow O_2(v_3) + O_2$	8.256×10^{-22}	3.033	9076.1	[126]
176[b]	$O_2 + O_2 \rightarrow O_2(v_1) + O_2$	2.064×10^{-22}	3.033	11281.0	[126]
177[b]	$O_2(v_1) + O_2 \rightarrow O_2(v_2) + O_2$	4.128×10^{-22}	3.033	11281.0	[126]
178[b]	$O_2(v_2) + O_2 \rightarrow O_2(v_3) + O_2$	6.192×10^{-22}	3.033	11281.0	[126]
179[b]	$O_2(v_3) + O_2 \rightarrow O_2(v_4) + O_2$	8.256×10^{-22}	3.033	11281.0	[126]
180[b]	$O_2(v_1) + O \rightarrow O_2 + O$	4.500×10^{-15}	1.000	0.0	[126]
181[b]	$O_2(v_2) + O \rightarrow O_2(v_1) + O$	9.000×10^{-15}	1.000	0.0	[126]
182[b]	$O_2(v_3) + O \rightarrow O_2(v_2) + O$	1.350×10^{-14}	1.000	0.0	[126]
183[b]	$O_2(v_4) + O \rightarrow O_2(v_3) + O$	1.800×10^{-14}	1.000	0.0	[126]
184[b]	$O_2 + O \rightarrow O_2(v_1) + O$	4.500×10^{-15}	1.000	2205.0	[126]
185[b]	$O_2(v_1) + O \rightarrow O_2(v_2) + O$	9.000×10^{-15}	1.000	2205.0	[126]
186[b]	$O_2(v_2) + O \rightarrow O_2(v_3) + O$	1.350×10^{-14}	1.000	2205.0	[126]
187[b]	$O_2(v_3) + O \rightarrow O_2(v_4) + O$	1.800×10^{-14}	1.000	2205.0	[126]
	Excitation of electronic levels by electron impact				
188[c]	$e^- + N_2 \rightarrow e^- + N_2(A^3\Sigma)$	5.131×10^{-14}	0.823	74373.0	[167]
		5.223×10^{-13}	0.762	82862.0	
		6.435×10^{-13}	0.760	92768.0	
189[c]	$e^- + N_2 \rightarrow e^- + N_2(B^3\Pi)$	5.665×10^{-11}	0.451	87343.0	[167]
		6.031×10^{-11}	0.426	94787.0	
		3.152×10^{-12}	0.613	96565.0	
190[c]	$e^- + N_2 \rightarrow e^- + N_2(a'^1\Sigma)$	6.829×10^{-15}	1.184	91787.0	[167]
		9.090×10^{-10}	0.000	93206.0	
		2.899×10^{-10}	0.219	108190.0	
191[c]	$e^- + N_2 \rightarrow e^- + N_2(C^3\Pi)$	1.667×10^{-9}	0.309	135740.0	[167]
		1.560×10^{-5}	−1.011	134140.0	
		5.237×10^{-14}	0.958	137680.0	
192[c]	$e^- + N_2 \rightarrow e^- + N + N(^2D)$	2.502×10^{-11}	0.649	153730.0	[167]
193[b,c]	$e^- + O_2 \rightarrow e^- + O_2(a^1\Delta)$	3.481×10^{-15}	1.232	12003.0	[169]
194[b,c]	$e^- + O_2 \rightarrow e^- + O_2(b^1\Sigma)$	7.313×10^{-14}	0.815	19326.0	[169]
195[b,c]	$e^- + O_2 \rightarrow e^- + O_2(4.5eV)$	7.652×10^{-10}	0.121	58792.0	[169]
196[b,c]	$e^- + O_2 \rightarrow e^- + O + O$	3.796×10^{-7}	−0.374	78030.0	[169]
		1.000×10^{-4}	−0.606	100890.0	
		4.160×10^{-17}	1.832	200000.0	
197[b,c]	$e^- + O_2(a^1\Delta) \rightarrow e^- + O + O$	3.796×10^{-7}	−0.374	78030.0	[169]
198[b,c]	$e^- + O_2(b^1\Sigma) \rightarrow e^- + O + O$	3.796×10^{-7}	−0.374	78030.0	[169]
199[b,c]	$e^- + O \rightarrow e^- + O(^1D)$	1.368×10^{-10}	0.349	25445.0	[170]
200[b,c]	$e^- + O \rightarrow e^- + O(^1S)$	8.179×10^{-11}	0.216	49438.0	[170]
201[b,c]	$e^- + H_2O \rightarrow e^- + H_2 + O(^1S)$	1.375×10^{-10}	0.000	200000.0	[166]
202[b,c]	$e^- + H_2O \rightarrow e^- + H_2 + O(^1D)$	1.648×10^{-16}	1.618	145740.0	[169]
203[b,c]	$e^- + H_2O \rightarrow e^- + OH + H$	4.651×10^{-5}	−0.844	111040.0	[166]
204	$e^- + O_3 \rightarrow e^- + O_2 + O$	1.000×10^{-8}	0.000	0.0	[130]

Table A.1: (Continued)

No.	Reaction	A (cm^3/s)[a]	n (-)	E_A (K)	Ref.
205[b]	$e^- + OH \rightarrow e^- + O + H$	2.080×10^{-7}	−0.760	80071.0	[130]
206[b,c]	$e^- + H_2 \rightarrow e^- + H + H$	2.749×10^{-13}	0.967	100640.0	[171]
		1.100×10^{-11}	0.644	129940.0	
		1.248×10^{-7}	−0.143	140330.0	
207[b]	$e^- + H_2O_2 \rightarrow e^- + OH + OH$	2.360×10^{-9}	0.000	0.0	[131]
	De-excitation of electronic levels by electron impact				
208[c]	$e^- + N_2(A^3\Sigma) \rightarrow e^- + N_2$	3.995×10^{-9}	−0.157	68169.0	[167]
209[b,c]	$e^- + O_2(a^1\Delta) \rightarrow e^- + O_2$	9.110×10^{-13}	0.695	8143.2	[169]
210[b,c]	$e^- + O(^1D) \rightarrow e^- + O$	4.260×10^{-8}	−0.237	22083.0	[170]
211[b,c]	$e^- + O(^1S) \rightarrow e^- + O$	6.906×10^{-9}	−0.369	48016.0	[170]
	Ionization by electron impact				
212[b,c]	$e^- + Ar \rightarrow e^- + e^- + Ar^+$	2.670×10^{-11}	0.685	184490.0	[172]
213[b,c]	$e^- + H \rightarrow e^- + e^- + H^+$	2.082×10^{-11}	0.597	157550.0	[169]
214[b,c]	$e^- + N \rightarrow e^- + e^- + N^+$	1.094×10^{-18}	0.000	200000.0	[169]
215[b,c]	$e^- + O \rightarrow e^- + e^- + O^+$	7.308×10^{-16}	1.868	200000.0	[169]
216[b,c]	$e^- + N_2 \rightarrow e^- + e^- + N^+ + N$	3.275×10^{-19}	0.000	200000.0	[173]
217[b,c]	$e^- + O_2 \rightarrow e^- + e^- + O^+ + O$	6.062×10^{-18}	0.000	199860.0	[174]
218[b,c]	$e^- + H_2 \rightarrow e^- + e^- + H_2^+$	6.992×10^{-12}	0.732	178390.0	[175]
219[b,c]	$e^- + N_2 \rightarrow e^- + e^- + N_2^+$	1.210×10^{-12}	0.898	179180.0	[173]
220[c]	$e^- + N_2(A^3\Sigma) \rightarrow e^- + e^- + N_2^+$	5.780×10^{-6}	−0.482	159130.0	[169]
221[b,c]	$e^- + O_2 \rightarrow e^- + e^- + O_2^+$	5.261×10^{-16}	1.538	134640.0	[174]
222[b,c]	$e^- + O_2(a^1\Delta) \rightarrow e^- + e^- + O_2^+$	6.403×10^{-6}	−0.494	159250.0	[169]
223[b,c]	$e^- + O_2(b^1\Sigma) \rightarrow e^- + e^- + O_2^+$	5.862×10^{-6}	−0.480	159080.0	[169]
224[b,c]	$e^- + OH \rightarrow e^- + e^- + OH^+$	6.226×10^{-11}	0.573	159770.0	[176]
225[b,c]	$e^- + NO \rightarrow e^- + e^- + NO^+$	4.787×10^{-11}	0.510	132390.0	[177]
226[b,c]	$e^- + NO \rightarrow e^- + e^- + O^+ + N$	2.609×10^{-19}	−0.612	199990.0	[177]
227[b,c]	$e^- + NO \rightarrow e^- + e^- + N^+ + O$	5.551×10^{-21}	−0.062	199800.0	[177]
228[b,c]	$e^- + N_2O \rightarrow e^- + e^- + N_2O^+$	1.770×10^{-10}	0.440	156060.0	[178]
229[b,c]	$e^- + NO_2 \rightarrow e^- + e^- + NO_2^+$	3.056×10^{-6}	−0.273	184200.0	[179]
230[b,c]	$e^- + H_2O \rightarrow e^- + e^- + H_2O^+$	2.162×10^{-11}	0.609	152680.0	[166]
231[b,c]	$e^- + H_2O \rightarrow e^- + e^- + H^+ + OH$	5.400×10^{-11}	0.000	200000.0	[166]
232[b,c]	$e^- + H_2O \rightarrow e^- + e^- + OH^+ + H$	3.403×10^{-18}	1.976	200000.0	[166]
233[b,c]	$e^- + H_2O \rightarrow e^- + e^- + O^+ + H_2$	2.776×10^{-20}	0.000	200000.0	[166]
234[b,c]	$e^- + H_2O \rightarrow e^- + e^- + H_2^+ + O$	2.220×10^{-20}	0.000	200000.0	[166]
	Electron-ion recombination				
235[b,c]	$e^- + e^- + Ar^+ \rightarrow e^- + Ar$	2.981×10^{-7}	0.000	177900.0	[172]
236[b]	$e^- + N_2^+ \rightarrow N + N$	8.325×10^{-7}	−0.390	0.0	[126]
		7.492×10^{-7}	−0.390	0.0	
		8.325×10^{-8}	−0.390	0.0	
237[b]	$e^- + O_2^+ \rightarrow O + O$	8.047×10^{-6}	−0.700	0.0	[126]
		5.852×10^{-6}	−0.700	0.0	

Table A.1: (Continued)

No.	Reaction	A (cm^3/s)[a]	n (-)	E_A (K)	Ref.
		7.315×10^{-7}	−0.700	0.0	
238[b]	$e^- + NO^+ \rightarrow O + N$	1.071×10^{-5}	−0.850	0.0	[126]
		4.285×10^{-5}	−0.850	0.0	
239	$e^- + N_3^+ \rightarrow N_2 + N$	3.464×10^{-6}	−0.500	0.0	[126]
240	$e^- + N_4^+ \rightarrow N_2 + N_2$	4.727×10^{-5}	−0.530	0.0	[126]
241[b]	$e^- + N_2O^+ \rightarrow N_2 + O$	3.464×10^{-6}	−0.500	0.0	[126]
242[b]	$e^- + NO_2^+ \rightarrow NO + O$	3.464×10^{-6}	−0.500	0.0	[126]
243	$e^- + O_4^+ \rightarrow O_2 + O_2$	2.425×10^{-5}	−0.500	0.0	[126]
244[b]	$e^- + N^+ + e^- \rightarrow N + e^-$	9.821×10^{-9}	−4.500	0.0	[126]
245[b]	$e^- + O^+ + e^- \rightarrow O + e^-$	9.821×10^{-9}	−4.500	0.0	[126]
246[b]	$e^- + N^+ + M \rightarrow N + M$	3.118×10^{-23}	−1.500	0.0	[126]
247[b]	$e^- + O^+ + M \rightarrow O + M$	3.118×10^{-23}	−1.500	0.0	[126]
248[b]	$e^- + H_2^+ \rightarrow H + H$	2.250×10^{-6}	−0.400	0.0	[129]
249[b]	$e^- + OH^+ \rightarrow O + H$	1.300×10^{-6}	−0.500	0.0	[129]
250[b]	$e^- + H^+ \rightarrow H$	2.280×10^{-10}	−0.700	0.0	[129]
251[b]	$e^- + H_2O^+ \rightarrow H + OH$	8.600×10^{-8}	−0.500	0.0	[131]
252[b]	$e^- + H_2O^+ \rightarrow O + H_2$	3.050×10^{-7}	−0.500	0.0	[131]
253[b]	$e^- + H_2O^+ \rightarrow O + H + H$	3.870×10^{-8}	−0.500	0.0	[131]
	Electron attachment				
254[c]	$e^- + O \rightarrow O^-$	2.441×10^{-16}	0.205	396.6	[180]
255[c]	$e^- + NO \rightarrow NO^-$	8.198×10^{-7}	−0.772	85860.0	[178]
256[c]	$e^- + H_2O \rightarrow H_2O^-$	1.000×10^{-4}	−1.189	73793.0	[178]
257[c]	$e^- + N_2O \rightarrow N_2O^-$	4.170×10^{-14}	0.614	4089.4	[178]
258[c]	$e^- + O_2 \rightarrow O^- + O$	1.864×10^{-8}	−0.421	58810.0	[174]
259[c]	$e^- + NO \rightarrow O^- + N$	9.519×10^{-7}	−0.786	85993.0	[177]
260[c]	$e^- + O_3 \rightarrow O^- + O_2$	1.677×10^{-8}	−0.282	5230.0	[169]
261[c]	$e^- + O_3 \rightarrow O_2^- + O$	1.034×10^{-10}	0.213	5764.6	[169]
262[c]	$e^- + H_2O \rightarrow OH^- + H$	2.160×10^{-10}	−0.232	62064.0	[166]
263[c]	$e^- + H_2O \rightarrow O^- + H_2$	2.117×10^{-14}	0.743	51290.0	[166]
264[c]	$e^- + H_2O \rightarrow H^- + OH$	9.870×10^{-5}	−1.138	71673.0	[166]
265[c]	$e^- + O_2 \rightarrow O_2^-$	4.534×10^{-8}	−0.481	64996.0	[169]
266[c]	$e^- + O_2 + M \rightarrow O_2^- + M$	1.500×10^{-35}	0.000	0.0	[181]
267[c]	$e^- + O_2(a^1\Delta) \rightarrow O^- + O$	1.217×10^{-8}	−0.251	43919.0	[169]
268[c]	$e^- + O_2(b^1\Sigma) \rightarrow O^- + O$	1.217×10^{-8}	−0.251	43919.0	[169]
269	$e^- + NO_2 \rightarrow O^- + NO$	1.000×10^{-11}	0.000	0.0	[126]
270	$e^- + O + O_2 \rightarrow O^- + O_2$	1.000×10^{-31}	0.000	0.0	[126]
271	$e^- + O + O_2 \rightarrow O_2^- + O$	1.000×10^{-31}	0.000	0.0	[126]
272	$e^- + O_3 + M \rightarrow O_3^- + M$	1.000×10^{-31}	0.000	0.0	[126]
273	$e^- + NO + M \rightarrow NO^- + M$	8.000×10^{-31}	0.000	0.0	[126]
274	$e^- + N_2O + M \rightarrow N_2O^- + M$	6.000×10^{-33}	0.000	0.0	[126]
275	$e^- + O_2 + N_2 \rightarrow O_2^- + N_2$	9.900×10^{-27}	−2.000	70.0	[182]

Table A.1: (Continued)

No.	Reaction	A (cm^3/s)[a]	n (-)	E_A (K)	Ref.
276	$e^- + NO + H_2 \rightarrow NO^- + H_2$	1.560×10^{-27}	-1.500	680.0	[129]
277	$e^- + O_2 + H_2O \rightarrow O_2^- + H_2O$	1.400×10^{-29}	0.000	0.0	[130]
278[c]	$e^- + H_2O_2 \rightarrow O^- + H_2O$	8.050×10^{-7}	-0.924	1699.7	[183]
279[c]	$e^- + H_2O_2 \rightarrow OH^- + OH$	7.277×10^{-6}	-0.960	2957.3	[183]
	Electron detachment				
280[c]	$e^- + O^- \rightarrow O + e^- + e^-$	6.112×10^{-6}	-0.426	52133.0	[169]
281[c]	$e^- + H^- \rightarrow H + e^- + e^-$	2.000×10^{-11}	0.756	9362.6	[184]
282[c]	$e^- + O_2^- \rightarrow O_2 + e^- + e^-$	2.096×10^{-11}	0.794	48241.0	[185]
283[c]	$e^- + OH^- \rightarrow OH + e^- + e^-$	4.285×10^{-10}	0.504	42490.0	[186]
284	$O^- + O \rightarrow O_2 + e^-$	1.400×10^{-10}	0.000	0.0	[126]
285	$O^- + N \rightarrow NO + e^-$	2.600×10^{-10}	0.000	0.0	[126]
286	$O^- + NO \rightarrow NO_2 + e^-$	2.600×10^{-10}	0.000	0.0	[126]
287	$O^- + N_2 \rightarrow N_2O + e^-$	5.000×10^{-13}	0.000	0.0	[126]
288	$O^- + O_2 \rightarrow O_3 + e^-$	5.000×10^{-15}	0.000	0.0	[126]
289	$O^- + O_2(a^1\Delta) \rightarrow O_3 + e^-$	3.000×10^{-10}	0.000	0.0	[126]
290	$O^- + O_2(b^1\Sigma) \rightarrow O + O_2 + e^-$	6.900×10^{-10}	0.000	0.0	[126]
291	$O^- + N_2(A^3\Sigma) \rightarrow O + N_2 + e^-$	2.200×10^{-9}	0.000	0.0	[126]
292	$O^- + N_2(B^3\Pi) \rightarrow O + N_2 + e^-$	1.900×10^{-9}	0.000	0.0	[126]
293	$O^- + O_3 \rightarrow O_2 + O_2 + e^-$	3.000×10^{-10}	0.000	0.0	[126]
294	$O_2^- + O \rightarrow O_3 + e^-$	1.500×10^{-10}	0.000	0.0	[126]
295	$O_2^- + N \rightarrow NO_2 + e^-$	5.000×10^{-10}	0.000	0.0	[126]
296	$O_2^- + O_2 \rightarrow O_2 + O_2 + e^-$	2.700×10^{-10}	0.500	5590.0	[126]
297	$O_2^- + O_2(a^1\Delta) \rightarrow O_2 + O_2 + e^-$	2.000×10^{-10}	0.000	0.0	[126]
298	$O_2^- + O_2(b^1\Sigma) \rightarrow O_2 + O_2 + e^-$	3.600×10^{-10}	0.000	0.0	[126]
299	$O_2^- + N_2 \rightarrow O_2 + N_2 + e^-$	1.900×10^{-12}	0.500	4990.0	[126]
300	$O_2^- + N_2(A^3\Sigma) \rightarrow O_2 + N_2 + e^-$	2.100×10^{-9}	0.000	0.0	[126]
301	$O_2^- + N_2(B^3\Pi) \rightarrow O_2 + N_2 + e^-$	2.500×10^{-9}	0.000	0.0	[126]
302	$O_3^- + O \rightarrow O_2 + O_2 + e^-$	3.000×10^{-10}	0.000	0.0	[126]
303	$NO^- + N \rightarrow N_2O + e^-$	5.000×10^{-10}	0.000	0.0	[126]
304	$O_3^- + N \rightarrow NO + O_2 + e^-$	5.000×10^{-10}	0.000	0.0	[126]
305	$N_2O^- + N \rightarrow NO + N_2 + e^-$	5.000×10^{-10}	0.000	0.0	[126]
306	$NO_2^- + N \rightarrow NO + NO + e^-$	5.000×10^{-10}	0.000	0.0	[126]
307	$NO_3^- + N \rightarrow NO + NO_2 + e^-$	5.000×10^{-10}	0.000	0.0	[126]
308	$NO^- + O \rightarrow NO_2 + e^-$	1.500×10^{-10}	0.000	0.0	[126]
309	$N_2O^- + O \rightarrow NO + NO + e^-$	1.500×10^{-10}	0.000	0.0	[126]
310	$NO_2^- + O \rightarrow NO + O_2 + e^-$	1.500×10^{-10}	0.000	0.0	[126]
311	$NO_3^- + O \rightarrow NO + O_3 + e^-$	1.500×10^{-10}	0.000	0.0	[126]
312	$O_3^- + N_2(A^3\Sigma) \rightarrow O_3 + N_2 + e^-$	2.100×10^{-9}	0.000	0.0	[126]
313	$NO^- + N_2(A^3\Sigma) \rightarrow NO + N_2 + e^-$	2.100×10^{-9}	0.000	0.0	[126]
314	$N_2O^- + N_2(A^3\Sigma) \rightarrow N_2O + N_2 + e^-$	2.100×10^{-9}	0.000	0.0	[126]
315	$NO_2^- + N_2(A^3\Sigma) \rightarrow NO_2 + N_2 + e^-$	2.100×10^{-9}	0.000	0.0	[126]

Table A.1: (Continued)

No.	Reaction	A (cm^3/s)[a]	n (-)	E_A (K)	Ref.
316	$NO_3^- + N_2(A^3\Sigma) \rightarrow NO_3 + N_2 + e^-$	2.100×10^{-9}	0.000	0.0	[126]
317	$O_3^- + N_2(B^3\Pi) \rightarrow O_3 + N_2 + e^-$	2.500×10^{-9}	0.000	0.0	[126]
318	$NO^- + N_2(B^3\Pi) \rightarrow NO + N_2 + e^-$	2.500×10^{-9}	0.000	0.0	[126]
319	$N_2O^- + N_2(B^3\Pi) \rightarrow N_2O + N_2 + e^-$	2.500×10^{-9}	0.000	0.0	[126]
320	$NO_2^- + N_2(B^3\Pi) \rightarrow NO_2 + N_2 + e^-$	2.500×10^{-9}	0.000	0.0	[126]
321	$NO_3^- + N_2(B^3\Pi) \rightarrow NO_3 + N_2 + e^-$	2.500×10^{-9}	0.000	0.0	[126]
322	$NO^- + H_2 \rightarrow e^- + NO + H_2$	6.300×10^{-12}	0.000	960.0	[129]
323	$O^- + H_2 \rightarrow e^- + H_2O$	8.000×10^{-10}	0.000	0.0	[129]
324	$O^- + H_2O \rightarrow e^- + H_2O_2$	6.000×10^{-13}	0.000	0.0	[129]
325	$O_2^- + H \rightarrow e^- + HO_2$	1.200×10^{-9}	0.000	0.0	[129]
326	$H^- + O_2 \rightarrow e^- + HO_2$	1.200×10^{-9}	0.000	0.0	[129]
327	$H^- + H \rightarrow e^- + H_2$	1.800×10^{-9}	0.000	0.0	[129]
328	$OH^- + O \rightarrow e^- + HO_2$	1.800×10^{-9}	0.000	0.0	[129]
329	$OH^- + H \rightarrow e^- + H_2O$	1.000×10^{-9}	0.000	0.0	[129]
330	$O^- + H \rightarrow e^- + OH$	5.300×10^{-10}	0.000	0.0	[130]
331	$O_2^- + H_2O \rightarrow e^- + O_2 + H_2O$	5.000×10^{-9}	0.000	5000.0	[130]
	Optical transitions and predissociation				
332	$N_2(A^3\Sigma) \rightarrow N_2$	5.000×10^{-1}	0.000	0.0	[126]
333	$N_2(B^3\Pi) \rightarrow N_2(A^3\Sigma)$	1.340×10^{5}	0.000	0.0	[126]
334	$N_2(a'^1\Sigma) \rightarrow N_2$	1.000×10^{2}	0.000	0.0	[126]
335	$N_2(C^3\Pi) \rightarrow N_2(B^3\Pi)$	2.450×10^{7}	0.000	0.0	[126]
336	$O_2(a^1\Delta) \rightarrow O_2$	2.600×10^{-4}	0.000	0.0	[126]
337	$O_2(b^1\Sigma) \rightarrow O_2(a^1\Delta)$	1.500×10^{-3}	0.000	0.0	[126]
338	$O_2(b^1\Sigma) \rightarrow O_2$	8.500×10^{-2}	0.000	0.0	[126]
339	$O_2(4.5eV) \rightarrow O_2$	1.100×10^{1}	0.000	0.0	[126]
	Quenching and excitation of N_2				
340	$N_2(A^3\Sigma) + O \rightarrow NO + N(^2D)$	7.000×10^{-12}	0.000	0.0	[126]
341	$N_2(A^3\Sigma) + O \rightarrow N_2 + O(^1S)$	2.100×10^{-11}	0.000	0.0	[126]
342	$N_2(A^3\Sigma) + N \rightarrow N_2 + N$	2.000×10^{-12}	0.000	0.0	[126]
		1.796×10^{-9}	-0.667	0.0	
343	$N_2(A^3\Sigma) + O_2 \rightarrow N_2 + O + O(^1D)$	2.100×10^{-12}	0.550	0.0	[126]
344	$N_2(A^3\Sigma) + O_2 \rightarrow N_2 + O_2(a^1\Delta)$	2.000×10^{-13}	0.550	0.0	[126]
345	$N_2(A^3\Sigma) + O_2 \rightarrow N_2 + O_2(b^1\Sigma)$	2.000×10^{-13}	0.550	0.0	[126]
346	$N_2(A^3\Sigma) + O_2 \rightarrow N_2O + O$	2.000×10^{-14}	0.550	0.0	[126]
347	$N_2(A^3\Sigma) + N_2 \rightarrow N_2 + N_2$	3.000×10^{-16}	0.000	0.0	[126]
348	$N_2(A^3\Sigma) + NO \rightarrow N_2 + NO$	6.900×10^{-11}	0.000	0.0	[126]
349	$N_2(A^3\Sigma) + N_2O \rightarrow N_2 + N + NO$	1.000×10^{-11}	0.000	0.0	[126]
350	$N_2(A^3\Sigma) + NO_2 \rightarrow N_2 + O + NO$	1.000×10^{-12}	0.000	0.0	[126]
351	$N_2(A^3\Sigma) + N_2(A^3\Sigma) \rightarrow N_2 + N_2(B^3\Pi)$	3.000×10^{-10}	0.000	0.0	[126]
352	$N_2(A^3\Sigma) + N_2(A^3\Sigma) \rightarrow N_2 + N_2(C^3\Pi)$	1.500×10^{-10}	0.000	0.0	[126]
353	$N_2(B^3\Pi) + N_2 \rightarrow N_2(A^3\Sigma) + N_2$	3.000×10^{-11}	0.000	0.0	[126]

Table A.1: (Continued)

No.	Reaction	A (cm^3/s)[a]	n (-)	E_A (K)	Ref.
354	$N_2(B^3\Pi) + N_2 \rightarrow N_2 + N_2$	2.000×10^{-12}	0.000	0.0	[126]
355	$N_2(B^3\Pi) + O_2 \rightarrow N_2 + O + O$	3.000×10^{-10}	0.000	0.0	[126]
356	$N_2(B^3\Pi) + NO \rightarrow N_2(A^3\Sigma) + NO$	2.400×10^{-10}	0.000	0.0	[126]
357	$N_2(C^3\Pi) + N_2 \rightarrow N_2(a'^1\Sigma) + N_2$	1.000×10^{-11}	0.000	0.0	[126]
358	$N_2(C^3\Pi) + O_2 \rightarrow N_2 + O + O(^1S)$	3.000×10^{-10}	0.000	0.0	[126]
359	$N_2(a'^1\Sigma) + N_2 \rightarrow N_2(B^3\Pi) + N_2$	1.900×10^{-13}	0.000	0.0	[126]
360	$N_2(a'^1\Sigma) + O_2 \rightarrow N_2 + O + O$	2.800×10^{-11}	0.000	0.0	[126]
361	$N_2(a'^1\Sigma) + NO \rightarrow N_2 + N + O$	3.600×10^{-10}	0.000	0.0	[126]
362	$N_2(a'^1\Sigma) + N_2(A^3\Sigma) \rightarrow N_4^+ + e^-$	4.000×10^{-12}	0.000	0.0	[126]
363	$N_2(a'^1\Sigma) + N_2(a'^1\Sigma) \rightarrow N_4^+ + e^-$	1.000×10^{-11}	0.000	0.0	[126]
364	$N + N + N_2 \rightarrow N_2(A^3\Sigma) + N_2$	1.700×10^{-33}	0.000	0.0	[126]
365	$N + N + O_2 \rightarrow N_2(A^3\Sigma) + O_2$	1.700×10^{-33}	0.000	0.0	[126]
366	$N + N + NO \rightarrow N_2(A^3\Sigma) + NO$	1.700×10^{-33}	0.000	0.0	[126]
367	$N + N + N \rightarrow N_2(A^3\Sigma) + N$	1.000×10^{-32}	0.000	0.0	[126]
368	$N + N + O \rightarrow N_2(A^3\Sigma) + O$	1.000×10^{-32}	0.000	0.0	[126]
369	$N + N + N_2 \rightarrow N_2(B^3\Pi) + N_2$	2.400×10^{-33}	0.000	0.0	[126]
370	$N + N + O_2 \rightarrow N_2(B^3\Pi) + O_2$	2.400×10^{-33}	0.000	0.0	[126]
371	$N + N + NO \rightarrow N_2(B^3\Pi) + NO$	2.400×10^{-33}	0.000	0.0	[126]
372	$N + N + N \rightarrow N_2(B^3\Pi) + N$	1.400×10^{-32}	0.000	0.0	[126]
373	$N + N + O \rightarrow N_2(B^3\Pi) + O$	1.400×10^{-32}	0.000	0.0	[126]
	Deactivation of N metastables				
374	$N(^2D) + O \rightarrow N + O(^1D)$	4.000×10^{-13}	0.000	0.0	[126]
375	$N(^2D) + O_2 \rightarrow NO + O$	5.200×10^{-12}	0.000	0.0	[126]
376	$N(^2D) + NO \rightarrow N_2 + O$	1.800×10^{-10}	0.000	0.0	[126]
377	$N(^2D) + N_2O \rightarrow NO + N_2$	3.500×10^{-12}	0.000	0.0	[126]
378	$N(^2D) + N_2 \rightarrow N + N_2$	1.000×10^{-13}	0.000	510.0	[187]
379	$N(^2P) + N \rightarrow N + N$	1.800×10^{-12}	0.000	0.0	[187]
380	$N(^2P) + O \rightarrow N + O$	1.000×10^{-12}	0.000	0.0	[188]
381	$N(^2P) + N \rightarrow N(^2D) + N$	6.000×10^{-13}	0.000	0.0	[187]
382	$N(^2P) + N_2 \rightarrow N + N_2$	6.000×10^{-14}	0.000	0.0	[187]
383	$N(^2P) + N(^2D) \rightarrow N_2^+ + e^-$	1.000×10^{-13}	0.000	0.0	[187]
384	$N(^2P) + O_2 \rightarrow NO + O$	2.600×10^{-12}	0.000	0.0	[182]
385	$N(^2P) + NO \rightarrow N_2(A^3\Sigma) + O$	3.000×10^{-11}	0.000	0.0	[126]
	Quenching and excitation of O_2				
386[b]	$O_2(a^1\Delta) + O \rightarrow O_2 + O$	7.000×10^{-16}	0.000	0.0	[126]
387[b]	$O_2(a^1\Delta) + N \rightarrow NO + O$	2.000×10^{-14}	0.000	600.0	[126]
388[b]	$O_2(a^1\Delta) + O_2 \rightarrow O_2 + O_2$	3.800×10^{-18}	0.000	205.0	[126]
389[b]	$O_2(a^1\Delta) + N_2 \rightarrow O_2 + N_2$	3.000×10^{-21}	0.000	0.0	[126]
390[b]	$O_2(a^1\Delta) + NO \rightarrow O_2 + NO$	2.500×10^{-11}	0.000	0.0	[126]
391	$O_2(a^1\Delta) + O_3 \rightarrow O_2 + O_2 + O(^1D)$	5.200×10^{-11}	0.000	2840.0	[126]
392[b]	$O_2(a^1\Delta) + O_2(a^1\Delta) \rightarrow O_2 + O_2(b^1\Sigma)$	7.000×10^{-28}	3.800	−700.0	[126]

Table A.1: (Continued)

No.	Reaction	A (cm^3/s)[a]	n (-)	E_A (K)	Ref.
393	$O + O_3 \rightarrow O_2 + O_2(a^1\Delta)$	1.000×10^{-11}	0.000	2300.0	[126]
394[b]	$O_2(b^1\Sigma) + O \rightarrow O_2(a^1\Delta) + O$	8.100×10^{-14}	0.000	0.0	[126]
395[b]	$O_2(b^1\Sigma) + O \rightarrow O_2 + O(^1D)$	6.014×10^{-11}	−0.100	4200.0	[126]
396[b]	$O_2(b^1\Sigma) + O_2 \rightarrow O_2(a^1\Delta) + O_2$	4.300×10^{-22}	2.400	281.0	[126]
397[b]	$O_2(b^1\Sigma) + N_2 \rightarrow O_2(a^1\Delta) + N_2$	5.667×10^{-18}	1.000	0.0	[126]
398[b]	$O_2(b^1\Sigma) + NO \rightarrow O_2(a^1\Delta) + NO$	6.000×10^{-14}	0.000	0.0	[126]
399	$O_2(b^1\Sigma) + O_3 \rightarrow O_2 + O_2 + O$	2.200×10^{-11}	0.000	0.0	[126]
400[b]	$O_2(4.5eV) + O \rightarrow O_2 + O(^1S)$	9.000×10^{-12}	0.000	0.0	[126]
401[b]	$O_2(4.5eV) + O_2 \rightarrow O_2(b^1\Sigma) + O_2(b^1\Sigma)$	3.000×10^{-13}	0.000	0.0	[126]
402[b]	$O_2(4.5eV) + N_2 \rightarrow O_2(b^1\Sigma) + N_2$	9.000×10^{-15}	0.000	0.0	[126]
	Deactivation of O metastables				
403[b]	$O(^1D) + O \rightarrow O + O$	8.000×10^{-12}	0.000	0.0	[126]
404[b]	$O(^1D) + O_2 \rightarrow O + O_2$	6.400×10^{-12}	0.000	−67.0	[126]
		1.000×10^{-12}	0.000	0.0	
		2.600×10^{-11}	0.000	−67.0	
405[b]	$O(^1D) + N_2 \rightarrow O + N_2$	2.300×10^{-11}	0.000	0.0	[126]
406	$O(^1D) + O_3 \rightarrow O_2 + O + O$	1.200×10^{-10}	0.000	0.0	[126]
407	$O(^1D) + O_3 \rightarrow O_2 + O_2$	1.200×10^{-10}	0.000	0.0	[126]
408[b]	$O(^1D) + NO \rightarrow O_2 + N$	1.700×10^{-10}	0.000	0.0	[126]
409[b]	$O(^1D) + N_2O \rightarrow NO + NO$	7.200×10^{-11}	0.000	0.0	[126]
410[b]	$O(^1D) + N_2O \rightarrow O_2 + N_2$	4.400×10^{-11}	0.000	0.0	[126]
411[b]	$O(^1S) + O \rightarrow O(^1D) + O$	5.000×10^{-11}	0.000	300.0	[182]
412[b]	$O(^1S) + N \rightarrow O + N$	1.000×10^{-12}	0.000	0.0	[126]
413[b]	$O(^1S) + O_2 \rightarrow O(^1D) + O_2$	1.300×10^{-12}	0.000	850.0	[182]
414[b]	$O(^1S) + O_2 \rightarrow O + O + O$	3.000×10^{-12}	0.000	850.0	[126]
415[b]	$O(^1S) + N_2 \rightarrow O + N_2$	1.000×10^{-17}	0.000	0.0	[126]
416[b]	$O(^1S) + O_2(a^1\Delta) \rightarrow O + O_2(4.5eV)$	1.100×10^{-10}	0.000	0.0	[126]
417[b]	$O(^1S) + O_2(a^1\Delta) \rightarrow O(^1D) + O_2(b^1\Sigma)$	2.900×10^{-11}	0.000	0.0	[126]
418[b]	$O(^1S) + O_2(a^1\Delta) \rightarrow O + O + O$	3.200×10^{-11}	0.000	0.0	[126]
419[b]	$O(^1S) + NO \rightarrow O + NO$	2.900×10^{-10}	0.000	0.0	[126]
420[b]	$O(^1S) + NO \rightarrow O(^1D) + NO$	5.100×10^{-10}	0.000	0.0	[126]
421	$O(^1S) + O_3 \rightarrow O_2 + O_2$	2.900×10^{-10}	0.000	0.0	[126]
422	$O(^1S) + O_3 \rightarrow O_2 + O + O(^1D)$	2.900×10^{-10}	0.000	0.0	[126]
423[b]	$O(^1S) + N_2O \rightarrow O + N_2O$	6.300×10^{-12}	0.000	0.0	[126]
424[b]	$O(^1S) + N_2O \rightarrow O(^1D) + N_2O$	3.100×10^{-12}	0.000	0.0	[126]
	Bimolecular nitrogen-oxygen reactions				
425[b]	$N + NO_2 \rightarrow O + O + N_2$	9.100×10^{-13}	0.000	0.0	[126]
426[b]	$N + NO_2 \rightarrow O + N_2O$	3.000×10^{-12}	0.000	0.0	[126]
427[b]	$N + NO_2 \rightarrow N_2 + O_2$	7.000×10^{-13}	0.000	0.0	[126]
428[b]	$N + NO_2 \rightarrow NO + NO$	2.300×10^{-12}	0.000	0.0	[126]
429[b]	$NO + NO \rightarrow N + NO_2$	5.716×10^{-15}	−0.500	39200.0	[126]

Table A.1: (Continued)

No.	Reaction	A (cm^3/s)[a]	n (-)	E_A (K)	Ref.
430[b]	$NO + NO \rightarrow N_2 + O_2$	5.100×10^{-13}	0.000	33660.0	[126]
431	$NO + O_3 \rightarrow O_2 + NO_2$	2.500×10^{-13}	0.000	765.0	[126]
432	$O_2 + O_2 \rightarrow O + O_3$	2.000×10^{-11}	0.000	49800.0	[126]
433	$O_2 + NO_2 \rightarrow NO + O_3$	2.800×10^{-12}	0.000	25400.0	[126]
434	$NO_2 + O_3 \rightarrow O_2 + NO_3$	1.200×10^{-13}	0.000	2450.0	[126]
435	$NO_3 + O_2 \rightarrow NO_2 + O_3$	1.500×10^{-12}	0.000	15020.0	[126]
436[b]	$NO_3 + NO_3 \rightarrow O_2 + NO_2 + NO_2$	4.300×10^{-12}	0.000	3850.0	[126]
437[b]	$N + N \rightarrow N_2^+ + e^-$	2.700×10^{-11}	0.000	67400.0	[126]
438[b]	$N + O \rightarrow NO^+ + e^-$	1.755×10^{-14}	0.500	32000.0	[126]
		7.944×10^{-13}	1.500	32000.0	
	Dissociation of nitrogen-oxygen molecules				
439[c]	$e^- + H_2^+ \rightarrow H^+ + H + e^-$	1.041×10^{-10}	0.412	6299.3	[176]
440	$N_2 + N_2 \rightarrow N + N + N_2$	5.400×10^{-8}	0.000	113200.0	[126]
		-5.400×10^{-8}	0.000	116550.0	
441	$N_2 + O_2 \rightarrow N + N + O_2$	5.400×10^{-8}	0.000	113200.0	[126]
		-5.400×10^{-8}	0.000	116550.0	
442	$N_2 + NO \rightarrow N + N + NO$	5.400×10^{-8}	0.000	113200.0	[126]
		-5.400×10^{-8}	0.000	116550.0	
443	$N_2 + O \rightarrow N + N + O$	3.564×10^{-7}	0.000	113200.0	[126]
		-3.564×10^{-7}	0.000	116550.0	
444	$N_2 + N \rightarrow N + N + N$	3.564×10^{-7}	0.000	113200.0	[126]
		-3.564×10^{-7}	0.000	116550.0	
445	$O_2 + N_2 \rightarrow O + O + N_2$	6.100×10^{-9}	0.000	59380.0	[126]
		-6.100×10^{-9}	0.000	61620.0	
446	$O_2 + O_2 \rightarrow O + O + O_2$	3.599×10^{-8}	0.000	59380.0	[126]
		-3.599×10^{-8}	0.000	61620.0	
447	$O_2 + O \rightarrow O + O + O$	1.281×10^{-7}	0.000	59380.0	[126]
		-1.281×10^{-7}	0.000	61620.0	
448	$O_2 + N \rightarrow O + O + N$	6.100×10^{-9}	0.000	59380.0	[126]
		-6.100×10^{-9}	0.000	61620.0	
449	$O_2 + NO \rightarrow O + O + NO$	6.100×10^{-9}	0.000	59380.0	[126]
		-6.100×10^{-9}	0.000	61620.0	
450	$NO + N_2 \rightarrow N + O + N_2$	8.700×10^{-9}	0.000	75994.0	[126]
451	$NO + O_2 \rightarrow N + O + O_2$	8.700×10^{-9}	0.000	75994.0	[126]
452	$NO + O \rightarrow N + O + O$	1.740×10^{-7}	0.000	75994.0	[126]
453	$NO + N \rightarrow N + O + N$	1.740×10^{-7}	0.000	75994.0	[126]
454	$NO + NO \rightarrow N + O + NO$	1.740×10^{-7}	0.000	75994.0	[126]
455	$O_3 + N_2 \rightarrow O_2 + O + N_2$	6.600×10^{-10}	0.000	11600.0	[126]
456	$O_3 + O_2 \rightarrow O_2 + O + O_2$	2.508×10^{-10}	0.000	11600.0	[126]
457	$O_3 + N \rightarrow O_2 + O + N$	4.158×10^{-9}	0.000	11430.0	[126]
458	$O_3 + O \rightarrow O_2 + O + O$	4.158×10^{-9}	0.000	11430.0	[126]

Table A.1: (Continued)

No.	Reaction	A (cm^3/s)[a]	n (-)	E_A (K)	Ref.
459	$NO_2 + N_2 \rightarrow NO + O + N_2$	6.120×10^{-1}	−2.000	36180.0	[126]
460	$NO_2 + O_2 \rightarrow NO + O + O_2$	4.774×10^{-1}	−2.000	36180.0	[126]
461	$NO_2 + NO \rightarrow NO + O + NO$	4.774×10^{0}	−2.000	36180.0	[126]
462	$NO_2 + NO_2 \rightarrow NO + O + NO_2$	3.611×10^{0}	−2.000	36180.0	[126]
463	$NO_3 + N_2 \rightarrow NO_2 + O + N_2$	2.790×10^{0}	−2.000	25000.0	[126]
464	$NO_3 + O_2 \rightarrow NO_2 + O + O_2$	2.790×10^{0}	−2.000	25000.0	[126]
465	$NO_3 + NO \rightarrow NO_2 + O + NO$	2.790×10^{0}	−2.000	25000.0	[126]
466	$NO_3 + N \rightarrow NO_2 + O + N$	2.790×10^{1}	−2.000	25000.0	[126]
467	$NO_3 + O \rightarrow NO_2 + O + O$	2.790×10^{1}	−2.000	25000.0	[126]
468	$NO_3 + N_2 \rightarrow NO + O_2 + N_2$	5.580×10^{0}	−2.000	25000.0	[126]
469	$NO_3 + O_2 \rightarrow NO + O_2 + O_2$	5.580×10^{0}	−2.000	25000.0	[126]
470	$NO_3 + NO \rightarrow NO + O_2 + NO$	5.580×10^{0}	−2.000	25000.0	[126]
471	$NO_3 + N \rightarrow NO + O_2 + N$	6.696×10^{1}	−2.000	25000.0	[126]
472	$NO_3 + O \rightarrow NO + O_2 + O$	6.696×10^{1}	−2.000	25000.0	[126]
473	$N_2O_5 + M \rightarrow NO_2 + NO_3 + M$	1.666×10^{0}	−4.400	11080.0	[126]
	Recombination of nitrogen-oxygen molecules				
474	$N + N + N_2 \rightarrow N_2 + N_2$	8.300×10^{-34}	0.000	−500.0	[126]
475	$N + N + O_2 \rightarrow N_2 + O_2$	1.800×10^{-33}	0.000	−435.0	[126]
476	$N + N + NO \rightarrow N_2 + NO$	1.800×10^{-33}	0.000	−435.0	[126]
477	$N + N + N \rightarrow N_2 + N$	5.400×10^{-33}	0.000	−435.0	[126]
478	$N + N + O \rightarrow N_2 + O$	5.400×10^{-33}	0.000	−435.0	[126]
479	$O + O + N_2 \rightarrow O_2 + N_2$	2.800×10^{-34}	0.000	−720.0	[126]
480	$O + O + O_2 \rightarrow O_2 + O_2$	4.146×10^{-32}	−0.410	0.0	[126]
481	$O + O + N \rightarrow O_2 + N$	3.317×10^{-32}	−0.410	0.0	[126]
482	$O + O + O \rightarrow O_2 + O$	1.493×10^{-31}	−0.410	0.0	[126]
483	$O + O + NO \rightarrow O_2 + NO$	7.048×10^{-33}	−0.410	0.0	[126]
484	$N + O + N_2 \rightarrow NO + N_2$	1.732×10^{-31}	−0.500	0.0	[126]
485	$N + O + O_2 \rightarrow NO + O_2$	1.732×10^{-31}	−0.500	0.0	[126]
486	$N + O + N \rightarrow NO + N$	5.400×10^{-29}	−1.000	0.0	[126]
487	$N + O + O \rightarrow NO + O$	5.400×10^{-29}	−1.000	0.0	[126]
488	$N + O + NO \rightarrow NO + NO$	5.400×10^{-29}	−1.000	0.0	[126]
489	$O + O_2 + N_2 \rightarrow O_3 + N_2$	2.747×10^{-29}	−1.900	0.0	[126]
490	$O + O_2 + O_2 \rightarrow O_3 + O_2$	3.867×10^{-29}	−1.900	0.0	[126]
491	$O + O_2 + NO \rightarrow O_3 + NO$	3.867×10^{-29}	−1.900	0.0	[126]
492	$O + O_2 + N \rightarrow O_3 + N$	1.100×10^{-34}	0.000	1060.0	[126]
493	$O + O_2 + O \rightarrow O_3 + O$	1.100×10^{-34}	0.000	1060.0	[126]
494	$O + NO + N_2 \rightarrow NO_2 + N_2$	3.451×10^{-27}	−1.800	0.0	[126]
495	$O + NO + O_2 \rightarrow NO_2 + O_2$	2.692×10^{-27}	−1.800	0.0	[126]
496	$O + NO + NO \rightarrow NO_2 + NO$	2.692×10^{-27}	−1.800	0.0	[126]
497	$O + NO_2 + N_2 \rightarrow NO_3 + N_2$	8.010×10^{-27}	−2.000	0.0	[126]
498	$O + NO_2 + O_2 \rightarrow NO_3 + O_2$	8.010×10^{-27}	−2.000	0.0	[126]

Table A.1: (Continued)

No.	Reaction	A (cm^3/s)[a]	n (-)	E_A (K)	Ref.
499	$O + NO_2 + N \rightarrow NO_3 + N$	1.041×10^{-25}	-2.000	0.0	[126]
500	$O + NO_2 + O \rightarrow NO_3 + O$	1.041×10^{-25}	-2.000	0.0	[126]
501	$O + NO_2 + NO \rightarrow NO_3 + NO$	1.922×10^{-26}	-2.000	0.0	[126]
502	$NO_2 + NO_3 + M \rightarrow N_2O_5 + M$	5.302×10^{-20}	-4.100	0.0	[126]
	Positive ion reactions/charge exchange				
503	$N^+ + O \rightarrow N + O^+$	1.000×10^{-12}	0.000	0.0	[126]
504	$N^+ + O_2 \rightarrow O_2^+ + N$	2.800×10^{-10}	0.000	0.0	[126]
505	$N^+ + O_2 \rightarrow NO^+ + O$	2.500×10^{-10}	0.000	0.0	[126]
506	$N^+ + O_2 \rightarrow O^+ + NO$	2.800×10^{-11}	0.000	0.0	[126]
507	$N^+ + O_3 \rightarrow NO^+ + O_2$	5.000×10^{-10}	0.000	0.0	[126]
508	$N^+ + NO \rightarrow NO^+ + N$	8.000×10^{-10}	0.000	0.0	[126]
509	$N^+ + NO \rightarrow N_2^+ + O$	3.000×10^{-12}	0.000	0.0	[126]
510	$N^+ + NO \rightarrow O^+ + N_2$	1.000×10^{-12}	0.000	0.0	[126]
511	$N^+ + N_2O \rightarrow NO^+ + N_2$	5.500×10^{-10}	0.000	0.0	[126]
512	$O^+ + N_2 \rightarrow NO^+ + N$	8.557×10^{-13}	2.013	2137.2	[126]
513	$O^+ + O_2 \rightarrow O_2^+ + O$	3.464×10^{-10}	-0.500	0.0	[126]
514	$O^+ + O_3 \rightarrow O_2^+ + O_2$	1.000×10^{-10}	0.000	0.0	[126]
515	$O^+ + NO \rightarrow NO^+ + O$	2.400×10^{-11}	0.000	0.0	[126]
516	$O^+ + NO \rightarrow O_2^+ + N$	3.000×10^{-12}	0.000	0.0	[126]
517	$O^+ + N(^2D) \rightarrow N^+ + O$	1.300×10^{-10}	0.000	0.0	[126]
518	$O^+ + N_2O \rightarrow NO^+ + NO$	2.300×10^{-10}	0.000	0.0	[126]
519	$O^+ + N_2O \rightarrow N_2O^+ + O$	2.200×10^{-10}	0.000	0.0	[126]
520	$O^+ + N_2O \rightarrow O_2^+ + N_2$	2.000×10^{-11}	0.000	0.0	[126]
521	$O^+ + NO_2 \rightarrow NO_2^+ + O$	1.600×10^{-9}	0.000	0.0	[126]
522	$N_2^+ + O_2 \rightarrow O_2^+ + N_2$	1.039×10^{-9}	-0.500	0.0	[126]
523	$N_2^+ + O \rightarrow NO^+ + N$	2.252×10^{-9}	-0.500	0.0	[126]
524	$N_2^+ + O_3 \rightarrow O_2^+ + O + N_2$	1.000×10^{-10}	0.000	0.0	[126]
525	$N_2^+ + N \rightarrow N^+ + N_2$	2.400×10^{-15}	1.000	0.0	[126]
526	$N_2^+ + NO \rightarrow NO^+ + N_2$	3.300×10^{-10}	0.000	0.0	[126]
527	$N_2^+ + N_2O \rightarrow N_2O^+ + N_2$	5.000×10^{-10}	0.000	0.0	[126]
528	$N_2^+ + N_2O \rightarrow NO^+ + N + N_2$	4.000×10^{-10}	0.000	0.0	[126]
529	$O_2^+ + N_2 \rightarrow NO^+ + NO$	1.000×10^{-17}	0.000	0.0	[126]
530	$O_2^+ + N \rightarrow NO^+ + O$	1.200×10^{-10}	0.000	0.0	[126]
531	$O_2^+ + NO \rightarrow NO^+ + O_2$	6.300×10^{-10}	0.000	0.0	[126]
532	$O_2^+ + NO_2 \rightarrow NO^+ + O_3$	1.000×10^{-11}	0.000	0.0	[126]
533	$O_2^+ + NO_2 \rightarrow NO_2^+ + O_2$	6.600×10^{-10}	0.000	0.0	[126]
534	$N_3^+ + O_2 \rightarrow O_2^+ + N + N_2$	2.300×10^{-11}	0.000	0.0	[126]
535	$N_3^+ + O_2 \rightarrow NO_2^+ + N_2$	4.400×10^{-11}	0.000	0.0	[126]
536	$N_3^+ + N \rightarrow N_2^+ + N_2$	6.600×10^{-11}	0.000	0.0	[126]
537	$N_3^+ + NO \rightarrow NO^+ + N + N_2$	7.000×10^{-11}	0.000	0.0	[126]
538	$N_3^+ + NO \rightarrow N_2O^+ + N_2$	7.000×10^{-11}	0.000	0.0	[126]

Table A.1: (Continued)

No.	Reaction	A (cm^3/s)[a]	n (-)	E_A (K)	Ref.
539	$NO_2^+ + NO \rightarrow NO^+ + NO_2$	2.900×10^{-10}	0.000	0.0	[126]
540	$N_2O^+ + NO \rightarrow NO^+ + N_2O$	2.900×10^{-10}	0.000	0.0	[126]
541	$N_4^+ + N_2 \rightarrow N_2^+ + N_2 + N_2$	1.000×10^{-10}	0.000	0.0	[126]
542	$N_4^+ + O_2 \rightarrow O_2^+ + N_2 + N_2$	2.500×10^{-10}	0.000	0.0	[126]
543	$N_4^+ + O \rightarrow O^+ + N_2 + N_2$	2.500×10^{-10}	0.000	0.0	[126]
544	$N_4^+ + N \rightarrow N^+ + N_2 + N_2$	1.000×10^{-11}	0.000	0.0	[126]
545	$N_4^+ + NO \rightarrow NO^+ + N_2 + N_2$	4.000×10^{-10}	0.000	0.0	[126]
546	$O_4^+ + O_2 \rightarrow O_2^+ + O_2 + O_2$	2.673×10^{4}	−4.000	5030.0	[126]
547	$O_4^+ + O_2(a^1\Delta) \rightarrow O_2^+ + O_2 + O_2$	1.000×10^{-10}	0.000	0.0	[126]
548	$O_4^+ + O_2(b^1\Sigma) \rightarrow O_2^+ + O_2 + O_2$	1.000×10^{-10}	0.000	0.0	[126]
549	$O_4^+ + O \rightarrow O_2^+ + O_3$	3.000×10^{-10}	0.000	0.0	[126]
550	$O_4^+ + NO \rightarrow NO^+ + O_2 + O_2$	1.000×10^{-10}	0.000	0.0	[126]
551	$N^+ + N_2 + N_2 \rightarrow N_3^+ + N_2$	2.706×10^{-24}	−2.100	0.0	[126]
552	$N^+ + O + M \rightarrow NO^+ + M$	1.000×10^{-29}	0.000	0.0	[126]
553	$N^+ + N + M \rightarrow N_2^+ + M$	1.000×10^{-29}	0.000	0.0	[126]
554	$O^+ + N_2 + M \rightarrow NO^+ + N + M$	5.400×10^{-24}	−2.000	0.0	[126]
555	$O^+ + O + M \rightarrow O_2^+ + M$	1.000×10^{-29}	0.000	0.0	[126]
556	$O^+ + N + M \rightarrow NO^+ + M$	1.000×10^{-29}	0.000	0.0	[126]
557	$N_2^+ + N_2 + N_2 \rightarrow N_4^+ + N_2$	1.464×10^{-23}	−2.200	0.0	[126]
558	$N_2^+ + N + N_2 \rightarrow N_3^+ + N_2$	9.000×10^{-30}	0.000	−400.0	[126]
559	$O_2^+ + O_2 + O_2 \rightarrow O_4^+ + O_2$	2.028×10^{-22}	−3.200	0.0	[126]
560	$H^+ + O \rightarrow O^+ + H$	3.800×10^{-10}	0.000	0.0	[129]
561	$H^+ + NO \rightarrow NO^+ + H$	1.900×10^{-9}	0.000	0.0	[129]
562	$O^+ + H \rightarrow H^+ + O$	2.300×10^{-11}	0.500	0.0	[129]
563	$O^+ + H_2 \rightarrow OH^+ + H$	2.000×10^{-9}	0.000	0.0	[129]
564	$O^+ + H_2O \rightarrow H_2O^+ + O$	2.300×10^{-9}	0.000	0.0	[129]
565	$H_2^+ + N_2 \rightarrow N_2^+ + H_2$	1.180×10^{-11}	0.000	2000.0	[129]
566	$H_2^+ + H_2O \rightarrow H_2O^+ + H_2$	3.600×10^{-9}	0.000	0.0	[129]
567	$OH^+ + H \rightarrow O^+ + H_2$	4.460×10^{-10}	0.000	8000.0	[129]
568	$OH^+ + H_2 \rightarrow H_2O^+ + H$	1.500×10^{-9}	0.000	0.0	[129]
569	$OH^+ + H_2O \rightarrow H_2O^+ + OH$	1.600×10^{-10}	0.000	0.0	[129]
570	$N_2^+ + H_2 \rightarrow H_2^+ + N_2$	2.000×10^{-11}	0.000	0.0	[129]
571	$N_2^+ + H_2O \rightarrow H_2O^+ + N_2$	2.200×10^{-9}	0.000	0.0	[129]
572	$NO^+ + H \rightarrow H^+ + NO$	2.620×10^{-9}	0.000	50900.0	[129]
573	$H_2O^+ + O \rightarrow O^+ + H_2O$	4.790×10^{-10}	0.000	10600.0	[129]
574	$H_2O^+ + H \rightarrow OH^+ + H_2$	2.170×10^{-9}	0.000	9000.0	[129]
575	$H_2O^+ + H_2 \rightarrow H_2^+ + H_2O$	6.430×10^{-9}	0.000	31300.0	[129]
576	$H_2O^+ + N_2 \rightarrow N_2^+ + H_2O$	2.310×10^{-9}	0.000	33300.0	[129]
577	$N_4^+ + H_2O \rightarrow H_2O^+ + N_2 + N_2$	1.900×10^{-9}	0.000	0.0	[129]
578	$N^+ + OH \rightarrow NO^+ + H$	3.400×10^{-10}	0.000	0.0	[130]
579	$N^+ + H_2O \rightarrow H_2O^+ + N$	2.600×10^{-9}	0.000	0.0	[130]

Table A.1: (Continued)

No.	Reaction	A (cm^3/s)[a]	n (-)	E_A (K)	Ref.
580	$H_2O^+ + O_2 \rightarrow O_2^+ + H_2O$	2.000×10^{-10}	0.000	0.0	[130]
581	$H_2O^+ + NO \rightarrow NO^+ + H_2O$	5.900×10^{-10}	0.000	0.0	[130]
582	$N^+ + O + H_2O \rightarrow NO^+ + H_2O$	1.000×10^{-29}	0.000	0.0	[130]
583	$O^+ + OH \rightarrow O_2^+ + H$	6.235×10^{-8}	−0.500	0.0	[131]
584	$O^+ + OH \rightarrow OH^+ + O$	6.235×10^{-8}	−0.500	0.0	[131]
585	$OH^+ + O \rightarrow O_2^+ + H$	7.100×10^{-10}	0.000	0.0	[131]
586	$OH^+ + O_2 \rightarrow O_2^+ + OH$	5.900×10^{-10}	0.000	0.0	[131]
587	$OH^+ + OH \rightarrow H_2O^+ + O$	1.212×10^{-8}	−0.500	0.0	[131]
588	$H_2O^+ + O \rightarrow O_2^+ + H_2$	4.000×10^{-11}	0.000	0.0	[131]
	Negative ion reactions				
589	$O^- + O_2(a^1\Delta) \rightarrow O_2^- + O$	1.000×10^{-10}	0.000	0.0	[126]
590	$O^- + O_3 \rightarrow O_3^- + O$	8.000×10^{-10}	0.000	0.0	[126]
591	$O^- + NO_2 \rightarrow NO_2^- + O$	1.200×10^{-9}	0.000	0.0	[126]
592	$O^- + N_2O \rightarrow NO^- + NO$	2.000×10^{-10}	0.000	0.0	[126]
593	$O^- + N_2O \rightarrow N_2O^- + O$	2.000×10^{-12}	0.000	0.0	[126]
594	$O_2^- + O \rightarrow O^- + O_2$	3.300×10^{-10}	0.000	0.0	[126]
595	$O_2^- + O_3 \rightarrow O_3^- + O_2$	3.500×10^{-10}	0.000	0.0	[126]
596	$O_2^- + NO_2 \rightarrow NO_2^- + O_2$	7.000×10^{-10}	0.000	0.0	[126]
597	$O_2^- + NO_3 \rightarrow NO_3^- + O_2$	5.000×10^{-10}	0.000	0.0	[126]
598	$O_3^- + O \rightarrow O_2^- + O_2$	1.000×10^{-11}	0.000	0.0	[126]
599	$O_3^- + NO \rightarrow NO_3^- + O$	1.000×10^{-11}	0.000	0.0	[126]
600	$O_3^- + NO \rightarrow NO_2^- + O_2$	2.600×10^{-12}	0.000	0.0	[126]
601	$O_3^- + NO_2 \rightarrow NO_2^- + O_3$	7.000×10^{-11}	0.000	0.0	[126]
602	$O_3^- + NO_2 \rightarrow NO_3^- + O_2$	2.000×10^{-11}	0.000	0.0	[126]
603	$O_3^- + NO_3 \rightarrow NO_3^- + O_3$	5.000×10^{-10}	0.000	0.0	[126]
604	$NO^- + O_2 \rightarrow O_2^- + NO$	5.000×10^{-10}	0.000	0.0	[126]
605	$NO^- + NO_2 \rightarrow NO_2^- + NO$	7.400×10^{-10}	0.000	0.0	[126]
606	$NO^- + N_2O \rightarrow NO_2^- + N_2$	2.800×10^{-14}	0.000	0.0	[126]
607	$NO_2^- + O_3 \rightarrow NO_3^- + O_2$	1.800×10^{-11}	0.000	0.0	[126]
608	$NO_2^- + NO_2 \rightarrow NO_3^- + NO$	4.000×10^{-12}	0.000	0.0	[126]
609	$NO_2^- + NO_3 \rightarrow NO_3^- + NO_2$	5.000×10^{-10}	0.000	0.0	[126]
610	$NO_2^- + N_2O_5 \rightarrow NO_3^- + NO_2 + NO_2$	7.000×10^{-10}	0.000	0.0	[126]
611	$NO_3^- + NO \rightarrow NO_2^- + NO_2$	3.000×10^{-15}	0.000	0.0	[126]
612	$O_4^- + N_2 \rightarrow O_2^- + O_2 + N_2$	1.000×10^{-10}	0.000	1044.0	[126]
613	$O_4^- + O_2 \rightarrow O_2^- + O_2 + O_2$	1.000×10^{-10}	0.000	1044.0	[126]
614	$O_4^- + O \rightarrow O_3^- + O_2$	4.000×10^{-10}	0.000	0.0	[126]
615	$O_4^- + O \rightarrow O^- + O_2 + O_2$	3.000×10^{-10}	0.000	0.0	[126]
616	$O_4^- + O_2(a^1\Delta) \rightarrow O_2^- + O_2 + O_2$	1.000×10^{-10}	0.000	0.0	[126]
617	$O_4^- + O_2(b^1\Sigma) \rightarrow O_2^- + O_2 + O_2$	1.000×10^{-10}	0.000	0.0	[126]
618	$O_4^- + NO \rightarrow NO_3^- + O_2$	2.500×10^{-10}	0.000	0.0	[126]
619	$O^- + O_2 + M \rightarrow O_3^- + M$	3.300×10^{-28}	−1.000	0.0	[126]

Table A.1: (Continued)

No.	Reaction	A (cm^3/s)[a]	n (-)	E_A (K)	Ref.
620	$O^- + NO + M \rightarrow NO_2^- + M$	1.000×10^{-29}	0.000	0.0	[126]
621	$O_2^- + O_2 + M \rightarrow O_4^- + M$	1.050×10^{-28}	−1.000	0.0	[182]
622	$O_2^- + H \rightarrow OH^- + O$	1.200×10^{-9}	0.000	0.0	[129]
623	$O_2^- + H \rightarrow H^- + O_2$	1.200×10^{-9}	0.000	0.0	[129]
624	$H^- + H_2O \rightarrow OH^- + H_2$	4.800×10^{-9}	0.000	0.0	[131]
625	$O^- + H_2O \rightarrow OH^- + OH$	1.400×10^{-9}	0.000	0.0	[131]
	Ion-ion recombination				
626	$O^- + N^+ \rightarrow O + N$	3.464×10^{-6}	−0.500	0.0	[182]
627	$O^- + N_2^+ \rightarrow O + N_2$	3.464×10^{-6}	−0.500	0.0	[182]
628	$O^- + O^+ \rightarrow O + O$	3.464×10^{-6}	−0.500	0.0	[182]
629	$O^- + O_2^+ \rightarrow O + O_2$	3.464×10^{-6}	−0.500	0.0	[182]
630	$O^- + NO^+ \rightarrow O + NO$	3.464×10^{-6}	−0.500	0.0	[182]
631	$O^- + N_2O^+ \rightarrow O + N_2O$	3.464×10^{-6}	−0.500	0.0	[182]
632	$O^- + NO_2^+ \rightarrow O + NO_2$	3.464×10^{-6}	−0.500	0.0	[182]
633	$O_2^- + N^+ \rightarrow O_2 + N$	3.464×10^{-6}	−0.500	0.0	[182]
634	$O_2^- + N_2^+ \rightarrow O_2 + N_2$	3.464×10^{-6}	−0.500	0.0	[182]
635	$O_2^- + O^+ \rightarrow O_2 + O$	3.464×10^{-6}	−0.500	0.0	[182]
636	$O_2^- + O_2^+ \rightarrow O_2 + O_2$	3.464×10^{-6}	−0.500	0.0	[182]
637	$O_2^- + NO^+ \rightarrow O_2 + NO$	3.464×10^{-6}	−0.500	0.0	[182]
638	$O_2^- + N_2O^+ \rightarrow O_2 + N_2O$	3.464×10^{-6}	−0.500	0.0	[182]
639	$O_2^- + NO_2^+ \rightarrow O_2 + NO_2$	3.464×10^{-6}	−0.500	0.0	[182]
640	$O_3^- + N^+ \rightarrow O_3 + N$	3.464×10^{-6}	−0.500	0.0	[182]
641	$O_3^- + N_2^+ \rightarrow O_3 + N_2$	3.464×10^{-6}	−0.500	0.0	[182]
642	$O_3^- + O^+ \rightarrow O_3 + O$	3.464×10^{-6}	−0.500	0.0	[182]
643	$O_3^- + O_2^+ \rightarrow O_3 + O_2$	3.464×10^{-6}	−0.500	0.0	[182]
644	$O_3^- + NO^+ \rightarrow O_3 + NO$	3.464×10^{-6}	−0.500	0.0	[182]
645	$O_3^- + N_2O^+ \rightarrow O_3 + N_2O$	3.464×10^{-6}	−0.500	0.0	[182]
646	$O_3^- + NO_2^+ \rightarrow O_3 + NO_2$	3.464×10^{-6}	−0.500	0.0	[182]
647	$NO^- + N^+ \rightarrow NO + N$	3.464×10^{-6}	−0.500	0.0	[182]
648	$NO^- + N_2^+ \rightarrow NO + N_2$	3.464×10^{-6}	−0.500	0.0	[182]
649	$NO^- + O^+ \rightarrow NO + O$	3.464×10^{-6}	−0.500	0.0	[182]
650	$NO^- + O_2^+ \rightarrow NO + O_2$	3.464×10^{-6}	−0.500	0.0	[182]
651	$NO^- + NO^+ \rightarrow NO + NO$	3.464×10^{-6}	−0.500	0.0	[182]
652	$NO^- + N_2O^+ \rightarrow NO + N_2O$	3.464×10^{-6}	−0.500	0.0	[182]
653	$NO^- + NO_2^+ \rightarrow NO + NO_2$	3.464×10^{-6}	−0.500	0.0	[182]
654	$N_2O^- + N^+ \rightarrow N_2O + N$	3.464×10^{-6}	−0.500	0.0	[182]
655	$N_2O^- + N_2^+ \rightarrow N_2O + N_2$	3.464×10^{-6}	−0.500	0.0	[182]
656	$N_2O^- + O^+ \rightarrow N_2O + O$	3.464×10^{-6}	−0.500	0.0	[182]
657	$N_2O^- + O_2^+ \rightarrow N_2O + O_2$	3.464×10^{-6}	−0.500	0.0	[182]
658	$N_2O^- + NO^+ \rightarrow N_2O + NO$	3.464×10^{-6}	−0.500	0.0	[182]
659	$N_2O^- + N_2O^+ \rightarrow N_2O + N_2O$	3.464×10^{-6}	−0.500	0.0	[182]

Table A.1: (Continued)

No.	Reaction	A (cm^3/s)[a]	n (-)	E_A (K)	Ref.
660	$N_2O^- + NO_2^+ \rightarrow N_2O + NO_2$	3.464×10^{-6}	−0.500	0.0	[182]
661	$NO_2^- + N^+ \rightarrow NO_2 + N$	3.464×10^{-6}	−0.500	0.0	[182]
662	$NO_2^- + N_2^+ \rightarrow NO_2 + N_2$	3.464×10^{-6}	−0.500	0.0	[182]
663	$NO_2^- + O^+ \rightarrow NO_2 + O$	3.464×10^{-6}	−0.500	0.0	[182]
664	$NO_2^- + O_2^+ \rightarrow NO_2 + O_2$	3.464×10^{-6}	−0.500	0.0	[182]
665	$NO_2^- + NO^+ \rightarrow NO_2 + NO$	3.464×10^{-6}	−0.500	0.0	[182]
666	$NO_2^- + N_2O^+ \rightarrow NO_2 + N_2O$	3.464×10^{-6}	−0.500	0.0	[182]
667	$NO_2^- + NO_2^+ \rightarrow NO_2 + NO_2$	3.464×10^{-6}	−0.500	0.0	[182]
668	$NO_3^- + N^+ \rightarrow NO_3 + N$	3.464×10^{-6}	−0.500	0.0	[182]
669	$NO_3^- + N_2^+ \rightarrow NO_3 + N_2$	3.464×10^{-6}	−0.500	0.0	[182]
670	$NO_3^- + O^+ \rightarrow NO_3 + O$	3.464×10^{-6}	−0.500	0.0	[182]
671	$NO_3^- + O_2^+ \rightarrow NO_3 + O_2$	3.464×10^{-6}	−0.500	0.0	[182]
672	$NO_3^- + NO^+ \rightarrow NO_3 + NO$	3.464×10^{-6}	−0.500	0.0	[182]
673	$NO_3^- + N_2O^+ \rightarrow NO_3 + N_2O$	3.464×10^{-6}	−0.500	0.0	[182]
674	$NO_3^- + NO_2^+ \rightarrow NO_3 + NO_2$	3.464×10^{-6}	−0.500	0.0	[182]
675	$O^- + N_2^+ \rightarrow O + N + N$	1.000×10^{-7}	0.000	0.0	[182]
676	$O^- + N_3^+ \rightarrow O + N + N_2$	1.000×10^{-7}	0.000	0.0	[182]
677	$O^- + N_4^+ \rightarrow O + N_2 + N_2$	1.000×10^{-7}	0.000	0.0	[182]
678	$O^- + O_2^+ \rightarrow O + O + O$	1.000×10^{-7}	0.000	0.0	[182]
679	$O^- + O_4^+ \rightarrow O + O_2 + O_2$	1.000×10^{-7}	0.000	0.0	[182]
680	$O^- + NO^+ \rightarrow O + N + O$	1.000×10^{-7}	0.000	0.0	[182]
681	$O^- + N_2O^+ \rightarrow O + N_2 + O$	1.000×10^{-7}	0.000	0.0	[182]
682	$O^- + NO_2^+ \rightarrow O + N + O_2$	1.000×10^{-7}	0.000	0.0	[182]
683	$O_2^- + N_2^+ \rightarrow O_2 + N + N$	1.000×10^{-7}	0.000	0.0	[182]
684	$O_2^- + N_3^+ \rightarrow O_2 + N + N_2$	1.000×10^{-7}	0.000	0.0	[182]
685	$O_2^- + N_4^+ \rightarrow O_2 + N_2 + N_2$	1.000×10^{-7}	0.000	0.0	[182]
686	$O_2^- + O_2^+ \rightarrow O_2 + O + O$	1.000×10^{-7}	0.000	0.0	[182]
687	$O_2^- + O_4^+ \rightarrow O_2 + O_2 + O_2$	1.000×10^{-7}	0.000	0.0	[182]
688	$O_2^- + NO^+ \rightarrow O_2 + N + O$	1.000×10^{-7}	0.000	0.0	[182]
689	$O_2^- + N_2O^+ \rightarrow O_2 + N_2 + O$	1.000×10^{-7}	0.000	0.0	[182]
690	$O_2^- + NO_2^+ \rightarrow O_2 + N + O_2$	1.000×10^{-7}	0.000	0.0	[182]
691	$O_3^- + N_2^+ \rightarrow O_3 + N + N$	1.000×10^{-7}	0.000	0.0	[182]
692	$O_3^- + N_3^+ \rightarrow O_3 + N + N_2$	1.000×10^{-7}	0.000	0.0	[182]
693	$O_3^- + N_4^+ \rightarrow O_3 + N_2 + N_2$	1.000×10^{-7}	0.000	0.0	[182]
694	$O_3^- + O_2^+ \rightarrow O_3 + O + O$	1.000×10^{-7}	0.000	0.0	[182]
695	$O_3^- + O_4^+ \rightarrow O_3 + O_2 + O_2$	1.000×10^{-7}	0.000	0.0	[182]
696	$O_3^- + NO^+ \rightarrow O_3 + N + O$	1.000×10^{-7}	0.000	0.0	[182]
697	$O_3^- + N_2O^+ \rightarrow O_3 + N_2 + O$	1.000×10^{-7}	0.000	0.0	[182]
698	$O_3^- + NO_2^+ \rightarrow O_3 + N + O_2$	1.000×10^{-7}	0.000	0.0	[182]
699	$NO^- + N_2^+ \rightarrow NO + N + N$	1.000×10^{-7}	0.000	0.0	[182]
700	$NO^- + N_3^+ \rightarrow NO + N + N_2$	1.000×10^{-7}	0.000	0.0	[182]

Table A.1: (Continued)

No.	Reaction	A (cm^3/s)[a]	n (-)	E_A (K)	Ref.
701	$NO^- + N_4^+ \rightarrow NO + N_2 + N_2$	1.000×10^{-7}	0.000	0.0	[182]
702	$NO^- + O_2^+ \rightarrow NO + O + O$	1.000×10^{-7}	0.000	0.0	[182]
703	$NO^- + O_4^+ \rightarrow NO + O_2 + O_2$	1.000×10^{-7}	0.000	0.0	[182]
704	$NO^- + NO^+ \rightarrow NO + N + O$	1.000×10^{-7}	0.000	0.0	[182]
705	$NO^- + N_2O^+ \rightarrow NO + N_2 + O$	1.000×10^{-7}	0.000	0.0	[182]
706	$NO^- + NO_2^+ \rightarrow NO + N + O_2$	1.000×10^{-7}	0.000	0.0	[182]
707	$N_2O^- + N_2^+ \rightarrow N_2O + N + N$	1.000×10^{-7}	0.000	0.0	[182]
708	$N_2O^- + N_3^+ \rightarrow N_2O + N + N_2$	1.000×10^{-7}	0.000	0.0	[182]
709	$N_2O^- + N_4^+ \rightarrow N_2O + N_2 + N_2$	1.000×10^{-7}	0.000	0.0	[182]
710	$N_2O^- + O_2^+ \rightarrow N_2O + O + O$	1.000×10^{-7}	0.000	0.0	[182]
711	$N_2O^- + O_4^+ \rightarrow N_2O + O_2 + O_2$	1.000×10^{-7}	0.000	0.0	[182]
712	$N_2O^- + NO^+ \rightarrow N_2O + N + O$	1.000×10^{-7}	0.000	0.0	[182]
713	$N_2O^- + N_2O^+ \rightarrow N_2O + N_2 + O$	1.000×10^{-7}	0.000	0.0	[182]
714	$N_2O^- + NO_2^+ \rightarrow N_2O + N + O_2$	1.000×10^{-7}	0.000	0.0	[182]
715	$NO_2^- + N_2^+ \rightarrow NO_2 + N + N$	1.000×10^{-7}	0.000	0.0	[182]
716	$NO_2^- + N_3^+ \rightarrow NO_2 + N + N_2$	1.000×10^{-7}	0.000	0.0	[182]
717	$NO_2^- + N_4^+ \rightarrow NO_2 + N_2 + N_2$	1.000×10^{-7}	0.000	0.0	[182]
718	$NO_2^- + O_2^+ \rightarrow NO_2 + O + O$	1.000×10^{-7}	0.000	0.0	[182]
719	$NO_2^- + O_4^+ \rightarrow NO_2 + O_2 + O_2$	1.000×10^{-7}	0.000	0.0	[182]
720	$NO_2^- + NO^+ \rightarrow NO_2 + N + O$	1.000×10^{-7}	0.000	0.0	[182]
721	$NO_2^- + N_2O^+ \rightarrow NO_2 + N_2 + O$	1.000×10^{-7}	0.000	0.0	[182]
722	$NO_2^- + NO_2^+ \rightarrow NO_2 + N + O_2$	1.000×10^{-7}	0.000	0.0	[182]
723	$NO_3^- + N_2^+ \rightarrow NO_3 + N + N$	1.000×10^{-7}	0.000	0.0	[182]
724	$NO_3^- + N_3^+ \rightarrow NO_3 + N + N_2$	1.000×10^{-7}	0.000	0.0	[182]
725	$NO_3^- + N_4^+ \rightarrow NO_3 + N_2 + N_2$	1.000×10^{-7}	0.000	0.0	[182]
726	$NO_3^- + O_2^+ \rightarrow NO_3 + O + O$	1.000×10^{-7}	0.000	0.0	[182]
727	$NO_3^- + O_4^+ \rightarrow NO_3 + O_2 + O_2$	1.000×10^{-7}	0.000	0.0	[182]
728	$NO_3^- + NO^+ \rightarrow NO_3 + N + O$	1.000×10^{-7}	0.000	0.0	[182]
729	$NO_3^- + N_2O^+ \rightarrow NO_3 + N_2 + O$	1.000×10^{-7}	0.000	0.0	[182]
730	$NO_3^- + NO_2^+ \rightarrow NO_3 + N + O_2$	1.000×10^{-7}	0.000	0.0	[182]
731	$O_4^- + N^+ \rightarrow O_2 + O_2 + N$	1.000×10^{-7}	0.000	0.0	[182]
732	$O_4^- + N_2^+ \rightarrow O_2 + O_2 + N_2$	1.000×10^{-7}	0.000	0.0	[182]
733	$O_4^- + O^+ \rightarrow O_2 + O_2 + O$	1.000×10^{-7}	0.000	0.0	[182]
734	$O_4^- + O_2^+ \rightarrow O_2 + O_2 + O_2$	1.000×10^{-7}	0.000	0.0	[182]
735	$O_4^- + NO^+ \rightarrow O_2 + O_2 + NO$	1.000×10^{-7}	0.000	0.0	[182]
736	$O_4^- + N_2O^+ \rightarrow O_2 + O_2 + N_2O$	1.000×10^{-7}	0.000	0.0	[182]
737	$O_4^- + NO_2^+ \rightarrow O_2 + O_2 + NO_2$	1.000×10^{-7}	0.000	0.0	[182]
738	$O_4^- + N_3^+ \rightarrow O_2 + O_2 + N_2 + N$	1.000×10^{-7}	0.000	0.0	[182]
739	$O_4^- + N_4^+ \rightarrow O_2 + O_2 + N_2 + N_2$	1.000×10^{-7}	0.000	0.0	[182]
740	$O_4^- + O_4^+ \rightarrow O_2 + O_2 + O_2 + O_2$	1.000×10^{-7}	0.000	0.0	[182]
741	$O^- + N^+ + M \rightarrow O + N + M$	3.118×10^{-19}	−2.500	0.0	[182]

Table A.1: (Continued)

No.	Reaction	A (cm^3/s)[a]	n (-)	E_A (K)	Ref.
742	$O^- + N_2^+ + M \rightarrow O + N_2 + M$	3.118×10^{-19}	−2.500	0.0	[182]
743	$O^- + O^+ + M \rightarrow O + O + M$	3.118×10^{-19}	−2.500	0.0	[182]
744	$O^- + O_2^+ + M \rightarrow O + O_2 + M$	3.118×10^{-19}	−2.500	0.0	[182]
745	$O^- + NO^+ + M \rightarrow O + NO + M$	3.118×10^{-19}	−2.500	0.0	[182]
746	$O_2^- + N^+ + M \rightarrow O_2 + N + M$	3.118×10^{-19}	−2.500	0.0	[182]
747	$O_2^- + N_2^+ + M \rightarrow O_2 + N_2 + M$	3.118×10^{-19}	−2.500	0.0	[182]
748	$O_2^- + O^+ + M \rightarrow O_2 + O + M$	3.118×10^{-19}	−2.500	0.0	[182]
749	$O_2^- + O_2^+ + M \rightarrow O_2 + O_2 + M$	3.118×10^{-19}	−2.500	0.0	[182]
750	$O_2^- + NO^+ + M \rightarrow O_2 + NO + M$	3.118×10^{-19}	−2.500	0.0	[182]
751	$O^- + N^+ + M \rightarrow NO + M$	3.118×10^{-19}	−2.500	0.0	[182]
752	$O^- + N_2^+ + M \rightarrow N_2O + M$	3.118×10^{-19}	−2.500	0.0	[182]
753	$O^- + O^+ + M \rightarrow O_2 + M$	3.118×10^{-19}	−2.500	0.0	[182]
754	$O^- + O_2^+ + M \rightarrow O_3 + M$	3.118×10^{-19}	−2.500	0.0	[182]
755	$O^- + NO^+ + M \rightarrow NO_2 + M$	3.118×10^{-19}	−2.500	0.0	[182]
756	$O_2^- + N^+ + M \rightarrow NO_2 + M$	3.118×10^{-19}	−2.500	0.0	[182]
757	$O_2^- + O^+ + M \rightarrow O_3 + M$	3.118×10^{-19}	−2.500	0.0	[182]
758	$O_2^- + NO^+ + M \rightarrow NO_3 + M$	3.118×10^{-19}	−2.500	0.0	[182]
759	$H^- + H^+ \rightarrow H + H$	6.750×10^{-6}	−0.500	0.0	[129]
760	$H_2O^+ + O^- \rightarrow H_2O + O$	4.000×10^{-7}	0.000	0.0	[130]
761	$H_2O^+ + O_2^- \rightarrow H_2O + O_2$	4.000×10^{-7}	0.000	0.0	[130]
762	$O_3^- + N^+ + M \rightarrow O_3 + N + M$	3.118×10^{-19}	−2.500	0.0	[182]
763	$O_3^- + N_2^+ + M \rightarrow O_3 + N_2 + M$	3.118×10^{-19}	−2.500	0.0	[182]
764	$O_3^- + O^+ + M \rightarrow O_3 + O + M$	3.118×10^{-19}	−2.500	0.0	[182]
765	$O_3^- + O_2^+ + M \rightarrow O_3 + O_2 + M$	3.118×10^{-19}	−2.500	0.0	[182]
766	$O_3^- + NO^+ + M \rightarrow O_3 + NO + M$	3.118×10^{-19}	−2.500	0.0	[182]
767	$O_3^- + N_2O^+ + M \rightarrow O_3 + N_2O + M$	3.118×10^{-19}	−2.500	0.0	[182]
768	$O_3^- + NO_2^+ + M \rightarrow O_3 + NO_2 + M$	3.118×10^{-19}	−2.500	0.0	[182]
769	$NO^- + N^+ + M \rightarrow NO + N + M$	3.118×10^{-19}	−2.500	0.0	[182]
770	$NO^- + N_2^+ + M \rightarrow NO + N_2 + M$	3.118×10^{-19}	−2.500	0.0	[182]
771	$NO^- + O^+ + M \rightarrow NO + O + M$	3.118×10^{-19}	−2.500	0.0	[182]
772	$NO^- + O_2^+ + M \rightarrow NO + O_2 + M$	3.118×10^{-19}	−2.500	0.0	[182]
773	$NO^- + NO^+ + M \rightarrow NO + NO + M$	3.118×10^{-19}	−2.500	0.0	[182]
774	$NO^- + N_2O^+ + M \rightarrow NO + N_2O + M$	3.118×10^{-19}	−2.500	0.0	[182]
775	$NO^- + NO_2^+ + M \rightarrow NO + NO_2 + M$	3.118×10^{-19}	−2.500	0.0	[182]
776	$N_2O^- + N^+ + M \rightarrow N_2O + N + M$	3.118×10^{-19}	−2.500	0.0	[182]
777	$N_2O^- + N_2^+ + M \rightarrow N_2O + N_2 + M$	3.118×10^{-19}	−2.500	0.0	[182]
778	$N_2O^- + O^+ + M \rightarrow N_2O + O + M$	3.118×10^{-19}	−2.500	0.0	[182]
779	$N_2O^- + O_2^+ + M \rightarrow N_2O + O_2 + M$	3.118×10^{-19}	−2.500	0.0	[182]
780	$N_2O^- + NO^+ + M \rightarrow N_2O + NO + M$	3.118×10^{-19}	−2.500	0.0	[182]
781	$N_2O^- + N_2O^+ + M \rightarrow N_2O + N_2O + M$	3.118×10^{-19}	−2.500	0.0	[182]
782	$N_2O^- + NO_2^+ + M \rightarrow N_2O + NO_2 + M$	3.118×10^{-19}	−2.500	0.0	[182]

Table A.1: (Continued)

No.	Reaction	A (cm^3/s)[a]	n (-)	E_A (K)	Ref.
783	$NO_2^- + N^+ + M \rightarrow NO_2 + N + M$	3.118×10^{-19}	-2.500	0.0	[182]
784	$NO_2^- + N_2^+ + M \rightarrow NO_2 + N_2 + M$	3.118×10^{-19}	-2.500	0.0	[182]
785	$NO_2^- + O^+ + M \rightarrow NO_2 + O + M$	3.118×10^{-19}	-2.500	0.0	[182]
786	$NO_2^- + O_2^+ + M \rightarrow NO_2 + O_2 + M$	3.118×10^{-19}	-2.500	0.0	[182]
787	$NO_2^- + NO^+ + M \rightarrow NO_2 + NO + M$	3.118×10^{-19}	-2.500	0.0	[182]
788	$NO_2^- + N_2O^+ + M \rightarrow NO_2 + N_2O + M$	3.118×10^{-19}	-2.500	0.0	[182]
789	$NO_2^- + NO_2^+ + M \rightarrow NO_2 + NO_2 + M$	3.118×10^{-19}	-2.500	0.0	[182]
790	$NO_3^- + N^+ + M \rightarrow NO_3 + N + M$	3.118×10^{-19}	-2.500	0.0	[182]
791	$NO_3^- + N_2^+ + M \rightarrow NO_3 + N_2 + M$	3.118×10^{-19}	-2.500	0.0	[182]
792	$NO_3^- + O^+ + M \rightarrow NO_3 + O + M$	3.118×10^{-19}	-2.500	0.0	[182]
793	$NO_3^- + O_2^+ + M \rightarrow NO_3 + O_2 + M$	3.118×10^{-19}	-2.500	0.0	[182]
794	$NO_3^- + NO^+ + M \rightarrow NO_3 + NO + M$	3.118×10^{-19}	-2.500	0.0	[182]
795	$NO_3^- + N_2O^+ + M \rightarrow NO_3 + N_2O + M$	3.118×10^{-19}	-2.500	0.0	[182]
796	$NO_3^- + NO_2^+ + M \rightarrow NO_3 + NO_2 + M$	3.118×10^{-19}	-2.500	0.0	[182]

[a] 1/s and cm^6/s for single and three–body reactions, respectively.

[b] retained in reduced mechanism.

[c] calculated from electron-impact cross sections integrated over Maxwellian EEDF.